ATOMIC MAGNETOMETRY FOR NUCLEAR THREAT REDUCTION APPLICATIONS

by

ABIGAIL RICHARDS

A thesis submitted to the University of Birmingham for the degree of

DOCTOR OF PHILOSOPHY

College of Engineering and Physical Sciences

School of Physics and Astronomy

University of Birmingham

March 2021

Abstract

The work within this thesis explores the applicability of atomic magnetometry to nuclear threat reduction applications. The scope of nuclear threat reduction is explored in the context of UK Government strategy with research conducted at the Atomic Weapons Establishment. An application space is defined which includes nuclear treaty verification, nuclear forensics and detection science. Within these areas, the requirement to detect shielded nuclear and radiological materials is established and eddy current induction methods are proposed to meet the detection of a sub-set of these materials.

Eddy current induction measurements are conventionally met using coil based technologies, however, the sensitivities of these systems increase as a function frequency. Eddy current induction is a frequency dependent measurement, where penetration through an object is reduced at larger values due to the skin-depth effect. These factors combine to be counterproductive for the measurement of objects in thickly shielded configurations. Atomic magnetometers, which measure magnetic fields through the inference of Zeeman splitting within alkali metal vapours, are proposed as an alternative to coil based sensors. Atomic magnetometer technologies benefit from high sensitivities which can be achieved across broad range of frequencies.

Two systems are explored within this work, the first focusses on the detection of targets in challenging shielding configurations. These include through high conductivity (aluminium), ferrous (steel) and high density (lead) materials which necessitated low frequency measurements and were achieved using a commercially available atomic

magnetometer. The second system examines the detection of smaller unshielded objects with a focus on tuning the excitation frequency to higher values. Tuning the frequency enabled the maximisation of the magnetic field phase response of nuclear materials such as uranium and plutonium. This was achieved by constructing a radio-frequency atomic magnetometer.

In the low frequency regime, an imaging system was constructed that allowed raster scan images of high conductivity materials to be obtained behind aluminium shielding up to 63 mm thick at distances > 200 mm. These same objects were also imaged behind steel plates up to 12 mm thick and lead shielding 100 mm thick, where these values represent the maximum thickness tested. These high conductivity objects are of interest for the confirmation of declarations made within treaty verification or for the detection of illicit items in bag/personnel scanning. Lower conductivity materials such as conductivity surrogates for uranium were imaged behind 35 mm of aluminium and the aforementioned material thickness values for steel and lead.

In the high frequency regime, a rubidium based radio-frequency magnetometer was constructed, optimised and integrated into an eddy current imaging system. Images of the lower conductivity plutonium surrogate were obtained at frequencies above 20 kHz. Additional work was identified across both the magnetometer and the imaging system to allow the full sensitivity of the system to be exploited. Outside of the imaging function of the system, the frequency of the eddy current excitation field was successfully tuned to enhance the measurement of the uranium and plutonium surrogates over higher conductivity samples such as copper and aluminium.

Acknowledgements

The work in this thesis was funded by the Atomic Weapons Establishment as contracted by the Ministry of Defence, Defence Nuclear Organisation and the Home Office, Office of Security and Counter Terrorism. At AWE, I would like to thank my supervisor, Joe Watson, who encouraged me to pursue a PhD and has provided invaluable help. I would also like to thank my other colleagues at AWE, in particular Neil Gaspar who has given up much of his own time to help me further develop my work. Additionally, I'd like to thank Preetma Soin who has been a constant friend and given me so much valuable advice and support.

I would also like to thank my supervisors from Birmingham University: Vera Guarerra and Kai Bongs who have always been willing to answer my questions. Additionally, I am thankful to other university partners who have involved me in their academic communities.

Foremost, I would like to thank my family and friends, especially my husband, Anthony, who has been supportive and endlessly patient.

Contents

List of Figures

List of Tables

Abbreviations

AM	atomic magnetometer
AOM	acousto-optical modulator
AWE	Atomic Weapons Establishment
CBRN	chemical, biological, radiological, nuclear
CBRNE	chemical, biological, radiological, nuclear, explosive
CTBT	Comprehensive Test Ban Treaty
CONTEST	Counter Terrorism Strategy
DS	Detection Science
DU	depleted uranium
ECI	eddy current induction
FR	full reference; used in IQA
IQA	image quality analysis
MIT	magnetic induction tomography
MTJ	magnetic tunnel junction
NDT	non-destructive quality testing
NF	Nuclear Forensics
NORM	naturally occurring radioactive sources
NR	no reference; used in IQA
NSS	National Security Strategy
NTR	Nuclear Threat Reduction
NTV	Nuclear Treaty Verification
RF	radio-frequency
RR	reduced-reference; used in IQA
SERF	Spin-Exchange Relaxation Free
SNM	special nuclear materials
SQUID	Superconducting Quantum Interference Device
SVD	Single Value Decomposition
TRL	Technology Readiness Level
UXO	unexploded ordnance

Conductivity of typical materials

Copper	59 MS/m
Aluminium	37 MS/m
Hafnium	3 MS/m
Uranium	3 MS/m
Steel	7 MS/m
Plutonium	0.7 MS/m
Bismuth	0.8 MS/m
Biological	0.007-0.5 S/m

High Conductivity	≥ 10 MS/m	Copper, Aluminium
Medium	1 MS/m ≤ 0.1 MS/m	Uranium, Plutonium
Low	≤ 0.1 MS/m	Semi-Conductors, Biological Tissue

Chapter 1

Introduction

The Atomic Weapons Establishment (AWE) was founded in 1952 with the objective of developing the UK's atomic programme. Based at Aldermaston in Berkshire, AWE maintains the UK's nuclear warhead stockpile, covering the entire life cycle of a weapon from development to construction, maintenance and decommissioning. These activities are conducted without the use of nuclear tests since 1996 in line with the Comprehensive Test Ban Treaty (CTBT). As such, AWE has a comprehensive programme to certify the safety and performance of the deterrent to provide continual assurance to the UK's policy on nuclear deterrence.

In addition to activities supporting the warhead programme, AWE also supplies the UK Government with expertise to understand and reduce radiological and nuclear threats in the form of the Nuclear Threat Reduction (NTR) programme. NTR includes the detection and identification of radiological and nuclear materials or devices; it has applications ranging from portal monitoring at borders, to the verification of international treaties. Within each of these areas there is a requirement to conduct fundamental level research for the continued development of detection technologies and the generation of new sensors, categorised as low Technology Readiness Level (TRL). NTR is tasked with developing low-TRL novel detection methods to address nuclear threats; inclusive

of non-radiological signatures. One such signature is provided by eddy current induction (ECI).

ECI is commonly utilised within security applications for personnel screening. This technology uses an AC excitation magnetic field to induce circulating currents within a conductive object which in turn generate a characteristic magnetic signature; this response can be detected using a magnetometer. The premise of ECI is employed across a number of industries, one of the longest standing is non-destructive quality testing (NDT). NDT uses the ECI signature to examine components in real time for defects as part of quality control within production. Examples of this include the inspection of aircraft components, pipes and waste for the sorting of recyclable materials. In addition to these industrial applications and security screening, magnetic induction is also used in more specialised scenarios such as the detection of UneXploded Ordnance (UXO).

ECI is currently investigated within NTR with a focus on the use of induction based magnetometers. Coil based detection systems for ECI are widely used, however, one disadvantage is that they have a sensitivity which scales linearly with the frequency of the excitation field that makes them unsuitable for thick shielding configurations. This thesis discusses the use of atomic magnetometers (AMs), a comparatively new technology, as a more sensitive replacement for induction magnetometers across both low and high frequency regimes.

This work is motivated within NTR as the use of more sensitive magnetometers could improve the measurement of ECI signatures for the detection of less conductive materials. This would include medium conductivity materials such as uranium (3 MS/m) or plutonium (0.8 MS/m) in more challenging detection scenarios, for example, through thick, highly conductive or ferrous shielding.

The following Section explores the NTR problem space in more detail, providing context on the differing applications, objects of interest and detection scenarios. Definition of these factors allows identification of areas where AMs could add value and areas in

which the technology may not currently be practical. The remainder of this Chapter discusses the current applications and technology used within ECI.

1.1 NTR Motivation

The context for NTR activities is discussed in the National Security Strategy (NSS) published by the UK Government in 2010 [1]. The NSS outlines a tier system for the categorisation of national security priorities. The top two tiers, indicating the highest priorities, include the following risks:

- Tier 1: International terrorism affecting the UK or its interests including the use of chemical, biological, radiological or nuclear (CBRN) attacks.
- Tier 2: An attack on the UK or its overseas territories by another state or proxy through the use of CBRN weapons.

Additional detail tackling the tier 1 risk can be found within the Home Office 2018 Counter Terrorism Strategy (CONTEST) [2]. This document defines a number of pillars which group the homeland and overseas response, of which the PROTECT pillar encompasses the following targeted by the NTR mission:

- Enhancement of capability to detect activities involving chemical, biological, radiological, nuclear and explosive (CBRNE) materials.
- Maintain and develop the UK capability for screening and detection technologies at the border, including the development and deployment of enhanced innovative systems.
- Reduction of the threat from radiological and nuclear weapons through providing expertise and assistance to states for the implementation of the UN Security Council Resolution 1540. This resolution imposes obligations to nuclear non-

proliferation including prevention of non-state actors from acquiring, transferring or using nuclear weapons and their delivery systems.

- Initial and specialist response to an incident supported by government agencies including AWE for nuclear events.

These documents provide the motivation for the NTR programme from the UK Government and broadly focuses on the detection of threat objects/materials. However, NTR can be sub-divided into a number of specialist areas with specific applications, these include:

- Nuclear Treaty Verification (NTV): Development of methodologies and technologies to advise the UK Government on the management of nuclear arms-control verification treaties. This includes fulfilling the commitment to the CTBT with international monitoring and verification. Work is also conducted towards the verification of declarations made on nuclear disarmament through the inspection of warhead components within sealed containers. NTV is required to confirm the contents of containers whilst respecting the non-proliferation of warhead technologies from other states.

- Nuclear Forensics (NF): Response to scenarios ranging from a serious nuclear incident to the discovery of materials outside of regulatory control (e.g. resulting from theft or illicit trafficking).

- Detection Science (DS): Homeland security and in-land detection and identification of radiological and nuclear materials, including the development of new detector technologies.

In an effort to populate a risk-application matrix within which the use of atomic magnetometry can be assessed, the threat materials as defined within the NSS and CONTEST are grouped and specified in more detail.

- Group 1, Chemical and Biological: The Chemical Weapons Convention (CWC) [3] and Biological Weapons Convention (BWC) [4] define these threats as toxic chemical or biological substances that can cause death, temporary incapacitation or permanent harm.

- Group 2, Radiological: Materials with an alpha, beta or gamma emission that are not classified as nuclear.

- Group 3, Nuclear: The International Atomic Energy Agency (IAEA) defines nuclear material as source material or special fissionable materials. Where source material specifically refers to uranium (U) in natural isotope mixtures (99% ^{238}U, 0.7% ^{235}U, $<$ 0.1% ^{234}U) and depleted in ^{235}U (spent nuclear fuel) or thorium. Whilst special fissionable materials are ^{239}Pu, ^{233}Ur and uranium enriched in either ^{235}U or ^{233}U [5].

- Group 4, Explosives: Substances classified as class 1 under the UN Recommendations on the Transport of Dangerous Goods [6]. Class 1 explosive substances are described as a solid or liquid which is itself capable by chemical reaction of producing gas at such a temperature, pressure and speed such that it causes damage to surroundings.

The application space defined by the different NTR areas can be split into different scenarios for the purpose of ECI detection. As the primary material property which governs ECI is electrical conductivity, groups are split into high, medium or low conductivity targets obscured behind high, medium or low conductivity shields. In this instance, high conductive targets and shields are those with conductivities above 10 MS/m including commonly encountered metals such as copper, aluminium and gold. Medium conductivity materials are those less than 10 MS/m but greater than 0.1 MS/m such as uranium and plutonium. Finally, low conductivity materials are those less than 0.1 MS/m and include materials such as semi-conductors and biological tissue. Whilst these boundaries

are arbitrarily defined, they allow materials to be readily grouped by their response to AC fields and aid exploration of the problem space.

- Scenario I: High conductive objects in Med/Low shielding configuration.
- Scenario II: High conductive objects in High shielding configurations.
- Scenario III: Med/Low conductive objects in Med/Low shielding configuration.
- Scenario IV: Med/Low conductive objects in High shielding configuration.

The combination of NTR application, threat group and detection scenario can be complied into the ECI-NTR application matrix displayed in Table 1.1. This Table provides more detail on the applications of ECI within each NTR area and specific to each of the threat groups. The context of this work is low TRL scientific research towards future techniques and is not aligned with current systems.

The detection of chemical, biological agents and radiological materials are largely outside the remit of NTV. NTV focuses on nuclear and explosive materials along with applications that require the detection of metallic objects. Due to the constraint of counter-proliferation of warhead technology, these applications require identification of materials but not isotopes and are prohibited from imaging. The NF area is primarily focussed on the nuclear and explosive threat groups with many applications involving no shielding and therefore being categorised as scenario III. Detection Science (DS) have interest across all threat groups, however, are specifically tasked with tackling radiological and nuclear threats. Unlike the previous two areas, DS has a wider number of detection scenarios across a range of constrained and unconstrained environments.

	Nuclear Treaty Verification (NTV)	Nuclear Forensics (NF)	Detection Science (DS)
Group 1: Chemical or Biological	N/A	N/A	**Scenarios III, IV:** Detection of chemical and biological agents are of interest for a multi-mode detection solution but not within the DS remit.
Group 2: Radiological	N/A	N/A	**Scenarios I, II:** Detection of radiological samples obscured in a range of non-conductive (parcels/ handbags) and conductive (briefcases) enclosures. Applications in constrained (bag scanner) and unconstrained (passive monitoring) environments. Imaging preferable. **Scenarios III, IV:** Discrimination of naturally occurring radioactive sources (NORM) to reduce alarm rates.
Group 3: Nuclear	**Scenarios III, IV:** Required to validate a warhead disarmament declaration adhering to the non-proliferation of nuclear weapons technology. Determining the presence of nuclear material/alloys but not the isotope mixture. Technology should not image the container contents. The containers are typically of aluminium and lead. The exact specifications are known.	**Scenario III**: Examine nuclear material signatures during the fuel cycle to find origin. Isotopic and alloying information needed. **Scenario III**: Examine materials from a nuclear event. Isotopic and alloying information required. Potential sub-gram sample size.	**Scenarios I, II:** As above
Group 4: Explosives	**Scenario III:** Determine the presence and type of explosive materials within a sealed container but not shape. Containers are non-metallic The exact specifications are known.	**Scenario III**: Distinguish explosive material from nuclear. Information on the type of explosive required.	**Scenario III, IV:** Detection of explosives is of interest for an multi-mode detection solution but not within the DS remit.
Other	**Scenarios I,IV:** Determine types of conductive materials within a sealed Container but not shape. **Scenarios I:** Determine if an enclosure has been tampered with or has remained sealed. Exact specifications are known.	N/A	**Scenario I-IV:** Detection of gun-components and other illicit items are also of interest as part of a multi-mode system.

Table 1.1: ECI-NTR application matrix providing detail on the applications for the detection of specific materials of interest within NTR which aims to summarise future ECI applications as opposed to current systems.

ECI is optimal for detecting high conductivity objects in low shielding configurations. Detection through shielding materials is dependent on the frequency of the applied field, with lower frequencies allowing penetration through thicker or more conductive materials. The utilisation of AMs as a more sensitive sensor within ECI provides an avenue to expand the number of applications within NTR which can met by this technique. ECI and AM technology has the potential to meet all of the instances discussed in Table 1.1, however significant evaluation is required to determine the practicalities of achieving each.

1.2 Eddy Current Induction (ECI)

ECI is a widely researched field based on the fundamental principle that an external, time varying magnetic field will produce a current flow within a conductive material. This eddy current will have a strength and distribution dependent on the material's electrical and geometric properties and will generate an opposing secondary magnetic field as dictated by Faraday's law. The interaction of the primary and secondary fields can be measured using a magnetometer and properties of the material can be inferred. The interaction of eddy currents within materials is, in part, governed by the skin-depth equation that describes the standard depth (δ) at which the intensity of the current is reduced by $1/e$. This is given as:

$$\delta = \sqrt{\frac{2}{\omega\mu\sigma}} \tag{1.1}$$

and highlights the dependency on the angular excitation frequency, ω, along with the material permeability (μ) and conductivity (σ). Discussions of ECI techniques focus on these parameters. The skin-depth effect is discussed in greater detail within Chapter 2.

Applications of ECI span from industrial NDT to medical imaging and security

screening. The broad nature of these applications has resulted in several different ECI methodologies, these can be separated into excitation techniques and sensor types. Excitation techniques can be categorised into single frequency, multi-frequency and pulsed; where single frequency is an external field generated with one frequency component, multi-frequency with two or more components and pulsed with a spectrum of frequencies over a short time interval. The use of each of these methods depends on the specifics of the application: single frequencies may be used for surface inspection, whereas multi-frequency and pulsed modes are used to penetrate deeper into a material. The different sensor types are also dependent on the application and the excitation frequency range dictated by it. The different applications and sensor types are considered in the subsequent Sections.

1.2.1 Non-Destructive Testing and Industrial Applications

NDT is widely used across a number of industrial applications for the inspection of conductive components for quality testing. These components range from generic to specific such as ferrous pipes [7], steel/aluminium plates [8] [9] to non-magnetic steam generator tubes within nuclear power plants [10]. These applications require the inspection of ferrous or medium/high conductive materials such as carbon-steel or aluminium and are met with a range of single, multi-frequency and pulsed techniques. The frequencies of these excitations are in the 10-200 kHz range; the sensor types which correspond with these frequencies include coils and magneto-resistance based systems. In general the technique has the potential to detect cracks/defects < 1 mm in size [11].

NDT is not strictly limited to the detection of bulk or high conductive materials. It is of particular interest within the aerospace industry to examine the thin-honeycomb structure of some aircraft panels [12] and for the detection of warping within carbon-fibre reinforced plastics [13]. The thinner and lower conductivity nature of these components necessitates an increase in the excitation frequency into the MHz range where coil sensors

are often used.

In addition to component defect inspection, ECI can also be utilised to measure layer thickness. The industrial applications of this include quality inspection of protective coatings, where thickness plays an important role in predicting the life-time of the underlying component. Layer thickness can be determined on the 10 μm - 0.5 mm range [14,15], with some applications measuring thicker layers on the order of 10 mm [16–18]. Dependent on the target thickness and conductivity, the excitation frequencies of these applications may be on the kHz range.

Lower frequency ($<$ 1 kHz) NDT can be applied for the detection of sub-surface irregularities and can be used to not only assess corrosion [19] but also the condition of buried components such as street lighting poles [20] and other steel sub-structures [21].

1.2.2 Biomedical

A commonly researched application of ECI within the biomedical industry is magnetic induction tomography (MIT). Here, the same principles as previously discussed are utilised to construct tomographic image slices of a biological sample. The most notable difference between biological ECI and many of the industrial applications is the very low conductivity of the target materials. Many biological materials have electrical conductivities $<$ 2 S/m including the heart (0.5 S/m), lungs (0.05 S/m) and spine (0.007 S/m) [22], these are orders of magnitude smaller than NDT where steel (7 MS/m) or aluminium (37 MS/m) are common. These low conductivity values require the use of high excitation frequencies, commonly exceeding MHz [23]. Specific applications of MIT include the detection and monitoring of intra-cranial haemorrhages [24, 25], but can also be used to construct conductivity maps of the heart for the detection of specific arrhythmias [26]. A particular study detailed within [27] utilised a single coil detection scheme at 12.5 MHz to create conductivity distribution images of the spinal column.

1.2.3 Security Screening

The most relevant application of ECI to NTR are those within security screening or imaging. ECI is an established technique for metal detection, commonly employing hand-held systems with a large number of commercially available sensors. These systems are capable of detecting small conductive objects such as razor blades, operating at frequencies of kHz [28].

Whilst ECI is commonly seen in personnel screening, it can also be utilised for the stand-off detection of threat objects such as UXO and anti-personnel mines. These applications seek to detect either ferrous, small conductive components or sub-surface voids which may indicate the presence of UXO. As previously discussed for NDT, these applications utilise frequencies in the kHz-MHz range [29–31].

ECI for national security applications has been considered at AWE for a number of years [32–34] and includes fundamental research with academic partners [35–37]. To date, AWE has focused on the imaging of high conductive targets, considering both double and single sided detection using coil-array systems. These systems typically involve the detection of shielded targets with applications specifically in bag/parcel scanning. Work relevant to this includes a number of studies imaging targets within or behind aluminium and steel barriers. This work includes a study conducted with inductive sensors which were able to image copper targets (30 mm diameter and 3 mm thick) within an aluminium enclosure with 20 mm thick walls [35, 36].

AMs have also been used to explore security applications, with one study detecting copper targets behind aluminium and steel shielding 1-3 mm thick [38–40] using a rubidium based RF sensor. Other AM systems such as that discussed in [9] are not explicitly utilised for security screening, however they are applied to examine a similar shielding configuration to detect defects in steel through 0.5-1.5 mm thick aluminium plates. Similar defect detection has also been examined using a magneto-resistance based sensor which was able to detect defects in the reverse side of a 20 mm thick aluminium

plate [41].

As discussed in the previous Section, one of the primary motivations of NTR is the detection of special nuclear materials (SNM) which have conductivities between 0.6-4 MS/m. Of the literature previously examined, the detection of materials is focussed either on high conductive targets such as copper/aluminium or very low conductive materials as encountered in biomedical applications. The eddy current detection of materials in the conductivity range of plutonium or uranium is less common. An eddy current based measurement of SNM, specifically uranium, can be found within a study conducted by R. Cofield [42]. This study, which dates from 1957 and was issued in collaboration with the US Atomic Energy Commission, measured the change in conductivity of uranium samples with increasing molybdenum content. These results demonstrated a linear decrease in electrical conductivity between alloy percentages of 0-3%, translating to conductivity changes of $\sim 60\%$. More modern eddy current measurements made of uranium focus on the detection of depleted uranium (DU) for the recovery of buried DU munitions, these measurements are conducted at 100 kHz-15 MHz [43, 44].

A study which addresses the shielded detection of an object within the conductivity range of SNM (0.6-4 MS/m) utilised an inductive sensor to detect 1 mm thick manganese targets behind 1.5 mm of aluminium [45]. To the author's knowledge, no studies have been published which focus on the ECI detection of thickly shielded SNM for security screening.

1.3 Magnetometers

As the principle of ECI involves the application of a primary magnetic field and the modification of that field by the secondary induced in the target; a magnetometer is required in a detection system. The choice of magnetometer is dependent on the application which will dictate parameters such as the frequency and stand-off distances.

A limited number of magnetometer types are considered here, these include inductor coils, fluxgates, tunnelling magneto-resistance based sensor, super-conducting quantum interference devices (SQUID) and AMs.

1.3.1 Induction Coil Magnetometers

Induction coil magnetometers are a class of sensors which, based on Faraday's law, passively measure a magnetic field through the current induced in coils of wire. Coil based sensors have been utilised for many years across all of the disciples discussed within the previous Section. The operation of induction coils depends upon the frequency of the field and geometric parameters. A relation for the ideal sensitivity of an induction coil for comparison with AMs was derived within [46] and is given in the low frequency limit ($< 10\,\mathrm{kHz}$), B_{LF}, as

$$\Delta B_{\mathrm{LF}} = \frac{8}{\omega d_c}\sqrt{\frac{k_B T \rho}{V_w}} \tag{1.2}$$

where B_{LF} is the magnetic field, d_c is the diameter of the coil, T is the temperature, ρ is the resistivity of the coil wire, k_B is Boltzmann's constant and V_w is the winding volume. The winding volume is given as

$$V_w = \pi d_c W^2 \tag{1.3}$$

for a square winding cross section, $W \times W$, and a mean coil diameter, d_c. In the high frequency limit, B_{HF}, the ideal sensitivity is given as

$$\Delta B_{\mathrm{HF}} = \frac{8}{\omega d_c}\sqrt{\frac{k_B T \rho}{1.8\pi d_c W \delta}} \tag{1.4}$$

where δ is the standard depth. The number of turns on the coil can be calculated as $N_c = 4W^2/\pi d_w^2$ for a wire diameter d_w. In the low frequency regime the sensitivity

linearly improves with the frequency. This linearity is modified at high frequencies by the skin-depth effect as eddy current losses between turns become more significant. Following the discussion within [46], the inductor sensitivity for a small coil of $d_c = 50\,\text{mm}$ and $W = 10\,\text{mm}$ surpasses the fT scale above approximately 300 kHz. Below 1 kHz the fundamental sensitivity is limited to the pT range.

The advantages of coil based sensors is that they are largely passive, in-expensive and can be easily manufactured. Disadvantages are their variable sensitivity with frequency, the requirement to have larger coils with more turns to improve sensitivity and a narrow bandwidth.

1.3.2 Fluxgate

Fluxgate magnetometers are another sensor type which has been utilised within ECI for a number of years. These sensors are constructed from a core made of a high permeability material wrapped in two coils of wire, a drive coil and a sensing coil. The drive coil is supplied with an AC current which creates a magnetic saturation cycle within the core, driving it from magnetised through demagnetised and to inversely magnetised. This changing field induces a secondary current within the sensing coil which can be read out.

There are a variety of core shape designs, however a number are constructed in two parts. In the absence of an external magnetic field the magnetisation cycles of the two parts are synchronised and cancel, with no net field felt by the sensing coil. With the application of an external field, the portion of the core aligned to it will cycle through saturation quicker, whilst the portion aligned opposite will cycle slower. As the cycles are now out of phase, they produce a net field from the cores proportional to the strength of the external field. This induces a current within the sensing coil which can be measured [47].

The fundamental sensitivity of fluxgate sensors was considered within [48] and de-

termined based on a number of numerical simulations. The value was found to be dependent on the core permeability, temperature and volume. Values of $0.1\,\mathrm{pT}/\sqrt{\mathrm{Hz}}$ were calculated for a room temperature sensor with a core volume of $2.2 \times 10^{-2}\,\mathrm{cm}^3$ at a measurement frequency of 1 kHz. These calculations were based on a fluxgate geometry described within [49] which had a core of length of 76 mm. The total form factor of the sensor was not explicitly stated, however, the core size suggests a sensor size not dissimilar from current commercial fluxgates which can have lengths of ~ 200 mm [50].

Fluxgate sensors provide better sensitivity at lower frequencies than coils of the same volume, however, are more expensive.

1.3.3 Magnetic Tunnel Junctions (MTJs)

A magnetic tunnel junction (MTJ) comprises two ferromagnetic layers separated by an insulating barrier. A bias voltage is applied across the two layers with a junction barrier thin enough to allow electrons to tunnel between the layers. The junction exhibits tunnelling magneto-resistance (TMR), in which the tunnelling current is proportional to the magnetization of the ferromagnetic layers which is modified with the application of an external magnetic field [51].

The sensitivity of a sensor using a MTJ was recently quoted to range between 0.1-2 pT for frequencies < 100 Hz [52]. However, in general, commercially available MTJ sensors have sensitivities in the μT - mT range but operate up to frequencies of 10 kHz [53] and are only slightly more expensive than coil sensors per unit.

1.3.4 Super-Conducting Quantum Interference Device (SQUID)

Super-conducting quantum interference devices (SQUIDs) are considered to be examples of the most sensitive magnetometers and are routinely used within medical imaging. SQUIDs are constructed from two Josephson junctions which separate two sections of a superconducting loop. In the absence of a magnetic field, a current applied to the

loop is split equally through each half. An external magnetic field induces a screening current which flows round the loop, adding to the current in one half whilst subtracting from the current in the other. The addition of current along one branch can exceed the critical current of the junction which creates a voltage that can be measured.

SQUID sensors can be made to be DC or RF and are associated with fT sensitivities but require cryogenic cooling to achieve these values [54]. The frequency range of SQUIDs is also very large, with RF SQUIDs extending into the hundreds of MHz [55]. Due to the cooling restrictions these sensors are expensive and are associated with a large amount of auxiliary equipment.

1.3.5 Atomic Magnetometers

Atomic magnetometers (AMs) are a class of magnetic sensor which use light to monitor the evolution of atomic spin in response to an applied magnetic field. These sensors are typically constructed using cells containing alkali-metal vapours (Cs, K, Rb). The atoms in these vapours have a magnetic moment which experiences a torque when placed in a magnetic field, causing a precession of the magnetic moment about the applied field. The frequency of this precession, known as the Larmor frequency, is proportional to the applied field where the constant of proportionality is the gyromagnetic ratio of the alkali-species. A measurement of the Larmor frequency can be made by examining the intensity or polarisation of light as it travels through the medium, allowing a measurement of the field to be extracted.

Atomic magnetometry in itself is a broad field with a large number of different types of sensor, included within these are Radio-Frequency (RF) and Spin-exchange Relaxation Free (SERF) AMs [46, 56, 57]. RF AMs can be used for the detection of RF magnetic fields which is achieved by tuning the Zeeman splitting of the alkali-metal atoms through the application of a DC bias field to match the frequency of the RF field [46]. These sensors have practical sensitivities in the pT-fT range with frequencies

reported in the hundreds of Hz [58] and GHz [59]. SERF AMs are focussed on the detection of low frequency and DC fields. These sensors utilise the same base principle of all AMs but achieve greater sensitivities through the suppression of spin-exchange collisions which reduce the performance of AMs. The influence of these collisions is reduced by heating the vapour to higher temperatures (120-200°C) which commonly requires the construction of cell ovens. Despite the additional operational requirements, SERF sensors are commercially available [60]. The fundamental sensitivity limitations of both types of AMs depend upon the configuration of the specific sensor but are typically sub fT [46, 57]. The bandwidth of AMs is in the hundreds of Hz around the Larmor frequency which, in the instance of the RF magnetometer, can be tuned through adjustment of a bias field. The optimal sensing frequency of the QuSpin SERF sensor has also been tuned to higher frequencies as demonstrated in [61], however, this is an adaptation to the commercial sensor.

AM sensors operate at temperatures between ambient and 200°C and therefore are more practical when compared with SQUIDs for comparable sensitivities. However, similarly to SQUIDs, to achieve the highest sensitivities, AMs require some sort of magnetic field shielding. Examples of this include either passive in the form of a mu-metal enclosure or active field cancellation systems.

1.4 ECI for NTR Applications

The previous Sections have examined the objectives of the Nuclear Threat Reduction programme and highlighted the requirement to investigate alternative signatures, specifically ECI, for the detection of threat objects. The selection of a detector type is dependent on the application, with key factors being the sensitivity and operational frequency. Figure 1.1 displays a coarse illustration of the frequency and sensitivity ranges covered by the previously discussed sensor types. The security applications summarised within

Table 1.1 cover both low and high conductivity targets, and as discussed across the different applications in Section 1.2, this requires a sensor which can operate in both the low and high frequency regimes.

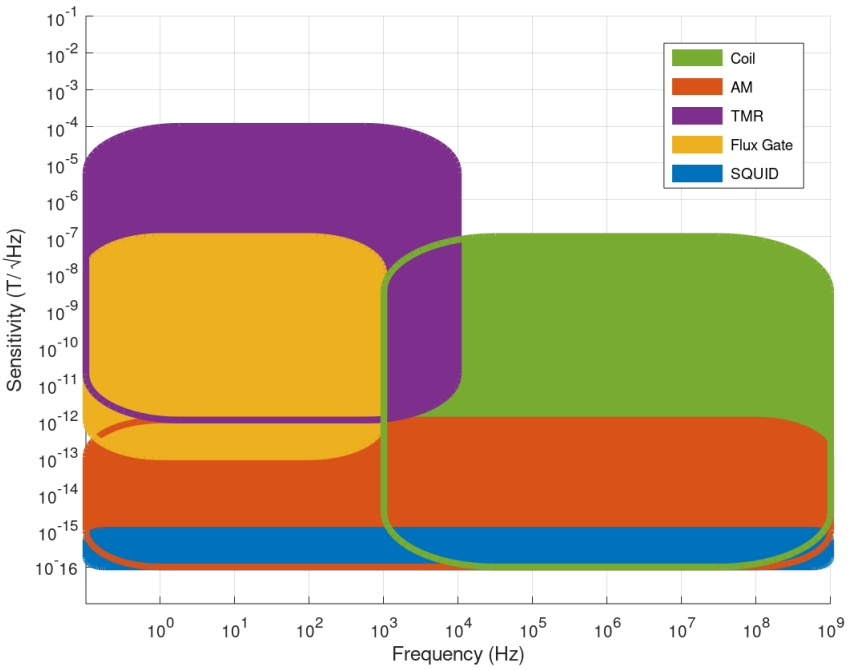

Figure 1.1: Illustration of the sensitivity and frequency ranges covered by a selection of magnetometer technologies.

Examination of Figure 1.1 indicates that to best cover this range with maximal sensitivity, AMs or SQUID sensors would be most appropriate. Considering the challenges associated with SQUID sensors such as cost and cryogenic cooling, AMs offer a more practical alternative. AM technology has the potential to provide good sensitivity across the operational frequency range with the DC and low frequency regime ($< 500\,\text{Hz}$) addressed by the SERF AMs, whilst the RF AMs are tunable in frequencies above these values.

A review of the currently published literature demonstrates that there are a number of ECI systems which are able to penetrate through conductive materials between 10-

20 mm thick [35, 41]. A few also discussed the detection of shielded SNM in a security screening context [38, 40, 45], however none to the author's knowledge which directly focus on optimisation for the detection of SNM or the detection of SNM through thick shields.

This thesis explores the applicability to the NTR application space of both low frequency (< 500 Hz) and high frequency (> 10 kHz) ECI using AMs. In low frequency applications a commercially available SERF sensor is considered (QuSpin), whilst to examine the high frequency regime a RF AM was constructed.

1.5 Thesis Structure

This thesis is structured to first discuss the principles of ECI and atomic magnetometry in greater detail within Chapters 2 and 3. Eddy current generation within targets is then considered further in Chapter 4 using a finite-element modelling package. In Chapter 5 the different data analysis algorithms required to extract information from ECI images is examined. Chapter 6 details the low frequency ECI explored using the commercial SERF AM. This includes the imaging system constructed and measurements of targets obtained within thick shielding configurations, relevant to the previously discussed scenarios II and IV. Finally, Chapter 7 discusses the construction and optimisation of the RF AM, along with the integration into an imaging system and the high frequency ECI measurements obtained to explore scenarios I and III.

Chapter 2

Electromagnetic Induction

The objective of this Chapter is to outline the principles behind ECI measurements as a basis to discuss the experimental results presented in later Chapters. To achieve this, the behaviour of the induced eddy current distribution within a finite object is derived from Maxwell's laws. This derivation is extended into a general description of the behaviour of the magnitude and phase of the axial induced magnetic field, defining length scales (δ, L) associated with each.

The principles behind electromagnetic induction within conductive objects can be described using Maxwell's laws of electromagnetism, specifically Faraday's law of induction which in differential form is expressed as

$$\nabla \times \bar{\mathcal{E}} = -\frac{\partial \bar{B}}{\partial t}. \tag{2.1}$$

This equation states that a circulating electric field, $\bar{\mathcal{E}}$, can be generated within a material by a time varying magnetic field, $\bar{B}$. A circulating electric field will drive a current density, J, according to Ohm's law. This induced current is known as an eddy current and can be expressed as

$$\rho(\nabla \times \bar{J}) = -\frac{\partial \bar{B}}{\partial t} \tag{2.2}$$

if the material resistivity is given by ρ. A current flowing in a material will produce a secondary magnetic field according to Ampere's law,

$$\nabla \times \bar{B} = \mu \bar{J} \tag{2.3}$$

where μ is the magnetic permeability of the material. The time derivative of equation 2.3 can be taken and the magnetic field parameter eliminated through substitution of equation 2.2, this produces

$$\frac{\mu}{\rho}\frac{d\bar{J}}{dt} = -[\nabla \times (\nabla \times \bar{J})] = \nabla^2 \bar{J}. \tag{2.4}$$

The above expression can be used to describe the behaviour of induced eddy currents with standard solutions detailed within [62]. The solution can be formed by considering a material of continuous permeability that occupies half space and is illuminated by a uniform magnetic field. Half space is defined as the medium extending across all positive values of z. In this instance equation 2.4 can be written as a function of depth, z, through the material, for a frequency of ω,

$$\frac{j\omega\mu}{\rho} J_x = j\omega\mu\sigma J_x = \frac{\partial^2 J_x}{\partial z} \tag{2.5}$$

where $\sigma = 1/\rho$ is the electrical conductivity of the material and ω is the angular frequency of the current. As this is a function of a single variable, z, the solution is in the form

$$J_x = C_1 e^{-(j\omega\mu\sigma)^{\frac{1}{2}} z} + C_2 e^{(j\omega\mu\sigma)^{\frac{1}{2}} z} \tag{2.6}$$

with real and imaginary (j) components where $(2j)^{\frac{1}{2}}$ can be written as $1 + j$.

The values of constants C_1 and C_2 can be obtained through the application of boundary conditions. The first boundary condition defines the current at the surface ($z = 0$) as equal to an initial value J_0. The second condition is that any eddy current distribution

will minimise the resistive power (P_w) dissipation [63] where the power summed across the total thickness of the material, $\mathbb{T}$, is given as

$$P_w = \int_0^{\mathbb{T}} \rho J_x J_x^* dz. \tag{2.7}$$

A parameter δ can be defined as

$$\delta = \left(\frac{2}{\omega\mu\sigma}\right)^{\frac{1}{2}} \tag{2.8}$$

which allows C_1 and C_2 to be expressed as

$$C_1 = \frac{J_0}{1 - e^{-2(j+1)\frac{\mathbb{T}}{\delta}}} \tag{2.9}$$

$$C_2 = \frac{J_0}{1 - e^{2(j+1)\frac{\mathbb{T}}{\delta}}}. \tag{2.10}$$

The real part of equation 2.6 can be expressed in terms of δ as

$$J_x(z) = C_1 e^{-\frac{z}{\delta}} \cos\left[-\frac{2\pi z}{L}\right] + C_2 e^{\frac{z}{\delta}} \cos\left[\frac{2\pi z}{L}\right]. \tag{2.11}$$

Inspection of this results allows two components to be identified, one which decays exponentially and the other which is oscillatory in nature. A wavelength type quantity, $L = 2\pi\delta$, is defined such that these component can be discussed in terms of two related length scales. The component that decays exponentially is the magnitude of the current, the strength of which is dictated by the length scale δ. Conversely, the oscillating component, which modulates this decay, is indicative of the phase of the current and changes on the length scale of L.

The attenuation of the current with depth through a conductor is typically described as the skin-depth effect. The key parameter of δ is known as the standard depth and

is equivalent to a decay of the initial current magnitude by $1/e$ or $\sim 37\%$. The skin-depth effect can be qualitatively understood as the induced currents at different depths combining in a constructive or destructive manner according to equation 2.6 with a net decay across the bulk of the material. This effect scales with the material properties specifically σ and μ along with the angular frequency of the external field, ω.

The distribution of the magnetic field through the material follows the induced eddy currents. The application of an external primary/excitation field, B_p, will generate a secondary magnetic field, B_s, that opposes the first. This effect is illustrated in Figure 2.1.

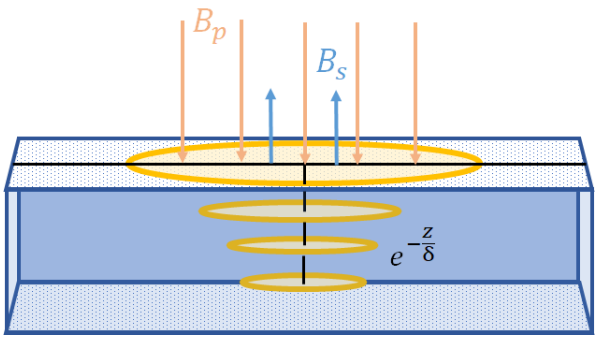

Figure 2.1: Illustration of the application of a time varying magnetic field to a sample, as in Faraday's law of induction, the eddy currents are generated within the sample which in turn generate a secondary magnetic B_s field that opposes the primary field B_p.

As with the eddy currents, the magnetic field propagation through the depth of the material can be described by taking the time derivative of equation 2.3. In this instance, instead of eliminating $\bar{B}$, J can be eliminated through substitution of equation 2.2. This produces an equation of the same form as equation 2.5 and is given as

$$\frac{\mu}{\rho}\frac{d\bar{B}}{dt} = -[\nabla \times (\nabla \times \bar{B})] = -\nabla^2 \bar{B}, \tag{2.12}$$

with a solution of the same form given as

$$B_z = C_3 e^{-\frac{z}{\delta}} \cos\left[-\frac{2\pi z}{L}\right] + C_4 e^{\frac{z}{\delta}} \cos\left[\frac{2\pi z}{L}\right]. \tag{2.13}$$

Again the magnitude of the field exponentially decreases as a function of z, modulated by an oscillating component that indicates a change in phase with respect to the field at the surface. The combination of an exponential decrease in the magnitude of the induced secondary fields and the linear change in the phase, θ_s, is represented pictorially by Figure 2.2.

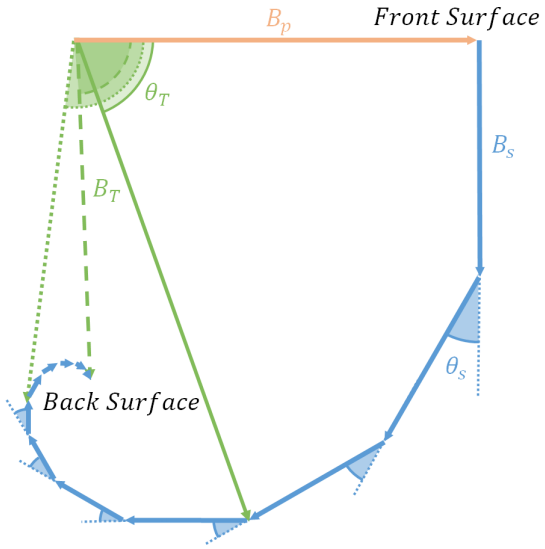

Figure 2.2: Schematic of the vector integral of contributions to the resulting magnetic field from the distribution of eddy currents. Integration is displayed through the thickness of the conductor from the front face through to the back face. Thinner conductors stop the integration at earlier points in the path. The vectors indicate the primary field, B_p (orange), and the induced secondary field, B_s (blue), which has an associated phase change, θ_s. The resultant field vector, B_T, and phase, θ_T are given in green for the instance where the magnitude reaches a maximum (solid), where the phase reaches a maximum (dotted) and for the final B_s vector (dashed), demonstrating a decrease in both magnitude and phase from the respective maxima.

In this diagram the primary field (orange) results in the induction of a secondary field (blue) which lags by 90°; each arrow is representative of an infinitesimal step in z. The phase of B_s then changes linearly with each step whilst the magnitude decreases

exponentially. Drawing the resultant field vector, B_T, produces a magnitude which reaches a maximum (solid green) at the point where the field turns back on itself. This is proceeded by a maxima in the phase (dotted green line) which occurs after several subsequent steps. These are produced by a "curvature" in the secondary field vectors, the impact of this is dictated by the balance of the strength in the exponential decay and the linear increase in phase and therefore the values of δ and L.

This effect can be explored by considering any conductive object as a set of infinitesimal current loops producing the secondary field [63]. These current loops can be expressed individually using the Biot-Savat law:

$$B_s(z) = \int_0^{\mathbb{R}} \int_0^{\mathbb{T}} \frac{\mu J r^2}{2(r^2 + (z_p - z)^2)^{\frac{3}{2}}} dz dr \tag{2.14}$$

and integrated across the total radius ($\mathbb{R}$) and thickness ($\mathbb{T}$) of an object to determine the secondary field at a point z_p along the z-axis. Here, r is the radius of the current loop and z is its z coordinate. The current is taken from equation 2.6. The magnetic field calculated by equation 2.14 is the secondary field component at a specific point in space, however, the construction of the eddy current distribution would inherently imply a uniform primary field on the left hand side of the target.

The scenario is illustrated in Figure 2.3, with the magnitude and phase of the field calculated as a function of object thickness and displayed in Figure 2.4. These data display turning points as a function of object thickness where the magnitude precedes the phase. Data was calculated at 300 Hz and 40 Hz, showing the shift of the turning points to higher thickness values; this results from changes in the curvature of the secondary field vectors as illustrated in Figure 2.2.

The thickness value at which the turning point occurs is found to be linear with the wavelength quantity, L. This linearity is displayed in Figure 2.5 for the magnitude (T_m) and phase (T_p). Values were calculated across a number of object radii and a number of

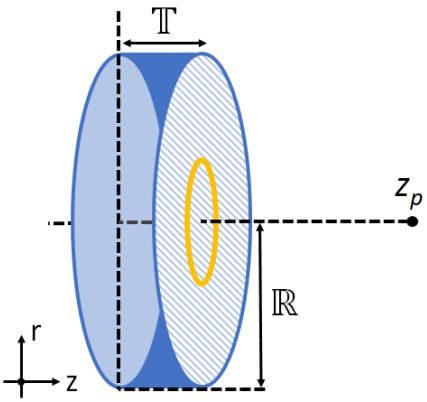

Figure 2.3: Illustration of a conductive object of thickness $\mathbb{T}$ and radius $\mathbb{R}$. The field produced from the object at a point along the z-axis, z_p, can be calculated by integration of current loops across the object thickness and radius.

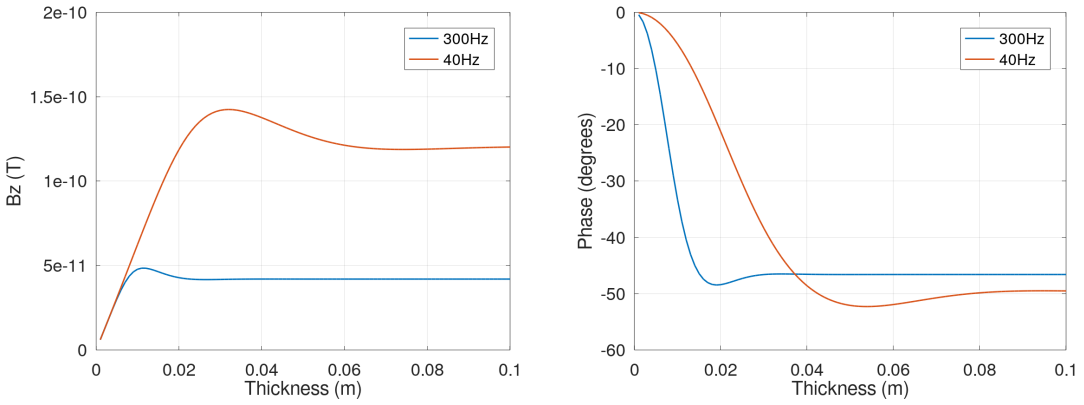

(a) Magnitude (b) Phase

Figure 2.4: Secondary field, B_s magnitude (left) and phase (right) as a function of aluminium object thickness calculated numerically. The object has a radius of $\mathbb{R} = 100\,\text{mm}$, data are obtained at an inspection point $z_p = 247\,\text{mm}$ at frequencies of 300 Hz (blue) and 40 Hz (red).

frequencies to produce the relationships,

$$T_m = 0.37L - 0.0001(\text{m}) \tag{2.15}$$

$$T_p = 0.65L - 0.0005(\mathrm{m}). \tag{2.16}$$

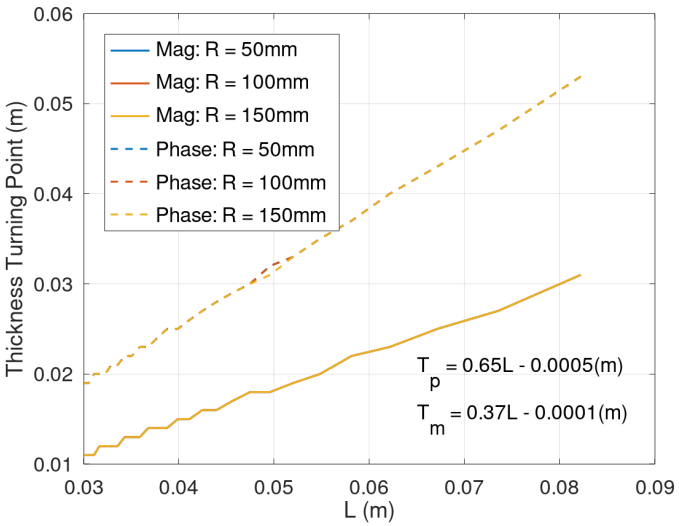

Figure 2.5: Aluminium object thickness corresponding to the turning point in magnitude (solid) and phase (dashed) as a function of the wavelength-quantity, L. Data was calculated numerically with an object of radius $\mathbb{R} = 50\,\mathrm{mm}$ (blue), $\mathbb{R} = 100\,\mathrm{mm}$ (red) and $\mathbb{R} = 150\,\mathrm{mm}$ (yellow).

The turning point in the magnitude is found to occur at 0.37 times the wavelength, L; in phase this is shifted to $0.65L$. The comparative independence with object radius can be extracted from equation 2.14 where B_s scales as $\ln(r)$ once integrated, however, it should also be noted that the radial profile of the current density was not accounted for within equation 2.6. Whilst these results are presented in terms of the object thickness, the nature of L is such that these turning point are also observed in frequency. A frequency scan of an object will produce another characteristic curve indicative of the material properties and thickness.

A similar treatment of the induced field from a finite conductive object is discussed in [23, 64] which presents an analytical solution for the ratio of primary and secondary fields. This approach uses a transmission orientation with an excitation coil aligned on-

axis with a measurement point, z_p, where the object is equidistant (z_a) from both the coil and z_p as illustrated in Figure 2.6. Unlike the previous description, this approach assumes a standard depth much greater than the thickness of the object ($\delta >> \mathbb{T}$).

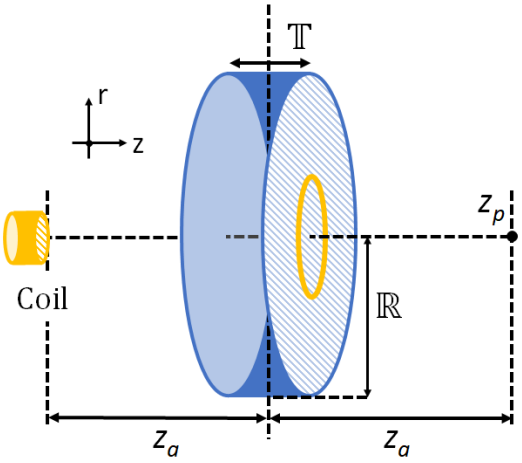

Figure 2.6: An Illustration of a induction measurement geometry with a coil aligned axially with a measurement point z_p. A thin object of thickness, $\mathbb{T}$ and radius, $\mathbb{R}$ is placed in the perpendicular plane.

The object is placed in the perpendicular plane and has a radius $\mathbb{R}$ and thickness $\mathbb{T}$. By considering the current within thin annuli of the disc and integrating across the radius, a ratio of

$$\frac{B_s}{B_p} = G_1(\mu_r - 1) + G_2(\omega\epsilon_0\epsilon_r - j\sigma)\omega\mu_0 \tag{2.17}$$

is produced. The parameters G_1 and G_2 are geometry terms given as

$$G_1 = \frac{z_a^3\mathbb{T}\mathbb{R}^2(8z_a^2 - \mathbb{R}^2)}{2(z_a^2 + \mathbb{R}^2)^4}, \tag{2.18}$$

$$G_2 = \frac{z_a^3\mathbb{T}}{2}\Big[\frac{1}{z_a^2} - \frac{z_a^2 + 2\mathbb{R}^2}{(z_a^2 + \mathbb{R}^2)^2}\Big]. \tag{2.19}$$

Equation 2.17 allows the contributions from various material properties to be sep-

arated. The 1st term on the RHS represents the permeability of the material, whilst the 2nd term encompasses both the permittivity, ϵ, and conductivity. The permeability term describes the magnetization of the sample and is independent of frequency. The permittivity term signifies contributions from displacements fields, D, which parametrize the polarization of the material from the induced electric fields, where $D = \epsilon\mathcal{E}$. At frequencies below MHz the permittivity is often considered negligible as in the Biot-Savart description above. The permeability and permittivity terms constitute the real part of equation 2.17, whilst the imaginary contribution which induces a phase change between the primary and secondary fields is dictated by the conductivity of the material and is the component relating to the induced eddy currents.

The different magnetic field components can be visually represented using a phasor diagram such as that displayed in Figure 2.7. The phasor in Figure 2.7a is equivalent to the first step within Figure 2.2 with the permittivity term neglected. Both illustrations in Figure 2.7 assume a material with $\mu_r = 1$ and as such the secondary field contribution is almost entirely dictated by the conductivity of the material, producing a phase change of 90° from the primary. All of these components sum to produce a total field (B_T) which lags the primary field by an angle θ.

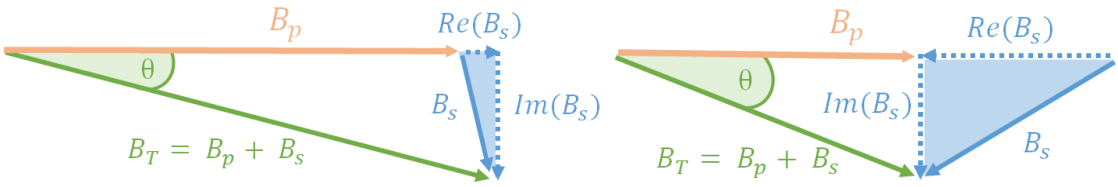

(a) Very low conductive samples ($< 1\,S/m$)

(b) Metallic samples ($> 100\,S/m$)

Figure 2.7: Phasor diagrams depicting the primary magnetic field (B_p) and the resultant secondary magnetic field (B_s) induced in a sample including the real and imaginary components. The total magnetic field B_T is the vector sum of these components.

The phasor descriptions in Figures 2.2 and 2.7a assume small phase angles. In the Biot-Savart description this is valid in the assumption of an infinitesimal step. However,

in Figure 2.7a this is met by having a very small material conductivity such that $\delta >> \mathbb{T}$. In the example of a bulk material with a high conductivity these phasors are not a suitable description. Instead it is more appropriately described by the phasor in Figure 2.7b. Here, the real component is not the permittivity, which can still be neglected for sub MHz frequencies, instead it is the screening of the field described in the skin-depth effect.

These descriptions aim to provide a basis with which to understand the eddy current induction images obtained through-out this work. However, a number of assumptions are made such as a uniform field. To further the understand the experimentally obtained measurements, a series of COMSOL simulations are constructed. These are discussed in Chapter 4.

Chapter 3

Atomic Magnetometry

Atomic magnetometry broadly describes the sensing of magnetic fields through the observation of light which has interacted with an atomic vapour. There are a number of sub-categories of atomic magnetometer (AM), however in general all share the same basic components, including:

- a cell containing an alkali-metal vapour,
- a source of interacting light,
- an optical read-out,

and operate based on the following principles [65]:

- atomic spin polarisation creation,
- evolution of the net atomic spin polarisation through the application of an external magnetic field,
- detection of the polarised state through interaction of the medium with a light source.

A singular atom can be considered to have atomic magnetic moment which originates from the orbital angular momentum of the electrons (L) in combination with the intrinsic spins of the electrons (S) and nuclei (I). In the presence of an external magnetic field, $\bar{B}$, the magnetic moment experiences a torque. In the limit that the applied field is sufficiently small, the magnetic moment is independent from $\bar{B}$ and therefore precesses about $\bar{B}$ at a rate known as the Larmor frequency (ω_L); this is given as

$$\omega_L = \gamma |B| \tag{3.1}$$

where γ is the gyromagnetic ratio of the vapour which describes the ratio of the atom's magnetic moment to its angular momentum and is property of the atomic isotope.

Changes in the circular birefringence, detailed in Section 3.3.3, of the vapour at the Larmor frequency encodes the Larmor precession on the properties of the light and allows a direct measurement of the applied magnetic field.

The AM systems explored within this work were selected to address both the low and high frequency applications captured in Chapter 1. The low frequency regime was targeted using a commercially available Spin-Exchange Relaxation Free (SERF) sensor, whilst the high frequency range is explored using a Radio-Frequency (RF) magnetometer assembled at AWE. The RF magnetometer was constructed using a rubidium vapour cell. Orthogonal pump (circularly polarised) and probe (linear polarised) beams were used, with the bias field directed along the pump direction as illustrated in Figure 3.1. The pump beam was resonant with the transition between the ground state of the rubidium to the second excited state, referred to as the D2 transition. The probe was red-detuned from the pumping transition by 700 MHz. An RF field was applied perpendicular to the pump and probe beam plane, driving the evolution of the spin polarisation.

The principles of the RF AM are examined in greater detail within the subsequent Sections of this Chapter. As the operation of RF AMs have been explored in-depth

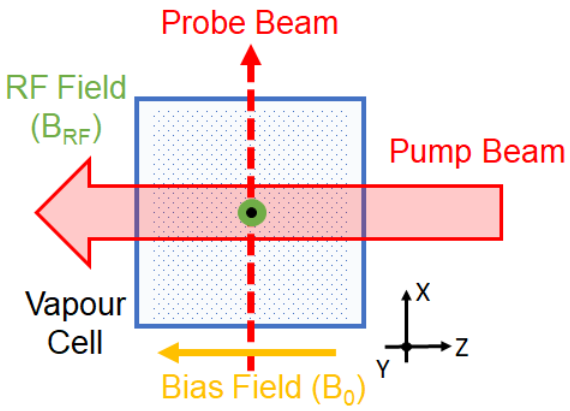

Figure 3.1: Illustration of the orthogonal pump and probe arrangement of the radio frequency atomic magnetometer constructed at AWE. A circularly polarised pump beam was directed along the z-axis, orthogonal to a probe beam directed along the x-axis. A DC bias magnetic field, B_0, is applied along the pump direction whilst an AC magnetic field is applied along the y-axis.

within the literature, this discussion draws on a number of existing studies and applies the concepts to the specific magnetometer system detailed here. Included in this discussion are the properties of the vapour, the Zeeman effect, and the operations specific to SERF AMs.

3.1 Properties of Rubidium

The alkali-metal vapour species utilised in both the RF AM and the commercial AM was rubidium. In the RF AM the vapour cell contained a natural abundance which consists of 72% rubidium-85 (^{85}Rb) and 28% rubidium-87 (^{87}Rb) [66]. The commercially available QuSpin sensor used exclusively ^{87}Rb.

The atomic energy levels for both rubidium isotopes are displayed in Figure 3.2 where each level is labelled with spectroscopic notation of the form $n^{2S+1}L_F$; these correspond to quantum numbers specified as n (principal), L (orbital), S (electron spin), I (nuclear spin) and F (total angular momentum). This figure illustrates the orbital, fine and hyperfine structure. Here, the degeneracy of energy levels are lifted due to modifications

made when accounting for the orbital motion of the electrons (orbital), the spin-orbit coupling between the internal spin, S, of the electron and its orbital motion (fine); and the nuclear spin, I (hyperfine).

Alkali-metal mediums are chosen as they have a single un-paired valance electrons which simplifies the structure into a hydrogen-like arrangement. This valance electron has a spin $S = \pm 1/2$ and, as all closed shells have zero angular momentum, the total angular momentum, F is given by the sum of L, S and I. This dictates that the hyperfine ground state energy levels have $F = I \pm 1/2$. The degeneracy of the hyperfine levels is lifted with the application of an external magnetic field which exerts a torque on the magnetic moment of the atoms. This phenomena, known as the Zeeman effect, produces energy splitting of $m_F = -F, -F + 1...F - 1, F$ where m_F is the component of total angular momentum projected along the axis of the applied field, B. There are two primary transitions considered within each isotope, the D1 and D2 lines which correspond to transitions between the first and second excited states of the fine structure respectively. In rubidium these transitions are separated by $\sim 7\,\mathrm{THz}$; this compares to $\sim 16\,\mathrm{THz}$ for cesium [67] and $\sim 2\,\mathrm{THz}$ for potassium [68]. As a consequence of this, the contributions from the D1 and D2 levels in rubidium can be considered separately in subsequent Sections.

Each energy level has an associated linewidth (Γ_{nat}) which originates from a fundamental quantum mechanical uncertainty in its energy (natural linewidth) and can be broadened through several mechanisms including collisions between atoms (pressure broadening, Γ_p) or thermal motion (Doppler broadening, Γ_G). The natural linewidth of the fine transitions within both isotopes of rubidium are $5.75\,\mathrm{MHz}$ and $6.07\,\mathrm{MHz}$ for the D1 and D2 transition respectively [69]. These widths can be pressured broadened through collisions between alkali atoms or with additional quenching/buffer gases; these are commonly added to vapour cells to preserve the polarisation created in optical pumping.

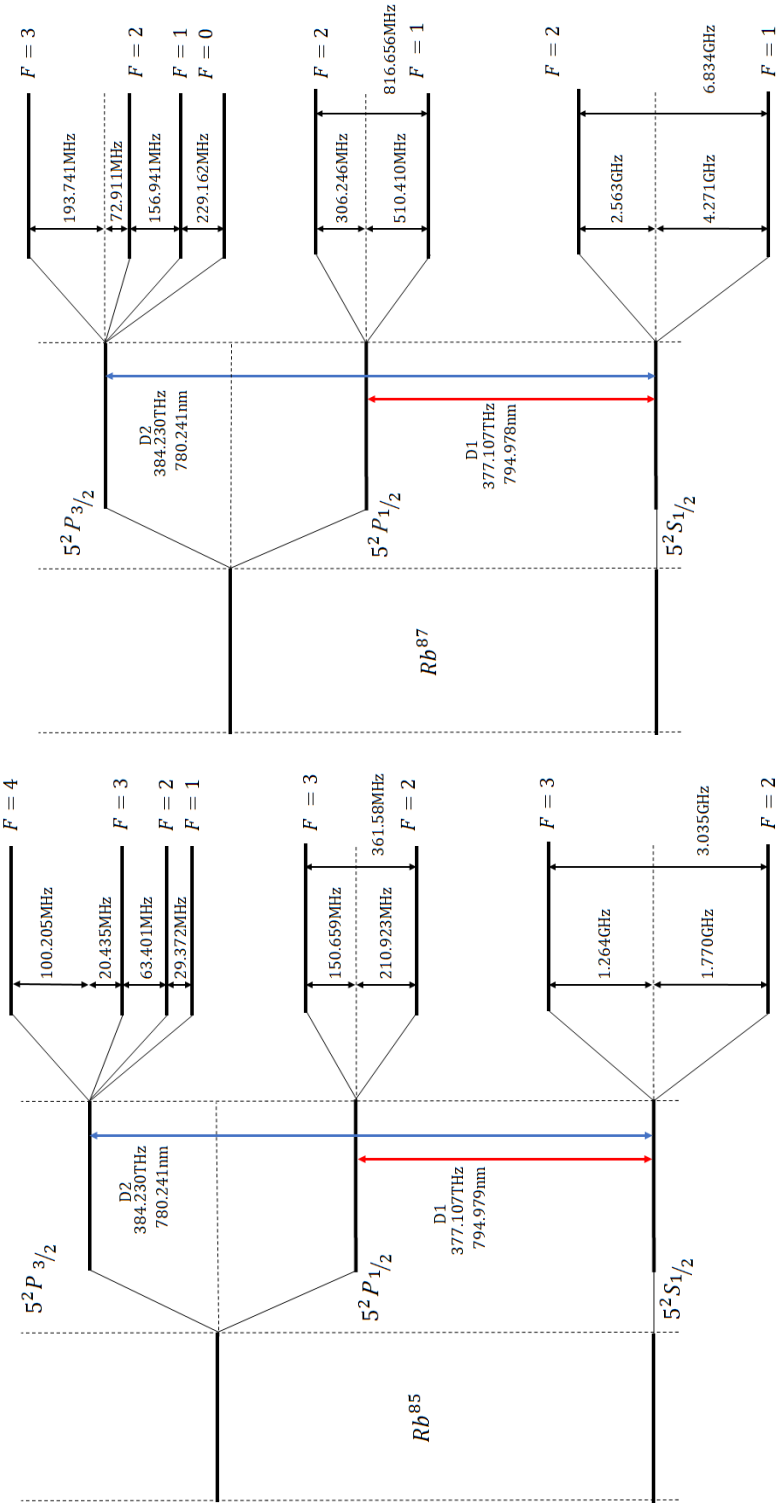

(a) Rubidium-85 (b) Rubidium-87

Figure 3.2: Hyperfine atomic structure of Rubidium-85 ($I = 5/2$) and Rubidium-87 ($I = 3/2$)

The natural and pressure linewidths sum to produce a total linewidth, $\Gamma_L = \Gamma_{nat} + \Gamma_p$, which needs to be considered when calculating the expected absorption profile of the vapour. Whilst the natural linewidth is specific to the species, the pressure contribution will be dependent upon the species and pressure of any added gases. The expected absorption which arises from these mechanisms has a Lorentzian profile, $\mathcal{L}$, [70] when plotted as a function of the resonant light frequency, υ. This is given as

$$\mathcal{L}(\upsilon) = \frac{\Gamma_L/2\pi}{(\upsilon - \upsilon_0)^2 + (\Gamma_L/2)^2} \tag{3.2}$$

where the centre frequency (υ_0) is given by the resonance of the transition and Γ_L is the Full-Width-Half-Max (FWHM) of the distribution.

Within this work, the vapour cell used in the RF AM included a nitrogen buffer gas at 70 Torr. The linewidth broadening was experimentally determined in [71] for nitrogen and found to be 17.8 GHz/amg and 18.1 GHz/amg for the D1 and D2 transitions of rubidium respectively. Using these values, at room temperature (20°C) and a pressure of 70 Torr, a broadening of $\Gamma_L = 1.5$ GHz for both transitions can be estimated for the experimentally used cell.

In addition to Γ_L, the thermal motion of the alkali-atoms themselves contribute to the linewidth through Doppler broadening, Γ_G. The origin of Doppler broadening can be explained by considering light of frequency υ which is detuned from resonance υ_0. Atoms moving with an appropriate added thermal velocity will absorb light of frequency υ as if it were on resonance, broadening the absorption profile. This absorption creates a Gaussian, $\mathcal{G}$, distributed linewidth which takes the form,

$$\mathcal{G}(\upsilon) = \frac{2\sqrt{\ln(2)/\pi}}{\Gamma_G} \exp\left(\frac{-4\ln(2)(\upsilon - \upsilon_0)^2}{\Gamma_G^2}\right), \tag{3.3}$$

in which Γ_G is specified as

$$\Gamma_G = \frac{2\upsilon_0}{c}\sqrt{\frac{2k_BT}{\mathfrak{M}}\ln(2)} \tag{3.4}$$

where k_B is the Boltzmann constant ($1.38 \times 10^{-23}\,\mathrm{J/K}$), T is the temperature of the vapour in Kelvin, c is the speed of light ($3 \times 10^8\,\mathrm{m/s}$) and $\mathfrak{M}$ is the atomic mass of the vapour species [70].

The summation of all these broadening mechanisms results in an absorption profile that is a combination of both Lorentzian and Gaussian distributions known as a Voigt profile. In the limit where $\Gamma_G >> \Gamma_L$, this distribution approaches a Gaussian absorption profile and for $\Gamma_G << \Gamma_L$ reduces to a Lorentzian distribution. The Voigt profile can be approximated using a linear combination of the Lorentzian ($\mathcal{L}$) and Gaussian ($\mathcal{G}$) distributions using the equations [72]:

$$\mathcal{V}(\upsilon) = \eta\mathcal{L} + (1-\eta)\mathcal{G}, \tag{3.5}$$

$$\eta = 1.36603\Big(\frac{\Gamma_L}{\Gamma_F}\Big) - 0.47719\Big(\frac{\Gamma_L}{\Gamma_F}\Big)^2 + 0.11116\Big(\frac{\Gamma_L}{\Gamma_F}\Big)^3, \tag{3.6}$$

$$\Gamma_F = (\Gamma_G^5 + 2.69269\Gamma_G^4\Gamma_L + 2.42843\Gamma_G^3\Gamma_L^2 + 4.47163\Gamma_G^2\Gamma_L^3 + 0.07842\Gamma_G\Gamma_L^4 + \Gamma_L^5)^{\frac{1}{5}}. \tag{3.7}$$

These equations can be used to calculate the photon absorption cross section (ς) for a vapour,

$$\varsigma = \pi r_e c u \sum_{F,F'} A_{F,F'}\mathcal{V}(\upsilon - \upsilon_0), \tag{3.8}$$

by following the derivation presented in [70] to plot the hyperfine structure of cesium. In this equation, r_e is the rest mass of an electron, u is the oscillator strength for the

Hyperfine Transition		Normalised	Detuned Transition
F	F'	Strength ($A_{F,F'}$)	Frequency (GHz)
2	1	1/8	1.657
2	2	35/216	1.686
2	3	7/54	1.750
3	2	5/108	-1.348
3	3	35/216	-1.284
3	4	3/8	-1.164

Table 3.1: Normalised hyperfine transition strengths for photon absorption of an $I = 5/2$ alkali species and the detuned transition frequency within D2 line of ^{85}Rb.

transition and $A_{F,F'}$ are the transition strengths which are provided in Table 3.1 [70] for an $I = 5/2$ alkali species, where F denotes the ground state and F' refers to the excited state. As anticipated, this methodology can be applied to obtain the expected absorption spectra from the vapour cell used within the AWE constructed RF AM. This is displayed in Figure 3.3 for excitation along the D2 line of ^{85}Rb ($u = 0.332$), specifying a 70 torr nitrogen buffer gas and with the vapour heated to a temperature of 60°C. Using these values it can be shown that the hyperfine structure of the second excited state is expected to be unresolved; a spectra in which these levels are resolved is included for comparison. The broadened spectra in Figure 3.3 neglects the pressure shift in the transition frequencies. In the example of the experimental cell this would equate to a shift of approximately 500 MHz [71].

Analysis of the absorption profile produces a Doppler broadening value of ~ 500 MHz and a pressure broadening of 1.5 GHz at the maximum operational temperature for the RF magnetometer (60°C). These values indicate that, at this temperature, the pressure broadening dominates and therefore a Lorentzian distribution is expected.

3.2 Zeeman Splitting

In addition to the splitting of atomic levels observed in the fine and hyperfine structure, as previously discussed, the degeneracy of energy levels can be further lifted by the

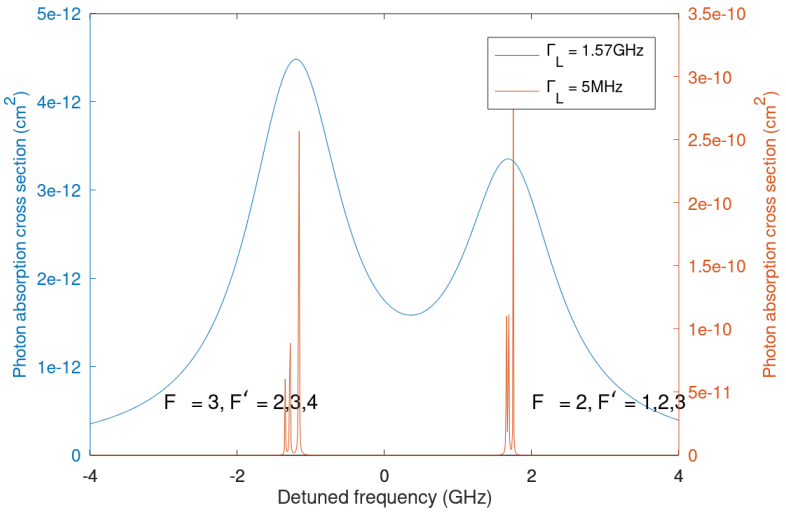

Figure 3.3: Photon absorption cross section for the D2 transition within ^{85}Rb as a function of frequency detuned from D2 resonance. Data is displayed for broad absorption profile (blue) with $\Gamma_L = 1.57\,\text{GHz}$, $\Gamma_G = 543\,\text{MHz}$ (at 60°C) and compared with the hyperfine structure resolved (red) with $\Gamma_L = 5\,\text{MHz}$ with $\Gamma_G = 1\,\text{MHz}$.

presence of an external magnetic field. This is described in the Zeeman effect in which each Zeeman sub-level is a projection of the total angular momentum (F) onto the external magnetic field axis. In the limit of a weak magnetic field the shift in the energy, E, of these levels is given as [65]:

$$\Delta E = \mu_B g_F m_F B \tag{3.9}$$

where μ_B is the Bohr magneton ($9.274 \times 10^{-24}\,\text{J/T}$) and g_F is the Landé factor which is expressed as the equations:

$$g_F = g_J \frac{F(F+1) + J(J+1) - I(I+1)}{2F(F+1)} + g_I \frac{F(F+1) + I(I+1) - J(J+1)}{2F(F+1)}, \tag{3.10}$$

$$g_J = 1 + \frac{J(J+1) + S(S+1) - L(L+1)}{2J(J+1)}. \tag{3.11}$$

In this limit, the energy splitting is linearly proportional to the applied magnetic field and is referred to as the linear Zeeman effect. The Larmor frequency describing the precession of the total angular momentum F within the magnetic field, is defined by the difference in energy between adjacent magnetic sub-levels (m_F, m_{F+1}) given as,

$$\omega_L = \frac{\Delta E_{m_F+1} - \Delta E_{m_F}}{\hbar} = 2\pi\gamma B \tag{3.12}$$

where γ is the gyromagnetic ratio of the alkali species and $\hbar$ is the reduced Planck's constant.

This linear relationship is applicable if the Zeeman shifts are much smaller than the other energy splittings. However as the strength of the field increases and the magnitude of the shifts become comparable with other effects, the Zeeman effect must be re-defined. In an intermediate field the ground state energy of the Zeeman sub-levels of hydrogen and all alkali-metals ($J = 1/2$) can be calculated using the Breit-Rabi formula which is specified as [69, 73, 74]:

$$E|J = 1/2, m_F\rangle = -\frac{\Delta E_{hf}}{2(2I+1)} + g_I \mu_B m_F B \pm \frac{\Delta E_{hf}}{2}\sqrt{1 + \frac{4m_F b}{2I+1} + b^2}, \tag{3.13}$$

$$b = \frac{(g_J - g_I)\mu_B B}{\Delta E_{hf}}. \tag{3.14}$$

The value of ΔE_{hf} is given as the energy difference between the ground hyperfine states, I is the nuclear spin of the alkali species, g_I is the nuclear g-factor, $g_J = 2.0023$ [75] is the Landé factor and m_F is the corresponding magnetic sub-level. In this equation the Bohr magneton can be expressed as $1.399 \cdot h\,\mathrm{MHz/G}$ and the $\pm$ sign references the

upper and lower ground states of $F = I + 1/2$ and $F = I - 1/2$.

The energy for the magnetic sub-levels as a function of the external magnetic field within both ^{85} Rb and ^{87}Rb are shown for the ground states ($5^2S_{1/2}$) in Figure 3.4, obtained using the values displayed within Table 3.2. Inspection of these results demonstrate that the non-linearity of the magnetic sub-level energies are apparent at larger fields ($> 500\,\mathrm{G}$) and that the energy shifts are opposite for the $F = I + 1/2$ and $F = I - 1/2$ ground states which indicates that atoms in these states precess in opposite directions.

A value of 500 G is 1000 times larger than the Earth's magnetic field (0.5 G) which itself corresponds to a Larmor frequency of 230 kHz in ^{85}Rb ($\gamma = 4.667 \times 10^5\,\mathrm{Hz/G}$). The operational range of the experiments in subsequent sections are less than 250 kHz which, as calculated using equation 3.12, corresponds to approximately 0.54 G. At these values, the difference in the energy of the $F = 2, m_F = 2$ level within ^{85}Rb between calculation with the linear approximation and the Breit-Rabi formula is displayed in Figure 3.5a. At B = 0.54 G this corresponds to a difference on the order of 0.00064% in ^{85}Rb; this faction appears small as it is relative to the hyperfine splitting.

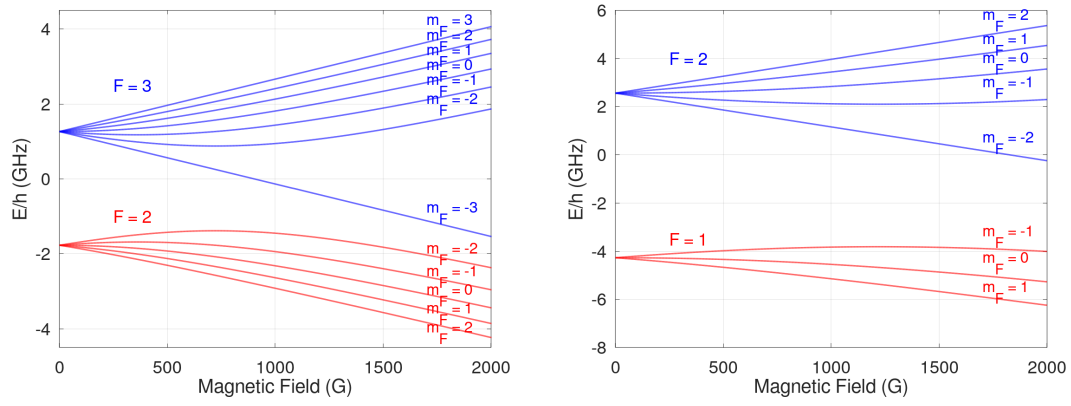

(a) ^{85}Rb (b) ^{87}Rb

Figure 3.4: Energy of ground state Zeeman levels as a function of the strength of the applied magnetic field. Data calculated using the Breit-Rabi formula with values for (3.4a) ^{85}Rb and (3.4b) ^{87}Rb.

Quantity	^{85}Rb	^{87}Rb
ΔE_{hf}	3.04 GHz $\cdot h$	6.84 GHz $\cdot h$
g_I	-2.93×10^{-4} [69]	9.95×10^{-4} [75]
I	5/2	3/2

Table 3.2: Values utilised to calculate the shifts in energy levels as a result of an external magnetic field within the Breit-Rabi formula.

As the Larmor frequency can be calculated by the energy difference between adjacent Zeeman levels as in equation 3.12, the difference in the energy splitting as calculated using the linear approximation and Breit-Rabi formula produces values of the Larmor frequency ω_L which deviate as the magnetic field increases, this is displayed in Figure 3.5b and corresponds to approximately 72 Hz.

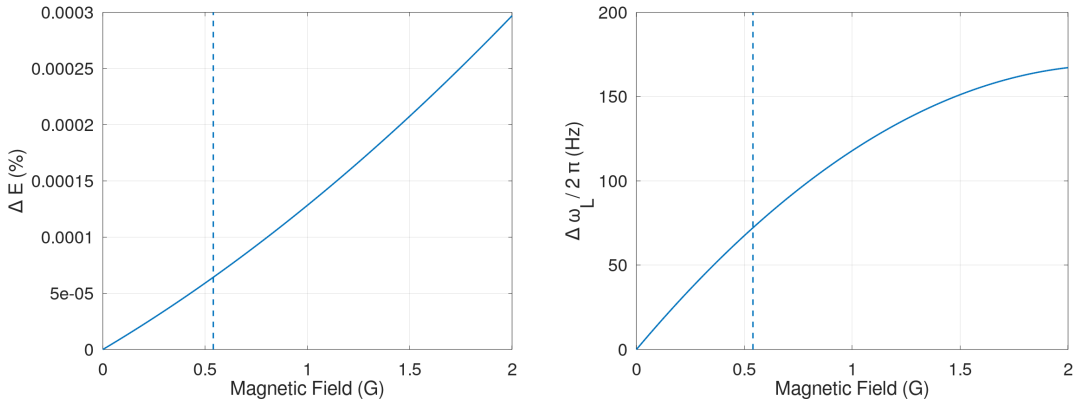

(a) ΔE (b) $\Delta\omega_L$

Figure 3.5: Relative difference between the energy splitting of the magnetic sub-levels between hyperfine value and the values as calculated with the linear approximation in equation 3.12 and the non-linear Breit-Rabi formula within equation 3.13. Data obtained for ^{85}Rb, $F = 2$, $m_F = 2$. Maximal operation field estimated as 0.54 G and indicated with dashed line.

3.3 Radio-Frequency Atomic Magnetometer

The problem space defined in Chapter 1 discusses the necessity to detect low conductive materials and/or small changes in conductivity (uranium alloys). This is made more

challenging when utilising the SERF sensors due to the limited operational frequency range ($< 500\,\text{Hz}$) which results in small eddy current induction signals as discussed in Chapter 2. A radio-frequency (RF) AM allows higher frequencies to be used and therefore greater eddy current signals to be generated from lower conductive objects. This Section examines the key features of atomic magnetometry in the context of a rubidium based RF magnetometer such as that constructed at AWE.

3.3.1 Optical Pumping

Atomic polarisation of a vapour is created by modifying the isotropic population distributions of atoms within the magnetic sub-levels of the atomic structure [76]. This is achieved through optical pumping in which atoms are excited with resonant light and undergo a cycle of absorption and de-excitation until the absorption state is depopulated. This is illustrated in Figure 3.6 which displays an initially un-polarised collection of spin 1/2 atoms with equal population across the two magnetic sub-levels (3.6a); these absorb resonant light and are promoted to the excited state before decaying to either sub-level. Repeating this process depopulates one of the sub-levels, causing the ensemble of atoms to no longer absorb the resonant light (3.6b)

The mechanisms involved in the pumping of a vapour depends upon the polarisation of the resonant light and the transition utilised. The allowed transitions are dictated by the selection rules,

$$\Delta F = 0, \pm 1 \tag{3.15}$$

$$\Delta L = \pm 1 \tag{3.16}$$

$$\Delta m_F = 0, \pm 1 \tag{3.17}$$

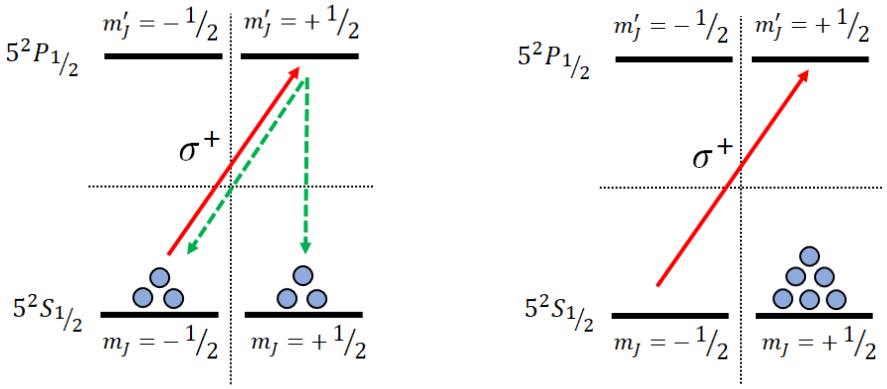

(a) Unpolarised (b) Polarised

Figure 3.6: Illustration of an initially unpolarised atomic population with spin 1/2 (a), evenly distributed between magnetic sub-levels. Through the process of optical pumping the population is made anisotropic (b)

these specify the requirement to have changes in total angular momentum, F, of 0 or ± 1, orbital angular momentum, L, of ± 1 and to undergo changes in the magnetic sub-level with values dependant on the polarisation of the resonant light. This originates in the need to conserve angular momentum in the atom-photon interaction; for example a circularly polarised ($\sigma^{\pm}$) photon carries angular momentum of $\pm\hbar$ depending on the helicity and therefore corresponds to changes in magnetic sub-level of $\Delta m_F = \pm 1$. Both the magnetometers discussed within this work utilised σ^+ polarised pumping beams.

The pumping mechanism also depends on the chosen transition. The AMs discussed in this report utilise different pumping schemes, with the QuSpin sensor pumping on the D1 line transition, and the RF magnetometer pumping along the D2 line. These transitions are discussed within Section 3.1.

Optical Pumping D1 Transition

The primary difference between pumping on the D1 rather than the D2 line is that it allows simple dark states to be formed. On the D1 line atoms can be excited from a ground state with an equal number of magnetic sub-levels as the excited state, as is shown in Figure 3.2. This alters the pumping mechanism, where atoms in the maximal m_J projections can no longer be excited along the D1 line ultimately resulting in a greater polarisation.

The D1 pumping scheme is illustrated in Figure 3.7 which displays the atomic structure but neglects the contribution from the nuclear spin I, leaving the total angular momentum $J = L + S$ with magnetic sub-levels m_J.

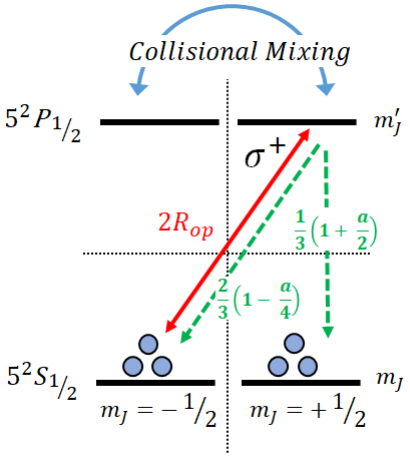

Figure 3.7: Illustration of pumping with circularly polarised light σ^+ on the D1 transition of an alkali atom, neglecting the contribution from the nuclear spin and including a the collisional mixing parameter, a.

The polarisation (P) of the ensemble of atoms can be derived from the behaviour of the atomic populations ($\mathcal{P}$) within each sub-level as detailed within [70]. Following this derivation, the rate at which atoms are excited from the ground state along the D1 line using circularly polarised light (σ^+) is given by the optical pumping rate, R_{OP}, which describes the rate of photons absorbed by unpolarised atoms averaged over atoms in all ground states. The pumping rate for a specific set-up can be calculated from the

photon absorption cross section and the photon flux [77]. The pumping rate for the D1 transition is $2R_{OP}$ where the factor of two originates from the fact that atoms can only be excited from the $m_J = -1/2$ with light of σ_+ polarisation.

The branching ratios of each decay from the excited state ($J^{'}, m_J^{'} = +1/2$) to the ground states ($J, m_J = \pm 1/2$) are given as 2/3 and 1/3 for the $m_J = -1/2$ and $m_J = +1/2$ respectively [70]. These values apply in the instance where there are no other transition mechanisms. In reality, the presence of a buffer or quenching gas would introduce collisional mixing. These collisions allow atoms to move between the excited states, equalising the populations and altering the branching ratios to 1/2 for each state.

Modifications made to the derivation in [70] by [38] defines a collisional mixing variable, a, where $a = 0$ indicates no mixing and $a = 1$ is complete mixing. The rate of population change for each ground state ($\mathcal{P}_+$ with $m_J = 1/2$, $\mathcal{P}_-$with $m_J = -1/2$) can be expressed for circularly positive polarised light, σ_+ as:

$$\frac{d}{dt}\mathcal{P}_- = -2R_{OP}\mathcal{P}_- + \frac{4}{3}(1 - \frac{a}{4})R_{OP}\mathcal{P}_-, \tag{3.18}$$

$$\frac{d}{dt}\mathcal{P}_+ = \frac{2}{3}(1 + \frac{a}{2})R_{OP}\mathcal{P}_-. \tag{3.19}$$

The spin polarisation (S_z) along the quantization axis (z) can be given as

$$\langle S_z \rangle = \frac{1}{2}(\mathcal{P}_+ - \mathcal{P}_-). \tag{3.20}$$

Equation 3.20 can be combined with equations 3.18 and 3.19 to produce

$$P = \frac{(2 + a)R_{OP}}{(2 + a)R_{OP} + 3R_{rel}} \tag{3.21}$$

for the steady state atomic polarisation, where $P = 2\langle S_z \rangle$.

Within this derivation a term, R_{rel}, is added to equations 3.18 and 3.19 to account

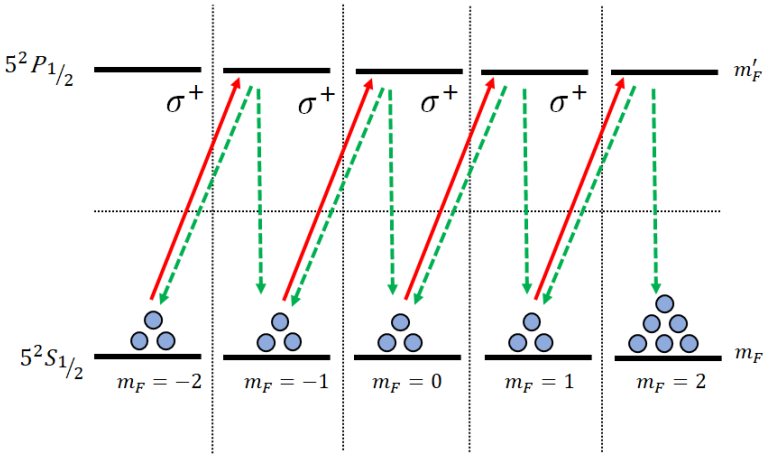

Figure 3.8: Illustration of the pumping scheme for an $I = 3/2$ alkali-metal vapour pumped with circularly polarised light σ^+ along the D1 transition.

for polarisation relaxation through mechanisms such as those described in Section 3.4. It can be seen that, as expected, a high polarisation depends upon a pumping rate (R_{OP}) considerably larger than the relaxation rate (R_{rel}).

The pumping scheme can also be examined in a structure which includes the nuclear spin contribution (I), such that the total angular momentum is $F = (L + S) + I$, producing magnetic sub-levels $m_F = -F, -F + 1..F - 1, +F$. These sub-levels are illustrated in Figure 3.8 for an $I = 3/2$ alkali-metal vapour such as ^{87}Rb which is the isotope used within the QuSpin sensors. In this example, atoms are excited from the ground state with circularly polarised light, undergoing a Δm_F transition. These atoms can then decay to a number of states, however, after a number of iterations, atoms become trapped in the $m_F = +2$ state which is transparent to the pumping light.

Optical Pumping on the D2 Transition

Optical pumping on the D2 transition differs from the D1 line as the number of magnetic sub-levels in the excited state can exceed the number in the ground state. As previously stated, this changes the pumping mechanism, where excitation of atoms in the maximal m_J projections can still be excited along the D2 line; this reduces the maximum achiev-

able polarisation in the presence of significant degrees of collisional mixing as discussed in the next Section.

As with the D1 transition, the transitions between the ground and excited state can be visualised in a structure neglecting the nuclear spin; this is displayed in Figure 3.9.

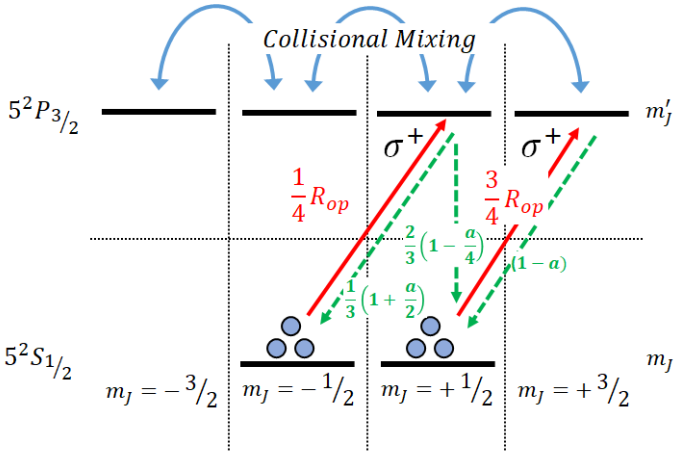

Figure 3.9: Illustration of pumping with circularly polarised light σ^+ on the D2 transition of an alkali atom, neglecting the contribution from the nuclear spin.

The derivation within [70] can again be utilised to determine the branching ratios. In this instance the pumping rate is instead split, with $\frac{R_{OP}}{4}$ and $\frac{3R_{OP}}{4}$ attributed to the $m_J = -1/2$ and $m_J = +1/2$ states respectively. The probability of decay from the $m_J^{'} = +1/2$ state is split 1/3, 2/3 for the $m_J = -1/2$ and $m_J = +1/2$ states, whilst there is only one allowed branch of decay for the $m_J^{'} = +3/2$ state. As previous, the degree of collisional mixing can equalise the excited states and modify these branching ratios to be equal at 1/2 for complete mixing ($a = 1$). The rate of change of the ground state populations are then given as

$$\frac{\partial}{\partial t}\mathcal{P}_- = -\frac{1}{4}R_{OP}\mathcal{P}_- + \frac{1}{3}(1+\frac{a}{2})\frac{R_{OP}}{4}\mathcal{P}_- \tag{3.22}$$

$$\frac{\partial}{\partial t}\mathcal{P}_+ = -\frac{3}{4}R_{OP}\mathcal{P}_+ + (1-a)\frac{3R_{OP}}{4}\mathcal{P}_+ + \frac{2}{3}(1-\frac{a}{4})\frac{R_{OP}}{4}\mathcal{P}_- \tag{3.23}$$

which can be translated into the atomic polarisation,

$$P = \frac{(2-5a)R_{OP}}{2(1+2a)R_{OP}+12R_{rel}}. \tag{3.24}$$

A comparison of equations 3.24 and 3.21 for the polarisation of the atoms via D1 and D2 line pumping demonstrates that the polarisation created by pumping along the D2 line is fundamentally limited compared to pumping on the D1 line. This is illustrated in Figure 3.10 which displays the polarisation of the ensemble as a function of the ratio of the pumping and relaxation rates (R_{OP}/R_{rel}).

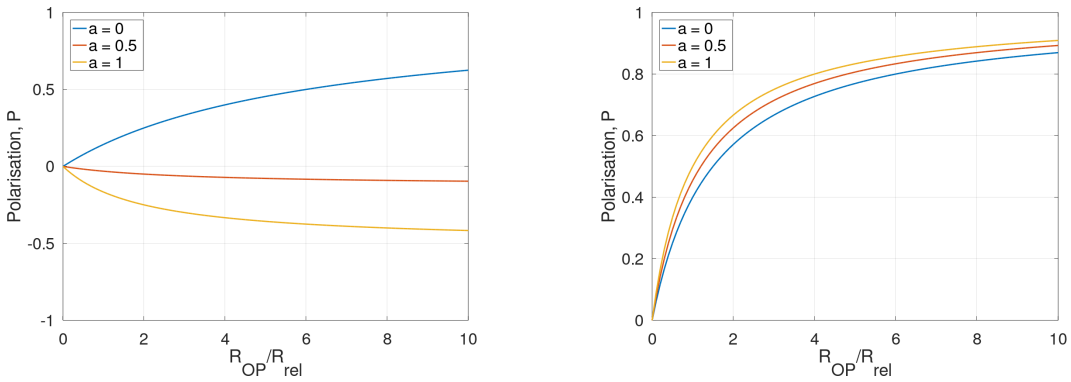

(a) D1 pumping (b) D2 pumping

Figure 3.10: Polarisation, P, of the atomic ensemble as a function of the ratio of optical pumping rate and the relaxation rate across collisional mixing degrees a = 0, a = 0.5 and a = 1 and for (a) D1 pumping and (b) D2 pumping.

In the instance where there is no collisional mixing ($a = 0$) the degree of atomic polarisation that can be achieved at any value of R_{OP}/R_{rel} is greater for D1 than D2. This originates from the cycling between the ground and excited state in the maximal projection of the D2 atomic structure. As the amount of collisional mixing increases, the polarisation achieved with the D1 pumping is comparatively unaffected whilst the

polarisation achieved along the D2 line starts to become negative. This effect comes from the re-distribution of atoms in the excited state such that the branching ratios reduce to 1/2, 1/2 and 0 (see Figure 3.9). In this instance the atoms no longer de-excite from the $m_J^{'} = 3/2$ to $m_J = 1/2$ state, reducing the accumulation of atoms in that state and having the effect that each pumped atom, on average, removes angular momentum from this state. The degree of collisional mixing will depend upon the constituents of the vapour cell. A smaller amount of collisional mixing will be observed when an anti-relaxation coating is used instead of a buffer gas to prevent wall collisions.

As previously, the pumping scheme on the D2 transition can be visualised including the nuclear spin contribution. Figure 3.11 displays this structure for an $I = 5/2$ atomic species such as ^{85}Rb. This isotope is specified as it is utilised within the RF AM. The RF AM cell contains a natural mix of rubidium (72% ^{85}Rb, 28% ^{87}Rb) and utilises the ^{85}Rb isotope for measurements of the magnetic field as it is more abundant than ^{87}Rb. The magnetometer signal scales with the number of atoms as discussed in Section 3.6. Excitation along the D2 transition will still create polarisation with a build up of atoms in the $m_F = 2$ state; however, unlike the D1 transition, this population will cycle between this state and the excited $m_F^{'} = 3$ state. This process creates a less complete pumping with an increasing value of collisional mixing, as can be observed from a comparison of equations 3.21 and 3.24. The RF magnetometer constructed at AWE uses the D2 transition despite the smaller degree of pumping expected. This decision allows existing equipment to be used, minimising programme costs. A similar set up was previously demonstrated by [38] using a buffer gas cell indicating that whilst it is not optimal, a high-performance ECI imaging system can be achieved. Pumping on the D2 transition rather than the D1 transition has a less significant effect in anti-relaxation coating cells as opposed to buffer gas cells and is used in [9] for another RF AM.

Whilst these figures display the magnetic sub-levels of a specific hyperfine transition, in a buffer gas cell such as those used in both the RF and QuSpin magnetometers, the

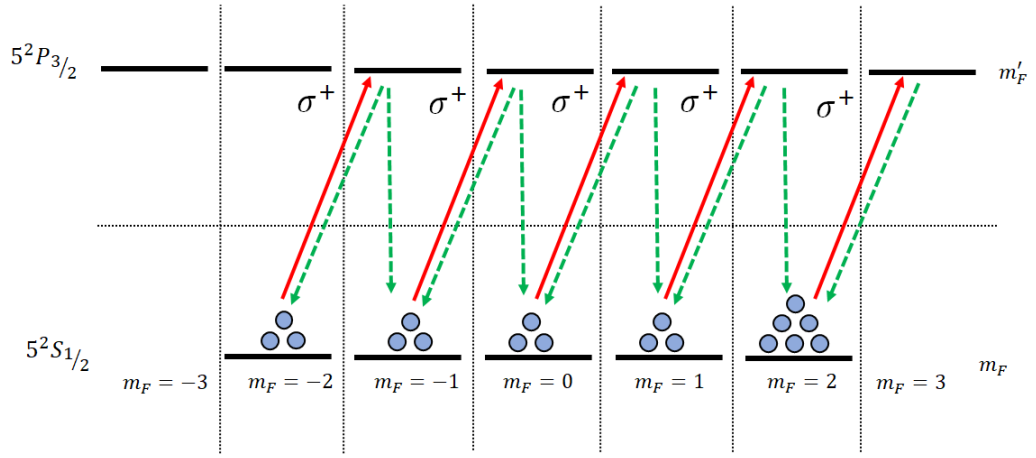

Figure 3.11: Illustration of the D2 pumping scheme for an $I = 5/2$ atomic species pumped with circularly positive polarised light σ^+.

excited hyperfine levels are typically unresolved due to effects of pressure and Doppler broadening as was discussed in Section 3.1. In the RF AM constructed at AWE, the pump beam was set to be resonant with the $F = 2$ to $F' = 3$ hyperfine transition; this was achieved using a spectroscopy unit that includes a cell without buffer gas and therefore does not account for any pressure shift. Whilst the hyperfine transitions are defined here, the broadening in the sensing vapour cell results in atoms being pumped across all the D2 hyperfine transitions.

3.3.2 Evolution of Atomic Polarisation

The previous Sections have considered quantum mechanical details in the description of the atomic energy structure and populations of states, this Section shifts to a more classical discussion of the evolution of the ensemble of atomic polarisations. The evolution of the atomic polarisation in an external magnetic field was explored by Bloch [78], here the magnetic moment, $\bar{M}$, is defined which is a vector representing the contributions from all individual nuclei magnetic moments. In this instance, the application of an external magnetic field, $\bar{B}_0$, results in a torque, $\mathcal{T}$, on $\bar{M}$ which precesses about $\bar{B}_0 = B_0\hat{z}$ at the Larmor frequency ($\omega_L = \omega_0$). This is described in Section 3.2 and the general

result re-iterated as

$$\omega_0 = \gamma B_0. \tag{3.25}$$

The precession of $\bar{M}$ is illustrated in Figure 3.12, with the torque given as

$$\mathcal{T} = \bar{M} \times \bar{B}_0. \tag{3.26}$$

In a classical description of angular momentum ($\mathcal{A}$), $\frac{d\mathcal{A}}{dt} = \mathcal{T}$ and $M = \gamma\mathcal{A}$, therefore the evolution of the magnetic moment over time can be given as

$$\frac{\partial \bar{M}}{\partial t} = \gamma(\bar{M} \times \bar{B}_0). \tag{3.27}$$

As $\bar{M}$ is a vector it can be split into longitudinal (M_z) and transverse components (M_x, M_y). In this approximation, M_z is considered constant in the absence of any relaxation mechanisms and M_x, M_y vary sinusoidally about the z-axis as illustrated in Figure 3.13.

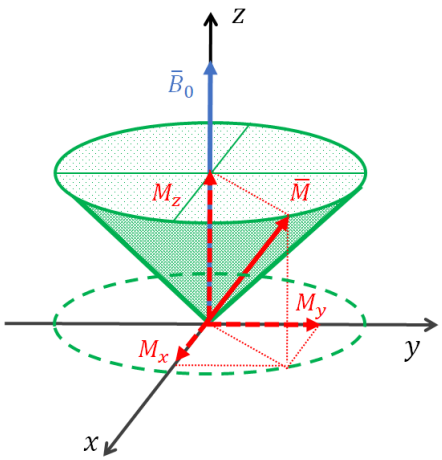

Figure 3.12: Illustration of the precession of the magnetic moment $\bar{M}$ about an applied field $\bar{B}_0$ along the z-axis.

In practice both longitudinal and transverse components vary in time due to various

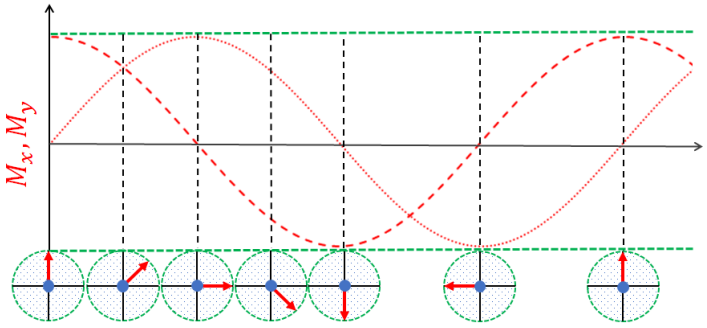

Figure 3.13: Sinusoidal variation in the values M_x (dashed line) and M_y (dotted line) components of the magnetic moment $\bar{M}$ as a function of time during the precession of $\bar{M}$ about a magnetic field $\bar{B}_0$ applied along the z-axis. The corresponding position of $\bar{M}$ (solid red line) is displayed in the x-y plane.

relaxation mechanisms which de-cohere the ensemble of atoms, these are characterised by the time scales τ_1 and τ_2 respectively and modify the magnetisation components as given by:

$$\frac{\partial M_z}{\partial t} = \frac{-(M_z - M_0)}{\tau_1}, \tag{3.28}$$

$$\frac{\partial M_x}{\partial t} = \frac{-M_x}{\tau_2}, \tag{3.29}$$

$$\frac{\partial M_y}{\partial t} = \frac{-M_y}{\tau_2}. \tag{3.30}$$

In the case of the longitudinal relaxation, the component of the magnetic moment along the z-axis relaxes back to a stationary value, M_0, whilst the transverse components decay to zero. These terms can be added to equation 3.27 to produce Bloch's equation as

$$\frac{\partial \bar{M}}{\partial t} = \gamma(\bar{M} \times \bar{B}_0) - \frac{M_x\hat{x} + M_y\hat{y}}{\tau_2} - \frac{(M_z - M_0)\hat{z}}{\tau_1}. \tag{3.31}$$

This equation can be solved for the components of $\bar{M}$ in the scenario where a weak ($B_1 << B_0$) oscillating magnetic field is applied perpendicular to $\bar{B}_0$, $\bar{B}_1 = -B_1 \cos(\omega t)\hat{y}$. This is representative of the operation of the RF AM.

To determine the components of $\bar{M}$, the motion of $\bar{M}$ can also be considered in a frame which rotates around the z-axis at the frequency of $\bar{B}_1$, ω. This frame is denoted by the coordinate system ($x^{'}$, $y^{'}$, $z^{'}$). In the laboratory frame the linearly polarised RF field can be written as two counter rotating components [70]:

$$\bar{B}_1 = -\frac{B_1}{2}(e^{i\omega t} + e^{-i\omega t})\hat{y}. \tag{3.32}$$

The transformation to the rotating frame allows the approximation to be made that any field far from ω can be neglected including the counter rotating component at $-\omega$; as such, the RF field is stationary in this frame. Another consequence of moving to the rotating frame is the modification of B_0 by a fictitious field. This modification produces an effective field, $\bar{B}_0^{'}$, given by

$$\bar{B}_0^{'} = (B_0 - \frac{\omega}{\gamma})\hat{z} = (\frac{\omega_0 - \omega}{\gamma})\hat{z} = \frac{\Delta\omega}{\gamma}\hat{z} \tag{3.33}$$

where the accent ($B_0^{'}$) denotes variables in the rotating frame and $\Delta\omega = \omega_0 - \omega$.

The addition of the perturbation field, $\bar{B}_1^{'} = -\frac{B_1}{2}\hat{y}$, gives the total effective field

$$\bar{B}^{'} = \frac{\Delta\omega}{\gamma}\hat{z} - \frac{B_1}{2}\hat{y}^{'} \tag{3.34}$$

which is displayed in Figure 3.14.

The magnetic moment, $\bar{M}$, precesses in the rotating frame at a frequency $\omega^{'}$ with components along each axis of $M_x^{'}$, $M_y^{'}$, and M_z [65].

The Bloch equation in the rotating frame can be expressed as

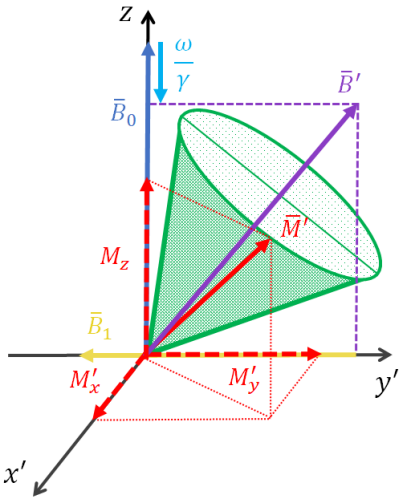

Figure 3.14: Illustration of the precession of the magnetic moment $\bar{M}$ about an effective field $\bar{B}^{'}$ in a frame ($x^{'}$, $y^{'}$, $z^{'}$) that rotates about the z-axis at a frequency ω. The effective field is constructed from the applied field, $\bar{B}_0$, an modification field $\bar{B}^{'}_0 = \omega/\gamma$ and a perturbation field $\bar{B}_1$ aligned along y-axis.

$$\frac{\partial \bar{M}^{'}}{\partial t} = \gamma(\bar{M}^{'} \times \bar{B}^{'}) - \frac{M^{'}_x \hat{x}^{'} + M^{'}_y \hat{y}^{'}}{\tau_2} - \frac{(M_z - M_0)\hat{z}}{\tau_1}. \tag{3.35}$$

The steady state solution ($\frac{\partial \bar{M}^{'}}{\partial t} = 0$) of this equation results in the components given as [65]

$$M^{'}_x = M_0 \frac{\gamma(B_1/2)\tau_2}{1 + \Delta\omega^2\tau_2^2 + \gamma^2(B_1/2)^2\tau_1\tau_2} \tag{3.36}$$

$$M^{'}_y = -M_0 \frac{\Delta\omega\gamma(B_1/2)\tau_2^2}{1 + \Delta\omega^2\tau_2^2 + \gamma^2(B_1/2)^2\tau_1\tau_2} \tag{3.37}$$

$$M_z = M_0 \frac{1 + \Delta\omega^2\tau_2^2}{1 + \Delta\omega^2\tau_2^2 + \gamma^2(B_1/2)^2\tau_1\tau_2}. \tag{3.38}$$

These components can be transformed back into the laboratory frame using $M_x = M^{'}_x\cos(\omega t) - M^{'}_y\sin(\omega t)$ and $M_y = M^{'}_x\sin(\omega t) + M^{'}_y\cos(\omega t)$. The projection observed by

the probe beam in the RF AM is M_x which is given as

$$M_x = M_x^{'}\cos(\omega t) - M_y^{'}\sin(\omega t) = \frac{1}{2}M_0\gamma B_1 \frac{\tau_2\cos(\omega t) + \Delta\omega\tau_2^2\sin(\omega t)}{1 + \Delta\omega^2\tau_2^2 + \gamma^2(B_1/2)^2\tau_1\tau_2}. \tag{3.39}$$

Inspection of this result demonstrates that in the x-y plane, the component M_x oscillates at the frequency of the RF-field (ω). The strength of the component M_x is also found to be proportional to the polarisation along the bias field axis (M_0), therefore for this particular configuration, the M_x component is maximised by aligning the pumping and bias fields, this would reduce to zero if orientated perpendicular.

This solution allows a prediction of the AM output to be made. A measurement of M_x results in a component which oscillates in-phase with the applied RF field ($M_x^{'}$), and a second component oscillating 90° out of phase ($M_y^{'}$), known as a quadrature component. If we specify a quantity;

$$\Gamma = \frac{1}{\tau_2}\sqrt{1 + (\gamma B_1/2)^2\tau_1\tau_2} \tag{3.40}$$

the components $M_x^{'}$ and $M_y^{'}$ can be written as

$$M_x^{'}(\omega) = \left[\frac{\Gamma}{\Gamma^2 + (\omega - \omega_0)^2}\right], \tag{3.41}$$

$$M_y^{'}(\omega) = \left[\frac{-\Gamma(\omega - \omega_0)}{\Gamma^2 + (\omega - \omega_0)^2}\right] \tag{3.42}$$

which take the form of a Lorentzian and anti-Lorentzian function, where Γ is the full-width half maximum (FWHM). These components are illustrated in Figure 3.15 for a FWHM of 200 Hz and a central frequency of 10 kHz ($\omega = 2\pi f$). A maximum is observed in the Lorentzian component when $\omega = \omega_0$, with a corresponding maximal gradient in the anti-Lorentzian function. It can be noted from equation 3.39 that M_x is increased

with the strength of the RF field (B_1), however this is tempered with the increase in Γ which has an impact on the sensitivity as discussed in Section 3.7.

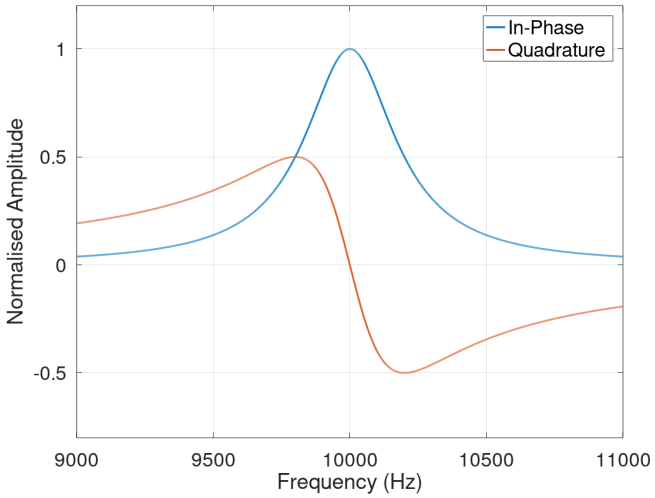

Figure 3.15: Normalised in-phase and quadrature components of the nuclear angular momentum component M_x for a $\Gamma = 200\,\text{Hz}$ and centre frequency 10 kHz.

3.3.3 Optical Detection

Within the RF AM, the evolution of the magnetic moment is observed through the polarisation rotation of a probe beam which propagates orthogonal to the pump beam and bias field axis. The beam used is linearly polarised which can be expressed as a combination of two balanced circular components of opposite helicity (σ^+, σ^-). One of these components will be preferentially dephased as it travels through the vapour, which in a polarised state, exhibits circular birefringence. Circular birefringence can be defined when the different helicities experience different refractive indices.

The change in refractive index can be expressed through the change in absorption co-efficient of each polarisation component which in turn is related to the population of the ground states and therefore the photon absorption cross section, ς. A derivation within [70] assumes an off-resonant, linearly polarised probe beam which propagates or-

thogonally to the pump beam; this is consistent with the RF magnetometer constructed at AWE. This derivation expresses the refractive index ($\mathcal{N}$) of the vapour as

$$\mathcal{N}(\upsilon) = 1 + \Big(\frac{nc^2 u r_e}{4\upsilon}\Big)\mathrm{Im}[\mathcal{L}(\upsilon - \upsilon_0)] \tag{3.43}$$

where n is the density of the vapour, υ is the frequency of the light, r_e is the classical electron radius ($2.82 \times 10^{-15}\,\mathrm{m}$) and u is the oscillator strength and represents the probability of absorption by either the D1 or D2 transition. In the instance where the hyperfine structure is considered to be unresolved and where the pressure broadening is much greater than the Doppler broadening ($\Gamma_L >> \Gamma_G$) the absorption profile can be considered predominantly Lorentzian (as discussed in Section 3.1).

The refractive index experienced by each helicity of light ($\mathcal{N}_+, \mathcal{N}_-$) depends upon the dephasing of each polarisation component. As discussed in Section 3.3.1 the allowed transitions within the magnetic sub-levels are dictated by the polarisation of the resonant light with $\Delta m_J = \pm 1$ for $\sigma^{\pm}$. For a linearly polarised probe beam, which can be split into two circular components, the refractive index includes the absorption branching ratios from both $\sigma^{\pm}$ transitions, given within Figure 3.16 for the D2 transition. Accounting for the respective level populations, $\mathcal{N}_+$ and $\mathcal{N}_-$ can be expressed as:

$$\mathcal{N}_+(\upsilon) = 1 + 2\Big(\frac{3}{4}\mathcal{P}_- + \frac{1}{4}\mathcal{P}_+\Big)\Big(\frac{nc^2 u_{D2} r_e}{4\upsilon}\Big)\mathrm{Im}[\mathcal{L}(\upsilon - \upsilon_0)], \tag{3.44}$$

$$\mathcal{N}_-(\upsilon) = 1 + 2\Big(\frac{3}{4}\mathcal{P}_+ + \frac{1}{4}\mathcal{P}_-\Big)\Big(\frac{nc^2 u_{D2} r_e}{4\upsilon}\Big)\mathrm{Im}[\mathcal{L}(\upsilon - \upsilon_0)]. \tag{3.45}$$

Inspection of these equations demonstrate that the circular birefringence ($\mathcal{N}_+ \neq \mathcal{N}_-$) occurs when there is an imbalance in the populations of the ground states, i.e. $\mathcal{P}_+ \neq \mathcal{P}_-$ and therefore a net polarisation P.

The polarisation rotation of the linear probe beam (θ) can be described as

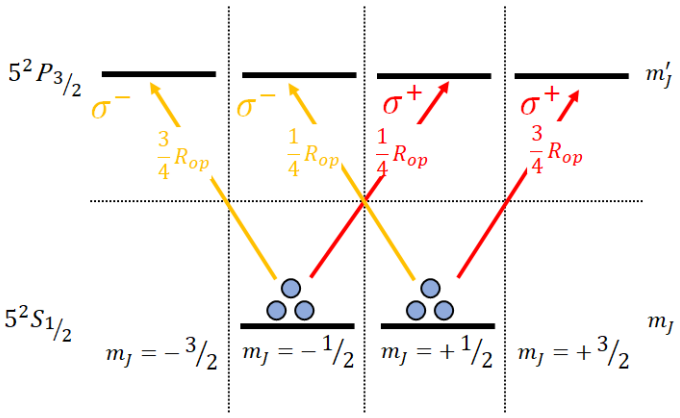

Figure 3.16: Absorption of linear polarised light split into balanced circularly polarised components of opposite helicity. Absorption displayed for the D2 transition, neglecting the nuclear spin component.

$$\theta(\upsilon) = \frac{\pi \upsilon l}{c}\Big[\mathcal{N}_+(\upsilon) - \mathcal{N}_-(\upsilon)\Big] \tag{3.46}$$

that, through substitution of equations 3.44 and 3.45 and $P_x = \mathcal{P}_+ - \mathcal{P}_-$ [70], produces

$$\theta(\upsilon) = \frac{\pi}{2} l n r_e c P_{D2}\Big(- u_{D1}\mathrm{Im}[\mathcal{L}(\upsilon - \upsilon_{0,D1})] + \frac{1}{2} u_{D2}\mathrm{Im}[\mathcal{L}(\upsilon - \upsilon_{0,D2})]\Big) \tag{3.47}$$

where l is the length of the cell, u_{D1}, u_{D2} are the oscillator strengths of the D1 and D2 transitions (for ^{85}Rb, $\mathrm{u}_{D1} = 0.332$, $\mathrm{u}_{D2} = 0.668$) and P_{D2} is the polarisation achieved pumping on the D2 transition.

This equation allows the optical rotation to be plotted as a function of frequency detuned from resonance. To approximate the polarisation rotation for the RF AM constructed at AWE, a temperature of 50°C is specified with a buffer gas pressure of 70 Torr and assuming a D2 transition with $P_{D2} = 0.5$. The resulting polarisation rotation is displayed in Figure 3.17, reaching a maximal rotation at ±0.7 GHz detuned from resonance.

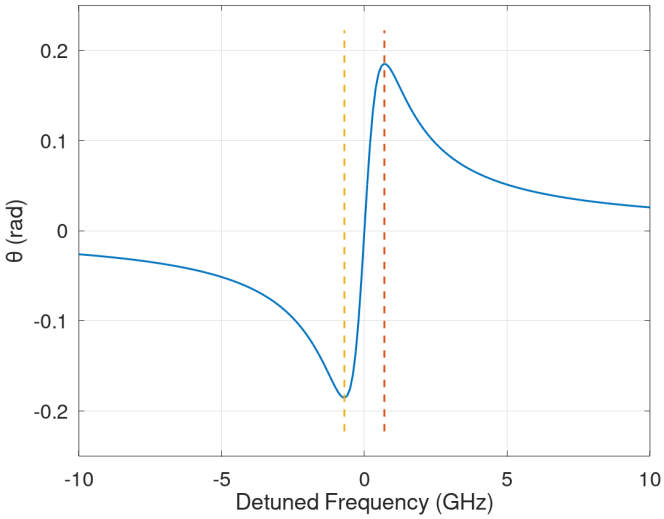

Figure 3.17: Polarisation rotation angle of linear polarised light travelling through a 25 mm cell filled with ^{85}Rb and a nitrogen buffer gas at 70 Torr, at a temperature of 50°C and with $P_{D2} = 0.5$. Maximum and minimum rotation angles are marked with (red/yellow) vertical lines; these occur at ± 0.7 GHz.

3.4 Spin Relaxation Mechanisms

Once a vapour has been optically pumped and a spin-polarisation created, the sensitivity of the system is dependent upon mechanisms which cause relaxation of this state. The primary origins of spin relaxation are collisions of the polarised alkali-atoms with other alkali-atoms, buffer/quenching gas atoms or with the cell walls. These effects are broadly separated into spin-exchange collisions which conserve the total angular momentum and spin destruction collisions in which this is not conserved.

The generic collision rate ($\mathcal{R}_i$) between the alkali-atoms and another species for any given process (i) can be expressed as

$$\mathcal{R}_i = n\sigma_i\bar{v}, \tag{3.48}$$

$$\bar{v} = \sqrt{\frac{8k_BT}{\pi\mathfrak{M}}}. \tag{3.49}$$

This equation accounts for the vapour density of the collisional species (n), the cross section of the collision (σ_i) and the thermal velocity of the atoms ($\bar{v}$). The thermal velocity is calculated with the temperature T in Kelvin and the reduced mass $\frac{1}{\mathfrak{M}_r} = \frac{1}{\mathfrak{m}} + \frac{1}{\mathfrak{m}'}$ obtained from the masses of the alkali atoms ($\mathfrak{m}$) and the second species ($\mathfrak{m}'$).

The longitudinal and transverse polarisation lifetimes (τ_1, τ_2) which contribute to the optical rotation signal (see Section 3.3.3), are given as

$$\frac{1}{\tau_1} = \frac{1}{q}(\mathcal{R}_{SD} + \mathcal{R}_{OP} + \mathcal{R}_{Pr}) + \mathcal{R}_{wall}, \tag{3.50}$$

$$\frac{1}{\tau_2} = \frac{1}{\tau_1} + \frac{1}{q_{SE}}\mathcal{R}_{SE} + \mathcal{R}_{gr}. \tag{3.51}$$

The τ_1 time is obtained using the nuclear slowing down factor (q) which characterises the degree to which spin coherence is maintained [70], the rate of photon absorption from the pump and probe beams ($\mathcal{R}_{OP}, \mathcal{R}_{pr}$), the rate of wall collisions $\mathcal{R}_{wall}$ and the spin destruction rate, $\mathcal{R}_{SD}$. The spin destruction rate ($\mathcal{R}_{SD} = \mathcal{R}_{SD}^{Self} + \mathcal{R}_{SD}^{B} + \mathcal{R}_{SD}^{Q}$) is calculated by considering the rate of the previously mentioned interactions, including the collision rate of the alkali-atoms with themselves ($\mathcal{R}_{SD}^{Self}$), the buffer gas atoms ($\mathcal{R}_{SD}^{B}$) and quenching gas atoms ($\mathcal{R}_{SD}^{Q}$) [70]. The calculation of the transverse polarisation lifetime, τ_2, includes all terms from the longitudinal lifetime, with the addition of a spin-exchange broadening factor $1/q_{SE}$, the rate of spin-exchange collisions $\mathcal{R}_{SE}$ and a term corresponding to the broadening as a result of magnetic field gradients $\mathcal{R}_{gr}$. Subsequent Sections explore a number of these factors in more detail.

3.4.1 Spin-Exchange Collisions

The spin-exchange interaction involves a collision between two alkali-atoms, one spin up and the other spin down. For example, atoms occupying the $F = I+1/2$ and $F = I-1/2$ hyperfine ground states. An interaction between these atoms results in the exchange of

the orientation of two spins but the conservation of overall spin. This is commonly expressed as the exchange between two states, $\mathfrak{A}$ and $\mathfrak{B}$:

$$\mathfrak{A}(\uparrow) + \mathfrak{B}(\downarrow) = \mathfrak{A}(\downarrow) + \mathfrak{B}(\uparrow). \tag{3.52}$$

The spin exchange rate for rubidium vapour, as was used within the RF AM constructed at AWE, can be estimated from equation 3.48. The spin-exchange cross section, σ_{SE}, for rubidium has been experimentally determined as $1.9 \times 10^{-14}\,\mathrm{cm}^2$ [79, 80]. This value can be paired with the mass of rubidium ($\mathfrak{m} = 85.5u$) and a room temperature of 25°C to produce a spin-exchange rate of $\mathcal{R}_{SE} = 6.7s^{-1}$. This value is of the same order of magnitude experimentally obtained for rubidium in [81]. Spin-exchange collisions are explored in greater depth for high density vapours in Section 3.5.

3.4.2 Spin Destruction

Spin destruction collisions are distinct from spin-exchange collisions in that they do not conserve the total angular momentum. As with equation 3.48, the rate of these collisions depend upon their corresponding cross sections which are usually considerably smaller than the those for spin-exchange interactions. As discussed in the previous section, the experimentally determined value of the spin exchange cross section is $\sigma_{SE} = 1.9 \times 10^{-14}\,\mathrm{cm}^2$ this can be compared with $\sigma_{SD}(Rb - Rb) = 9 \times 10^{-18}\,\mathrm{cm}^2$ for spin destruction interactions between rubidium atoms and $\sigma_{SD}(Rb - N_2) = 1 \times 10^{-22}\,\mathrm{cm}^2$ between rubidium atoms and nitrogen atoms [82]. Nitrogen is considered as it is used as the buffer gas within the RF AM cell.

Spin Exchange collisions are therefore the dominant relaxation process in standard operation at any particular pressure and temperature, however spin destruction rates are more relevant in the SERF regime where the effects of spin-exchange have been suppressed.

3.4.3 Wall Collisions

In collisions between alkali atoms and the walls of the vapour cell, the alkali-atom is adsorbed before being re-emitted in an interaction which completely depolarises the atom. Suppression of this type of depolarisation is commonly achieved by coating interior walls of the cell with an anti-relaxation coating or by including a buffer gas. A number of anti-relaxation coatings have been proposed including paraffin [83]. In general the coating places a barrier between the alkali-atoms and the glass from which they can inelastically scatter; this allows thousands of bounces before depolarisation.

Alternatively, the inclusion of a buffer gas aims to slow the diffusion of alkali-atoms out to the walls, extending the time between depolarisations. The pressure of the buffer gas balances the suppression of the wall collision rate with an increase in the spin destruction rate associated with collisions between the alkali-atoms and the buffer gas as discussed in the previous Section. Other effects can also be considered including the broadening of spectral lines associated with pressure broadening as discussed within Section 3.1.

3.4.4 Magnetic Field Gradients

Magnetic field gradients across distances comparable with the size of the vapour cell create variation in the precession frequencies across the ensemble, where the rate will be dictated by the local field. The effect of field gradients is influenced by the diffusion of the atoms within the cell. In a buffer gas cell, the presence of the gas restricts the volume within which the atoms move, reducing their ability to experience field gradients. Conversely having an anti-relaxation coating allows the atoms to sample the field across the cell, producing an averaged measurement [84].

Whilst the susceptibility to field gradients negatively impacts sensitivity by limiting transverse lifetime as in equation 3.51, having fast atomic diffusion can also limit the spatial resolution of the sensor. A consequence of reduced spatial resolution is that it

removes the potential to use multiple beams within the same vapour cell. Multiple beams through single cells have been utilised in a number of cases [85] to make gradiometric measurements which can improve sensitivity through the reduction of common-mode noise.

3.5 Spin Exchange Relaxation Free Magnetometers

The QuSpin AM utilised in this thesis operates in the spin-exchange relaxation free (SERF) regime. This regime is characterised by the suppression of spin-exchange broadening which is a primary source of noise in many standard configurations. Suppression of this source of broadening removes a limitation and allows the sensitivity of system to instead be governed by smaller effects such as spin destruction.

3.5.1 Spin-Exchange Relaxation Free Regime

The SERF regime is achieved by increasing the spin-exchange collision rate ($\mathcal{R}_{SE}$) to be much faster than the precession frequency; this can be achieved through a sufficiently small magnetic field ($\omega_L = \gamma B_0$) and high vapour density. In this regime each atom will rotate through a small precession angle before the next collision (see Figure 3.18a), and in one complete precession cycle will sample all ground state Zeeman sub-levels. A net polarisation is achieved as atoms spend slightly longer amounts of time in the $F = I + 1/2$ state (in the absence of pumping and in thermal equilibrium) which has a greater number of Zeeman levels, specifically the upper end state.

The atoms occupying the Zeeman ground states precess at the same frequency but in opposite directions, as illustrated in Figure 3.18b and described in Section 3.2. Examination of the optical rotation angle from Section 3.3.3 highlights that, as the density of the vapour is increased, so does the maximum rotation angle. However, continued increase in the density leads to a greater number of spin-exchange collisions which reduce

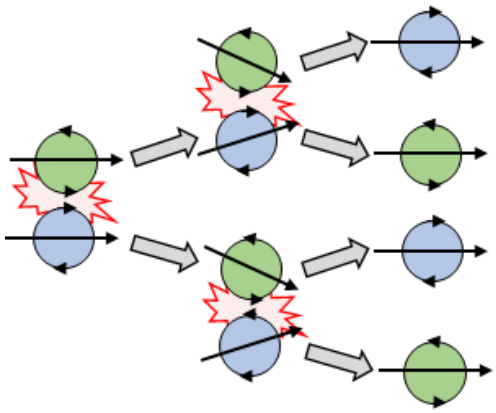

(a) Spin-exchange collisions in which small precession angles are undergone between collisions.

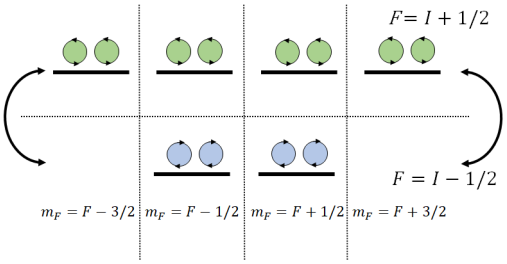

(b) Atoms in two ground states precessing in opposite directions

Figure 3.18: Illustration of atoms with opposite precession frequencies occupying the two ground states of an alkali-metal; spin-exchange collisions between atoms in these two states will result in a swap of the spin values (b). A high spin-exchange collision rate will result in a small precession angles being completed before each collision, producing an averaged polarisation (a).

sensitivity through depolarisation. The resonance broadening within the ultra-high density regime (SERF) was explored by Happer and Tam [86] who developed a statistical analysis of the effect of rapid spin exchange which is discussed below.

Two ground hyperfine states ($\mathfrak{A}$: $F = I + 1/2$ and $\mathfrak{B}$: $F = I - 1/2$) are considered in which the total angular momentum F oscillates at frequency $\omega_{\mathfrak{A}}$ whilst precessing in state $\mathfrak{A}$ and $\omega_{\mathfrak{B}}$ when in state $\mathfrak{B}$; $\omega_{\mathfrak{A}}$ and $\omega_{\mathfrak{B}}$ are similar in value but precess in opposite directions. A spin-exchange collision causes the atom to swap between states which occurs at a specified rate $\mathcal{R}_{SE}$, giving an average time in each state of $\tau_{\mathfrak{AB}}$. At low spin exchange rates, $\mathcal{R}_{SE} << \omega_{\mathfrak{A}}, \omega_{\mathfrak{B}}$ several precession cycles can be completed before the next collision which produces a distinct Fourier spectra with defined peaks at both frequencies. As the spin-exchange rate is increased, the atoms complete less full cycles before switching states, producing a less well defined Fourier spectra. Finally, once the spin-exchange rate is much larger than the individual frequencies, the atom completes a very fractional amount of a single cycle in each state, producing a single,

slower but more coherent waveform. This process is illustrated in Figure 3.19 which defines $\omega_{\mathfrak{A}} = 1\,\text{Hz}$, $\omega_{\mathfrak{B}} = -1.2\,\text{Hz}$ and displays the waveforms and corresponding Fourier spectra for $R_{SE} = 0.1, 1, 10$. The principle frequency components initially correspond to the frequency of each state (Figures 3.19a, 3.19b) before reducing to a single frequency of 0.08 Hz at rapid spin-exchange values (Figures 3.19e, 3.19f).

Common alkali metals chosen for SERF magnetometers are potassium, rubidium and cesium, with potassium having the greatest sensitivity due to its lower spin destruction cross section ($1 \times 10^{-14}\,\text{cm}^2$) [82], however, it requires the greatest amount of heating (typically 180°C) to achieve the required densities. At the other end of the scale, cesium requires less heating (typically $100 - 120°$) but has the lowest sensitivity with the highest spin destruction cross section ($2 \times 10^{-16}\,\text{cm}^2$) [82]. Rubidium occupies a middle ground (150°C) and is therefore a common choice for SERFs [76]. The QuSpin sensor utilises a ^{87}Rb vapour.

3.5.2 SERF Magnetometers

SERF magnetometers refer to sensors which suppress spin-exchange collisions, this refers to a property of the vapour rather than the mechanism of field measurement. The SERF sensor used within this work were the zero-field magnetometers manufactured by QuSpin in the US [60].

3.5.3 Commercial Atomic Magnetometer: QuSpin

The basic operation of the QuSpin magnetometer is described within [87]. A single beam, resonant on the D1 line of ^{87}Rb is employed to optically pump the vapour. The beam is circularly polarised and passed through a $3 \times 3 \times 3\,\text{mm}$ buffer gas cell. To achieve the densities required for the SERF regime, the cell is heated to 150°C and the optical absorption of the beam monitored using a photo-diode. At zero magnetic field a maximal intensity is observed as it corresponds to the maximal transparency of the

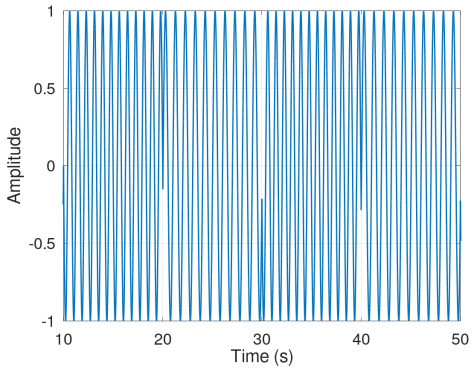

(a) Waveform $R_{\mathfrak{AB}} = 0.1$

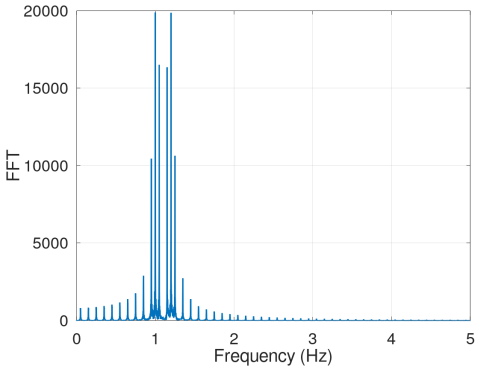

(b) Fourier Transform $R_{\mathfrak{AB}} = 0.1$

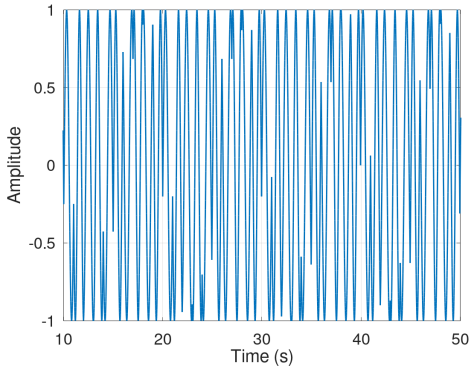

(c) Waveform $R_{\mathfrak{AB}} = 1$

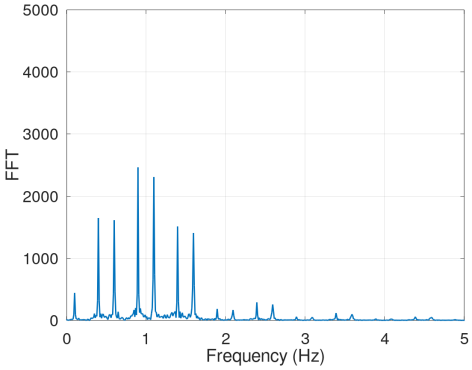

(d) Fourier Transform $R_{\mathfrak{AB}} = 1$

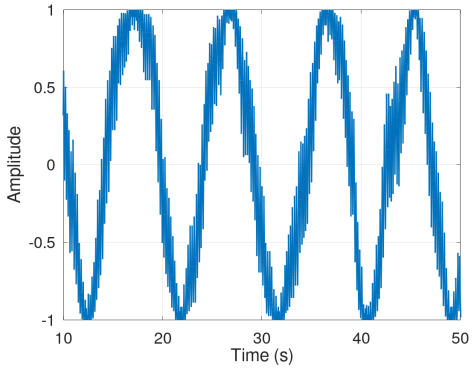

(e) Waveform $R_{\mathfrak{AB}} = 10$

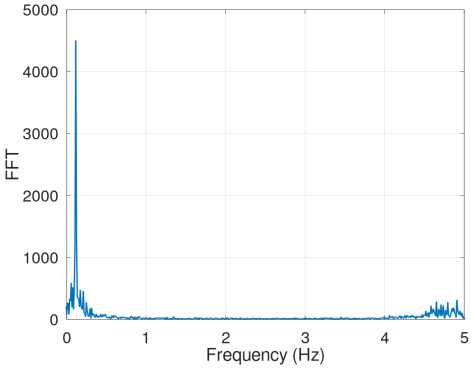

(f) Fourier Transform $R_{\mathfrak{AB}} = 10$

Figure 3.19: Waveform and Fourier spectra for a simulated two state system of frequency $\omega_{\mathfrak{A}} = 1\,\text{Hz}$ and $\omega_{\mathfrak{B}} = -1.2\,\text{Hz}$. At $R_{\mathfrak{AB}} = 0.1$ two frequencies are defined, these are less defined at $R_{\mathfrak{AB}} = 1$ and reduce down to a single frequency of $0.08\,\text{Hz}$ at $R_{\mathfrak{AB}} = 0.1$.

vapour to the pump beam as discussed within [88]; this produces a Lorentzian line shape when a magnetic field perpendicular to the pump beam is swept through zero, defining a linewidth of 30 nT.

As described in [88], the QuSpin utilises a lock-in detection method to improve the signal to noise ratio and decrease the effect of $1/f$ noise. An oscillating magnetic field is applied along a direction orthogonal to the pump resulting in modulations appearing on the pumping light at frequencies harmonic to the applied oscillating field (923 Hz). The output is demodulated using a lock-in amplifier to produce a dispersive line shape such as those illustrated in Figure 3.15. The sensitive axis of the sensor is defined by the direction of the oscillating field and can be defined along either axis perpendicular to the pump. Within these experiments the z-axis was utilised. A dual axis mode is possible through the application of two oscillating fields, however is reported to reduce the sensitivity by 30%.

3.6 Sensitivity Limits

The fundamental limitation of sensitivity for AMs is dependent upon a number of the experimental parameters, including the alkali-metal species and properties of the vapour and probe/pump light. The total noise in a measurement of the magnetic field, B, is given as

$$\delta B = \sqrt{\delta B_{SPN}^2 + \delta B_{PSN}^2 + \delta B_{LSN}^2} \tag{3.53}$$

which consists of contributions from the spin-projection noise (SPN), photon-shot noise (PSN) and light-shift noise (LSN) [70]. Where these noise sources derive from the finite number of alkali-atoms (SPN), the finite number of photons in the probe (PSN) and AC stark shifts from the pump and probe beams (LSN). Each of these noise sources are discussed in more detail in the following Sections.

3.6.1 Spin-Projection Noise

The spin-projection noise originates in the quantum mechanical uncertainty in measuring the projection of the spin. A discussion of the treatment of this is given in [70], in which the uncertainty in the measurement of the transverse spin component (F_x) is given as

$$\delta F_x = \sqrt{\frac{2F_z\tau_2}{N}} \tag{3.54}$$

for N independent measurements. This can be converted to an uncertainty in magnetic field to produce [38]

$$\delta B_{SPN} = \frac{1}{\gamma}\sqrt{\frac{8}{F_z n V \tau_2}} \tag{3.55}$$

which gives the variation in the magnetic field as a function of the alkali vapour density (n) and the sensor's active volume (V). The active volume for a buffer gas cell is the overlap between the pump and probe beams.

3.6.2 Photon-Shot Noise

Photon-shot noise in a polarimetry configuration arises from variation in the number of photons within each beam. The uncertainty in the angle of rotation (θ) is given as

$$\delta\theta = \sqrt{\frac{1}{2\Phi}} \tag{3.56}$$

as a function of the photon flux (Φ), assuming the angle of rotation is small and so the flux in each arm is comparable. From this equation the uncertainty in the spin-polarisation can be determined and through that, the uncertainty in the measured magnetic field to produce [38]

$$\delta B_{PSN} = \frac{2\sqrt{2}}{\pi l r_e n u c \gamma \tau_2 \sqrt{\Phi\zeta}\, Im[\mathcal{V}(\upsilon - \upsilon_0)]} \tag{3.57}$$

where ζ is the quantum efficiency of the photo-diodes and, as previously, l is the length of the cell, r_e is the classical electron radius, n is the alkali vapour density, u is the transition oscillator strength and c is the speed of light.

3.6.3 Light-Shift Noise

The origin of light-shift noise is shifts in the Zeeman energy levels through interaction with the oscillating electric field within the pump and probe beams, know as AC stark shift. Assuming the magnetic field is orientated perpendicular to the polarisation of the light, AC stark shifts are eliminated for linearly polarised light, which can be considered as two balanced circularly polarised components. Fluctuations in either of these components create ellipticity in the probe beam and therefore small shifts in the energy of the Zeeman levels.

When treated in the same fashion as the two beams within a polarimeter arrangement, the variation in the flux in one particular component produces an error in the polarisation (P) [70],

$$\delta P = \sqrt{\frac{2}{\Phi}}. \tag{3.58}$$

This is expressed as an uncertainty in the magnetic field as given by [38]

$$\delta B_{LSN} = \frac{\pi r_e c u \mathcal{V}(\upsilon - \upsilon_0)\sqrt{2\Phi}}{\gamma_e \mathfrak{a}} \tag{3.59}$$

in which γ_e is the gyromagnetic ratio of an electron, $\mathfrak{a}$ is the area of the beam and $\mathcal{V}$ is the Voigt profile.

3.7 DC Sensitivity

The DC sensitivity of an AM is the smallest detectable shift in the bias field δB_0. This value can be extracted from the resonance features described by equations 3.41 and 3.42 in Section 3.3.2, specifically the quadrature component where the gradient about the resonant frequency dictates the signal change for small shifts in B_{DC}.

To quantify this gradient and combine with fluctuations originating from all noise sources the ratio

$$\delta B_{DC} = \frac{\hbar}{g\mu_B}\frac{\Gamma}{\mathrm{SNR}} \tag{3.60}$$

can be used [89], where Γ is the FWHM of the in-phase component (equation 3.41) and SNR is the signal to noise ratio at the resonance frequency. The SNR can be obtained from the power spectral density (PSD) function of the photo-diode output of the magnetometer. This takes the ratio of the PSD at the resonance feature and the PSD baseline to produce a sensitivity with units of $\mathrm{T}/\sqrt{\mathrm{Hz}}$.

Chapter 4

COMSOL Simulations

The description of eddy current induction (ECI) provided in Chapter 2 makes various assumptions about the infinite nature of the objects or the uniformity of the primary/excitation field. In order to explore ECI closer to an experimental implementation, a numerical approach is considered. This Chapter discusses the use of COMSOL MultiPhysics [90] to examine changes in field magnitude and phase across a range of experimental parameters. COMSOL Multi-physics is a finite element analysis solver packaged within a Graphical User Interface (GUI). The physics module utilised within this work is the magnetic field package, allowing the simulation of magnetic fields in a stationary or frequency domain.

Each COMSOL simulation considered in this Chapter is constructed in 2D to be axially symmetric around the z-axis. The base configuration of each simulation was a single coil aligned along the z-axis with a target and an inspection point, z_p. The properties of the coil were specified to approximate the geometry of the solenoid used within the experimental work. As illustrated in Figure 4.1, the mid-point of the coil was at $z = 0$ and the target is specified with a radius $\mathbb{R}$ and thickness $\mathbb{T}$.

This Chapter focuses on the phase and magnitude response of the resultant field. This response is briefly examined in the context of different primary field distributions

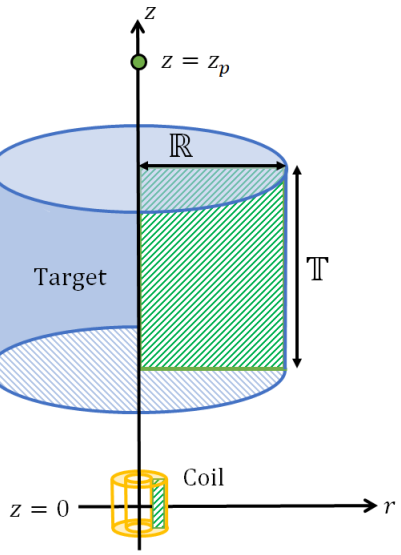

Figure 4.1: Illustration of the basic configuration simulated within COMSOL. Simulations were constructed in 2D to be axially symmetric around the z-axis. A coil (yellow) is aligned with a target (blue) and an inspection point at $z = z_P$. The mid-point of the coil was specified at $z = 0$. The target has a thickness $\mathbb{T}$ and a radius $\mathbb{R}$. The green rectangles represent the surfaces as specified within COMSOL.

along with a discussion on the bounds that approximate an infinite object. Subsequent discussions then focus on changes in the response with a target's geometric and electrical properties. This is extended to experimentally representative scenarios including shielded targets. The motivation of this Chapter is to provide a basis from which the experimental results given in Chapters 6 and 7 can be further discussed. Including the deviation from the infinite description of phase change through a target as a function of thickness or frequency.

4.1 Primary Field Distributions

The magnitude and phase response from a target in an excitation field depends on a range of its geometric and electrical properties, but is also influenced by the shape of the primary field. The primary field distribution is a function of the excitation coil

geometry and the relative location of the target. This is briefly explored by defining two generic primary field distributions: uniform and point. A uniform field is homogeneous across an object and can be generated using a Helmholtz pair. Conversely, a point-distribution diverges from a point such as generated using a solenoid. These distributions are illustrated in 2D-axis symmetric space in Figures 4.2 along with the induced current density within a copper target. The solenoid simulated in these data approximates the coil used within experimental work (coil radius, $r_c = 3\,\text{mm}$, 100 turns, length = 7.5 mm). Unless otherwise specified, this same solenoid configuration is consistent between the COMSOL models.

Inspection of these images highlight that the induced eddy current distribution is altered with the differing applied primary fields. Here, a uniform field creates a peak eddy current flow around the outside edge of the object, whilst for the point field this is shifted towards the centre. The implication of this is a modification of the induced field magnitude and phase response. Figure 4.3 displays the magnitude of the z-projection of the magnetic field (B_z) across the radius of the target for the uniform (a) and point (b) distributions. Whilst both results display a reduction from the measured background field, the Helmholtz scenario benefits from a flat distribution and a high contrast in the presence of the object. Conversely, the point-like distribution requires prior knowledge about the background field value to determine the presence of the object. The advantage of the point distribution is operational as it is smaller and generates a larger induced field for the same input current.

Similar observations can be made in the inspection of the phase of B_z. Here, the phase from the Helmholtz configuration is flat as shown in Figure 4.4a whilst in the solenoid configuration phase undergoes a 180° change. This phase change is due to the direction of the field changing as the flux curves back towards the solenoid. In this instance the turning point is coincidentally at approximately the width of the object, however, this can be altered by changing the radius of the coil or the separation between

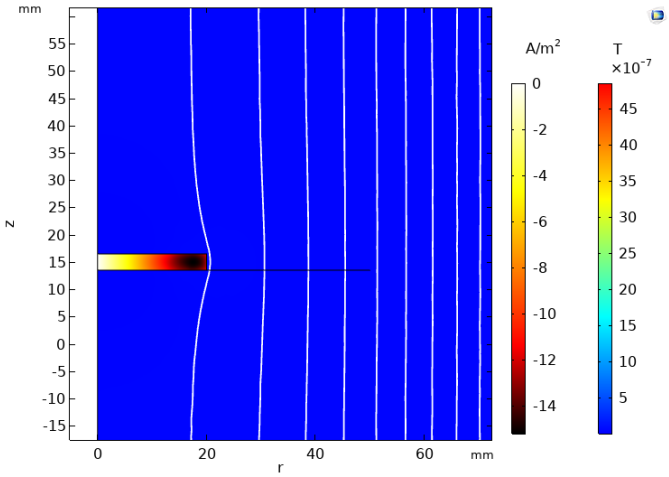

(a) Uniform

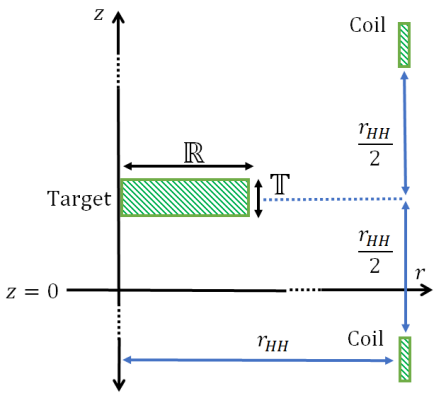

(b) Uniform Illustration

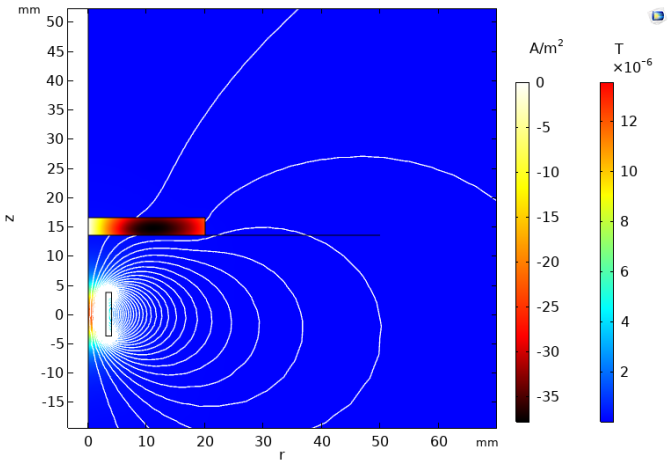

(c) Point

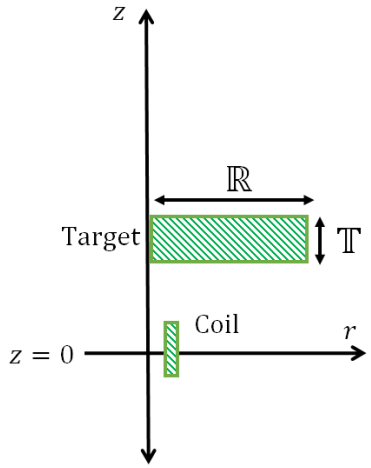

(d) Point Illustration

Figure 4.2: COMSOL 2D axially symmetric simulations of (top) uniform and (bottom) point primary field distributions in the z-r plane, symmetric about the z-axis. COMSOL simulations are displayed on the left, with the corresponding configuration illustrated on the right. The uniform distribution is generated using a Helmholtz pair of radius r_{HH}= 1000 mm, 100 turns, length = 7.5 mm with the target equidistant between coils. The point distribution is generated using a solenoid with radius $r_c = 3$ mm , 100 turns, length = 7.5 mm. In each instance a coil current of 1 mA is defined. The magnetic flux lines are displayed in each image, along with the magnitude of the z-projection of the magnetic field (outer colour bar) and the induced current density (A/m^2) within an $\mathbb{R} = 20$ mm, $\mathbb{T} = 3$ mm copper target (inner colour bar).

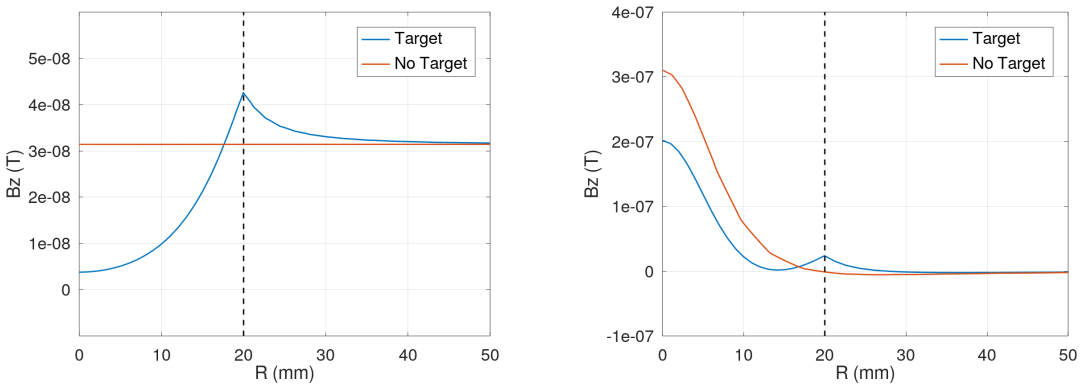

(a) Uniform (b) Point

Figure 4.3: COMSOL 2D axially symmetric simulations of (left) uniform and (right) point field distributions in the z-r space, symmetric about the z-axis. The magnitude of B_z is calculated as a function of radial position (r) across a $\mathbb{R} = 20\,\text{mm}$ copper target with a thickness $\mathbb{T} = 3\,\text{mm}$. Data is calculated for the primary (red) and total field (blue) and evaluated on the lower edge of the target at $z = 13.5\,\text{mm}$. The dashed line represents the edge of the target.

the coil and the target. It should be noted that as this latter distance is increased, the solenoid will generate a more uniform distribution at the target.

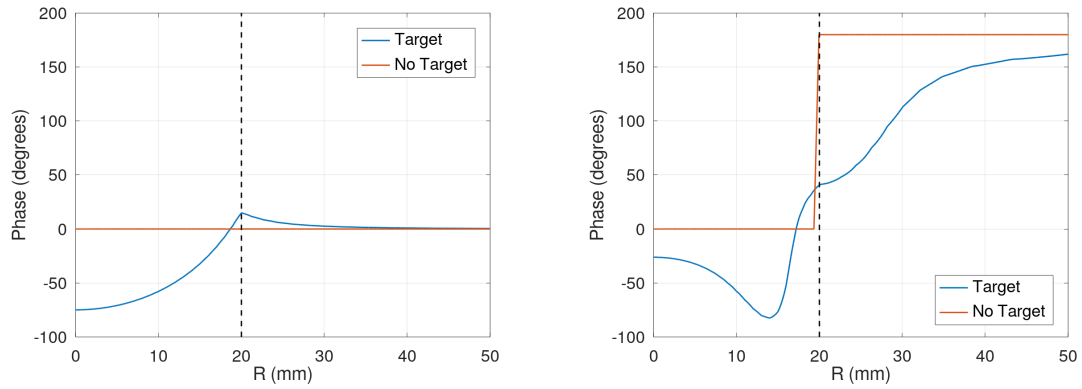

(a) Uniform (b) Point

Figure 4.4: COMSOL 2D axially symmetric simulations of (left) uniform and (right) point field distributions in the z-r space symmetric about the z-axis. The phase of the B_z component of the field is calculated as a function of radial distance (r) across a $\mathbb{R} = 20\,\text{mm}$ copper target with a thickness $\mathbb{T} = 3\,\text{mm}$. Data is calculated with (blue) and without (red) the target present. The dashed line represents the edge of the target.

In the experimental work, a solenoid coil is used to allow larger field strengths to be generated. To mitigate the effect of the more complex magnitude and phase distributions along the r direction, the solenoid coil and sensor are static and the target is moved. This produces a flat background, generating images with no background subtraction required.

4.2 Finite Targets

As previously discussed, some descriptions of eddy current behaviour described in Chapter 2 assumes an infinite target, however, the boundary between finite and infinite is not well quantified. The motivation of this Section is to explore, for a specific set-up, the dimensions of an finite target that approximate an infinite one. The description for the eddy current behaviour within an infinite object predicts an exponential decrease in the magnitude of the excitation field through the thickness of a target and a linear change in the phase as referenced to the field at the surface. The phase, ϕ, of the magnetic field changes linearly with depth through the material and can be expressed as

$$\phi = \frac{z}{\delta} \text{ rad.} \tag{4.1}$$

Equation 4.1 assumes an infinite object in half space (field external to object). This can be approximated in COMSOL with an object significantly larger, in both thickness and radius, than the radius of the coil as displayed in Figure 4.5. As predicted, the magnitude of the field decreases exponentially along the z-axis as it is attenuated. The phase maintains a linear increase with the depth through the object, rolling over at $\pm$ 180°. The gradient of the phase is well described by equation 4.1 with a value of 12100 degrees/m calculated in COMSOL compared with 12367 degrees/m from the analytical equation (copper target at 300 Hz).

Differences in the behaviour of the phase are particularly distinct between finite

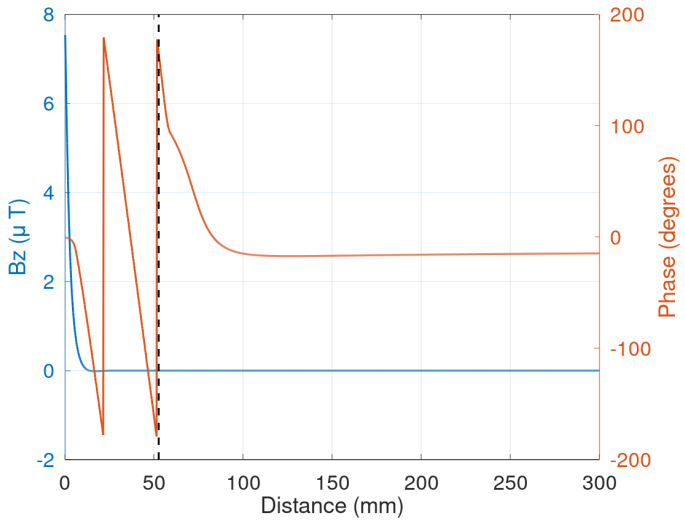

Figure 4.5: The z-projection of the magnetic field (blue) and the phase (red) along the z-axis. The object selected was a disc with a diameter of 125 mm and a thickness of 52 mm (15× larger than the solenoid radius of 3.5 mm). The back edge of the object is indicated by the dashed black line. The object material was defined as copper (conductivity, $\sigma = 59\,\mathrm{MS/m}$ with an excitation frequency of 300 Hz.

and infinite objects. The limit of these behaviours can be explored in COMSOL by specifying a large value (150 mm) of object thickness, $\mathbb{T}$, or radius, $\mathbb{R}$, and varying the other parameter between values less than the eddy current wavelength parameter, $L = 2\pi\delta$, and several times larger. To quantify the difference between finite and an approximation of infinite, the phase along z was fit with a straight line between the start of the object and extending up to a maxima of the first phase roll-over. The gradient of these fits are plotted as a function of the ratio between the target radius/thickness and the $L = 2\pi\delta$ value of the object; these data are displayed in Figure 4.6.

These results highlight that in the instance of thickness, the ratio is required to be comparable to L before the phase begins to approximate that of an infinite object. A similar relationship is demonstrated with the radius. Below these values the phase is not typically linear in z producing a fluctuating value of the gradient due to the less than optimal fit.

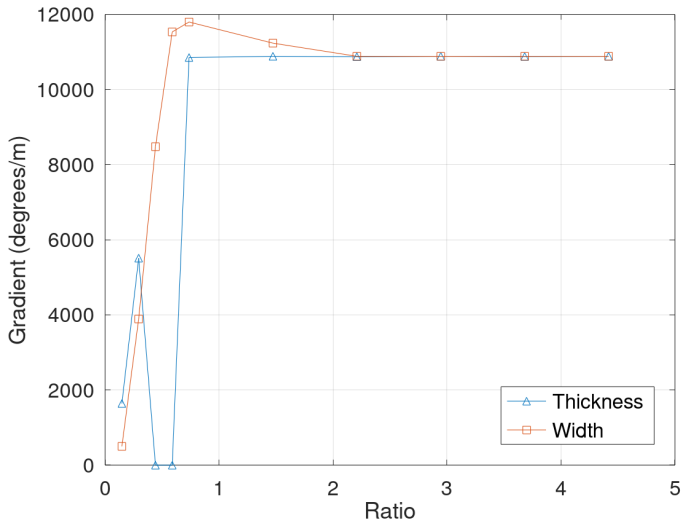

Figure 4.6: Gradient of initial phase change as a function of the thickness (blue) and radius (red) of a copper target expressed as a ratio of the eddy current wavelength parameter L for the excitation frequency of 300 Hz and conductivity of the target, $\sigma = 59\,\mathrm{MS/m}$ ($L = \sim 24\,\mathrm{mm}$). As the thickness or radius is varied the other (radius/thickness) parameter is fixed at 150 mm.

In all experimental configurations within this work, the dimensions of targets vary; these are summarised in Table 4.1. Whilst the larger two target radii are sufficient to be approximated as infinite using this definition, the data in Figure 4.6 demonstrate that both the thickness and radius need to be large. This is not the case for the materials tested which all have thickness ratios less than 0.2. The consequence of this is that, in the analysis of the experimental data, the analytical relationship in equation 4.1 is not valid, requiring the use of numerical methods.

4.2.1 Magnitude and Phase Response of Finite Targets

With the conclusion that the analytical solution is not valid for thin objects, the magnetic field from an example finite object is examined as a function of axial distance, z. It should be noted that the value of both B_z magnitude and phase depend on a wide variety of experimental parameters, these include: excitation voltage, frequency,

Target Materials	Radius (mm)	Ratio$_R$	Thickness (mm)	Ratio$_T$
Variety, max σ Copper	25	1.04	1	0.04
Variety, max σ Copper	12.5	0.52	1	0.04
Copper	20	0.83	3	0.13

Table 4.1: Dimension of the targets used within the experimental work. Also shown are the corresponding ratio of size with respect to the eddy current wavelength parameter $L = 2\pi\delta = 24\,\text{mm}$ calculated at a frequency of 300 Hz and with the conductivity of copper as 59 MS/m.

target conductivity, width, height, thickness and position relative to the coil. Due to the large parameter space, the subsequent Sections do not make an effort to define generalised relationships, instead examples are examined which relate to specific geometries to highlight relevant phenomena.

The example chosen is a copper sample with a radius of 20 mm and thickness of 3 mm. Copper is specified as the target material due to its high conductivity and therefore significant interaction with the excitation field at the specified frequencies, this allows the relevant phenomena to be better highlighted. Simulations can be extended to lower conductivities such as those for uranium or plutonium. The target is located 12 mm from the front edge of the coil. The current applied to the coil is 0.77 mA. This value is chosen to produce a primary field of 0.136μT at the target for a frequency of 300 Hz, as consistent with experimentally measured values.

The magnitude and phase response are displayed in Figure 4.12 along with the data obtained without the copper. In the presence of the target, the magnitude of B_z is reduced as expected from Faraday's law, with the effect greatest in the vicinity of the target and decaying away with increasing z. It can be noted that the field modification is also present on the coil side of the target, indicating that a single sided measurement could be obtained, however it is more localised to the target than the transmission orientation.

The phase data as a function of z demonstrates a greater change in the presence of the

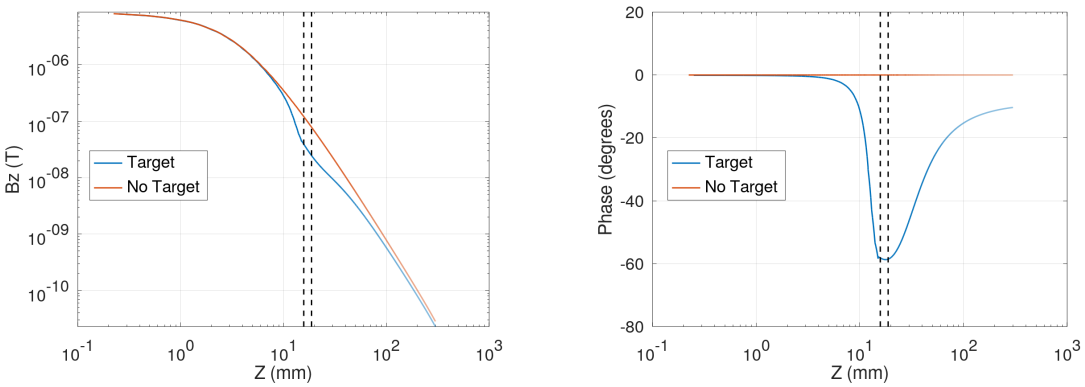

(a) Magnitude (b) Phase

Figure 4.7: Magnitude (left) and phase (right) of the z-projection of the magnetic field as a function of z simulated within COMSOL. Data is displayed with (blue) and without (red) a copper object with a radius of 20 mm and thickness of 3 mm. The target is located 15 mm from the front of a solenoid coil with $r_c = 3$ mm, length = 7.5 mm, 147 turns with 0.77 mA at 300 Hz to produce a field at the target of 0.136μT. A small artefact from a mesh discontinuity can be seen in the phase data (right) on the coil side of the target.

target than the magnitude, with a maxima in the phase change experienced around the target before decaying across this range to 10°. In the example of a single sided system measuring phase, as the phase changes from a zero baseline value, the change in signal appears greater in comparison to a magnitude measurement. In actuality the no-target phase value is unlikely to be zero and will be impacted by other objects illuminated by the coil.

4.3 Magnitude and Phase Response at Detection Point

As previously mentioned, the precise magnitude and phase response depends on a host of variables making it difficult to provide generalised solutions. To bound the problem space, the phase and magnitude are considered in a set of specific geometries, replicating the spacing of the sensor, target and excitation coil used within experiments. The coil to target spacing (15 mm) and current values are maintained from the previous study,

however, the phase and magnitude data are examined at a sensor point, z_P, along the z-axis. The distance to the sensor point z_P is measured from the centre of the coil at $z = 0$. The coil current values were chosen to replicate the values experimentally measured at the target.

4.3.1 Excitation Voltage and Frequency

In order to explore the response of the system with a changing excitation field strength, the current through the coil was modified and the magnitude and phase monitored at $z_P = 235\,\text{mm}$. A copper target with a radius of 20 mm and thickness of 3 mm was specified 15 mm from the previously described solenoid with an excitation frequency of 300 Hz; these results are displayed in Figure 4.8. The magnitude of the field measured at z_P increases linearly as a function of the current/excitation field strength as expected. Also as expected, the phase of the field is invariant of the excitation strength as described by equation 4.1.

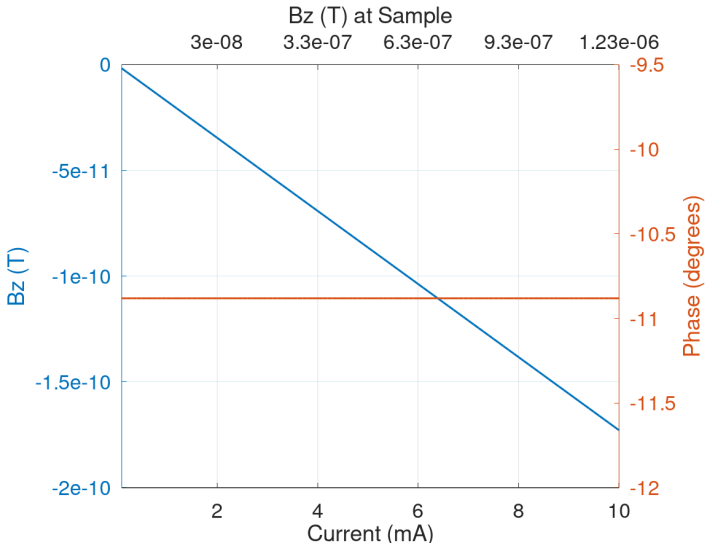

Figure 4.8: Magnitude (blue) and phase (red) of B_z as a function of current applied to a solenoid with $r_c = 3\,\text{mm}$, length= 7.5 mm and 147 turns. Measurements are obtained from a copper target of radius 20 mm and thickness 3 mm at 300 Hz. The corresponding magnetic field strength at the target is displayed along the top x-axis.

The system response is also expected to vary with the excitation frequency. Figure 4.9 displays the magnitude and phase as a function of frequency at a current of 0.77 mA in response to the copper target (radius = 20 mm, thickness=3 mm). Within these data the magnitude increases with frequency, expected as the strength of the circulating electric field is proportional to the rate of change of the primary field. The phase is also seen to change as a function of frequency but not with the $\sqrt{\omega}$ relationship dictated in the infinite case. Instead, the data is better fit with a second order polynomial; however, this is not representative of a physical phenomenon and should only be used to guide the eye. It should be noted that the simulation assumes a constant current at each frequency which is not achieved experimentally. In many instances the power applied to the excitation coil would be a constant voltage source. This is not an issue for the phase measurement which is independent of field strength as shown in Figure 4.8.

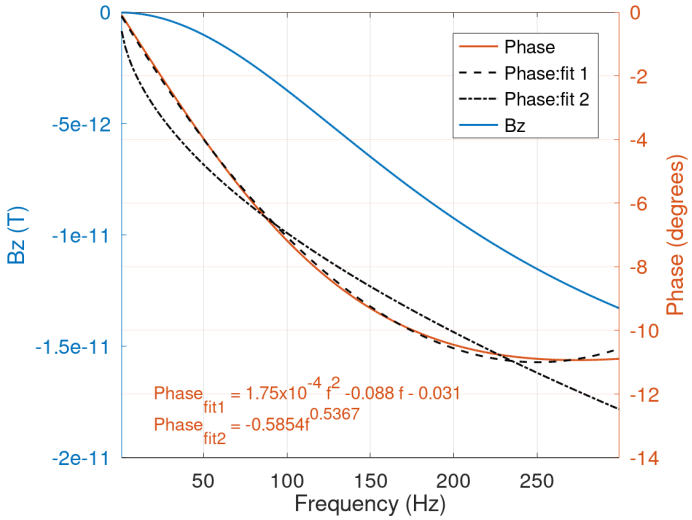

Figure 4.9: Change in magnitude (blue) and phase (red) as a function of frequency applied to a solenoid with $r_c = 3$ mm, length = 7.5 mm and 147 turns. Data obtained with a coil current of 0.77 mA. The phase data is fit with both a second order polynomial (dashed line) and a power curve (dotted line).

4.3.2 Target Conductivity

In addition to the frequency and strength of the excitation field, another key parameter in the eddy current response is the conductivity of the target. As consistent with the previous results, rather than selecting an arbitrary object, the simulation is constructed to mimic specific samples. In this instance a target with radius 25 mm is selected and the conductivity varied between 0.1 to 60 MS/m. The data in Figure 4.10 displays the change in magnitude and phase at a sensor point $z_P = 212$ mm as a function of the sample conductivity at 300 Hz. These data highlight the changes in field magnitude up to 14 pT and in phase up to 11 degrees for the highest conductivity sample (copper, 60 MS/m). As previously with frequency, the phase relationship is similar to, but cannot be precisely fit with a power curve.

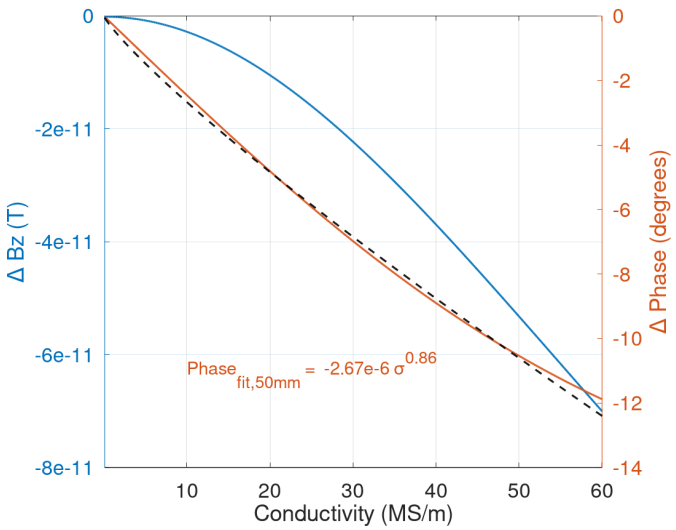

Figure 4.10: Change in B_z magnitude (blue) and phase (red) as a function of target conductivity. The target simulated had a radius $\mathbb{R} = 25$ mm and thickness of $\mathbb{T} = 1$ mm. Data is calculated at a coil to sensor distance of 212 mm. A power curve fit is displayed with a dashed black line.

These data are only valid for these particular target dimensions. Comparing these results with the 12.5 mm object specified in Table 4.1 highlights that the degree of

linearity depends upon the radius, with maximal differences ($\times 7$) in the phase change. These are greater than both the change in radius ($\times 2$) and volume ($\times 4$). This comparison is provided in Figure 4.11.

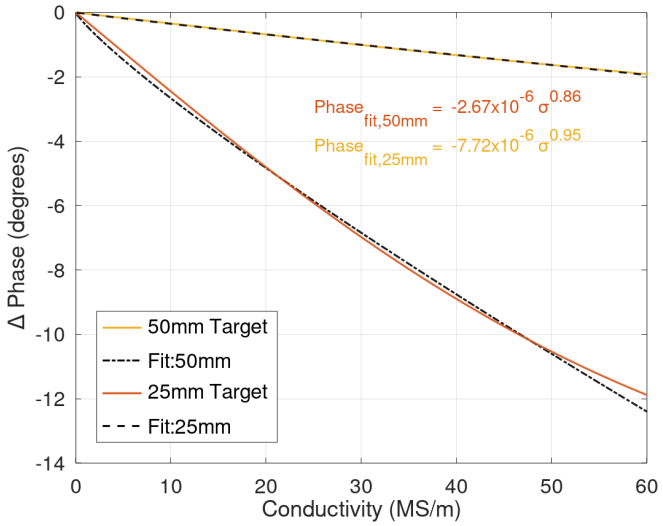

Figure 4.11: Change in B_z phase as a function of target conductivity. The target simulated had a radii $\mathbb{R} = 25\,\text{mm}$ (red) and $\mathbb{R} = 12.5\,\text{mm}$ (yellow). Both have a thickness of $\mathbb{T} = 1\,\text{mm}$. Data is calculated at a coil to sensor distance of of 212 mm. The lines of best fit are displayed as the dotted black lines.

The linear nature of the phase response for smaller targets shares similarities with the response predicted for the low conductivity samples discussed in Chapter 2. In these examples the conductivity of the samples are such that the primary field is minimally attenuated by the target. This is increasingly approximated for higher conductivities as the size of the samples is reduced. The results summarised here emphasise the importance of utilising COMSOL simulations to describe the magnitude and phase response from targets and the requirement to consider geometries specific to the experimental configurations.

4.4 Shielded Targets

A requirement of an imaging system used in security screening is the detection of targets behind shielding. Of specific interest within ECI are high conductivity and ferrous shielding, along with high density materials which can be used to screen radiological signatures. In keeping with the effort to tie these simulations directly to specific experimental conditions, shielding materials are considered across experimentally achievable thickness values from 1-70 mm. The phase and magnitude response to a copper target ($\mathbb{R} = 20\,\text{mm}$, $\mathbb{T} = 3\,\text{mm}$) is considered through these shielding materials as a function of thickness across different frequencies.

4.4.1 Shielding Materials

To better understand the impact of shielding on the induction signal of a target, the shielding material is first considered in isolation. The change in phase and magnitude as a function of aluminium shielding thickness without a target present is displayed in Figures 4.12a and 4.12b. These data are obtained for shield radius $\mathbb{R} = 150\,\text{mm}$ and at a sensing point $z_P = 247\,\text{mm}$ with frequencies of 40 Hz and 300 Hz corresponding to standard depth values of δ =13 mm and δ =4.7 mm respectively. The previously detailed COMSOL simulation was used including the same coil dimensions and a current of 0.77 mA. The shield thickness ($\mathbb{T}$) was increased along the negative z direction, reducing the distance between the coil and the shield rather than z_P and the shield.

The consideration of ECI discussed in Chapter 2 corroborates the magnitude and phase turning points within Figure 4.12. As previously discussed, these are a result of the exponential decay of the magnitude of the secondary field modified by a linear change in the phase. This was illustrated in Figure 2.2 and calculated in Figure 2.4. The calculation treated a finite object as a collection of individual current loops and integrated the Biot-Savart law across the object thickness and radius to determine the

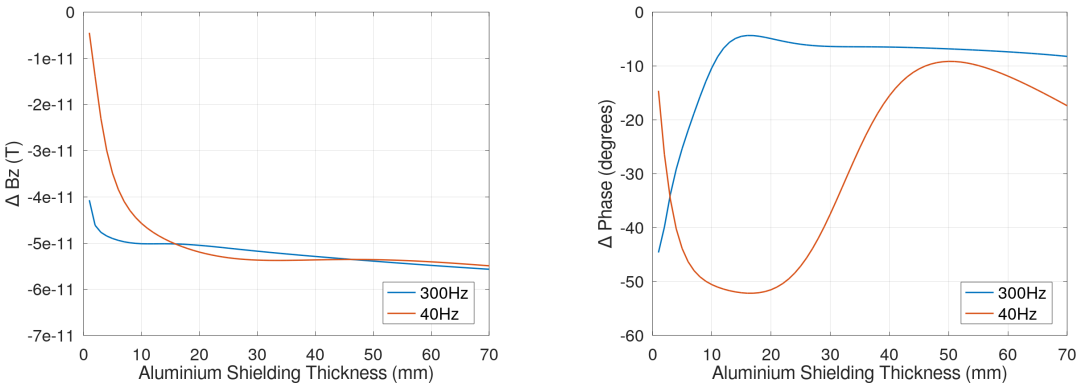

(a) Magnitude (b) Phase

Figure 4.12: Magnitude (left) and phase (right) as a function of aluminium shielding thickness simulated within COMSOL. The shield has a radius of $\mathbb{R} = 150\,\text{mm}$ and is located 100 mm from the edge of the excitation coil. Data are obtained at an inspection point $z_P = 247\,\text{mm}$.

secondary field at a sensing point.

The location of the turning points in both magnitude and phase as a function of object thickness were found to be linearly dependent on the wavelength quantity $L = 2\pi\delta$ which describes the length scale over which the phase of the eddy currents/secondary fields changes. These were calculated as

$$T_m = 0.37L - 0.0001(\text{m}), \tag{4.2}$$

$$T_p = 0.65L - 0.0005(\text{m}). \tag{4.3}$$

The turning point in magnitude, T_m, precedes that in phase, T_p, as is also seen in Figure 4.12. In aluminium with $\sigma = 37\,\text{MS/m}$ at 300 Hz and 40 Hz the value of L is calculated to be $L = 0.030\,\text{mm}$ and $L = 0.082\,\text{mm}$ respectively. These values corresponds to turning points summarised in Table 4.2 which can be compared with features observed at similar values in the COMSOL simulations.

	T_m	T_p
BS: 300 Hz	11 mm	19 mm
BS: 40 Hz	30 mm	53 mm
COMSOL: 300 Hz	12 mm	16 mm
COMSOL: 40 Hz	34 mm	50 mm

Table 4.2: Value of the magnitude (T_m) and phase (T_p) turning points at frequencies of 300 Hz and 40 Hz within aluminium ($\sigma = 37$ MS/m, relative permeability $\mu_r = 1$). Values calculated based on a Biot-Savart (BS) solution and with COMSOL.

The maximum magnitude changes within the COMSOL simulations occur at approximately the values calculated within the Biot-Savart solution. However, the calculated phase maximum appear to coincide with minimum in the COMSOL simulations. This discrepancy originates in the assumption of a uniform primary field within the formulation of equations 4.2 and 4.3 which are compounded with phase roll-overs. These factors make a direct comparison between Figures 2.4 and 4.12 difficult. Whilst the object radius is different between the two data sets (100 mm/150 mm), the distribution will be primarily impacted by the greater number of geometric considerations included in COMSOL, such as the radial eddy current distributions. These will influence the absolute values of phase and can therefore introduce phase roll-overs which substantially alter the distribution including the increasing/decreasing trend in phase values.

Another shielding material of interest from an ECI perspective is steel. Steel typically has a smaller conductivity (1.3 MS/m) than aluminium (37 MS/m), however has a relative permeability $> 100\times$ larger. The previous COMSOL simulation was modified to include steel material properties in place of the aluminium whilst retaining the same configuration. These simulations produce the magnitude and phase distributions at z_P with shield thickness displayed in Figure 4.13. As previously, turning points are observed with their position modified from the aluminium as would be expected from changing the value of L through an increase in μ.

Another comparison between the COMSOL simulations and the Biot-Savart solutions demonstrates that both share a similar distribution when using the values for steel. In

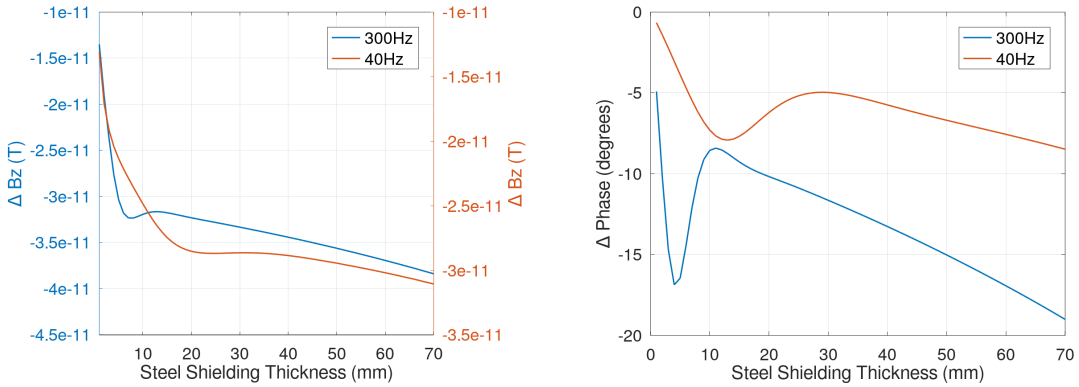

(a) Magnitude (b) Phase

Figure 4.13: Magnitude (left) and phase (right) as a function of steel shielding thickness simulated within COMSOL. The shield has a radius of $\mathbb{R} = 150\,\text{mm}$ and is located 100 mm from the edge of the excitation coil. Data are obtained at an inspection point $z_P = 247\,\text{mm}$. The shield conductivity is specified as $1.3\,\text{MS/m}$ with a $\mu_r = 100$.

	T_m	T_p
BS: 300 Hz	6 mm	10 mm
BS: 40 Hz	16 mm	28 mm
COMSOL: 300 Hz	8 mm	11 mm
COMSOL: 40 Hz	25 mm	29 mm

Table 4.3: Value of the magnitude (T_m) and phase (T_p) turning points at frequencies of 300 Hz and 40 Hz within steel ($\sigma = 1.3\,\text{MS/m}$, $\mu_r = 100$). Values calculated based on a Biot-Savart (BS) solution and with COMSOL.

this instance the values of L were calculated as $L = 0.016\,\text{mm}$ and $L = 0.043\,\text{mm}$ for frequencies of 300 Hz and 40 Hz respectively. This produced calculated turning points in magnitude and phase which can be compared with the COMSOL equivalents in Table 4.3. As previously, these values are similar with some variation expected from the non-uniformity of the primary field.

The other shielding material that could be considered is lead which presents a challenge from the perspective of conventional radiological signatures. However, as this has a lower conductivity than aluminium and a unity permeability, lead would not add more constraints than the case of aluminium.

4.4.2 Shielded Targets

Within the previous Section the magnitude and phase response at z_P is considered for the shield material only which simplifies the scenario to the interaction between the primary field and a single object. The addition of the target introduces a more complex scenario in which there is likely also an interaction between the target and the shield.

In the example of the aluminium shielding, the phase and magnitude response with the inclusion of a copper target ($\mathbb{R} = 20\,\text{mm}$, $\mathbb{T} = 3\,\text{mm}$) is displayed in Figure 4.14. This plot shows the data obtained at 300 Hz and includes the shield only data for comparison. The copper target has a value of $L = 0.024\,\text{mm}$ at 300 Hz. As previously noted with just the shield, the data displays turning points which in this instance are not substantially modified in location for either magnitude or phase.

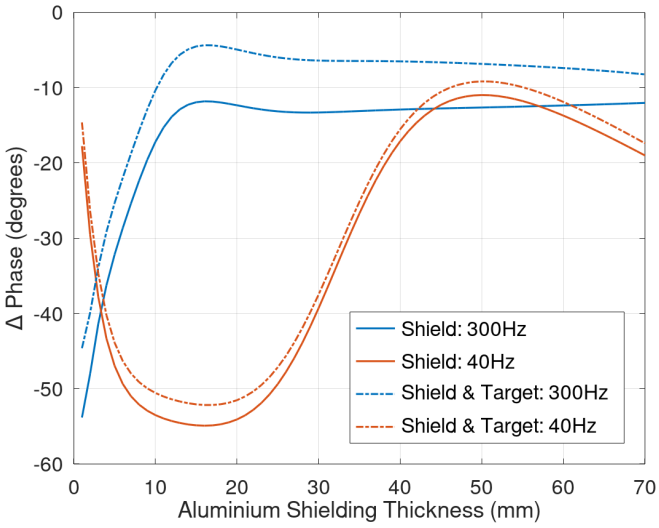

Figure 4.14: Change in magnitude (blue) and phase (red) as a function of aluminium shielding thickness obtained from COMSOL simulations. Data is shown for simulations including just the shield (solid line) and with both a shield and a copper ($\mathbb{R} = 20\,\text{mm}$ $\mathbb{T} = 3\,\text{mm}$) target (dashed).

In an operational context it is advantageous not to need prior information on the shielding material. Any background subtraction in this case will represent the difference

between the shield only and combined shield and target data shown in Figure 4.14. These data are displayed in Figure 4.15 for both the magnitude and phase of B_z at frequencies of 40 Hz and 300 Hz. In these data, the interaction between the shield and the target can be observed, producing an apparent shift in the phase turning point to 7 mm for 300 Hz and 37 mm for 40 Hz. The implication of these results is that a background subtraction ([shield + target] - shield) will not produce a shield-free result, and therefore it may be difficult to characterise a material based on an expected target magnitude or phase change alone.

A shield free measurement may be extracted by collecting information on the shield such as conductivity and thickness. In the scenario where the shield is much larger than the object, the thickness may be extracted through the frequency value of the turning point, which as seen in Figure 4.14 is minimally effected by the target. This would require the conductivity of the shield to be known and could be obtained using a high frequency measurement that interacts with the surface of the shield.

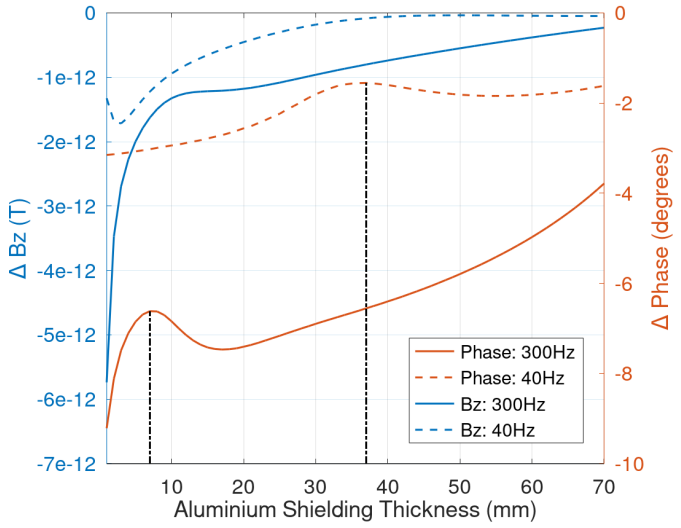

Figure 4.15: Magnitude (blue) and phase (red) change between data calculated with only an aluminium shield and with a combined shield and copper target ([Shield + target] - Shield). These are plotted as a function of shielding thickness. Data obtained at 300 Hz (solid) and 40 Hz (dashed).

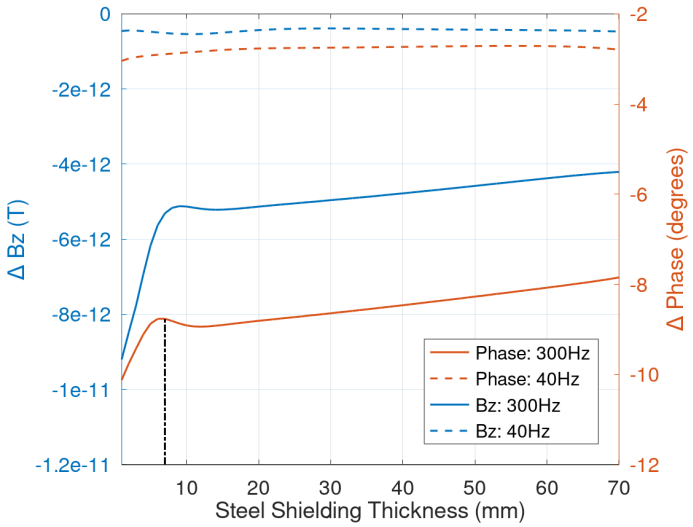

Figure 4.16: Magnitude (blue) and phase (red) change between data calculated with only an steel shield and with a combined shield and copper target ([Shield + target] - Shield). These are plotted as a function of shielding thickness. Data obtained at 300 Hz (solid) and 40 Hz (dashed).

A similar set of results are observed across the different shielding materials, with both steel and lead also resulting in non-uniform values of phase and magnitude as a function of shielding thickness. These results can also be extended to the measurement of uranium/plutonium targets behind the various shielding materials. In these examples, similar distributions were replicated with smaller absolute changes in magnitude and phase.

4.5 Magnetic Shielding

The previous Section discussed the modification of the phase and magnitude response of the system in the presence of shielding materials. This highlights the requirement to consider other conductive or permeable items expected in an experimental set-up; including any magnetic shielding. Figure 4.17 displays a COMSOL simulation which includes a three-layer mu-metal cylindrical enclosure. The sensing point is within the

enclosure at $z_P = 247\,\text{mm}$, whilst the target and coil are outside the enclosure in the same configuration as previous. The inner layer of the enclosure had a radius of 50 mm and length of 400 mm. Each layer was separated by 20 mm, with a thickness of 1 mm. The mu-metal is defined with a relative permeability $\mu_r = 30000$.

The magnitude and phase responses in this scenario across frequencies of 40 Hz and 300 Hz are displayed in Figure 4.18. These data can be compared with the target only results to demonstrate a decrease in magnitude but increase in phase as a function of frequency. These modifications are attributable to both the interaction between the enclosure and target along with distortion of the primary field.

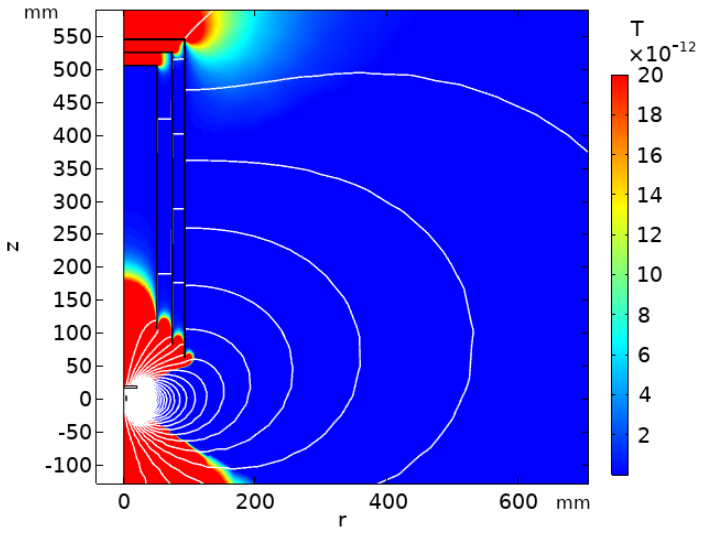

Figure 4.17: COMSOL simulation displaying the 2D axially symmetric arrangement of a coil illuminating a $\mathbb{R} = 20\,\text{mm}$, $\mathbb{T} = 3\,\text{mm}$ copper target outside of a three-layer mu-metal cylindrical enclosure. The colour bar displays the magnitude of B_z across z and r.

The purpose of this simulation is not to construct an accurate prediction of the absolute magnitude and phase values obtained from the system, but to note that the configuration of different conductive or permeable equipment within the experiment contribute to measurement in a way which cannot be background subtracted. As such, specific values obtained in one scenario cannot be used across another system. The

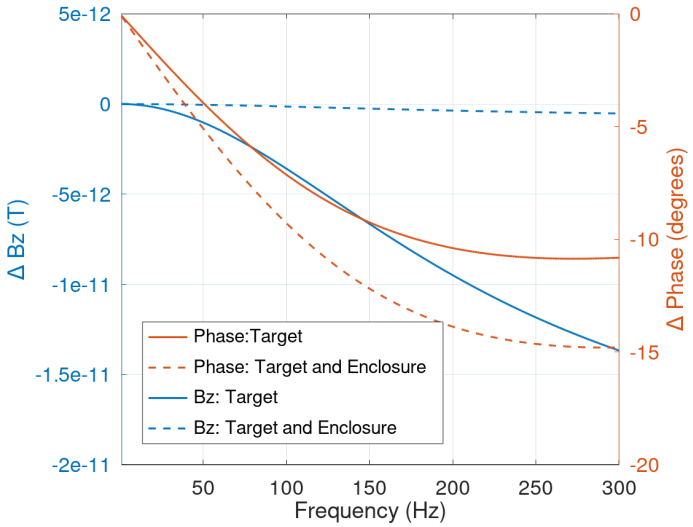

Figure 4.18: Change in magnitude (blue) and phase (red) as a function of frequency. Data is obtained in response to a copper target $\mathbb{R} = 20\,\text{mm}$, $\mathbb{T} = 3\,\text{mm}$ at a sensor point $z_P = 247\,\text{mm}$, without (solid) and with (dashed) a three-layer mu-metal enclosure. The inner layer of the enclosure has a radius of 50 mm and length of 400 mm. Each layer is separated by 20 mm, with a thickness of 1 mm. The mu-metal is defined with $\mu_r = 30000$.

impact of this is that each detection system may need to be precisely calibrated in-situ in order to identify any materials from these properties. This variability would limit the applicability of the ECI technique in some practical scenarios, specifically those with unconstrained environments such as Detection Science (DS) applications. However, the uniqueness of the measurement could be useful in others. For example, in Nuclear Treaty Verification (NTV) where the technique may be used to produce a "fingerprint" of an item to ensure it has not been modified.

4.6 ECI at High Frequencies

All preceding Sections have discussed the magnitude and phase response of a system at low frequencies ($\leq 300\,\text{Hz}$) suited to the detection of materials in thick shielding configurations. These scenarios are met by the commercially available QuSpin sensors which

have a small bandwidth operating around DC fields. The RF atomic magnetometer however, is tune-able across a larger frequency range. This gives the potential to explore modification of the phase or magnitude response to optimise the system to detect materials of specific conductivities. This premise is based on the description of phase and magnitude turning points discussed in Section 4.4.1.

Turning points in the phase and magnitude as a function of object thickness were found to linearly increase as a function of $L = 2\pi\delta$. Using the same description, a maximum in phase can be found by sweeping the frequency of the excitation field. These data are displayed in Figure 4.19b as simulated using COMSOL due to the finite nature of the target. The calculations assume a target of radius $\mathbb{R} = 12.5\,\text{mm}$, $\mathbb{T} = 1\,\text{mm}$ at a detection point $z_P = 88\,\text{mm}$ and predict a frequency turning point which varies as $1/\sigma$.

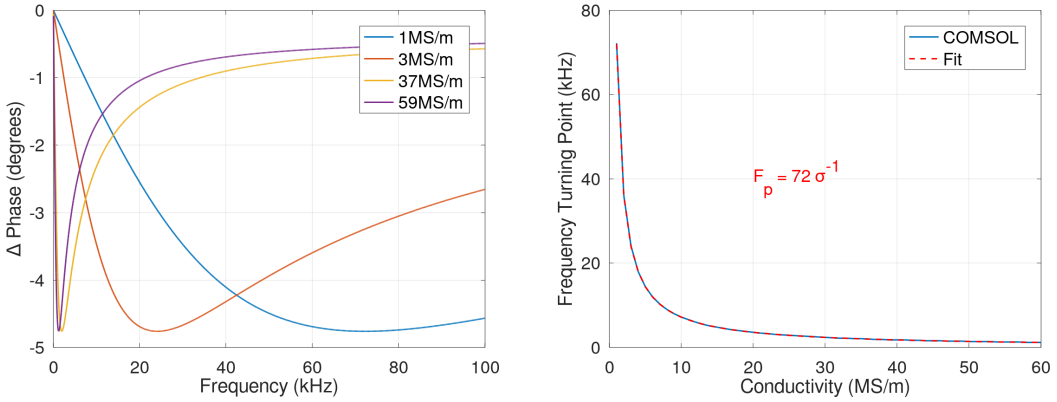

Figure 4.19: Change in phase as a function of frequency (left) and the corresponding frequency location of the phase turning points as a function of target conductivity (right).

A consequence of specifying the frequency to maximise the phase change in the presence of a particular conductivity target is the suppression of other values. As such, the simulations are modified to include lower conductivity materials such as uranium or plutonium. These results are illustrated in Figure 4.19a which displays the phase change as a function of frequency for conductivities of 1 MS/m (plutonium), 3 MS/m (uranium),

37 MS/m (aluminium) and 59 MS/m (copper), all with $\mu_r = 1$. These distributions indicate maximal responses at 72.2 kHz, 24.1 kHz, 1.9 kHz and 1.2 kHz respectively. Examining the phase across 72.2 kHz and 24.1 kHz highlight that the phase response for plutonium and uranium could be maximised whilst minimising signal from other potentially clutter materials such as aluminium or copper.

Chapter 5

Image Quality Analysis (IQA)

Before discussing the experimental results of the ECI imaging systems, the techniques applied for image analysis are reviewed. These methods were used for image noise quantification and subsequent reduction. This process helped to critically improve the quality of the AM-ECI images and therefore allowed the detection of targets in more challenging scenarios. This work developed a selection of image quality analysis (IQA) tools which were modified from those typically applied to optical images.

The ECI images obtained experimentally could be displayed in terms of either the magnitude or phase of the total magnetic field in reference to the applied excitation/primary field. These images were obtained across a range of frequencies which generated approximately 100 individual images for each measurement. When considered across several variables such as excitation voltage, target conductivity, shielding thickness, shielding conductivity and target size; upwards of 3700 separate images were obtained. This significant number necessitated an automated assessment which could make a consistent and quantitative comparison across all experimental parameters.

IQA is a vast field which aims to quantify every facet of image quality and can encompass parameters such as the signal to noise ratio (SNR), blur, noise, contrast, target detection and resolution. Due to the simplicity of the images obtained and the

information required for comparison, the parameters considered in this work were limited to noise and target detection.

IQA techniques which examine image noise primarily focus on image enhancement through de-noising. The literature on this topic spans a range of techniques, however, integral to many of these is the assumed knowledge of the noise level. In contrast, noise estimation algorithms are a less well researched field [91]. In general noise estimation methods can be considered across three categories, full reference (FR), reduced-reference (RR) and no-reference (NR). FR algorithms make comparisons based upon a "true" image which is devoid of all distortion [22, 92, 93], whilst NR employs techniques to quantify image quality where no true image is available. RR methods lie between the two techniques, where some information about the image is available but not the true image [94–97]. The work discussed here necessitates the use of a NR method, of which three are commonly discussed [98]; these are filtering [91, 99, 100], block [101–104] and Single Value Decomposition (SVD) based techniques [98, 103–105].

In addition to image noise, an object detection method is also proposed. The detection of objects within images is an extensively researched topic spanning numerous sophisticated techniques [16] ranging from template matching [106] to machine learning methods [107]. These algorithms are often challenged with the detection of complex features with little prior knowledge available. Any full implementation of a scanning system necessitates the use of one of these advanced algorithms. However, in the case where there is a limited database of training images and the approximate target size, shape and location are prior knowledge this can be simplified to fitting the expected output to the data.

The subsequent Section explores basic examples of filter, block and SVD based noise estimation algorithms; defining a noise estimation metric associated with each. This was either a direct estimate of an assumed white additive Gaussian distributed noise variance (κ_{est}) or a parameter expected to be linearly proportional to the noise. The response

of these metrics was first examined by adding a known noise distribution to a starting image. Each technique was applied to images with increasing noise variance (κ_1). Once the metric was examined as a function of simulated noise, the methods were applied to a selection of experimentally obtained images with visually verified noise levels. The consistency of each technique was explored along with other features such as algorithm speed and independence with respect to image parameters such as size and content.

In addition to the noise estimation, a simple method is proposed to confirm the presence of an object within the image. In this instance a basic expected fit method is examined based upon the simplicity and predictability of the image content.

5.1 Image Noise

A small number of methods are considered here for the quantification of noise within an image, these include methods based upon filtering, block and SVD techniques.

5.1.1 Filter Method

The NR filter based methods typically involve three primary steps [99]:

- Application of a low band-pass smoothing method to a starting noisy image.
- Subtraction of the smoothed and original images to produce a residual image.
- Evaluation of the variation within the residual to extract a noise metric.

In this instance, the first step was addressed through the application of a 2D low-band pass Gaussian filter. The filter was constructed by creating a discrete approximation of a Gaussian function also known as a mask. This can be obtained by sampling a 2D Gaussian function with the form

$$\mathfrak{G}(x,y) = \frac{1}{2\pi\kappa^2} e^{\frac{x^2+y^2}{2\kappa^2}} \tag{5.1}$$

where κ^2 is the variance of the distribution and x and y are spatial indices. A 3×3 mask can be constructed using $\kappa^2 = 1$ and is given as below.

$$\text{Mask} = \frac{1}{16}\begin{bmatrix} 1 & 2 & 1 \\ 2 & 4 & 2 \\ 1 & 2 & 1 \end{bmatrix} \tag{5.2}$$

The distribution and mask are illustrated in Figure 5.1. The chosen mask is one of many that could have be implemented, a 3×3 mask was selected due to the small number of pixels expected in each image ($\sim 40\,\text{px} \times 40\,\text{px}$). A larger mask would result in more pixels being lost during the convolution. A variance of $\kappa^2 = 1$ was also selected based on this principle, where a larger variance would require a larger mask to represent the Gaussian distribution out to three standard deviations.

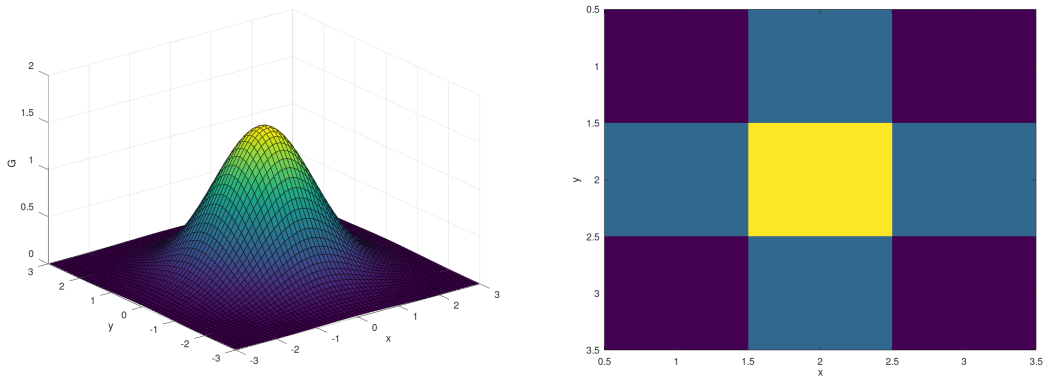

(a) 2D Gaussian distribution

(b) 3×3 Gaussian mask

Figure 5.1: An illustration of the 2D Gaussian distribution 5.1a with a zero mean and variance, $\kappa^2 = 1$, this function can be parameterised into a 2D mask which is displayed in 5.1b.

The mask was applied by splitting the image into 3×3 pixel groups each centred around a given pixel ($x \times y$). Element multiplication was then performed between the pixel group and the mask to produce a third matrix. All values within the third matrix

were summed and assigned to the centre pixel location $(x \times y)$. This method was applied for all pixels within the $X \times Y$ image except the outer edge. The resulting matrix formed a $(X-2) \times (Y-2)$ smoothed image. The smoothed image was then rescaled to retain the values of the original. Once a smoothed image was obtained, the filter method calculated the difference between it and the original to produce a residual image. Finally, the variance across the residual image was evaluated to indicate the degree of noise. This filter based technique is illustrated in the flow diagram displayed in Figure 5.2.

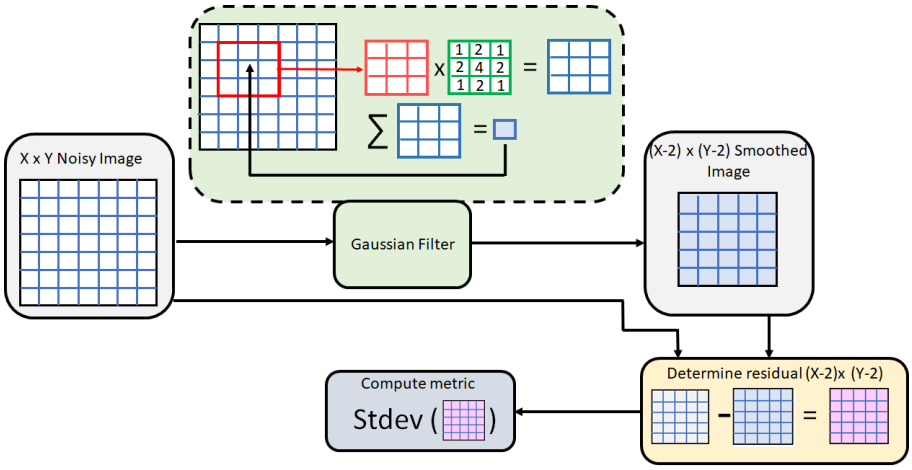

Figure 5.2: Flow diagram to illustrate the process involved in the filter based method to estimate image noise. A noisy image in smoothed using a 2D Gaussian filter discretised into a 3×3 mask. The smoothed image is subtracted from the original to produce a residual. The variability of the residual image is assessed to produce a noise metric.

Figures 5.3a and 5.3b display examples of experimentally obtained low and high noise images of a 40 mm $\times$40 mm $\times$3 mm copper square. These images were smoothed using the 2D Gaussian filter to produce those in 5.3c and 5.3d. The corresponding residual obtained through subtracting the original from the smoothed images are displayed in 5.3e and 5.3f. These images display a common pattern left behind as a result of the smoothing, however, it can be seen that the spread of values is greater in the high noise image in comparison to the low noise equivalent. This is better illustrated by examining the data as a histogram of values and is shown for both noise levels in Figure 5.4. The

spread of these data can be characterised by the residual standard deviation (RS); this metric produces values of 0.095 and 0.061 for the high and low noise images respectively.

To explore the behaviour of this noise metric, normally distributed noise with variance (κ_1) was added to the low noise image displayed in Figure 5.3b. Figure 5.5 displays this metric (RS) as a function of an increasing κ_1 value, where two of the resulting images ($\kappa_1 = 0.2, 0.5$) are shown in the insert.

The linear distribution between the RS value and the noise variance was found to be independent of image size, with a greater number of pixels just reducing the variability in the RS values at greater noise contributions. It was also found to be reasonably independent of image content, with a number of similarly low resolution images producing similar dependencies as displayed in Figure 5.6. These images are digital manipulations of the low noise image rather than experimentally obtained.

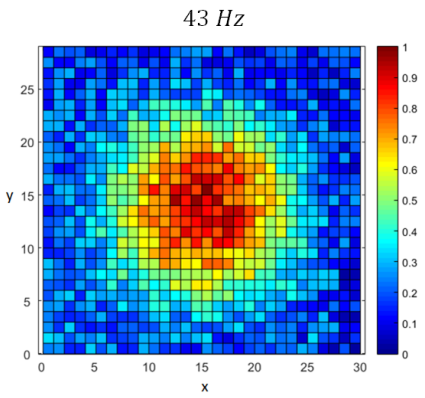

(a) Original high noise image

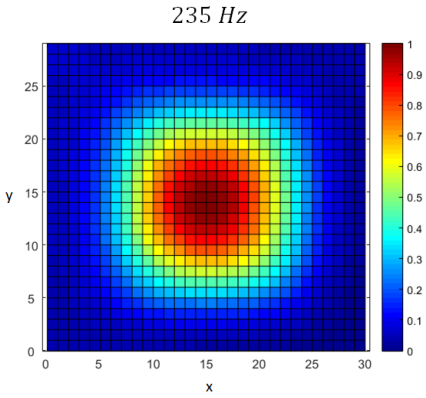

(b) Original low noise image

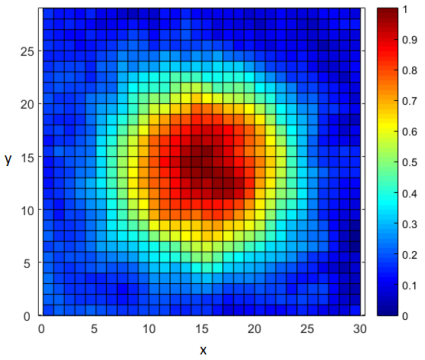

(c) Smoothed high noise image

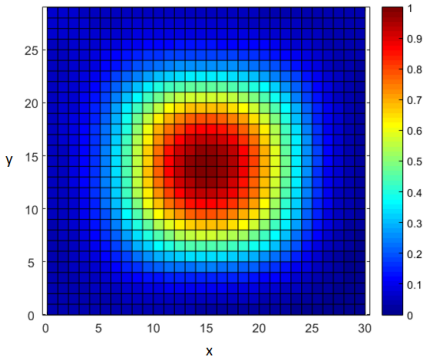

(d) Smoothed low noise image

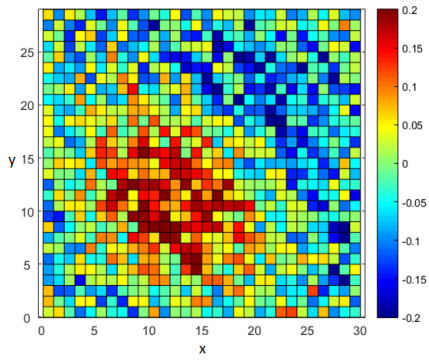

(e) Residual high noise image

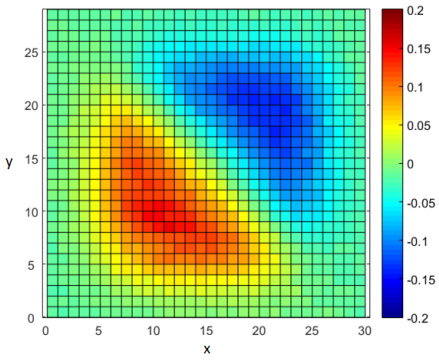

(f) Residual low noise image

Figure 5.3: Normalised, phase images obtained of a 40 mm $\times$40 mm copper square at two frequencies to produce examples of low noise (235 Hz) and high noise (43 Hz) images. Data obtained at $V = 3\,\mathrm{V}$. Original images are displayed in a-b, smoothed images displayed in c-d and the subtraction of the two shown in e-f. These images demonstrate the different steps of a filter based noise estimation method.

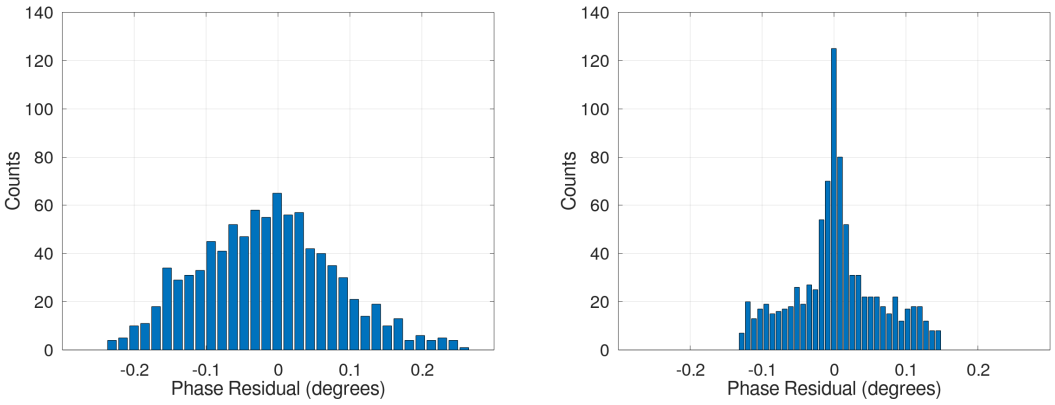

(a) High noise image (b) Low noise image

Figure 5.4: A histogram representation of the data within the residual image of a 40 mm×40 mm copper square at (5.4a) 43 Hz and (5.4b) 235 Hz, with an $V_{osc} = 3$ V.

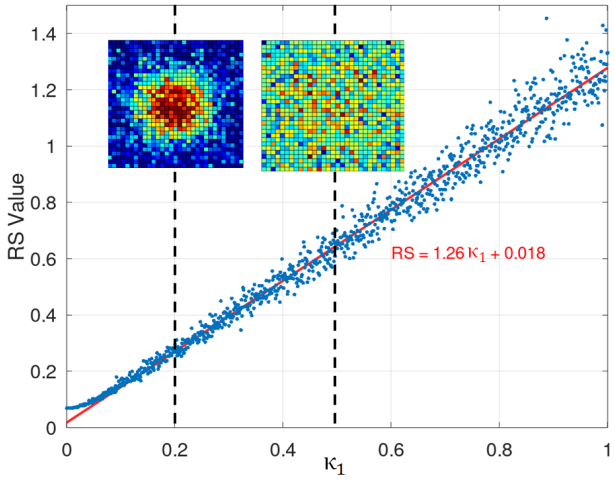

Figure 5.5: RS value as a function of the variance (κ_1) of Gaussian noise added to a low noise starting image. Images with the addition of the noise are displayed in the inserts for $\kappa_1 = 0.2$ and $\kappa_1 = 0.5$.

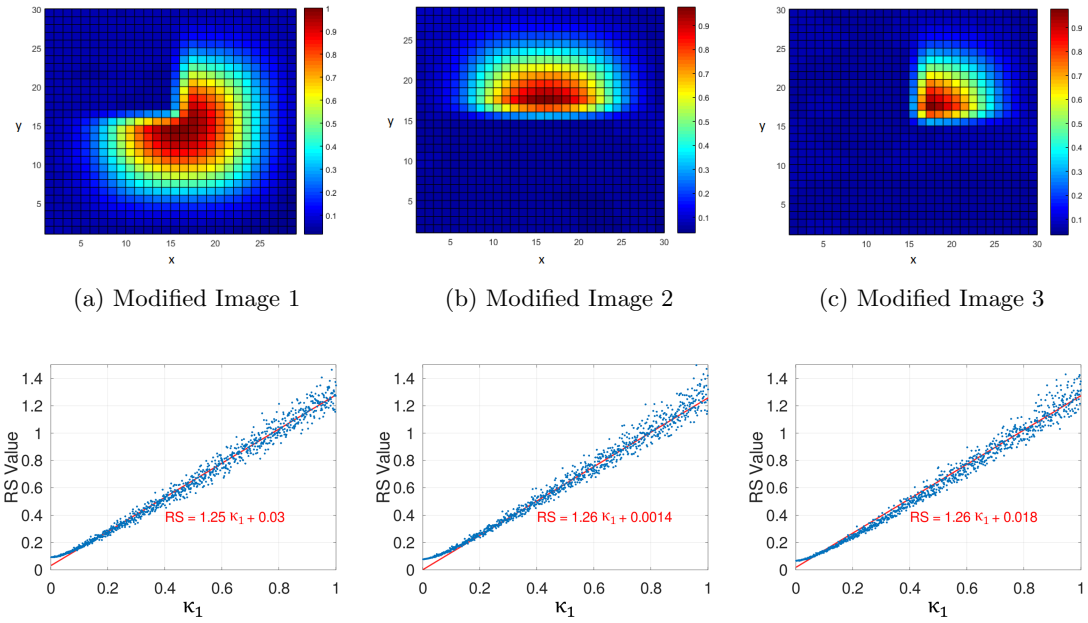

(a) Modified Image 1 (b) Modified Image 2 (c) Modified Image 3

(d) RS Values, Modified Image 1 (e) RS Values, Modified Image 2 (f) RS Values, Modified Image 3

Figure 5.6: Modified low noise images are displayed between 5.6a - 5.6c. The corresponding RS value as a function of the variance of added normally distributed noise is displayed between 5.6d - 5.6f.

5.1.2 Block Method

Block based methods also allow the noise to be quantified in no-reference image processing scenarios. The methodology of the block method can be summarised as the following [102].

- Division of an image into blocks.
- Calculation of the homogeneity of pixel intensity across blocks.
- Definition of a metric to quantify the noise.

The first step in this process can be approached in a variety of ways; techniques have been discussed which range from randomly selecting a percentage of blocks across the

image [103, 104] to selection based on homogeneity [102]. The technique considered here involves the use of a K-means clustering algorithm which is an unsupervised process used to segment an image based on pixel intensity. This algorithm employs a user defined number of bins (K) each centred about an intensity value, I_k for a particular bin k. Initial values of I_k are spread uniformly across the intensity range of the image and each pixel is assigned to the bin with the closest I_k value. This defines the initial population, Pop_k, of the bin k. Once the population is defined, the mean of that bin is calculated and assigned as a new value of I_k. These two steps are repeated, shifting the values of I_k until the populations of all the bins stabilise at a minimal value of average bin variance. Figure 5.7 displays a raw image and the segmented equivalent when $K = 6$ bins is defined. For the purposes of visual demonstration, only 6 bins are selected ($K = 6$) and the algorithm takes very few iterations to converge (< 50). The complete K-means cluster methodology is illustrated in Figure 5.8.

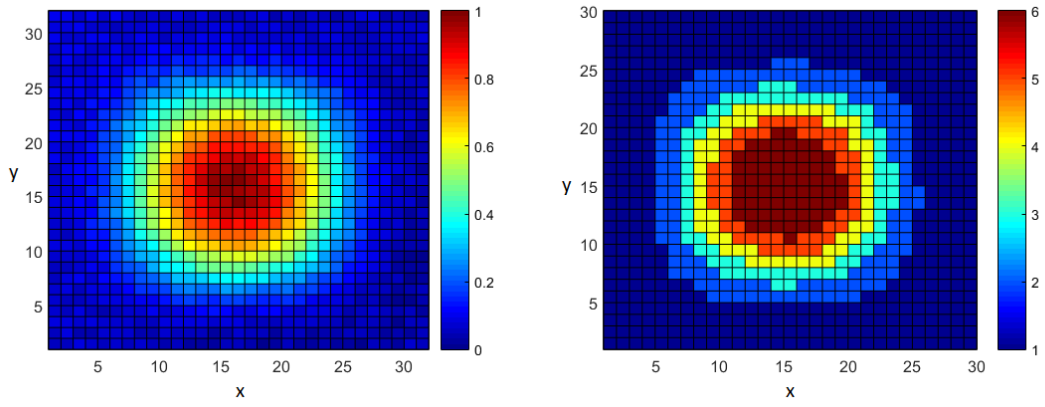

(a) Image (b) Segmented Image

Figure 5.7: An input (5.7a) image of a 40 mm $\times$40 $\times$ 3 mm copper square obtained at 121 Hz and the segmented image (5.7b) obtained using the K-means clustering algorithm.

Once the segments have been identified using the K-means clustering algorithm, the standard deviation across any of the regions can be calculated using data from the original image; producing an estimate of the noise RS_{Block}. The block noise estimation

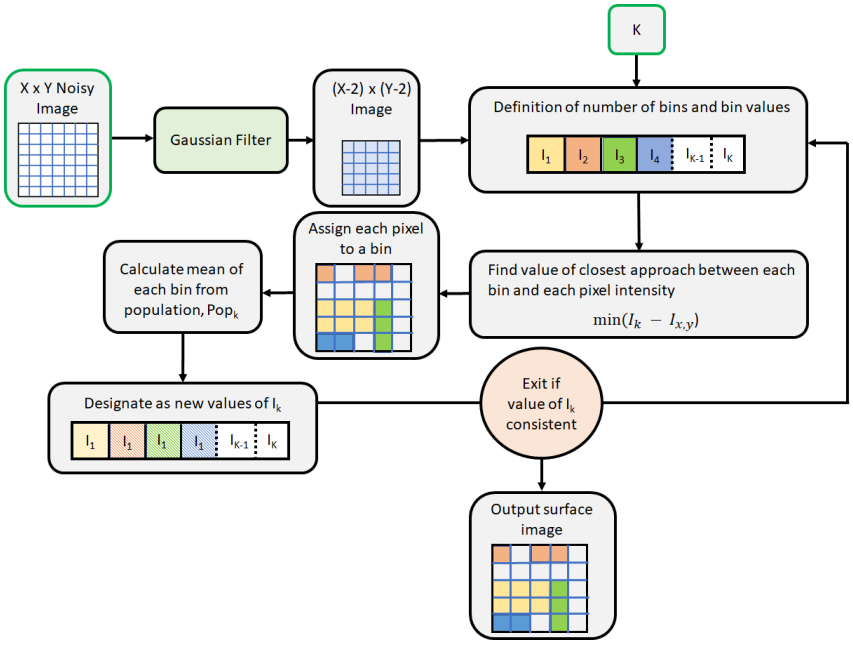

Figure 5.8: Illustration of the K-means clustering algorithm utilised to segment images. The process begins with a noisy input image which is smoothed using a Gaussian filter. A user defined, K number of bins are assigned across the intensity range of the image with centres I_k. Pixels are allocated to those bins based on points of closest approach to form a bin population Pop_k. The mean of the bin is taken and assigned as the new centre value. This process is repeated until the bin populations stabilise and an output surface image is created.

process is illustrated in Figure 5.9.

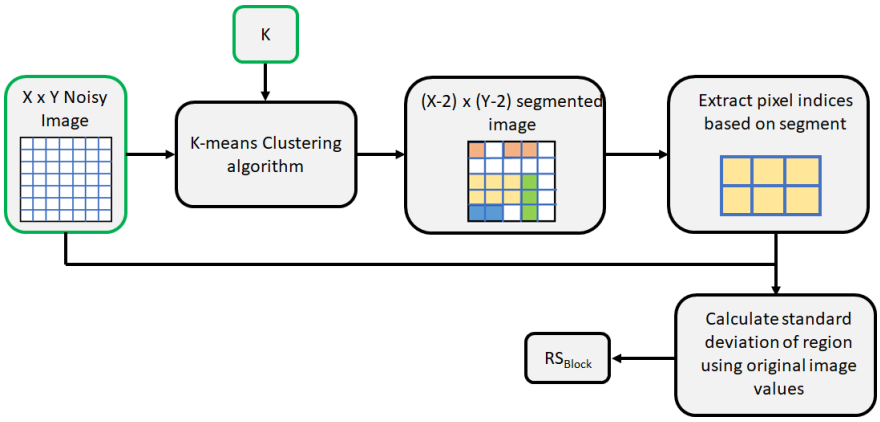

Figure 5.9: Illustration of the block based method used to approximate the amount of image noise.

As was previously explored with the filter method, normally distributed noise was added to the low noise image displayed in Figure 5.3b and the block method applied with $K = 10$ for greater homogeneity within each segment. This too was found to produce a linear relationship as a function of the variance of the noise distribution. This is shown in Figure 5.10, and demonstrated similar independence with image size and image content as the filter method. A comparison of the RS and RS_{Block} values at greater added variance values ($\kappa_1 > 0.2$) demonstrates a considerably greater variability in the RS_{Block} value with small changes in additive noise; this is attributed to the reduced sampling region resulting from the segmentation of the image. It was also found to be considerably slower than the filter method. To compute the 500 images between $\kappa_1 = 0.001$ and $\kappa_1 = 1$ the filter method took 11 seconds, compared to 160 seconds using the block method.

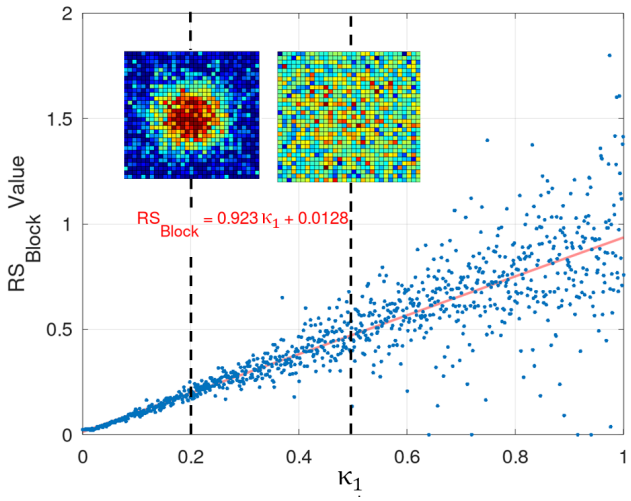

Figure 5.10: RS_{Block} value as a function of the variance (κ_1) of normally distributed noise added to a low noise starting image. Images with the addition of the noise are displayed in the inserts for $\kappa_1 = 0.02$ and $\kappa_1 = 0.5$.

5.1.3 Single Value Decomposition

Single Value Decomposition (SVD) is another noise quantification algorithm and is based upon the assumption that a matrix, Q, can be separated into the product of three different matrices as described by

$$Q = U \times S \times H^T. \tag{5.3}$$

Here, the columns of U are populated by the orthonormal eigenvectors of QQ^T, the columns of H are the orthonormal eigenvectors of Q^TQ and S is a diagonal matrix of rank $\mathfrak{r}$ containing the square root of the eigenvalues of either QQ^T or Q^TQ in descending order [98]. Here, the superscript T indicates the transpose matrix. Within this application, Q represents the input image and the values within matrix S (s) can be split into contributions from the image, s_s, and the noise, s_n, where $s = s_s + s_n$. In general the higher the noise contribution, the larger the values of s, where the initial values of s are preferentially influenced by the image content; this is illustrated in Figure 5.11.

A parameter PM can be defined which sums together the noise contributions from s; this is given as,

$$PM = \frac{1}{S_{LB}} \sum_{i=\mathfrak{r}-S_{LB}+1}^{\mathfrak{r}} s(i) \tag{5.4}$$

where S_{LB} is the lower bound of the s indices to sum over. The value of PM can be examined by adding normally distributed noise to an image and increasing the value of the variance, κ_1, as was previously demonstrated for the filter and block methods. Figure 5.11 displays the values of s as a function of diagonal index, i; increasing the variance increases the value of s across all indices, however, a comparison of $\kappa_1 = 0$ with $\kappa_1 > 0$ indicates that the image content is almost completely contained within $s(i < 5)$. The value of S_{LB} is debated in a number of the studies [98, 103] and is recommended to

be around $0.75\mathfrak{r}$ to ensure the noise contributions dominate. Inspection of Figure 5.11 demonstrates that this may not be applicable to these images which have less detail than those explored in the cited studies.

In this work, a 32×32 pixel image was examined and therefore has a rank, $\mathfrak{r} = 32$. Figure 5.12 displays the subsequently calculated values of PM as a function of κ_1 for $S_{LB} = 0.75\mathfrak{r} = 24$. Values were calculated by passing the image through an in-built SVD operation within MATLAB.

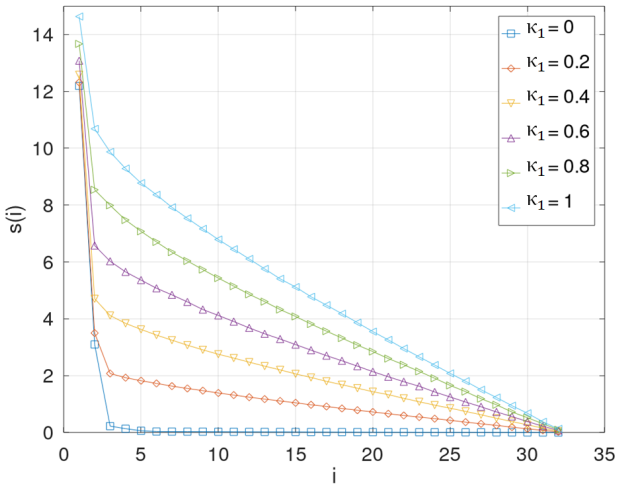

Figure 5.11: Non-zero values of diagonal matrix S, with rank $\mathfrak{r}$, as a function of matrix index, i. Values obtained from an image with added normally distributed noise of variance, κ_1.

The relationship between PM and κ_1 can be used as a noise calibration factor and is a linear function given as,

$$PM(\kappa_1) = \alpha\kappa_1 + \beta \tag{5.5}$$

where the gradient, α, is considered independent of image content, whilst β is content dependent. To generalise the formulation and remove the contribution from the image, a second image was derived from the first by adding a known amount of noise κ_2. This

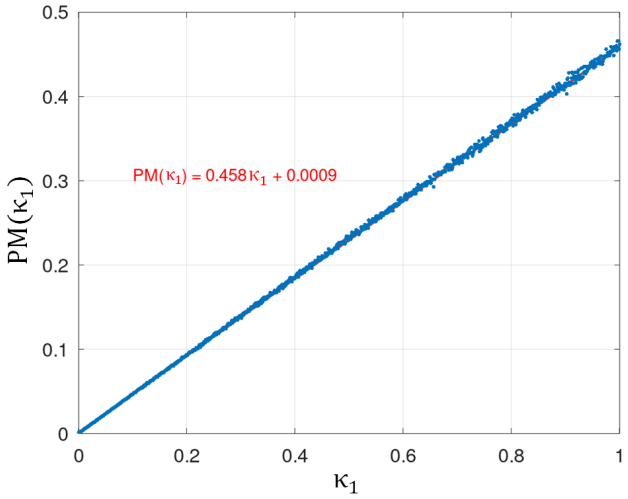

Figure 5.12: PM value as a function of the variance, κ_1 of zero-mean Gaussian distributed noise added to an original image. PM values represent a summation of values within the matrix S from index $i > 24$.

results in a combined amount of noise, $\kappa_3 = \sqrt{\kappa_1^2 + \kappa_2^2}$, which produces PM values as

$$PM(\kappa_3) = \alpha\sqrt{\kappa_1^2 + \kappa_2^2} + \beta. \tag{5.6}$$

Combining these equations yields an estimate of the image noise, κ_{est}:

$$\kappa_{est} = \frac{\alpha\kappa_2^2}{2(PM(\kappa_3) - PM(\kappa_1))} - \frac{PM(\kappa_3) - PM(\kappa_1)}{2\alpha}. \tag{5.7}$$

In this instance κ_{est} is an estimate of the applied noise κ_1. The complete process is illustrated in Figure 5.13.

If we take the value of $\alpha = 0.458$ from Figure 5.12 and specify a $\kappa_2 = 0.2$ then the estimate of image noise can be calculated as a function of the added noise. The results of this are displayed in Figure 5.14, where a good approximation of the applied noise was reconstructed using equation 5.7. The performance of this algorithm was found to be particularly dependent upon the value of κ_2, with difference between the applied variance and estimated value quickly diverging if κ_2 was set far from κ_1. This is demonstrated in

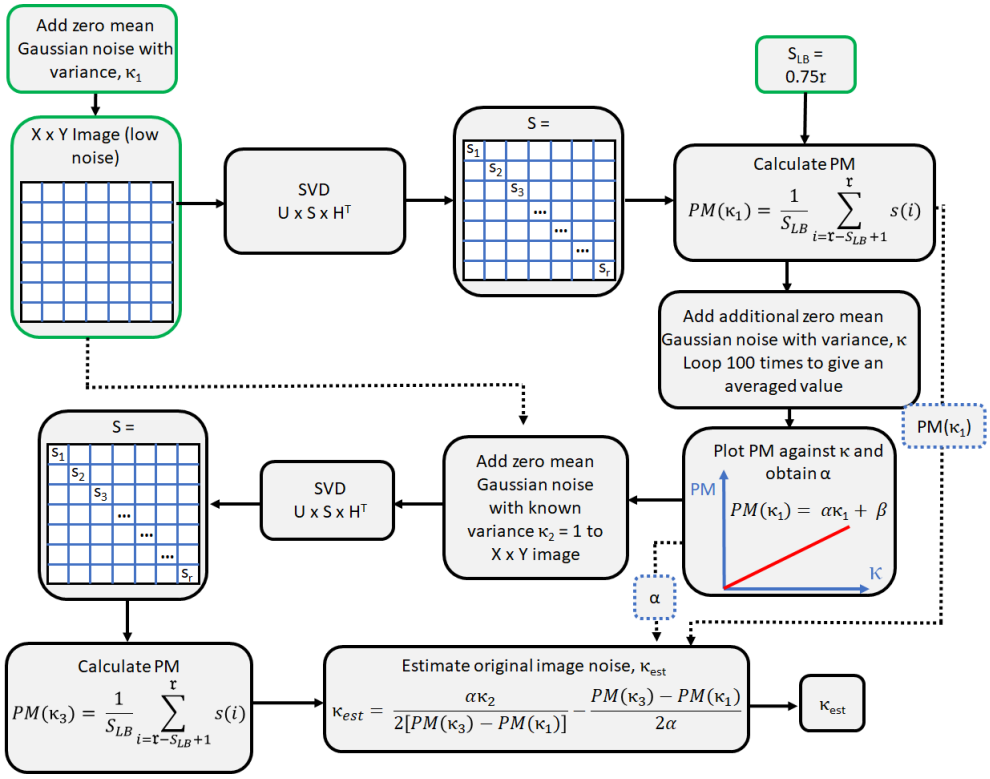

Figure 5.13: Illustration of estimation of image noise using a single value decomposition method (SVD).

Figure 5.15, which displays the absolute difference between the parameters as a function of κ_2.

Unlike the previous noise approximation methods, the SVD method gives an actual estimation of the original image noise rather than a quantity proportional to the noise. The SVD method analysed the 500 images between $\kappa_1 = 0.001$ and $\kappa_1 = 1$ in a time of 86 seconds, this compares to 11 seconds for the filter method and 160 seconds for the block method. Whilst the SVD method is independent of image content, unlike the previous measurement it is only independent of image size if α is dynamically generated for each image, rather than evaluated offline. The above duration (86 seconds) represents an offline calculation of α.

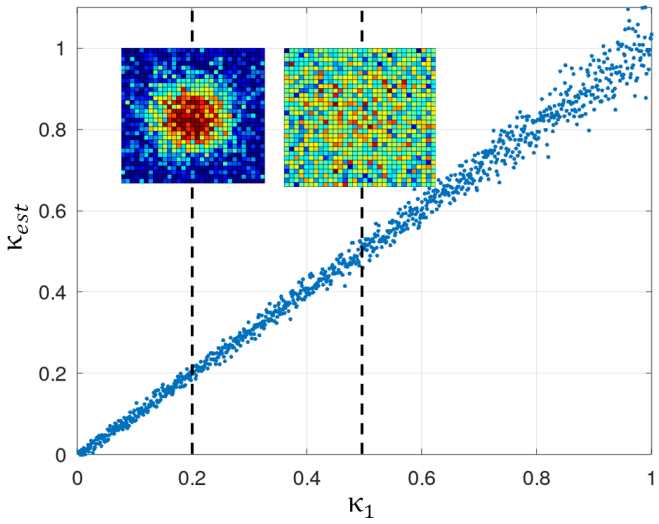

Figure 5.14: The estimated image variance as a function of the variance of normally distributed noise. Data obtained using $S_{LB} = 0.75\mathfrak{r}$, $\kappa_2 = 1$. Noise corrupted images displayed for $\kappa_1 = 0.2$ and 0.5.

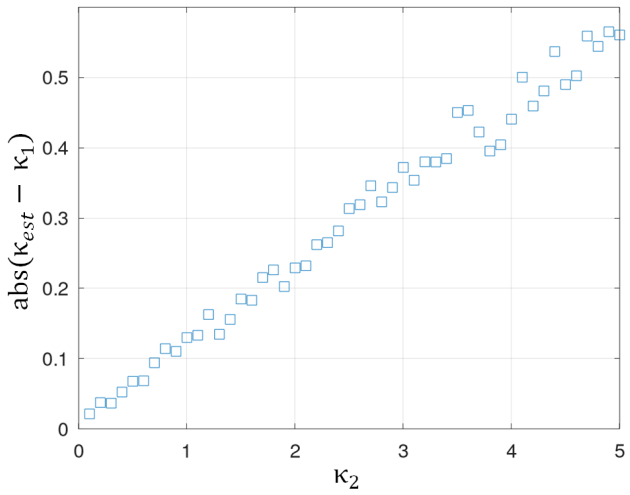

Figure 5.15: Difference between the applied noise variance ($\kappa_1 = 0.2$) and the SVD estimated value (κ_{est}) as a function of the value of κ_2.

5.1.4 Application to Experimental Images

The discussion thus far has made the assumption that image noise can be approximated as a zero-mean Gaussian distribution and is based on the assumption that multiple,

independent sources of noise sum to a normal distribution. In reality any noise distributions are unlikely to be precisely normally distributed and any metric will need to be reconciled with a human visual assessment. In an effort to quantify this for the range of noisy images expected from experimental data, a selection of images were obtained with the set-up which is discussed in Chapter 6. These images were visually assessed to have either "low", "medium" or "high" amounts of noise. Examples of these images are displayed in Figure 5.16. In total 300 images were selected with 100 allotted to each category.

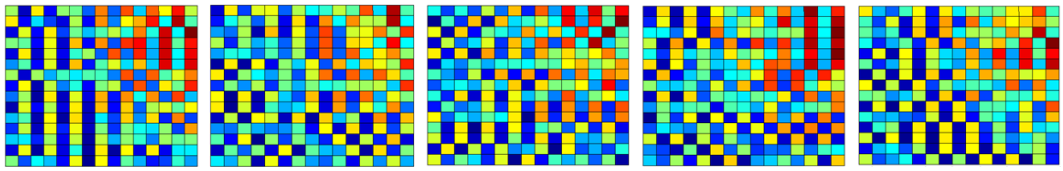

(a) High Noise

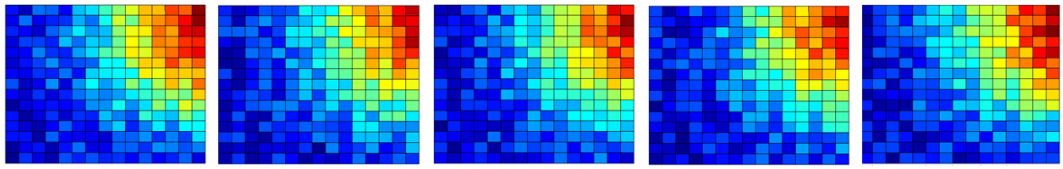

(b) Medium Noise

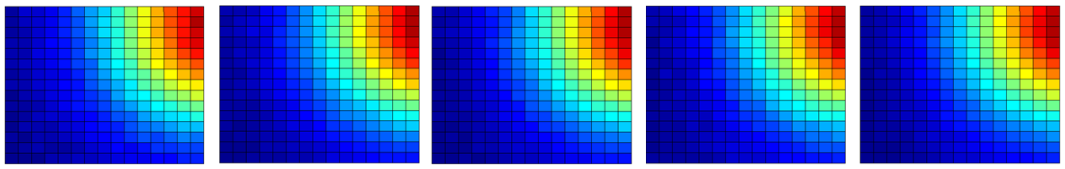

(c) Low Noise

Figure 5.16: A selection of images which are visually classified as "high", "medium" and "low" noise.

Each noise quantification approach was applied to the complete image set to determine how well the calculated noise metric meets visual inspection. Figure 5.17 displays the RS value calculated using the filter method as a function of image number. This technique successfully discriminated between each image category and demonstrated an RS value increase $> 50\%$ between each classification. A small variation in RS was

observed within the low noise category (standard deviation, $\text{stdev}_{low} = 0.0009$), however was found to increase for "medium" and "high" noise images ($\text{stdev}_{med} = 0.0063$, $\text{stdev}_{high} = 0.0143$). This variation is not unexpected when Figure 5.5 is considered which demonstrates an increase in variation between adjacent RS values for increasing values of κ_1. It should be noted that the variation may not be completely attributed to the calculation of the RS value and could also be assigned to the difficulty in visually classifying images with greater amounts of noise.

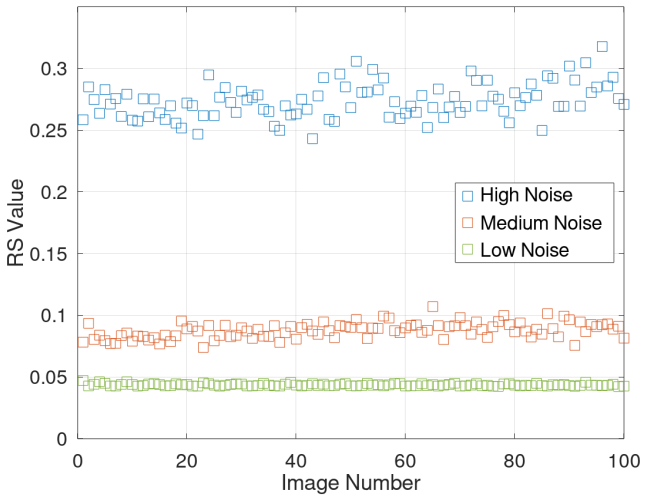

Figure 5.17: RS value metric of noise obtained using the filter based method plotted as a function of image number, where each image is visually classified as having "high", "medium" or "low" noise.

Figure 5.18 displays the RS_{block} noise metric as a function of image number for the same set of visually classified images. This graph demonstrates an increase in the percentage change between classifications ($> 68\%$) when compared with the filter method. However, the variation within each category was also found to be larger, particularly in the high noise images ($\text{stdev}_{low} = 0.0017$, $\text{stdev}_{med} = 0.0055$, $\text{stdev}_{high} = 0.0323$). This again can be expected from inspection of Figure 5.10 which demonstrated a larger range of RS_{block} values with an increasing κ_1 compared with the filter method.

Adaptation of the SVD method for the analysis of the experimental images involved

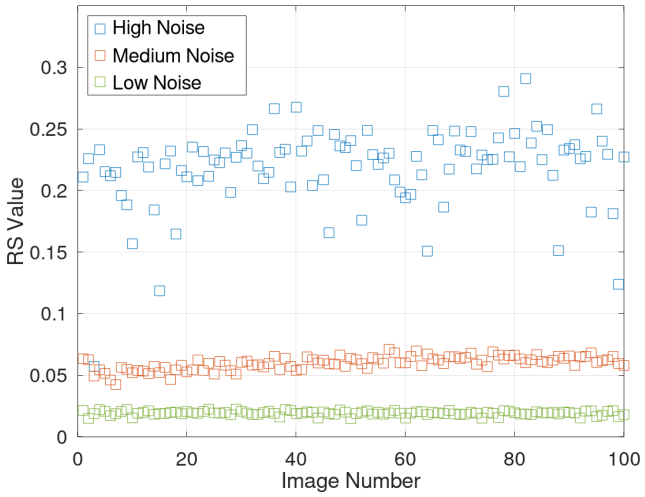

Figure 5.18: RS_{block} value metric of noise obtained using the block based method plotted as a function of image number, where each image is visually classified as having "high", "medium" or "low" noise.

the re-calculation of the calibration curve, PM vs κ_1, for the smaller image size (16×16 pixels). Figure 5.19 displays the calculated PM value for $S_{LB} = 0.75\mathfrak{r}$ as a function of κ_1. It was found that PM(κ_1) was no longer a linear function and that this could be altered by changing the value of S_{LB} to a smaller value.

Due to the increased linearity, $S_{LB} = 0.85$ with $\alpha = 0.096$ was carried forward and used to calculate the value of κ_{est}. Figure 5.20 displays this value as a function of image number for the different classifications of image. When applied to the experimental data rather than images with generated Gaussian noise, little discrimination was shown between visually determined noise categories.

Inspection of the s values generated from each image category demonstrate that, at this stage of the process, the images types can be classified by noise level. However the PM values obtained were significantly smaller than those generated through the addition of the Gaussian noise κ_1 and occupy the poorly fit linear region at the start of the PM curve. To determine what range of κ_1 would be more applicable, the PM values generated through the addition of Gaussian noise were inspected and a range of

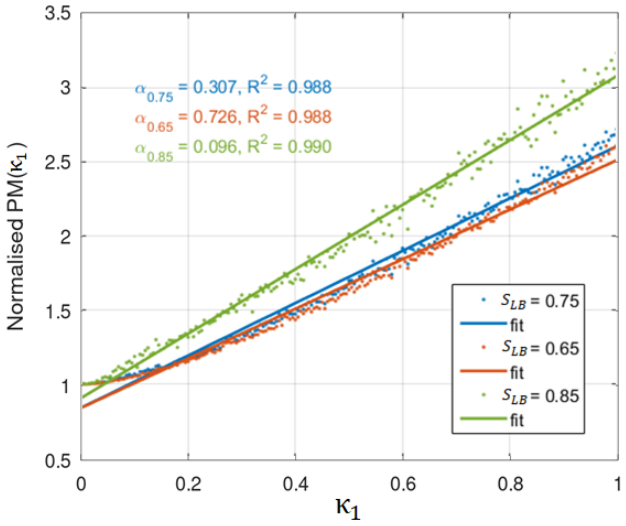

Figure 5.19: Normalised PM value as a function of applied noise variance, κ_1. This was calculated at $S_{LB} = 0.65$, 0.75 and 0.85.

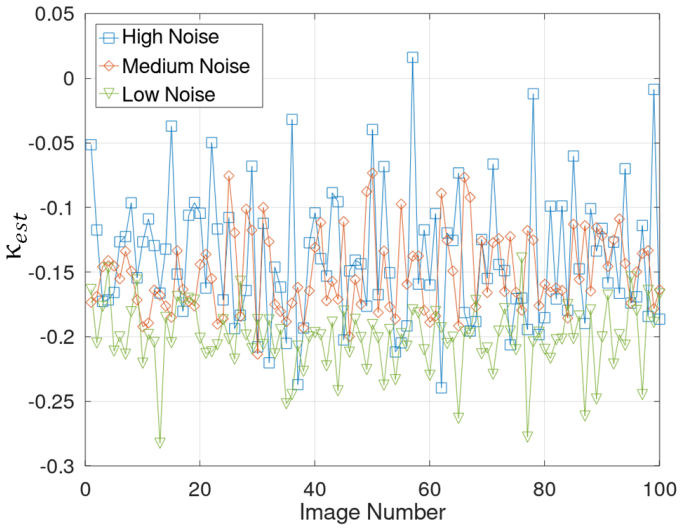

Figure 5.20: Estimated noise variance κ_{est} using a SVD based method as a function of image number. Data obtained with an $\kappa_2 = 1$, $S_{LB} = 0.85$, $\alpha = 0.096$ from a calibration curve taken between $\kappa_1 = 0$ to 1.

0 to 0.1 found to be more suitable. In this region the linearity was found to be more consistent as displayed in Figure 5.21a and therefore a value of $S_{LB} = 0.75\mathfrak{r}$ could be

utilised, yielding an $\alpha = 0.421$ with a $\kappa_2 = 0.1$. These values were used to re-calculate the estimated variance, κ_{est} as a function of the applied Gaussian noise κ_1 as displayed in Figure 5.21b; demonstrating a good reconstruction of the applied noise.

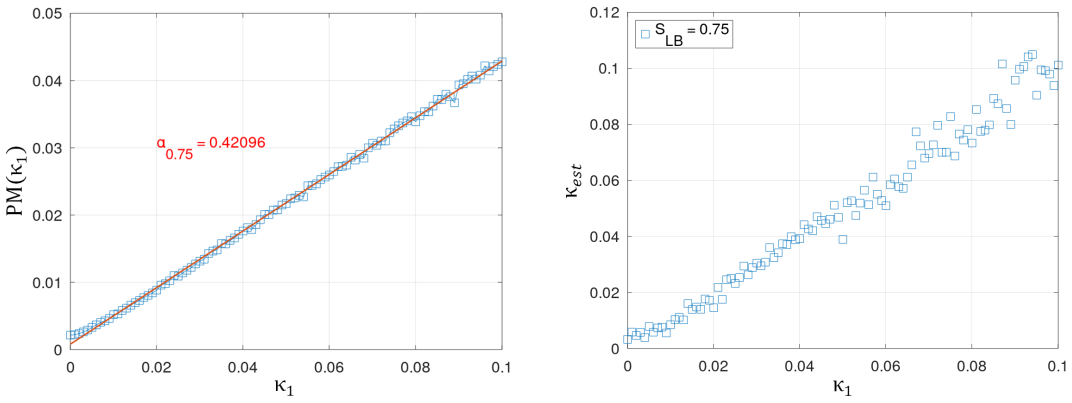

(a) PM calibration curve

(b) Estimation of noise variance

Figure 5.21: Re-calibration of the PM curve with applied noise variance κ_1 (5.21a) and the corresponding calculation of expected variance κ_{exp} (5.21b).

Once these modifications were implemented, the SVD method was re-applied to the experimental images to obtain the data in Figure 5.22. These data demonstrate a better discrimination between the low and medium noise images with changes of approximately 92%, however a lower percentage (39%) change in κ_{exp} between medium and high noise images than were obtained with the filter or block methods. The variation of κ_{exp} within each category was also found to be greater than the previous metrics ($\text{stdev}_{low} = 0.0034$, $\text{stdev}_{med} = 0.0166$, $\text{stdev}_{high} = 0.0142$). Improvements could be explored by altering the values of S_{LB}, κ_2 and the range of κ_1, however issues could be arising from the explicit assumption that the noise is normally distributed which may not be met in the experimental images. The requirement to tune the SVD method to this image set may also be true of other image sets, making the technique less easy to apply in general.

Each of the primary attributes of the three noise estimation techniques are summarised in Table 5.1. The factors considered are speed, image parameter independence,

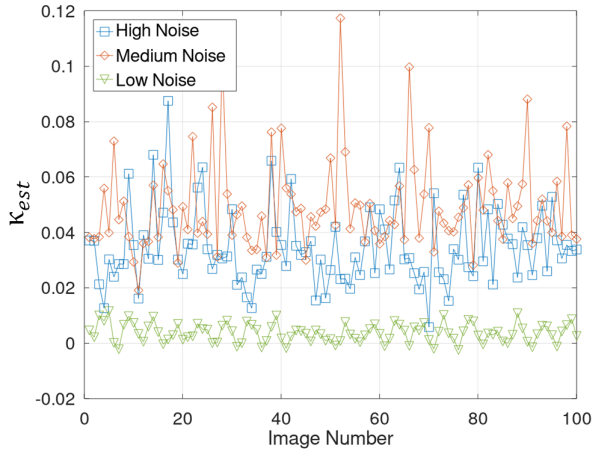

Figure 5.22: Estimated noise variance κ_{est} using a SVD based method as a function of image number. Data obtained with an $\kappa_2 = 0.3$ $S_{LB} = 0.75$, $\alpha = 0.39$ from a calibration curve taken between $\kappa_1 = 0$ to 0.1.

Attribute	Filter Method	Block Method	SVD Method
Speed (500 images)	11 seconds	160 seconds	86 seconds
Image Independence	size, content	size, content	content
(Metric$_{high}$ - Metric$_{med}$)/Metric$_{high}$	68%	72%	39%
(Metric$_{med}$ - Metric$_{low}$)/Metric$_{med}$	50%	68%	92%
stdev(Metric$_{high}$)	0.0143	0.0323	0.0142
stdev(Metric$_{med}$)	0.0063	0.0055	0.0166
stdev(Metric$_{low}$)	0.0009	0.0017	0.0034

Table 5.1: Summary of the primary attributes of the three noise quantification techniques examined. These include a filter based method, a block method and a technique based upon SVD.

percentage changes in the metrics between adjacent categories and metric variation within each category. Examination of these results suggest that the filter and block methods perform better than the SVD method in the classification of the experimental images. The block method better differentiates between categories, however has a greater variability within each category compared with the filter method. As the performance across these two categories are closely matched, the filter method is chosen based upon its increased speed which is $\times 15$ faster than the block method.

5.2 Object Detection

One of the primary disadvantages of the filter and block noise estimation methods over the SVD technique is that the optimal image is not necessarily the image with the lowest noise, but is instead the most homogeneous. In the examination of the numerous experimentally obtained images it is an important distinction between a homogeneous background image and a low noise image with a discernible object.

In all experiments conducted, the target was a simple uniform shape which, at the stand-off distances investigated, was expected to produce a roughly circularly symmetric image such as displayed in Figure 5.3b. Images such as these can be fitted along any line with a Gaussian function and an R^2 value can be calculated which gives a measure of the discrepancy between the fit and the data. An example of this applied to an image can be seen in Figure 5.23 which displays the previous example of a low noise image and its corresponding fit along the vertical and horizontal bisections.

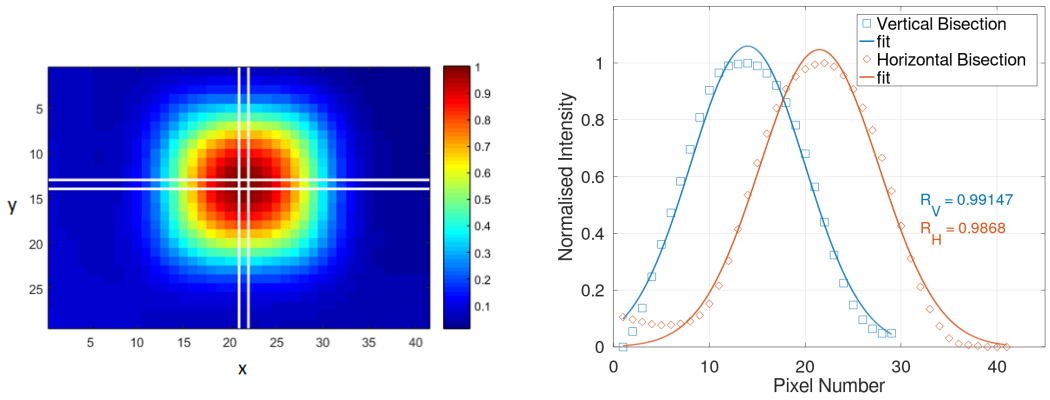

(a) Low noise image with bisections

(b) Intensity of bisections

Figure 5.23: An example of a low noise image of a 40 mm ×40 mm ×3mm copper square is displayed in (a) with the vertical and horizontal bisections highlighted in white. The pixel intensity of the horizontal and vertical bisections is displayed as a function of pixel number in (b) along with a Gaussian fit and a closeness of fit R^2.

As the addition of noise is expected to distort the circular symmetry of the image,

the R^2 value is averaged across a total of six lines, one along both the horizontal and vertical bisection and then additional lines at a quarter and three quarters across the image. This is illustrated in Figure 5.24.

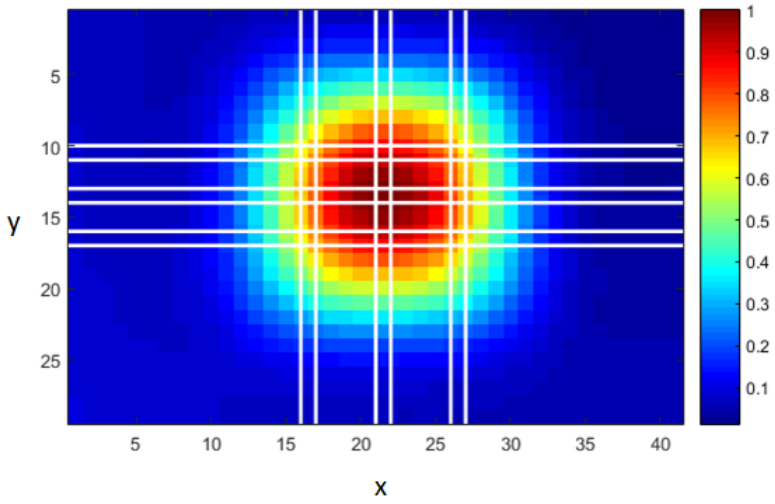

Figure 5.24: An example of a low noise image of a 40 mm $\times$40 $\times$ 3 mm copper square with the horizontal and vertical lines utilised to calculate an average fit parameter, R^2_{av}.

In each instance the fit parameter, R^2 was determined using a regression fit algorithm within MATLAB before being averaged across the six lines. To test the ability of this metric to indicate the presence of the expected distribution within an image, normally distributed noise was added to a test image in the same manner as was discussed in Section 5.1. Figure 5.25 displays the averaged fit parameter as a function of the variance of the added noise. The noise was added to a low noise image with an object in (blue) and without an object (black). Each image was visually examined and limits were defined at various values of R^2_{avg} depending upon how visible the object was perceived to be. Images obtained at each of these limits and at a lower value of R^2_{avg} = -0.2 are displayed in Figure 5.26. These figures right to left represent an example of where the object is clearly not present, when a shape begins to emerge at the centre of the image, when that image begins to resemble a circular feature, and finally when the feature

becomes distinct from the background. As it is difficult to specify a single threshold (or limit) above which the object can be classified as detected, a few possible values for this threshold are considered and displayed in Figure 5.26.

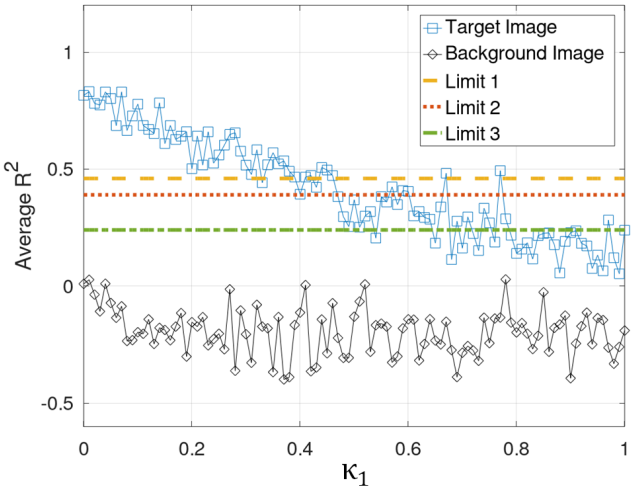

Figure 5.25: R^2_{avg} fit parameter as a function of added normally distributed noise variance. Images with an object in (blue) and without any object (black) where corrupted with additional noise of variance κ_1. A number of limits were defined at $R^2_{avg} = 0.46$ (limit 1), $R^2_{avg} = 0.39$ (limit 2) and $R^2_{avg} = 0.24$ (limit 3).

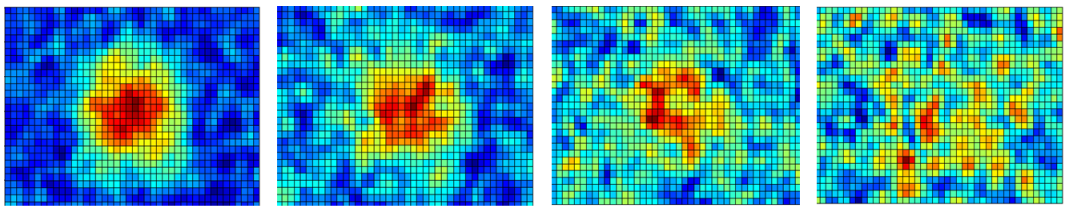

Figure 5.26: A low noise image of a 40 mm×40 mm ×3mm copper target corrupted noise of increasing variance. Images corresponding to R^2_{avg} values of 0.46, 0.39, 0.24 and -0.2 from left to right.

As previously, once the metric has been defined and tested on a set of simulated noisy images, the process can be applied to a set of experimentally obtained images. A number of different examples of images were tested, these included a frequency scan of a high conductivity copper object, a frequency scan of a lower conductivity hafnium object

and a frequency scan with no object, but with a strong background gradient. The values of R^2_{avg} in each of these instances are displayed in Figure 5.27 with a number of example images included as inserts. In the example of the copper target where the image noise is low, the R^2_{avg} values conform well with the simulated noise images. It is also possible to pick out a distorted image which occurs due to a phase roll over. Examination of the hafnium data demonstrates that the process and limits can still be applied to less ideal data; with image number 15 within Figure 5.27b reaching a value of R^2_{avg} above limit 2. In this instance, what can be considered a reasonable image may be adjusted depending upon the final application. Finally, consideration of the images without the target but with a strong background gradient, demonstrates that the process and limits can also be applied with no images falsely identified. It should be noted that whilst these limits can be applied in all three of these situations, these represent a small sub-set of the possible range of images. In each experiment any limits should be carefully considered to ensure they are appropriate for the data-set.

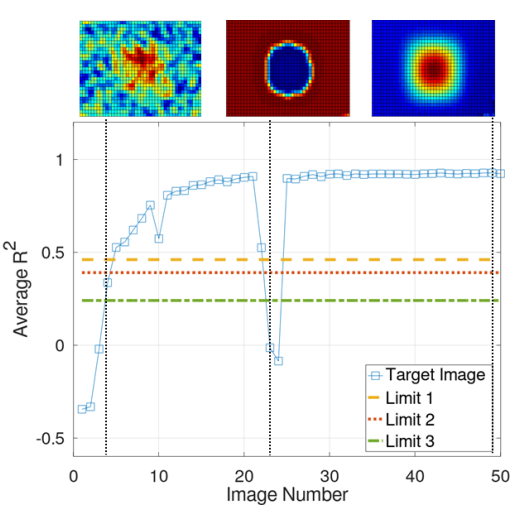

(a) Copper target

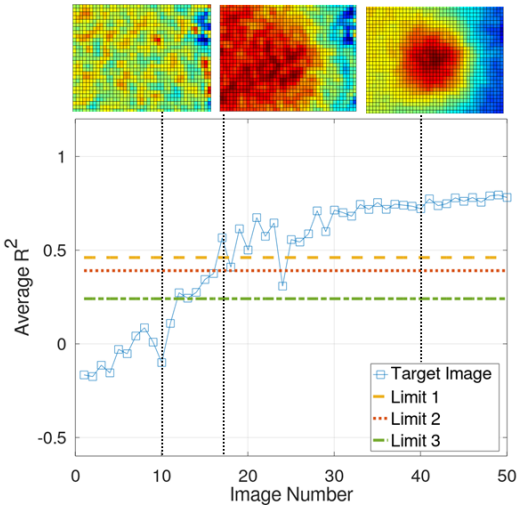

(b) Hf target

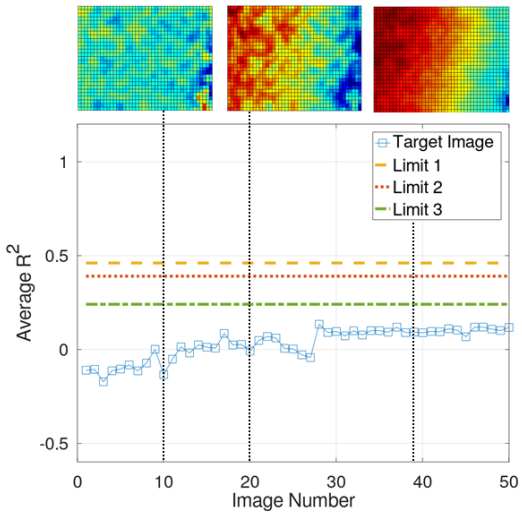

(c) No target

Figure 5.27: Averaged fit parameter R^2_{avg} as a function of image number (corresponding to a frequency range) for a set of images of a low noise copper target (a), less distinct hafnium target (b) and with no target present (c).

Chapter 6

Low Frequency ECI Imaging

Applications within Nuclear Threat Reduction (NTR) concern the detection of CBRN (chemical, biological, radiological and nuclear) threats across a number of application spaces including treaty verification, nuclear forensics and portal monitoring. Common to all these areas is the requirement to detect these materials in shielded configurations. Eddy Current Induction (ECI) utilises an excitation frequency to induce secondary fields within objects which are characteristic of their properties. The frequency of this excitation field dictates the penetration of the primary field, with a lower frequency required to reach greater depths.

To meet the requirement of shielded threats, a commercially available zero-field atomic magnetometer (AM) was investigated. This Chapter details the experimental arrangement of an imaging system constructed using a sensor (QZFM) manufactured by QuSpin [60]. A characterisation of the sensor and details on the construction of ECI images in magnitude and phase are given. This work was extended to explore the relationship between phase change as a function of target conductivity. The conductivity range chosen encompassed common metals such as copper (59 MS/m) and aluminium (37 MS/m), down to hafnium (3 MS/m) and bismuth (0.7 MS/m) chosen as surrogates for uranium and plutonium, respectively. These data are used to inform a conductivity-

resolution measure for the system. Finally, an exploration is made of two targets, one copper and one uranium surrogate, behind various thick shielding materials (1-100 mm). The shielding materials that were chosen present a specific challenge from the perspective of magnetic induction (high conductivity/ferrous) and from a radiological approach (high density).

6.1 Experimental Configuration

The experimental set-up utilised to obtain low frequency ECI images of targets with the QuSpin ZFAM is displayed in Figure 6.1. The arrangement consisted of a single QuSpin sensor, a magnetically shielded enclosure, two linear motion stages and an excitation coil. The QuSpin sensor (QZFM) was aligned on-axis with a ferrite cored excitation coil (MSCH895-681KU) of radius = 3 mm, length = 7.5 mm, inductance = 681μH, with 142 turns. The sensor itself was housed inside a three layer mu-metal enclosure which reduced the ambient field down to the nT range as measured using a fluxgate (Fluxmaster) magnetometer. A set of coils internal to the QuSpin sensor cancelled the residual field and were automated via the QuSpin controller. Cancellation of the residual field was performed with both stages positioned centrally over the opening of the enclosure to ensure minimal disruption from zero-field by movement across the sensor axis. The excitation frequency required to induce eddy currents within the target was supplied using a lock-in amplifier (Ametek 7230); this was also utilised to demodulate the analogue output of the sensor at the same frequency to obtain a measurement of magnitude (voltage) and phase (degrees).

Three stand-off parameters (z_1, z_2, z_3) were specified to describe the orientation of the sensor, coil and target within the system. The distance between the sensor and the edge of the magnetically shielded enclosure is given as z_1, whilst z_2 was the distance between the enclosure and the target, and finally z_3 for the separation of the target and

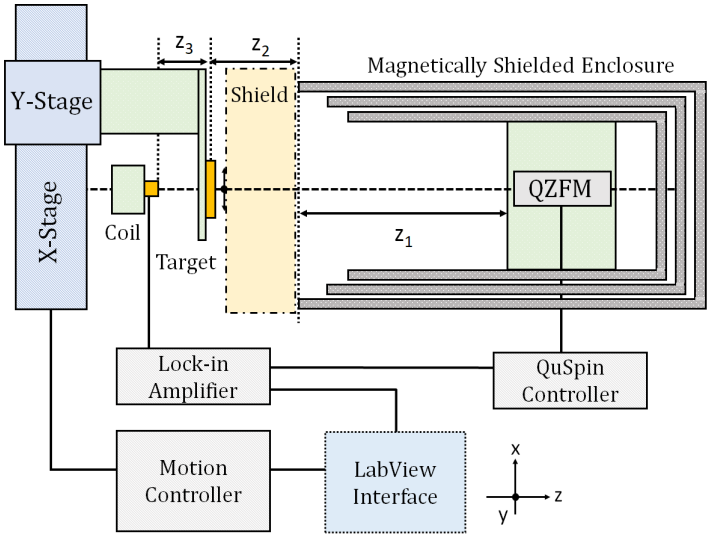

Figure 6.1: Illustration of the experimental set-up used to obtain images of a conductive target in a shielded configuration. The target object was attached to two linear stages using a 3D printed spacer and arm. The linear stages scanned the target object in the x-y plane. When shielding was utilised, this was placed between the target and the sensor as highlighted by the yellow region. The sensor was housed in a three-layer mu-metal enclosure.

excitation coil.

The sensor and coil remained static whilst the target was raster scanned using two orthogonal, linear stages (Newport) in the x-y plane. The motion of the stages was controlled through a motion controller (Newport) which was interfaced to LabView control software [108] to allow the phase and magnitude to be referenced to x and y coordinates. Phase and magnitude values were typically obtained across a range of excitation frequencies (1-300 Hz) encompassing the bandwidth of the sensor. Due to the low frequencies, the measurement time at each frequency value was relatively long (100 ms). In addition, a settling time of 2 seconds was included between each movement of the stage to allow any magnetic noise from the motors to fade before the measurement was triggered. In the instance where 50 frequencies were captured, measurements at each pixel took approximately 7 seconds. A 60×60 mm image with a scan step of 2 mm took approximately 3.5 hours to complete. As a number of the images were axially symmetric, half or quarter

images were occasionally taken to reduce scan times. Unless specified, all images were obtained without background subtraction. All measurements were also obtained with the magnetically shielded enclosure open at one end unless otherwise specified.

6.2 Sensor Characteristics

Before obtaining images, the output characteristics of the QZFM were evaluated separate from the lock-in detection acquisition. Included in these were the noise spectra of the sensor within the mu-metal enclosure. In addition, the output of the sensor was examined across the voltage input and frequency of the excitation coil. These measurements were performed within the configuration discussed in Section 6.1 but without the use of the stages and with no target or shielding.

6.2.1 Sensor Noise Spectra

The analogue output of the QuSpin sensor was first measured in the previously discussed configuration but with no externally applied field. In this environment, the power spectral density (PSD) function was calculated using the magnetic field conversion factor specified for the QZFM of 0.9 V/nT. This is displayed in Figure 6.2 with and without the end caps of the mu-metal enclosure in place.

Examination of these data allow some key features of the QZFM sensor to be identified. As expected there is a large spike in the noise spectra at the mains power frequency of 50 Hz, however there are also prominent features at both 150 Hz and 923 Hz. The first of these corresponds to a harmonic of the mains power but also represents the quoted band-width of the sensor above which the response rolls off gradually. The feature at 923 Hz corresponds to the modulation field applied within the sensor. This is applied along the sensing direction and is the frequency at which the output is demodulated to reduce sensor noise. Other features include the odd harmonics of 50 Hz but also a sec-

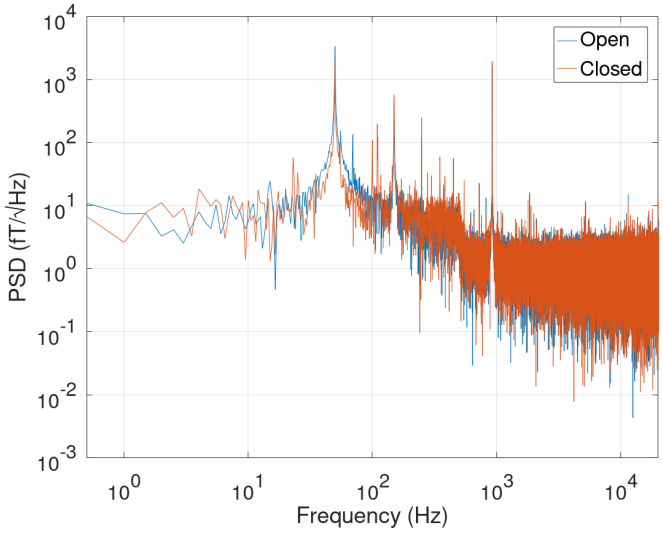

Figure 6.2: Power spectral density function obtained from the output of the QuSpin (QZFM) sensor. Data is obtained without any applied external field and with (blue) and without (red) the end caps of the mu-metal enclosure in place.

ond roll off in response at 500 Hz; this corresponds to a digital filter within the QuSpin controller designed to remove any residual response above this value.

A comparison between the data obtained with and without the end caps of the mu-metal enclosure in place demonstrate that, in this current configuration where the sensor is $z_1 = 140\,\text{mm}$ from the edge of the enclosure, the spectra are comparable with similar levels of noise. This is not unexpected as the enclosure shields ambient DC fields by deflecting around the cylindrical volume, rather than the flat ends; in each case the noise level is on the fT scale.

6.2.2 Sensor Response

The excitation coil used across all experimental work was a ferrite cored inductor coil aligned along the z-axis with the sensor, outside the enclosure. The QZFM response to the field generated by this coil can be characterised as a function of the input voltage and frequency supplied by the lock-in amplifier. These data are displayed in Figure 6.3.

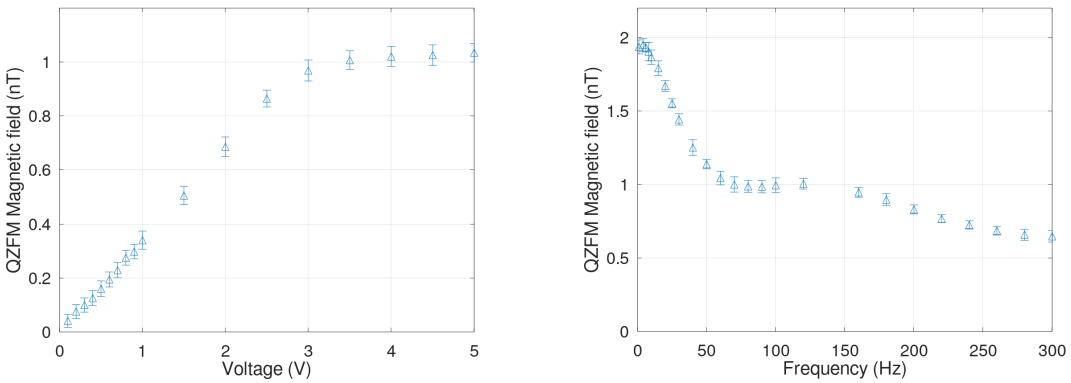

(a) Voltage at 150 Hz (b) Frequency at 3 V

Figure 6.3: Magnetic field measured as a function of voltage (left) and frequency (right) supplied to the excitation coil. Data obtained at a sensor to coil distance of 220 mm.

The sensor output as a function of supply voltage, as displayed in Figure 6.3a, is linear between voltages of 0.1 V and 3 V as would be expected, however saturates at values above this range. This effect is observed across other magnetometers and is a limitation in the output current of the voltage supply. The maximal field experienced at the sensor is therefore approximately 1 nT, however this value is only accurate at the applied frequency of 150 Hz. A frequency of 150 Hz corresponds to a noise spike in the above spectra (Figure 6.2), however, the data is of sufficient quality, indicating that magnetic measurements may be obtained at these values.

Examination of the sensor response as a function of frequency in Figure 6.3b demonstrates significant variation across the operated range of 300 Hz. These data may be a convolution of the sensor response and the change in inductance of the coil with increasing frequency. A coil inductance of 681μH will result in a minimal decrease in current over these frequencies. As a consequence, the distribution in Figure 6.3b is primarily attributable to the sensor which can be seen in the notable decrease above 150 Hz corresponding to the quoted sensor bandwidth [60].

6.3 Image Construction

ECI images of targets were constructed using a pair of orthogonal linear motorised stages. The stages raster scanned the target between the stationary excitation coil and the QZFM sensor as displayed in Figure 6.1. Each measurement at specific values of x and y position consisted of magnitude and phase data obtained by the demodulation of the analogue output across a range of input frequencies (1-300 Hz). These two data sets are displayed in Figure 6.4 for a central pixel with a copper target present (no background subtraction).

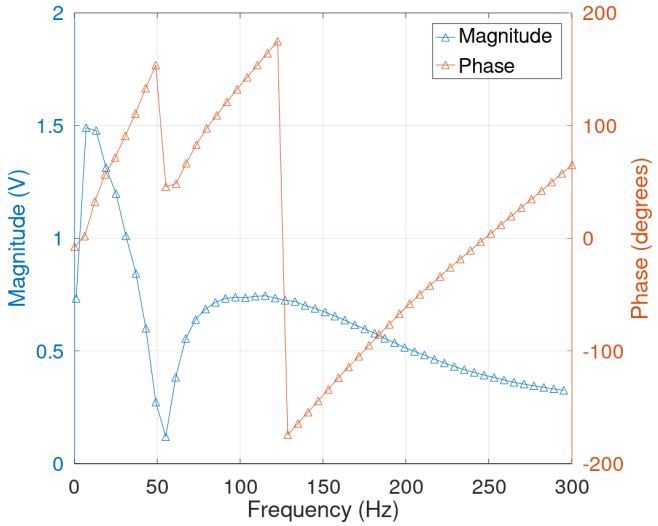

Figure 6.4: Magnitude (blue) and phase (red) as a function of frequency for a central pixel. The data were obtained at a stand-off distance of 235 mm and an excitation voltage of 5 V. In both magnitude and phase a feature can be observed at 50 Hz which is associated with mains noise disruption.

The expected change in magnitude and phase with the introduction of a conductive target is discussed in Chapter 2 and is specifically addressed by the phasor diagram in Figure 2.7b. In this description, the introduction of a highly conductive object will produce a secondary field to oppose the primary in proportion to its frequency. This effect is observed in Figure 6.4 with a reduction in the measured magnitude. The phase change

between the primary and the total measured field is determined by the combination of the real and imaginary components which produce an increasing phase with frequency.

The discussion in Chapter 2 defined the parameter $L = 2\pi\delta$ representative of a wavelength-type quantity of the induced eddy currents through a target. Turning points in the values of the magnitude and phase as a function of L were predicted. These were defined by equations 4.2 and 4.3. The behaviour of magnitude and phase in Figure 6.4 are consistent with these equations, which define expected magnitude and phase turning points at these frequencies for copper target thickness above 23 mm. However, it should be noted that these data are not background subtracted and that most of the change is due to environmental conductors rather than the copper target. These data also highlight the effects of noise, with the signal at 50 Hz significantly distorted by the mains power in both magnitude and phase. The mains power noise disruption is observed across all components of the experiment, it could be mitigated by longer integration times on the lock-in amplifier; however, this would result in slower frequency sweeps and therefore longer overall imaging times. In addition to the mains noise, a phase roll-over is observed, occurring at $\pm 180°$. This effect was previously discussed within Chapter 4.

The measurements of magnitude and phase are referenced against the position of the target to produce an image for each frequency. Example images of a $40 \times 40 \times 3$ mm square copper target at 300 Hz are displayed in Figures 6.5 and 6.6 along with the corresponding images obtained without the target to demonstrate the contrast.

6.4 Image Quality with Excitation Voltage and Frequency

In an unshielded configuration but with the magnetically shielded enclosure open, images of a $40 \times 40 \times 3$ mm copper target were obtained across a range of frequencies ($1 - 300$ Hz) and excitation voltages. These measurements were obtained with a total sensor

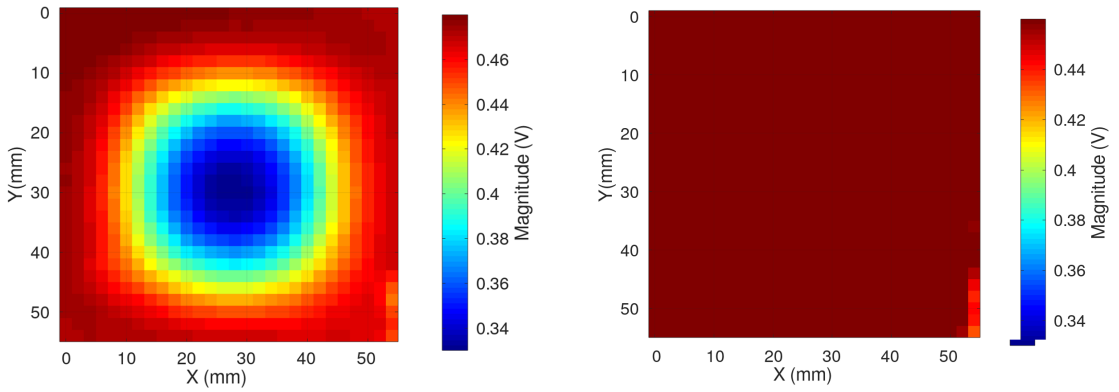

(a) Target (b) No Target

Figure 6.5: Magnitude image of a (a) $40 \times 40 \times 3$ mm copper square and a (b) background obtained at a stand-off distance of 230 mm, a frequency of 300 Hz and an excitation voltage of 5V. The image is raster scanned with steps of 2 mm.

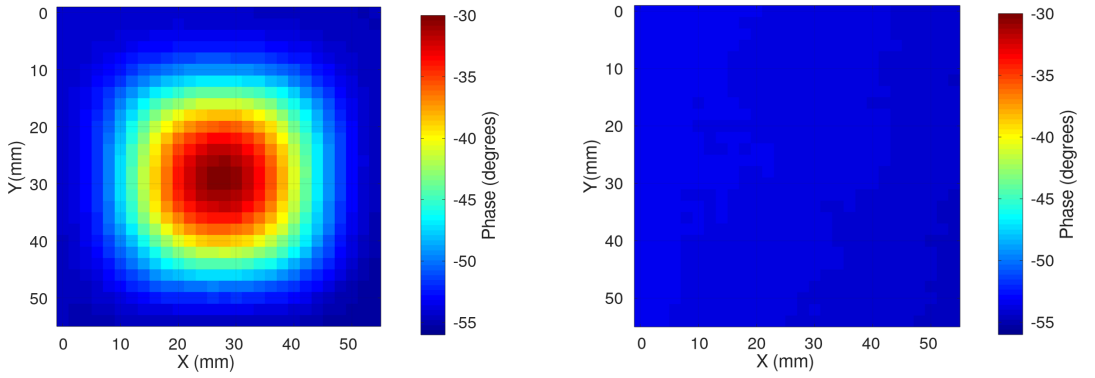

(a) Target (b) No Target

Figure 6.6: Phase image of a (a) $40 \times 40 \times 3$ mm copper square and a (b) background obtained at a stand-off distance of 230 mm, a frequency of 300 Hz and an excitation voltage of 5V. Image raster scanned with steps of 2 mm.

to coil distance of 235 mm. Each of the 900 images generated were analysed using the image processing techniques detailed within Chapter 5. An estimate of the background subtracted magnitude and phase was obtained using the K-means clustering algorithm which segmented the image into 6 groups based on their relative intensities. The average intensity of the pixels within each group was calculated before subtracting the highest

intensity region (R1) from the lowest (R6). Using these values, the change in magnitude and phase resulting from the target was determined as a function of both excitation frequency and voltage. Figure 6.7a considers these values first as a function of voltage. Both responses are as expected from both the discussion in Chapter 2 and the COMSOL modelling in Chapter 4. Here the magnitude data saturates with the current output of the lock-in amplifier which supplies the excitation voltage, as seen in Figure 6.3a.

In the frequency response displayed in Figure 6.7b the behaviour is as expected in distribution, with both increasing as a function of frequency. The magnitude change reduces at higher frequencies, potentially attributable to the attenuation by the magnetic enclosure as seen in the simulations in Section 4.5. The phase deviates as expected from the infinite case and, as simulated, has a distribution similar to, but which does not precisely fit a $\sqrt{w}$ relation. The values of phase are significantly larger (10 degrees) in the experimental data than in the COMSOL simulations conducted in Chapter 4. However, as discussed across Chapter 4, a background subtraction is problematic due to combined interactions between all conductive components, many of which were not included in simulations.

Both these data sets also include a number of measurements which do not fit the rest of the distribution. The method of obtaining measurements of magnitude and phase change gives a good approximation of these values when the image noise is low. However, there is no inherent knowledge of the target location, producing incorrect values when the target is less well resolved. Errors are also introduced during a phase roll-over, where the averaged data produces interpolated measurements, as seen in Figure 6.7b at approximately 130 Hz. To examine the voltage-frequency space in terms of image noise and object detectability, a number of image quality metrics as defined in Chapter 5 were applied to each set of images. The noise metric, RS-value, was defined to measure the standard deviation of a residual image obtained from a subtraction between the raw data and a highly smoothed version. This data is displayed across the voltage and frequency

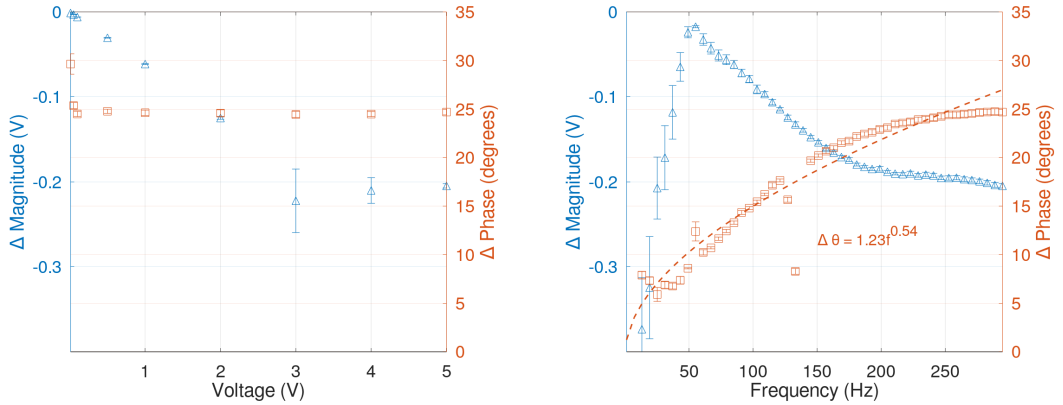

(a) Voltage, at 300 Hz (b) Frequency, at 3 V

Figure 6.7: Change in magnitude and phase in the presence of a $40 \times 40 \times 3$ mm copper square as measured using the QZFM sensor. Data obtained as a function of excitation voltage (left) and frequency (right). Error bars are constructed from 5 individual experiments.

ranges in Figures 6.8 and 6.9 for the magnitude and phase images respectively.

The RS metric is simply a measure of uniformity with no account of the target's presence, therefore this is combined with the R^2 metric, which describes the degree of fitting between a set of Gaussian distributions and slices of the images. This metric was also explored within Chapter 5 and a threshold of $R^2 = 0.46$ defined, data is omitted in these figures for images which fall below this threshold.

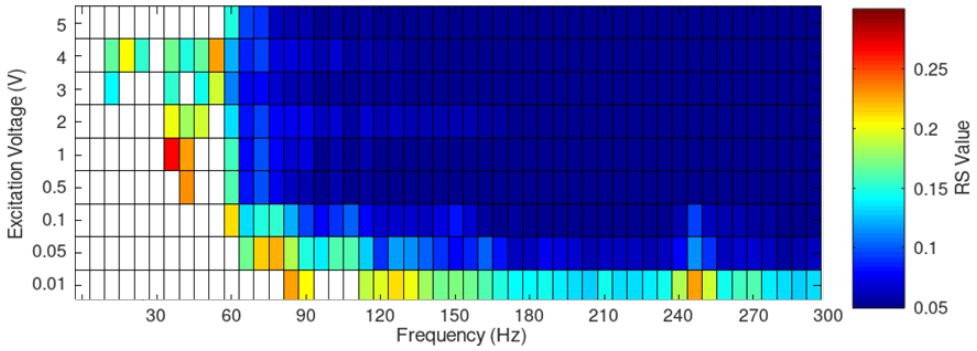

Figure 6.8: Noise metric (RS value) as a function of excitation voltage and frequency for magnitude images as determined using the no-reference filter method. Data is omitted if the image returned a $R^2 < 0.46$.

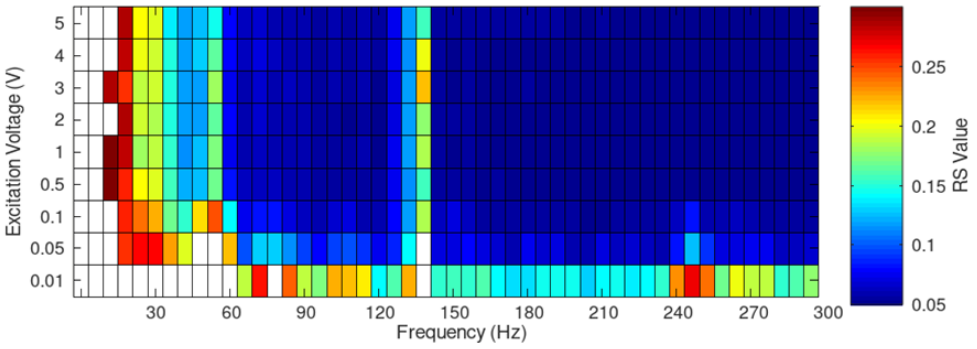

Figure 6.9: Noise metric (RS value) as a function of excitation voltage and frequency for phase images as determined using the no-reference filter method. Data is omitted if the image returned a $R^2 < 0.46$.

Many of the data points which lie outside the distributions described in Figure 6.7 fail to meet the $R^2 > 0.46$ threshold. Examination of these across voltage and frequency determine these are more prevalent at low values (of either voltage and frequency) where the eddy current response will be reduced. A notable feature between the two graphs is that a greater number of images met the object detection threshold when examined in phase rather than magnitude. This can be attributed to the invariability of phase with field strength, allowing phase to be better reconstructed as long as a field is detected. Measurements in phase therefore make images robust to unexpected changes in field strength; this is illustrated in a comparison of the images within Figures 6.5 and 6.6 where a distortion is present in the south-east corner in magnitude but not in phase. However, as can be observed from Figure 6.7b and 6.9, the phase data experience phase roll-overs which introduce more noise at those values, potentially from post-processing corrections. These observations are carried forward into subsequent measurements, where often only the phase images are utilised.

6.5 Target Conductivity

The discussion of the QZFM sensor for low frequency ECI imaging has focussed on a high conductivity copper target, however of particular interest to NTR applications is the detection of Special Nuclear Materials (SNM), including uranium and plutonium which are considerably less conductive (0.8-3 MS/m). To examine the system response to targets as a function of their conductivities, a series of $25 \times 25 \times 1$ mm targets were imaged at a total target to sensor distance of 176 mm. These images were obtained for targets with conductivities ranging from copper (59 MS/m) to bismuth (0.8 MS/m) at frequencies between 1-300 Hz. The resultant images were analysed as previously discussed, with the phase change extracted through the application of the K-means clustering algorithm that allows the measurement to be made without subtraction from a separate background image.

Unlike the previous measurements, a background normalisation was applied across the image to correct for the gradient created by the movement of the x-y stage. Movement of the stage resulted in a modification of the measured field, which was more notable due to the lower signal to noise (SNR) generated by the smaller, lower conductivity samples. To correct for the gradient whilst avoiding the need to perform a separate background subtraction, the first and last rows and columns of the images were sampled for a measure of the gradient in both the x and y directions. These data were averaged and fitted with second order polynomials which were applied across all rows and then columns to remove the sampled background gradient. An example of this processing is shown in Figure 6.10 which demonstrates the utility of adjusting the background gradient to better resolve the target. As a result of this correction, the object detection technique discussed in Chapter 5 can be better utilised to autonomously identify the presence of the target.

This correction was implemented after the image was smoothed but before it was

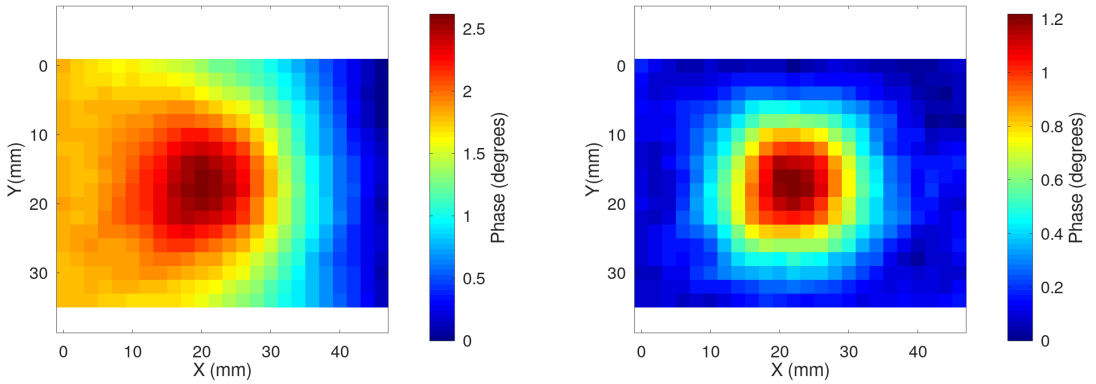

(a) No correction (b) Gradient correction

Figure 6.10: Image of a $25 \times 25 \times 1$ mm tin target obtained at a sensor to target distance of 176 mm at an excitation voltage of 2 V and a frequency of 290 Hz. Images are displayed without (a) and with (b) a background gradient correction.

analysed. The resulting phase change as a function of target conductivity and frequency is displayed in Figure 6.11. These data demonstrate that the greatest phase changes for each target conductivity is at maximal frequencies; with maximal change observed for the highest conductivity. This is despite any reduction in the measured field value at the sensor as seen in Figure 6.3b.

The phase change from the copper sample (6°) is smaller than previously observed (25°) as this sample is considerably smaller and thinner; resulting in a reduced interaction volume. The effect of target size on phase response was briefly shown in Chapter 4.

As previously, entries within Figure 6.11 were removed if the images produced had a value of $R^2 < 0.46$ that indicates the target is not easily distinguished. The increasing number of omitted entries highlight the difficulty of imaging the lowest conductivity targets, with no detection achieved of bismuth, the plutonium surrogate.

Across the complete range of target conductivities, the frequency is such that the ECI interaction is expected to be small. This can be observed from calculation of the standard depth, δ and L parameters. The highest conductivity target (copper, 59 MS/m) has δ values between 65 mm (1 Hz) and 4 mm (300 Hz); corresponding to $L = (411 - 23)$ mm.

This can be compared with the lowest conductivity sample (bismuth, 0.8 MS/m) with values of δ between 562 mm (1 Hz) and 32 mm (300 Hz); corresponding to values of $L = (3535 - 204)$ mm. The value of L indicates the thickness required for a complete period of the induced eddy current as discussed in Chapter 2. One period of L represents the significant portion of the interaction between the field and object. The minimal interaction between the field and the 1 mm thick targets in these measurements can be understood as representing only 0.04 of a period for copper and 0.005 for bismuth at 300 Hz.

A selection of the images obtained at 300 Hz are displayed in Figure 6.12; these include a high conductivity target, gold ($\sigma = 45$ MS/m) and SNM surrogates, hafnium and bismuth. It can be noted from these images, that whilst hafnium is detected, the image quality has degraded when compared with gold. Comparatively, bismuth is not resolved.

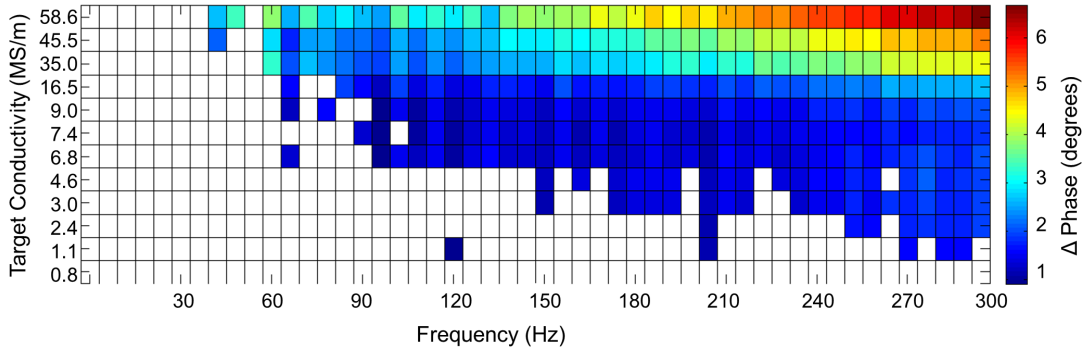

Figure 6.11: Average change in phase between the background (R1) and the highest intensity region (R6) of images obtained of a series of $25 \times 25 \times 1$ mm metallic targets with conductivities between 58 MS/m (copper) and 0.8 MS/m (bismuth). Images obtained at a target to sensor distance of 176 mm and an excitation voltage of 2 V. Entries are removed if the image analysis demonstrates a $R^2 < 0.46$.

In order to provide more comprehensive values for the phase response as a function of target conductivity, a series of high statistic measurements were obtained. These measurements did not involve the construction of complete images but instead consisted of repeated frequency sweeps at two separate pixel locations; one central to the target

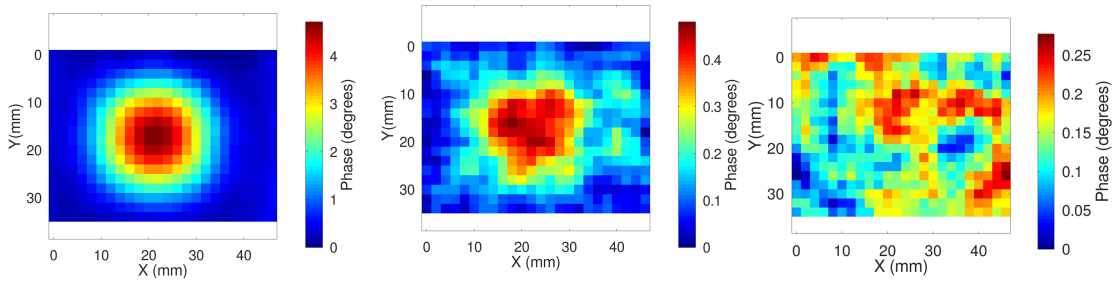

(a) Gold: 45.5 MS/m (b) Hafnium: 2.4 MS/m (c) Bismuth: 0.77 MS/m

Figure 6.12: Phase images obtained of a series of 25 × 25 × 1 mm metallic targets, specifically (a) gold (45.5 MS/m), (a) hafnium (2.4 MS/m) and (c) bismuth (0.77 MS/m). Images obtained at a target to sensor distance of 176 mm and an excitation voltage of 2 V.

and the other off-set to provide a background value. In total 300 frequency sweeps were performed for each target, at each location, across three experimental runs. The average of these data are displayed in Figure 6.13 at frequencies of 166 Hz (a mid-point but away from 150 Hz noise) and 300 Hz (maximal frequency). A maximal phase change of 6.5° is observed for copper (59 MS/m) decreasing to $< 1°$ for targets with conductivities lower than 10 MS/m.

Also displayed in this Figure is a baseline value (solid line) which represents the average phase change obtained without a target present and with the same two pixel subtraction as previously detailed. These data indicate that all targets with conductivities above 2.4 MS/m (titanium) are distinguishable from the baseline value. The values of the average phase change cross below zero due to the gradient across the imaging plane as displayed in Figure 6.10. This gradient was created by the movement of the stage arm as the target was raster scanned; this could be removed from the images but not from the two pixel measurements. These values would be altered with the selection of the background pixel.

Despite this behaviour, a conductivity resolution metric can be defined for the system. The resolution metric aims to quantify the smallest conductivity change which can be

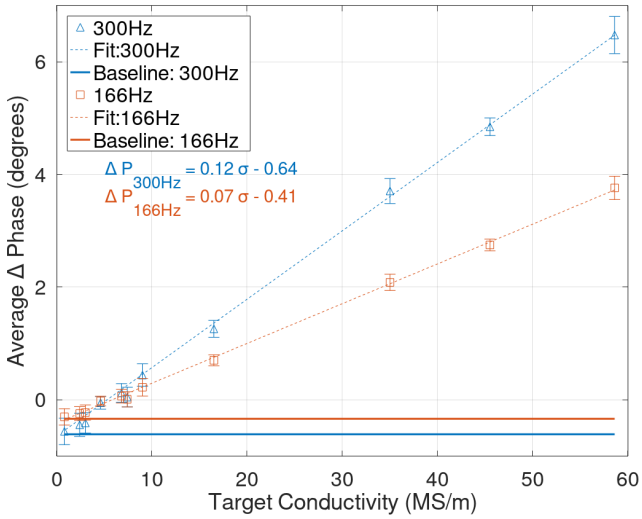

Figure 6.13: Change in phase between a central and background pixel as a function of target conductivity for 25 mm targets. Data is displayed for a frequency of 300 Hz (blue) and 166 Hz (red), linear fits are displayed for each data set (dashed) along with a baseline value (solid line) representing the base value obtained in a measurement without a target.

detected. The resolution is specified as the conductivity change required to produce a corresponding phase change greater than one standard deviation from the baseline value. One standard deviation from the baseline value can be calculated to be 0.23° at 300 Hz. This value is divided by the gradient of the distribution in Figure 6.13 (0.12°/MS/m) to produce a conductivity resolution value of 1.9 MS/m. Where 1.9 MS/m is defined as the smallest conductivity change that could be measured for these samples. Despite the issue of defining a background value, this resolution is broadly consistent with the targets measured, where tantalum (7.4 MS/m) can be distinguished from tin (9.0 MS/m) but not niobium (6.8 MS/m).

These results are specific for this particular target size (25 × 25 × 1 mm) which represents a relatively small target volume. This sized target challenges the limits of the sensor at these excitation field values (< 300 Hz) and sensor to target distance (176 mm). To highlight the dependency on sensor response with object dimensions, a sub-section of

conductivities were measured again with a larger target with dimensions of 50×50×1 mm. The same process as previous allows the phase change as a function of target conductivity to be plotted in Figure 6.14. Comparison with the data obtained for the 25 mm targets shows greater phase response and therefore a different conductivity resolution can be defined. Utilising the same definition as previous, one standard deviation of the baseline at 300 Hz is calculated as 0.16° and the gradient taken from Figure 6.14 to produce a conductivity resolution value of 0.3MS/m. This improved resolution can be observed in the differentiation of hafnium (2.9 MS/m) from titanium (2.3 MS/m).

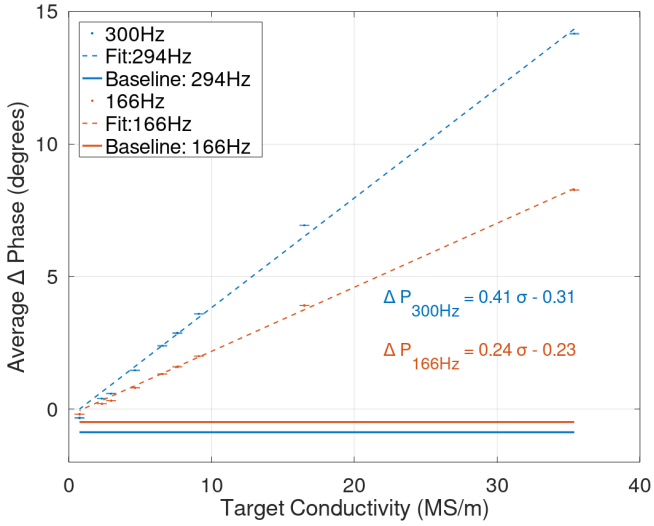

Figure 6.14: Change in phase between a central and background pixel as a function of target conductivity for 50 mm samples. Data is displayed for a frequency of 300 Hz (blue) and 166 Hz (red), linear fits are displayed for each data set (dashed) along with a baseline value (solid line) representing the base value obtained in a measurement without a target. The error bars are given as ±1 standard deviation.

This analysis concludes that no generic phase response can be constructed as the results will always be a convolution of a number of other parameters. These variables include object width, length and thickness, which must all be treated as independent parameters and cannot be represented by volume. This is seen in the COMSOL simulations discussed in Chapter 4 which explore the phase response of a finite object. As

a result of this, there is no unique phase response that would allow the identification of the presence of an object and therefore necessitates the bounding of the other variables to infer the target material. Whilst this is a disadvantage from the perspective of Detection Science (DS) applications (imaging of concealed objects) it may have utility in Nuclear Treaty Verification (NTV). The "uniqueness" of the measurement may allow a fingerprint of an object to be constructed and allow confirmation that an object has not be modified or tampered with without revealing specific materials or geometric detail.

6.6 Shielded Imaging

In the previous Sections, image quality analysis techniques were applied to examine the effect of excitation voltage and frequency on the noise and detectability of unshielded targets. This analysis concludes that a maximal frequency (and voltage) produces the lowest noise images with the greatest phase change. These results are only applicable in the unshielded or non-conductive shielding configurations described in Chapter 1 by scenarios I and III. In scenarios II and IV where the target is obscured by a conductive layer it is necessary to re-assess the excitation frequencies used.

It is expected from estimates of the standard depth (δ) that as the thickness of a conductive shield is increased, the attenuation of the magnetic field will increase as $e^{\frac{\delta}{z}}$. However, as indicated by Faraday's law of induction in equation 2.1 the strength of the secondary field is proportional and will increase as a function of the frequency of the excitation/primary field. The balance of these two effects is explored in this Section, where images of various targets were obtained behind shields of variable thickness, across a frequency range of $1 - 300\,\text{Hz}$. Images were obtained using the experimental configuration detailed in Section 6.1 with a total target to sensor distance of of 220 mm. The distance was increased from the previously discussed measurements to accommodate the thicker shielding materials (63 mm). An excitation voltage of 3 V was used; this corresponds to

a field strength of 136 nT at the object and measured as 0.6 nT at the sensor at 300 Hz.

This Section specifically covers the imaging of copper and hafnium targets; representative of a high conductivity object and a uranium surrogate respectively. These are examined behind an example of a high conductivity shield (aluminium), a ferrous shield (steel) and a high density shield (lead) as would be of interest in the detection of radiological or nuclear materials.

6.6.1 Aluminium Shielding

The aluminium shielding used was solid sections of aluminium, 300×300 mm with thickness values between 2 mm and 63 mm. At a frequency of 300 Hz, this constitutes a significant interaction with the excitation field, with values of $L = 30$ mm representing a complete period of the induced eddy current.

The image analysis processes described in the preceding Sections are again used to extract a measure of phase change, with the image quality metrics, RS and R^2 applied to examine degradation. The copper target had dimensions of $40 \times 40 \times 3$ mm whilst the SNM surrogate, hafnium, had dimensions of $50 \times 50 \times 1$ mm. In each instance the same geometric and excitation parameters were maintained. Full images were obtained for each combination of target and shield to inform the values of RS and R^2. However, a majority of the data were obtained from the two pixel measurement to obtain better statistics.

High Conductive Target

The inspection of a high conductive target behind high conductive shielding addresses scenario II. These targets are unlikely to be nuclear materials (classified as medium), but may be other illicit objects of interest in portal scanning application or items which can be assessed to corroborate a declaration within NTV. The phase change as a function of shielding thickness and frequency is displayed in Figure 6.15, as previously, entries are

excluded if the image quality metric $R^2 < 0.46$.

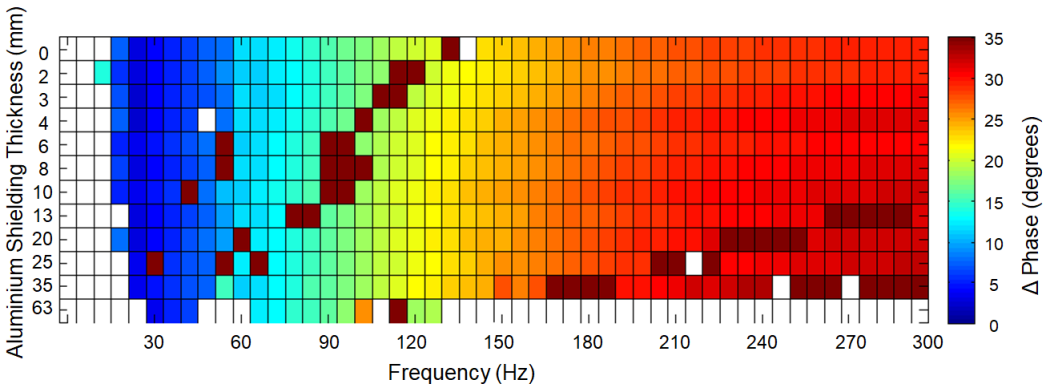

Figure 6.15: Average change in phase between central region (R6) and background region (R1) as a function of excitation frequency and aluminium shielding thickness across 300 measurements. Images obtained at an excitation voltage (3 V) of a copper object $30 \times 30 \times 3$ mm at a stand-off distance from sensor to target of 220 mm. Shielding materials had consistent dimensions of 300×300 mm.

Using the image quality analysis metrics, the data demonstrate that the copper target can be distinguished within each image behind aluminium shielding up to and including 63 mm thick. This value is the thickest to the author's knowledge within ECI security applications, with other induction magnetometers achieving double sided values of 20 mm [35] and AM technologies focussing on shields up to 3 mm [38] thick. Images of the copper target behind the 63 mm shield are displayed in Figure 6.16. An aluminium shielding thickness of 63 mm was the maximum value the copper target was imaged behind and was also the maximum thickness tested. Images with acceptable R^2 values are obtained at frequencies as low as 31 Hz up to 127 Hz. Above this frequency the images degrade in quality as the magnetic field fails to sufficiently penetrate the shield. As a result of this attenuation, the lock-in amplifier cannot demodulate the signal, causing large random changes in the phase.

As the data is averaged across 300 measurements, the shift in frequency of the phase roll overs creates a number of entries (dark red) within Figure 6.15 which should be excluded. However, as the removal of entries is based upon the original images rather

than the two pixel measurements, these entries were not excluded.

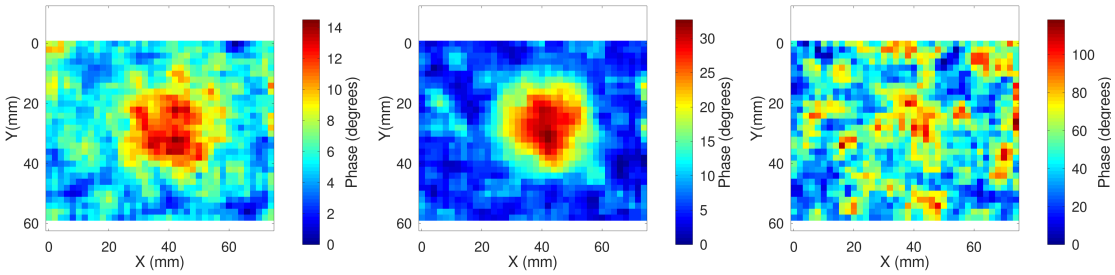

(a) 31 Hz (b) 121 Hz (c) 145 Hz

Figure 6.16: Selected images of a $40 \times 40 \times 3$ mm copper target obtained behind a $300 \times 300 \times 63$ mm aluminium shield. Two images were obtained at frequencies in which the $R^2 > 0.46$ condition was met (31 Hz, 121 Hz) and the other where it was not (145 Hz).

A closer examination of the phase as a function of shielding thickness and frequency are considered separately in Figure 6.17. To plot these data as a function of shielding thickness, a quantity, the effective shielding, is specified which accounts for variations in the conductivity of the different shields. The effective shielding value is defined as the ratio of the shield thickness and its standard depth value at a particular frequency. Whilst the phase response is largely flat at a particular frequency, there is variation outside of the error margins defined. This effect was considered in the COMSOL simulations within Chapter 4, with turning points identified in the magnitude and phase as a function of material thickness. A subtracted measurement such as those seen in Figure 6.17, identified a phase turning point at a thickness value of 6 mm (300 Hz) which corresponds to an effective thickness of 1.3. This roughly corresponds to the small peak feature in the experimental data obtained at 300 Hz. Whilst these data loosely resemble the simulated equivalent, there is variation, specifically at an effective shielding of 8.4 ($\mathbb{T} = 35$ mm). This difference may be attributed to measurement noise.

Whilst the phase response is relatively uniform across the shielding thickness values, significant variation is observed between shielding thickness values as a function of frequency as seen in Figure 6.17b. At low frequency values (< 100 Hz) the response from

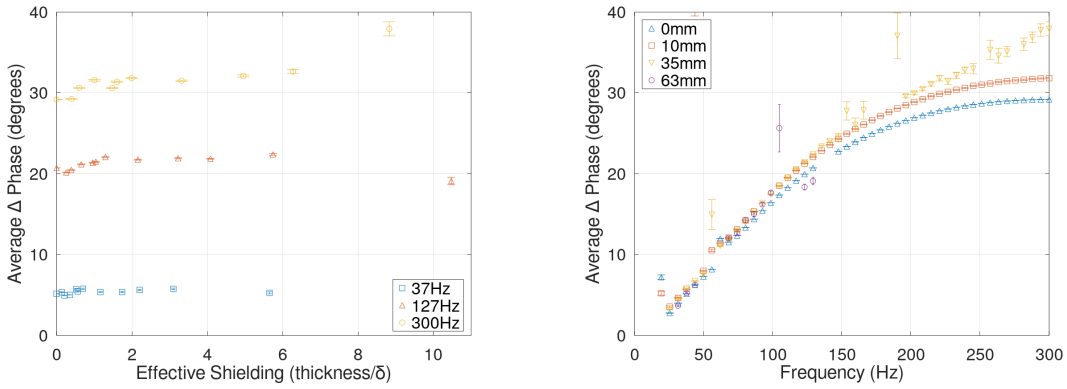

(a) Thickness (b) Frequency

Figure 6.17: Average change in phase from a $40 \times 40 \times 3$ mm copper target behind aluminium shielding. Data obtained across 300 frequency sweeps. Subtraction is obtained with the shield in place but with the target centred on the coil/sensor and offset from the edge by 65 mm.

the object is very similar across multiple thickness' however as the frequency increases these begin to deviate as would be expected from a greater interaction. In the instance where both the target and shield are unknown, it is difficult to extract the target conductivity from the shield conductivity and thickness, however, in the instance that some of these parameters are known, such as in NTV, a frequency sweep could be used to determine shielding thickness.

Due to the high conductivity of the aluminium, an improved image can be found at lower frequencies where the standard depth is larger, as observed in Figure 6.15. This can be further expressed by examining the SNR, balancing the greater phase change at higher frequencies, with the increased phase variation observed across the 300 measurements. These data are plotted in Figure 6.18. From the value of phase alone, the impact of the thinner shields seems negligible, however, an immediate decrease in the SNR can be observed. The SNR continues to decrease with increasing thickness and is particularly notable around 150 Hz. This frequency is identified in the first Section of this Chapter to have a significant background component. Utilising this metric, optimal imaging

frequencies can be defined, however, this only becomes necessary at thickness values above 10 mm. For the thickest shielding of 63 mm, the optimal frequency range is found to be between 60-130 Hz.

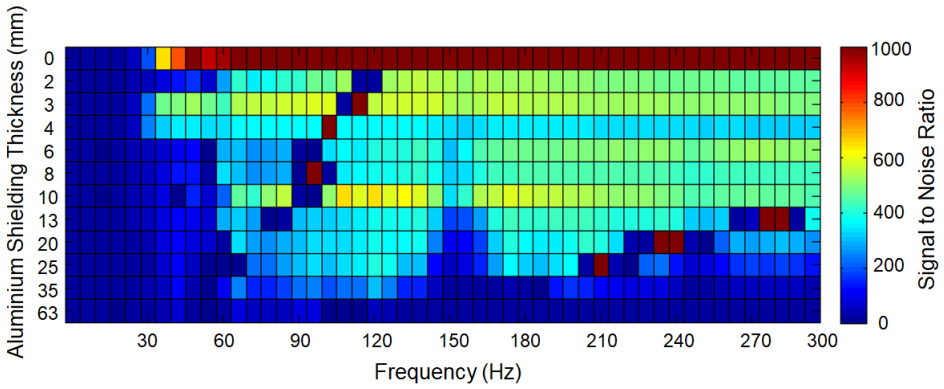

Figure 6.18: Signal to noise ratio as a function of excitation frequency and aluminium shielding thickness. Data obtained from single pixel measurements of a copper disk at a stand off-distance of 220 mm and with an excitation voltage of 3 V. The signal is defined in the phase change between a central pixel and background pixel, whilst the noise is the standard error across 300 repeated measurements.

SNM Surrogate

The copper target behind the aluminium meets the criteria for scenario II which represents only a sub-set of NTR applications. To explore scenario IV, which can be argued as the most challenging, the copper was replaced with a hafnium target. As mentioned above, the hafnium was used as a conductivity surrogate for SNM, having similar conductivity values (3 MS/m) as un-alloyed uranium. The same experimental parameters as previous were used along with the same data processing. Figure 6.19 displays the averaged phase change over 300 single pixel measurements with the entries removed as previous. Representative of the smaller conductivity of the hafnium sample, the phase change is much smaller than observed with the copper target and as such fewer images exceed the R^2 threshold. This restricts imaging of this target to frequencies above 60 Hz, and to aluminium shielding thickness values 35 mm and below. A selection of images of

the hafnium behind 35 mm of aluminium are shown in Figure 6.20 along with an image which falls below the IQA threshold for comparison.

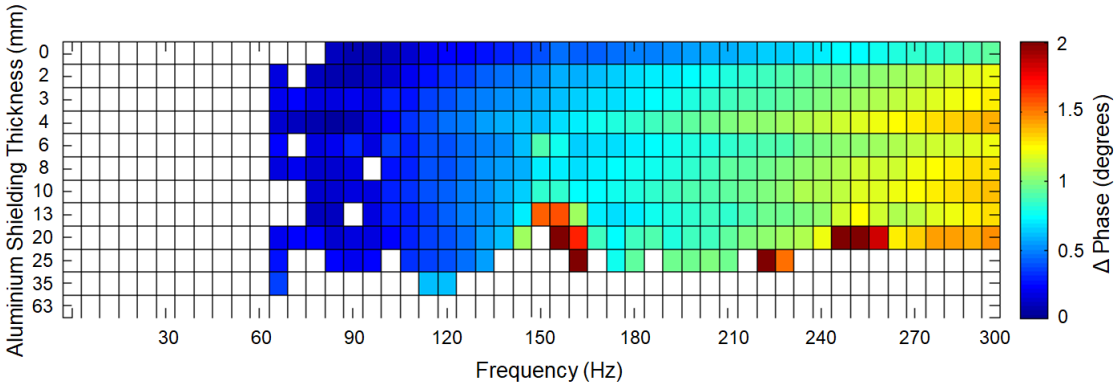

Figure 6.19: Average change in phase between central region (R6) and background region (R1) as a function of excitation frequency and aluminium shielding thickness across 300 measurements. Images obtained at an excitation voltage (3 V) of a hafnium object $50 \times 50 \times 1$ mm at a stand-off distance from sensor to target of 220 mm. Shielding materials had consistent dimensions of 300×300 mm.

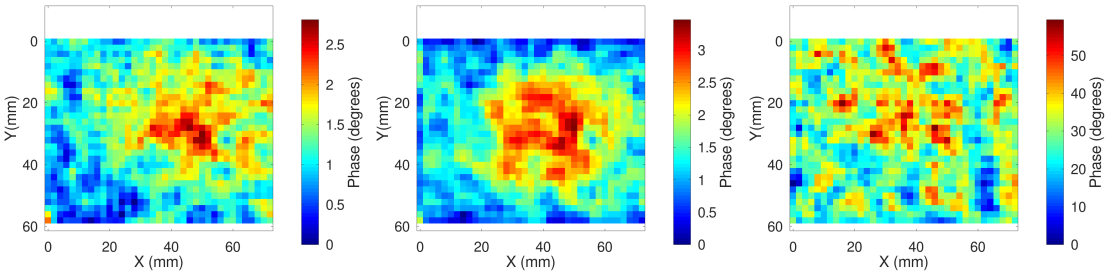

(a) 67 Hz (b) 121 Hz (c) 253 Hz

Figure 6.20: Selected images of a $50 \times 50 \times 1$ mm copper target obtained behind a $300 \times 300 \times 35$ mm aluminium shield. Two images were obtained at frequencies in which the $R^2 > 0.46$ condition was met (97 Hz, 121 Hz) and the other where it was not (253 Hz).

The phase change as a function of shielding thickness is also seen to follow the type of distribution described within the COMSOL simulations (Figure 4.13), this is again expressed as an effective shielding to normalise conductivity variation in the shielding materials as displayed in Figure 6.21a. A peak in the phase change is observed at the same value for the hafnium as the copper target, the location of this peak in the simula-

tions is similar for both copper and uranium with values of 7 mm and 9 mm respectively. These values fall between shielding thickness available in these experiments (6 mm and 8 mm). However the similarity between the copper and hafnium data sets could also suggest another property of the shield which has not been accounted for. If these data are valid, then this distribution could be used to provide information about the shield which is independent of the target (assuming the target is comparatively small). Properties of the target could then extracted from the value of the phase. These properties may also be extracted from the frequency distribution, which in this instance is much more linear than observed for the high conductivity target as displayed in Figure 6.21b.

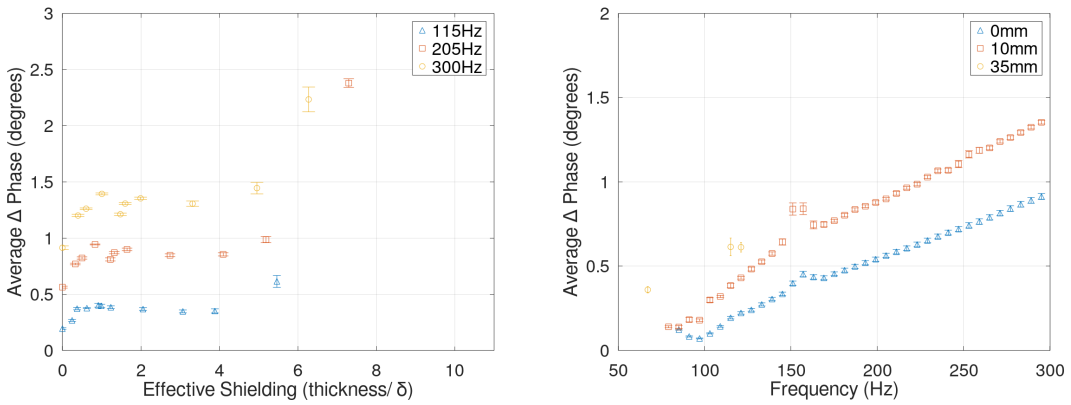

(a) Thickness (b) Frequency

Figure 6.21: Average change in phase from a $50 \times 50 \times 1$ mm hafnium target behind aluminium shielding. Data obtained across 300 frequency sweeps of a pixel central to the target and a pixel covering on the shield.

6.6.2 Steel Shielding

The target obscured by the aluminium shielding represents scenarios II and IV, as discussed in Chapter 1, which specify a high conductive shield defined for values of $\sigma > 10$ MS/m. Steel often has a conductivity lower than 10 MS/m which would be more representative of scenarios I and III. This is an incomplete picture due to the non-unity

magnetic permeability of steel which, when compared with aluminium, has a smaller standard depth for the same frequency. This makes steel more applicable to scenarios II and IV. Within this Section the phase response of the copper and hafnium targets are explored again but for changing steel shielding thickness between 0.9 mm and 12 mm.

High Conductive Target

The phase change as a function of steel shielding thickness and frequency is displayed in Figure 6.22. This graph is again utilised to illustrate the frequencies and shielding thickness over which images of the copper target can be successfully obtained as determined using the IQA metrics. These data demonstrate that the target is discernible behind the maximum thickness of 12 mm and across all frequencies above 20 Hz. The image quality is also maintained, with the shape not significantly distorted at 12 mm as can be seen in Figure 6.23.

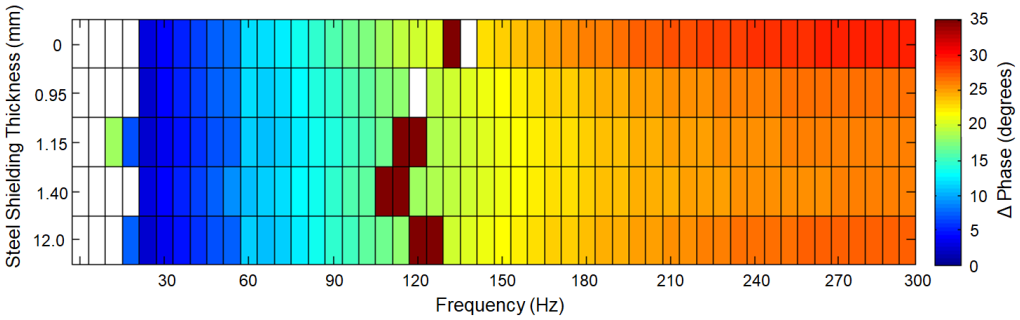

Figure 6.22: Change in phase as measured from a $40 \times 40 \times 3$ mm copper target as a function of excitation frequency and steel shielding thickness. Data obtained across 300 measurements of a background pixel and a pixel central to the object.

Unlike the copper target behind the aluminium shielding, the introduction of the steel shielding has produced a decrease in the observed phase change at a thickness of 12 mm; this is illustrated in Figure 6.24a. These data are more consistent with the simulations in Section 4, which showed a decrease in the phase response when subtracted from the shielding. As the phase is observed at an inspection point set back from the edge of the

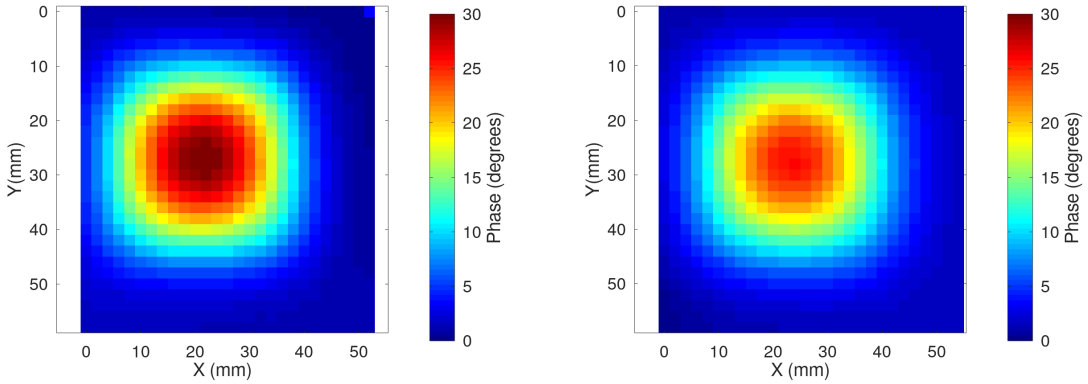

(a) Unshielded (b) 12 mm Steel

Figure 6.23: An images of a $40 \times 40 \times 3$ mm copper target obtained without shielding (left) and behind a $300 \times 300 \times 12$ mm steel shield (right). Two images were obtained at 300 Hz.

shielding and target, the position of this point can influence whether an increasing or decreasing phase is observed with shielding thickness. As previously discussed the phase undergoes a turning point which will depend upon the conductivity and permeability of the material and the frequency of the excitation field. For steel shielding with a copper target this is predicted to occur at a shielding thickness of approximately 7 mm causing the increase in phase at low thickness values and decrease in phase at thickness of 12 mm. The frequency distribution displayed in Figure 6.24b follows the measurements in the thickness, indicating that if the target properties are known, information could be extracted on the shield or vice versa.

SNM Surrogates

As was observed with the copper target, the shielding effect of the steel also has minimal effect on the ability of the system to image the hafnium target as seen in Figure 6.25 which displays minimal change from the no-shielding case. The image quality again shows no significant reduction even at the thickest shielding value of 12 mm, and is much more minimal than the change due to an aluminium shield of a similar thickness.

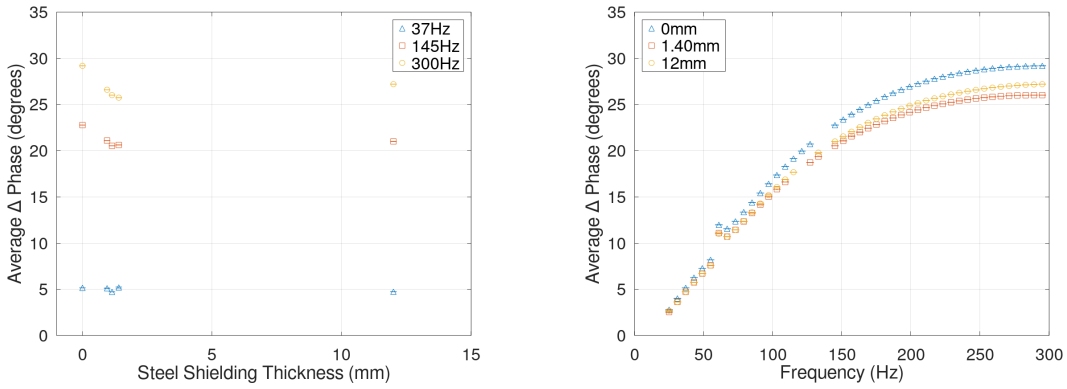

(a) Thickness (b) Frequency

Figure 6.24: Average change in phase from a $40 \times 40 \times 3$ mm copper target behind steel shielding. Data obtained across 300 frequency sweeps of a pixel central to the target and a pixel covering on the shield.

This can be seen in Figure 6.26 which displays images of the hafnium target without a shield in comparison with 12 mm of steel and 13 mm of aluminium. Due to the minimal shielding from the steel, no frequency optimisation is required within the operational frequency range of the sensor.

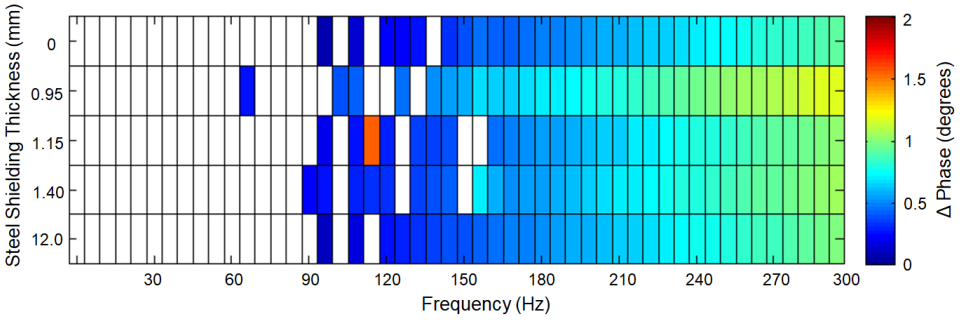

Figure 6.25: Change in phase as measured from a $50 \times 50 \times 1$ mm hafnium target as a function of excitation frequency and steel shielding thickness. Data obtained across 300 measurements of a background pixel and a pixel central to the object.

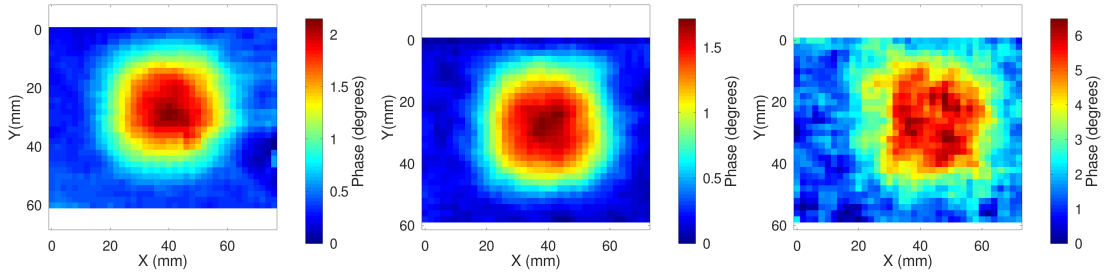

(a) No Shield (b) 12 mm Steel (c) 13 mm Aluminium

Figure 6.26: Selected images of a $50 \times 50 \times 1$ mm hafnium target obtained behind a $300 \times 300 \times 35$ mm aluminium shield. Two images were obtained at frequencies in which the $R^2 > 0.46$ condition was met (97 Hz, 121 Hz) and the other where it was not (253 Hz).

6.6.3 Lead Shielding

Whilst the aluminium and steel shielding are considered from the perspective of scenarios II and IV, lead is representative of scenarios I and III, with both a low conductivity (5 MS/m) and a unity value of magnetic permeability. As such, lead poses a comparatively small challenge within ECI imaging. The interest within NTR application comes from the ability to image SNM behind high density shielding which could be used to mask conventional radiological signatures. The shielding examined here was lead with a conductivity of 5 MS/m, the shields were constructed from individual $100 \times 100 \times 50$ mm blocks arranged in patterns of 4×1 to create a $200 \times 200 \times 50$ mm shield or 4×2 to create an $200 \times 200 \times 100$ mm shield. Each block had a chamfered edge to interlock with adjacent blocks. The coil was aligned with the centre of each shield.

The target examined in this instance was hafnium as it most closely represents the material of interest. To allow for the thicker shielding, the separation distance between the sensor and the coil was increased to 320 mm. Figure 6.27 displays the phase change as previously calculated applying the same image processing and quality threshold. These data and the corresponding images shown in Figure 6.28, demonstrate that the system can image the uranium surrogate through up to 100 mm of lead. The lead itself has a minimal impact on both the phase change measured and the image quality. A

comparison between these data and those taken with the hafnium imaged behind the other shielding, highlight that the increased separation between the sensor and coil has a greater negative impact than the lead. It is necessary that these data be considered in the context of the shield construction. Unlike previous experiments, the lead shielding is not single continuous plate. This results in a smaller shielding effect due to a reduction of the eddy currents by discontinuity in the conductivity of the block joins. This effect was also observed in other scenarios where the shielding was constructed from discrete components. Unlike aluminium or steel, lead shielding is commonly constructed from individual components due to its weight.

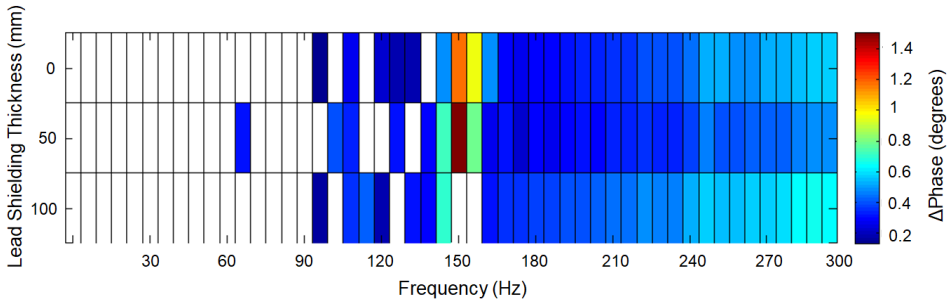

Figure 6.27: Change in phase as measured from a $50 \times 50 \times 1$ mm hafnium, target as a function of excitation frequency and lead shielding thickness. Data obtained across 300 measurements of a background pixel and a pixel central to the object. Data entries are removed when the corresponding image falls below the image quality threshold of $R^2 < 0.46$.

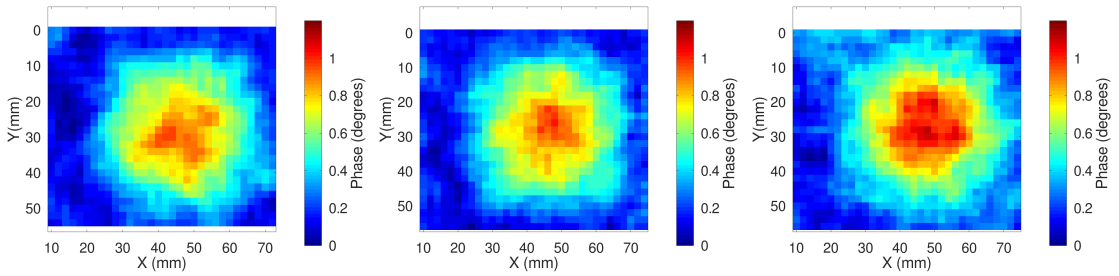

(a) No Shield (b) 50 mm Lead (c) 100 mm Lead

Figure 6.28: Selected images of a $50 \times 50 \times 1$ mm hafnium target obtained without shielding, and behind lead shield of thickness 50 mm and 100 mm.

6.7 Coil Array Imaging

The process of imaging targets using a raster scan such as described in Section 6.1 is time consuming and not practical for many of the NTR applications. This is particularly relevant for any portal scanning applications where a deployed system will be required to meet certain through-put targets.

In an effort to briefly explore a potential future system which can decrease imaging times, the excitation coil was replaced with an array of coils. The coil array consisted of 70 individual inductors of the same type as used to apply the excitation field in the previous experiments. These were arranged in a 10×7 grid, with centre to centre spacings of 10 mm. Maintaining the same configuration as discussed in Section 6.5, the $40 \times 40 \times 3$ mm copper target was imaged as illustrated in Figure 6.29 [109].

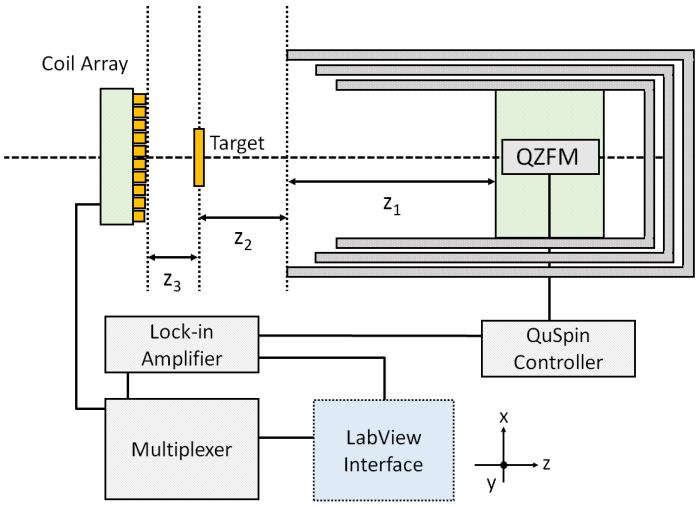

Figure 6.29: Illustration of the experimental set-up used to obtain images of a conductive target. All components in the set-up are static, with the field scanned across the imaging plane by sequentially exciting coils within a 10×7 mm array.

Images were obtained in two modes, one in which the coils were excited sequentially to create each pixel. The second mode excited the coils individually but also in adjacent pairs, to emulate a second set of coils between the actual coil spacings. Images of the copper target obtained in each of these modes is shown in Figure 6.30. Present in each

image is an artefact resulting from a defective excitation coil in the array; this can be observed in Figure 6.30 (a), in column number 4, row 4.

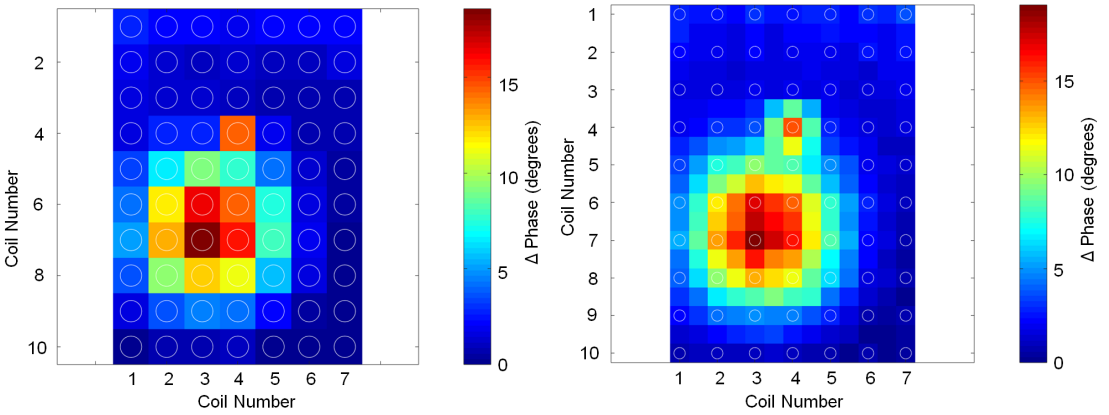

(a) Single Coil Excitation

(b) Dual Coil Excitation

Figure 6.30: Images obtained of a 40×40 mm copper target using an array of excitation coils rather than raster scanning. Images were constructed by sequential excitation of each coil individually (left) and in pairs (right).

A visual inspection of these images suggest that a greater amount of detail can be observed in the second mode, however a more in-depth study would be required to assess if this corresponds to an improvement in resolution, rather than just an interpolation between coils. If a greater resolution can be achieved, then more complex excitation patterns may allow this to be improved further. The importance of resolution is application dependent, however the diffuse nature of magnetic fields limits the resolution of any imaging system. Magnetic imaging is therefore unlikely to achieve the resolution of techniques such as X-ray imaging and would be better used as a complementary technique.

These preliminary results demonstrate that the target can be imaged in this different configuration which takes approximately 10 minutes (second mode), a significant improvement on the 2 hours for the raster scan process. This is likely tempered with a decrease in the SNR or image quality as a result of the alignment of the outer coils

and the sensor. A more detailed assessment would have to be conducted to quantify this and determine if any reduction in quality outweighs the benefit of faster scanning. This is likely to depend on the application, e.g. portal scanning compared with NTV. This technique could also be investigated from the perspective of coded illumination. Coded illumination is currently used within single pixel imaging [110] and uses patterns of illumination to create 3D images of objects using a single detector. Whilst the current application is within ballistic radiation, a "shadow" can be cast with an object in ECI as demonstrated in this Chapter and therefore may be applicable within ECI imaging.

Chapter 7

High Frequency ECI Imaging

ECI imaging has applications across a broad spectrum of NTR areas as summarised in Chapter 1. Of the scenarios discussed, low frequency ECI is suited to detection in high conductive or thick shielding configurations (scenarios I, III) as examined in Chapter 6 using the QuSpin QZFM atomic magnetometer (AM). However, scenarios in which there is no significant conductive barrier to detection will benefit from a system that can operate at higher frequencies. To access these higher frequencies and investigate the phase response as a function of frequency, a tune-able radio frequency (RF) AM was constructed.

This Chapter details the construction and optimisation of the RF AM. The RF AM was then used as part of an ECI imaging system to obtain images of hafnium and bismuth targets, utilised as surrogates for uranium and plutonium. The frequency of the RF AM was then tuned to optimise the phase response of the SNM surrogates over other higher conductivity targets. This has the dual benefit of increasing SNR of targets of interest whilst suppressing potential high conductivity clutter.

7.1 Experimental Configuration

The RF AM was constructed using a rubidium vapour cell with separate pump and probe beams orientated orthogonally in the x-z plane. An RF perturbation field was applied along the y-axis which also functioned as the ECI excitation field. In imaging experiments the target was located between the vapour cell and the excitation coil in a transmission configuration.

A schematic of the RF AM is displayed in Figure 7.2. This configuration used of a 780 nm Vescent DBR laser (DBR-200) which was frequency locked to the F = 2 to F$'$ = 3 transition within ^{85}Rb, as illustrated in Figure 7.1, using a paired spectroscopy unit (D2-100).

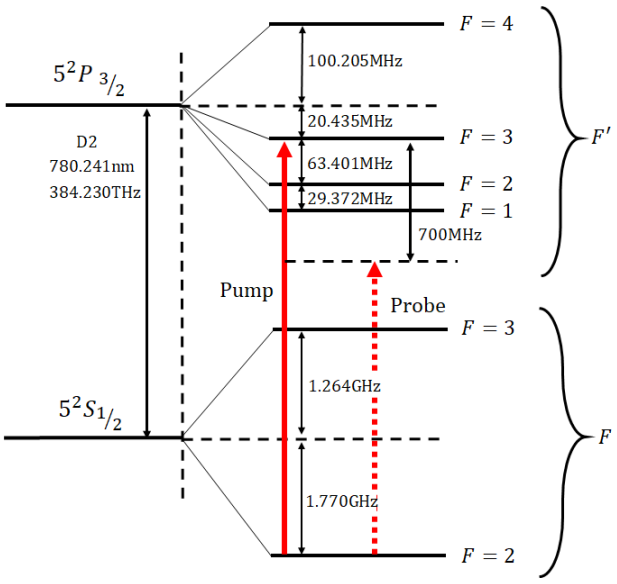

Figure 7.1: Illustration of the pumping (solid arrow) and probing transition (dashed arrow) within ^{85}Rb used for the RF atomic magnetometer. The pump beam was tuned along the D2 transition, between ground state F = 2 and excited state F$'$ = 3. The probe beam was red detuned from this transition by 700 MHz.

An optical isolator was utilised to prevent back-reflection into the laser cavity. Once frequency locked, the beam was passed to a half-wave plate (HWP) and a polarising beam splitting (PBS) cube, where the HWP could be used to adjust the total power

entering the rest of the system. A second HWP and PBS pair were utilised to split the beam into a separate pump and probe lines. The pump beam was expanded from a diameter of 2 mm to 8 mm using a beam expander (Thorlabs - GBE05-B) and circularly polarised using a quarter-wave plate (QWP). The probe beam was frequency de-tuned (red, as seen in Figure 7.1) by a double pass through an acousto-optic modulator (AOM) (Gooch & Housego), after which the polarisation was rotated using a QWP to direct the beam back through the PBS and onto the vapour cell. A HWP was used to adjust the polarisation of the probe beam before it travelled through the cell to orientate the linear polarisation along the pump direction. In each instance where the beam was reflected through a PBS, a Glan-Taylor polariser (GTP) was used to ensure complete linear polarisation of the beam. The probe travelled through the vapour cell and to a balanced polarimeter arrangement where the polarisation rotation of the signal was measured. To ensure maximal signals, the output was balanced between each photodiode using another HWP. A photograph of the optical set-up is displayed in Figure 7.3a.

The vapour cell used was a 25 mm $\times$ 25 mm $\times$25 mm pyrex cube (Triad Technologies) containing a natural mix of rubidium (72% ^{85}Rb, 28% ^{87}Rb) and 70 torr of nitrogen buffer gas at room temperature. The cube was placed at the intersection of the pump and probe beams and at the centre of a three-axis Helmholtz arrangement that was used to cancel ambient magnetic fields and apply a bias field along the pump beam (z-axis). This configuration was informed by the discussion in Chapter 3 which dictates that a maximal polarisation rotation is obtained when the bias field is aligned along the pumping direction due to a maximisation of the initial polarisation factor M_0. The perturbation RF field was applied along the y-axis, perpendicular to the bias field and supplied using a ferrite cored coil (radius = 3 mm, length = 7.5 mm, 143 turns).

The three-axis Helmholtz arrangement constructed around the vapour cell is illustrated in Figure 7.4, with a photograph displayed in Figure 7.3b. In this configuration

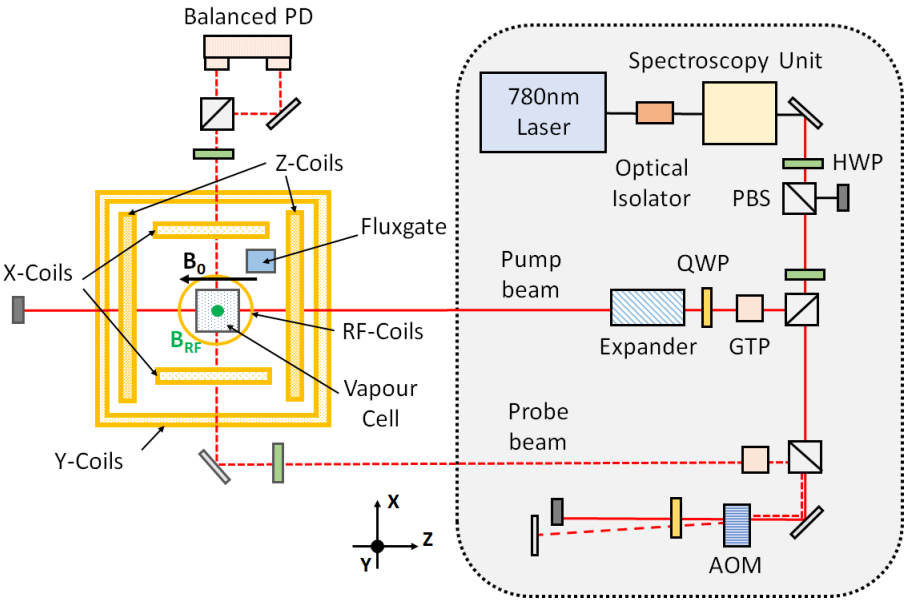

Figure 7.2: Schematic of the radio-frequency atomic magnetometer. The D2 transition of ^{85}Rb was pumped using a 780 nm laser which was split into orthogonal pumping and probe beams. The pump beam was circularly polarised using a quarter-wave plate (QWP) and expanded to a diameter of 8 mm using a beam expander. The probe beam was frequency shifted by 700 MHz using acousto-optical modulator (AOM) before being linearly polarised using a half-wave plate (HWP). The beams intersected at the centre of a 25 mm $\times$25 mm $\times$ 25 mm pyrex cube containing a natural mix of rubidium and 20 torr of nitrogen buffer gas. In each instance where the beam was reflected using a polarising beam splitter (PBS) cube; the polarisation was cleaned using a Glan-Taylor polariser (GTP). The bias field was applied along the direction of the pump, whilst the RF perturbation field was applied along the vertical axis (y-axis), orthogonal to both the pump and probe beams (z-axis). The cell was actively shielded using a three-axis Helmholtz arrangement. The rotation of the probe beam polarisation was measured using a balanced photo-diode arrangement.

there were three pairs of Helmholtz coils aligned along each axis, one to supply a large (μT) DC off-set, another to compensate for small DC and AC fields, and third which was wound in an anti-Helmholtz arrangement. The first of these coil pairs was necessary to cancel the large DC component resulting from the Earth's ambient magnetic field. The second pair were required to make small adjustments to the DC cancellation but also allow compensation of AC fields, specifically the 50 Hz contribution. This set were controlled using a proportional integral derivative (PID) system (SRS SIM960, SRS

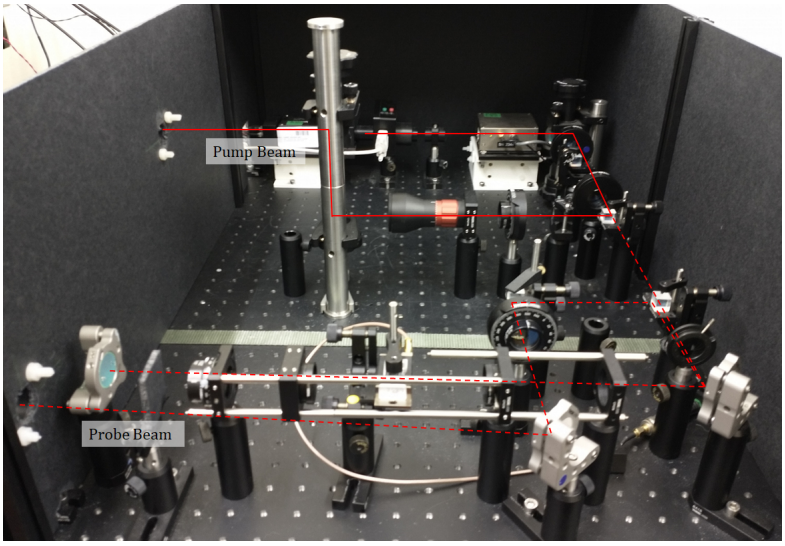

(a) Optical Set-up

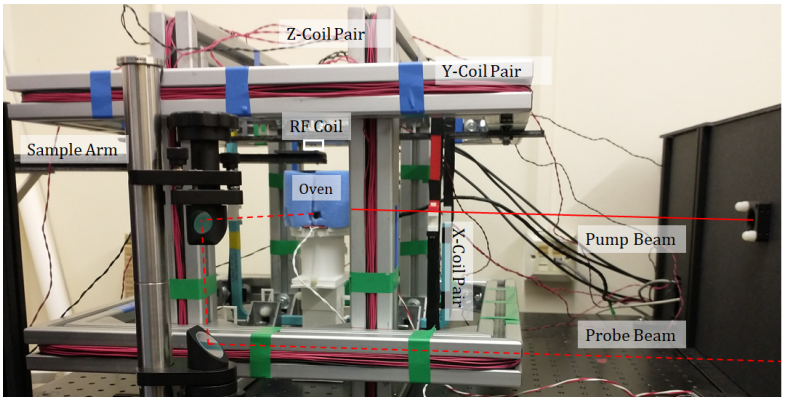

(b) Helmholtz Set-up

Figure 7.3: Photographs of (a) the optical set-up where the pump and probe beams are prepared and (b) of the Helmholtz arrangement and cell oven. The cell is located inside the oven at the intersection of the pump and probe beams. The balanced photo-diode arrangement is located behind the oven and is obscured in this image. The approximate pump (solid line) and probe beam (dashed line) paths are highlighted.

SIM900 mainframe) that actively cancelled the magnetic field referenced to a three-axis fluxgate sensor (Bartington MAG612U). Finally, the third pair were used to cancel any field gradients and were adjusted manually to optimise the resonance feature obtained from the balanced photo-diode. The DC set along the z-axis were used to apply the bias field. The dimensions and properties of each Helmholtz pair are summarised in Table

7.1.

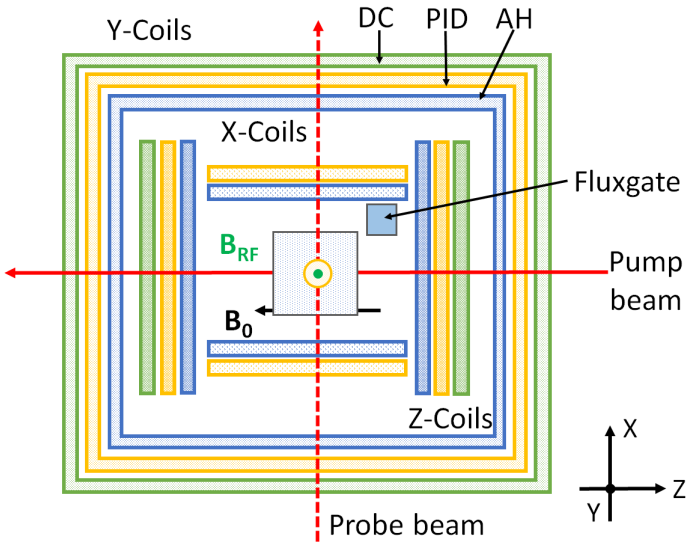

Figure 7.4: A schematic of the active cancellation system utilised to nullify ambient magnetic fields around the vapour cell. The arrangement consisted of three Helmholtz pairs along each axes, one to cancel the large DC component (yellow), another to cancel small changes in DC and AC (green) and a third pair in an anti-Helmholtz configuration to cancel field gradients (blue). The bias field was applied along the pump direction using the DC pair along the z-axis.

Axis	Coil Function	Radius (mm)	Turns
y-axis	DC	20.5	25
y-axis	PID	20.5	25
y-axis	Anti Helmholtz	20.5	10
x-axis	DC	13.5	25
x-axis	PID	13.5	25
x-axis	Anti Helmholtz	13.5	10
z-axis	DC	16.5	25
z-axis	PID	16.5	25
z-axis	Anti Helmholtz	16.5	10

Table 7.1: Summary of the Helmholtz pairs utilised in the active cancellation system for the RF atomic magnetometer.

7.1.1 Imaging Configuration

In order to image objects using the RF AM, a pair of orthogonal linear stages (Newport) were used to raster scan a target between the vapour cell and the excitation/perturbation coil. To minimise the movement of the stages from disrupting the bias field at the cell, the stages were located approximately 1 m from the cell and the target raster scanned on a non-conductive arm. This is illustrated in Figure 7.5. The separation between the centre of cell and the centre of the RF coil was $y_1 = 100\,\text{mm}$, whilst the distance between the centre of the cell and the target was $y_2 = 82\,\text{mm}$.

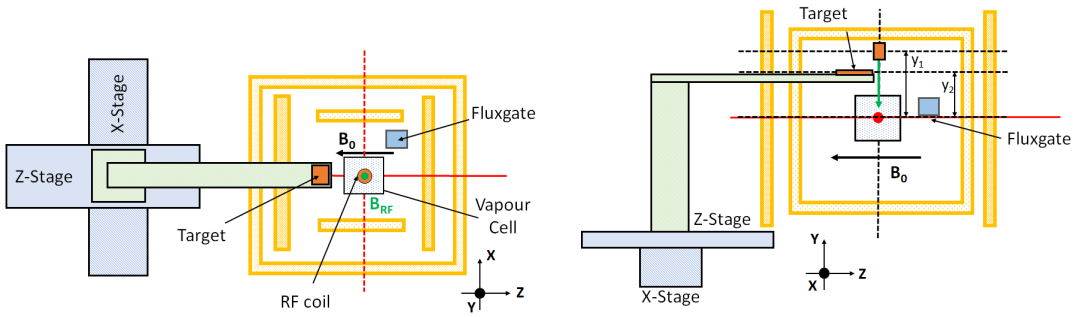

(a) Overhead View (b) Side View

Figure 7.5: Illustration of the experimental configuration utilised to image small metallic objects using the RF atomic magnetometer. The set-up includes the addition of two linear stages and a 3D printed sample arm which is displayed from an overhead view (a) and a side view (b).

The images were constructed using the same processes as the QuSpin QZFM AM detailed in Section 6.1. Here, the target was moved between the static cell and excitation coil, at each pixel location a frequency scan was taken that encompassed the resonance feature (3 kHz). The output of the balanced photo-diode was demodulated at each of these frequencies using a lock-in amplifier to provide a range of values for the in-phase (X) and quadrature (Y) components discussed in Section 3.3.2. These quantities can also be expressed as phase and magnitude values equivalent to those for the QZFM AM.

7.1.2 RF Heating

The temperature of the vapour can contribute to improvements in the SNR of the system through changes in the vapour density. An increase in density will increase the number of atoms (N) contributing to the signal and therefore a $\sqrt{N}$ reduction in the noise as dictated by equation 3.54. A boost in the SNR results in an improved DC sensitivity measure as discussed in Section 3.7. The primary challenge associated with heating the vapour cell was the construction of a non-magnetic, non-metallic system which did not produce any DC or AC magnetic signature that interfered with the operation of the AM.

RF heating was chosen in which an AC current was applied to an non-inductive loop of wire which radiated heat to the cell. This process was achieved using a commercially available silicon heat pad (RS-245499) with dimensions of 25 mm $\times$50 mm positioned under the cell. In order to supply an AC current to the pad, a H-bridge circuit was commissioned [111]. The H-bridge used an external reference at a user specified frequency to supply current to the pad through a temperature control PID unit (JUMO Quantrol LC100). A temperature sensor (PT-100) was attached to the side of the cell to feedback temperature information to the controller which switched the current to the pad as part of a PID loop.

To reduce the thermal loss from the cell, a small non-magnetic oven was constructed. As with the heating pad, the oven was required to have no magnetic signature or any metallic components which could induce eddy currents. A 50 mm $\times$50 mm $\times$50 mm enclosure was printed from PLA with 100% infill. This was mounted over the cell and encased in 20 mm thick foam insulation; ports were included in three of the faces to allow the pump and probe beams to pass through. The cell itself was placed inside a second 3D printed holder which allowed the PT100 to be in contact with the cell wall. This set-up is illustrated in Figure 7.6.

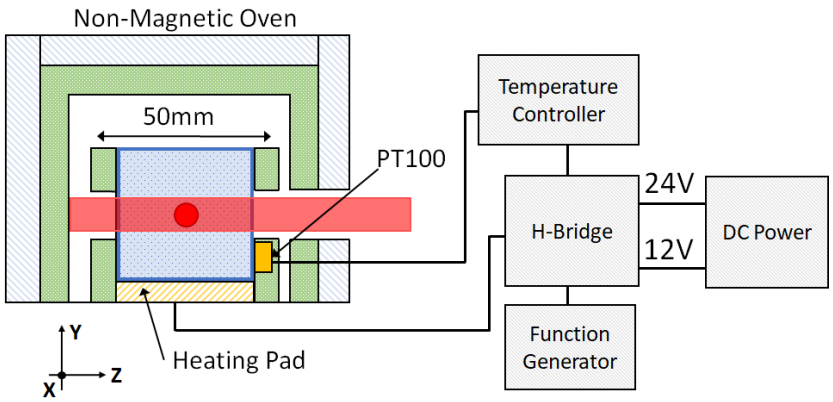

Figure 7.6: Schematic of the apparatus used to heat the vapour cell. The 25 mm ×25 mm ×25 mm rubidium cell was mounted in a 3D printer PLA holder which allowed a temperature sensor (PT100) to be placed in contact with the cell wall. A silicon pad heater was used to inductively heat the underside of the cell. The PT100 and heater formed a PID loop using a temperature controller which switched current on and off to the heater via a H-bridge circuit. The H-bridge circuit converted DC current into AC referenced from an external frequency applied using a function generator. A PLA enclosure covered in insulating foam surrounded the cell and heater to reduce thermal loss and aid temperature stability. Open access ports (without glass) allowed the pump and probe beam to pass through the cell.

7.2 RF Atomic Magnetometer Optimisation

The operation of the RF AM required the optimisation of various parameters. These include features of the active cancellation system, the strength of the RF field and the power of the pump and probe beams. The optimisation procedure discussed here aimed to maximise the sensitivity as defined in Section 3.7. This is reiterated here as:

$$\delta B = \frac{\hbar}{g\mu_B} \frac{\text{FWHM}}{\text{SNR}} \tag{7.1}$$

where the first term on the RHS is calculated from the vapour isotope and the second term can be obtained from the FWHM of the in-phase resonance feature and an estimate of the SNR. To maximise the sensitivity, parameters were tuned such that the FWHM was minimised and the SNR was maximised. During optimisation, rather than the SNR,

the amplitude of the in-phase component was used (Amplitude_X). Any calculation of the sensitivity used the full SNR as obtained from the PSD function of the output. The ratio maximised is given as

$$\text{Ratio} = \frac{\text{Amplitude}_X}{\text{FWHM}}. \tag{7.2}$$

This Section first discusses the process to zero the ambient magnetic fields within the active cancellation system, before examining the variation in the above ratio with the RF field strength, the power of the pump and probe beams and the cell temperature. Finally, a calculation is made for the DC sensitivity.

7.2.1 Active Cancellation System

The active cancellation system displayed in Figure 7.4 consisted of various Helmholtz pairs wound round three sets of aluminium frames constructed from 25 mm rails. The usage of each set of coils can be separated into DC, PID and Anti-Helmholtz as described in the previous Section. Along the y-axis a current of 348 mA was applied to the DC Helmholtz pair to cancel 40 μT of the measured 42 μT ambient field. The PID set of coils along this direction were then used to iterate the last DC component to zero but also to compensate for AC magnetic fields, particularly the 50 Hz mains power component. This AC cancellation is illustrated in Figure 7.7a which displays the fluxgate output along the y-axis without (blue) and with (red) PID compensation. The corresponding Fourier transform of these data is given in 7.7b, highlighting the reduction in the 50 Hz component.

The impact of these cancellations can also be observed on the shape of the in-phase component of the resonance feature. This, as previously discussed, is obtained by examining the output of the balanced photo-diode as the frequency of the RF field is scanned about the Larmor frequency. These traces are given in Figure 7.8 with DC compensation

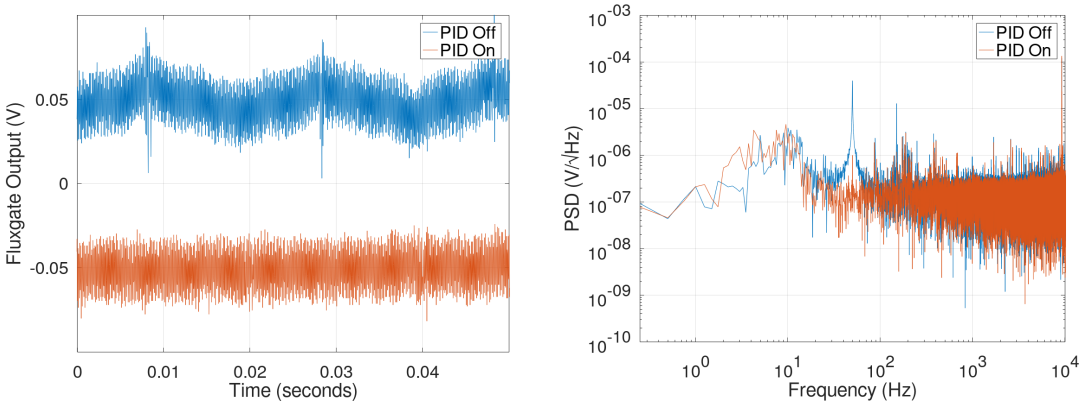

(a) Analogue Output (b) Power Spectrum

Figure 7.7: Data obtained from the analogue output of the Bartington Mag612U fluxgate along the y-axis without (blue) and with (red) PID compensation. Data is displayed in time (a) and Fourier transformed to provide the corresponding power spectra (b).

applied but PID compensation only applied along specified axes.

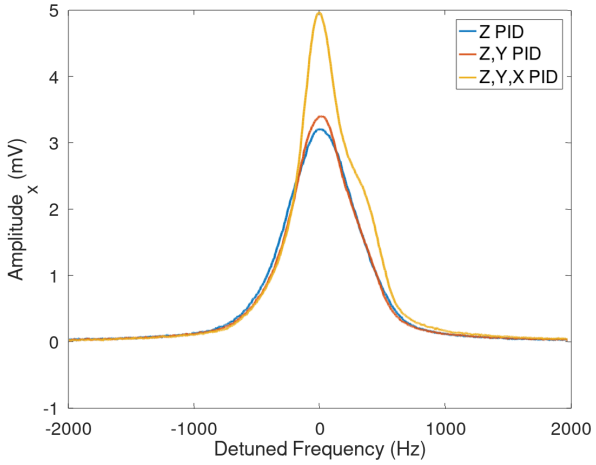

Figure 7.8: In-phase component of the resonance feature obtained as the RF field is swept through the Larmor frequency. Data is obtained with DC cancellation applied along all required axes but with PID compensation utilised along (blue) z-axis only, (red) z and y-axes only and (yellow) along z, y and x-axes.

Examination of the resonance features indicate that the PID controlled correction along the y-axis (B_{RF} direction) contributes a small increase to the height due to the

better alignment of the bias along the pump direction. A much larger increase in height is observed when the x-axis (probe direction) is compensated along with a narrowing of the resonance feature. In this instance, this was due to the larger DC correction applied by the PID along the x-axis as the ambient field along that direction was not compensated by DC coils. It should also be noted however, that PID compensation along this axis highlights an asymmetry in the resonance feature as the FWHM narrows. This could be due to imperfections in the compensation of the field resulting from the non-central positioning of the fluxgate within the x-axis coils. This is necessitated to maximise the distance between the cell and the fluxgate. To adjust for this, it was found that the set of anti-Helmholtz coils were able to reduce the asymmetry and narrow the resonance whilst maintaining the SNR; this is illustrated in the two resonance features displayed in Figure 7.9.

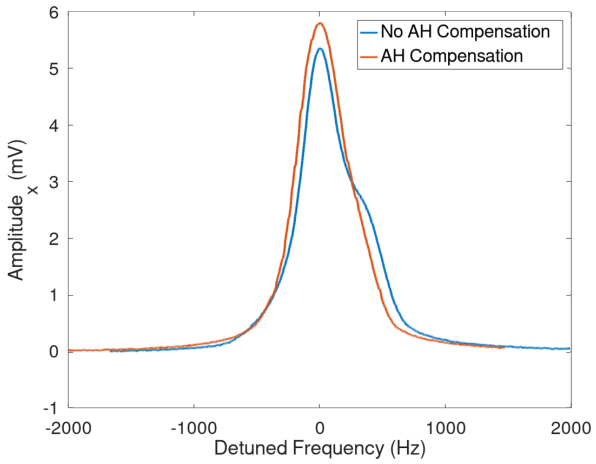

Figure 7.9: In-phase component of the resonance feature obtained as the RF field is swept through the Larmor frequency. Data is obtained without (blue) and with (red) the application of a field gradient along the x-axis.

Once the coarse DC, PID and any anti-Helmholtz cancellation had been applied, the DC compensation necessitated adjustment due to a off-set from zero field inherent within the fluxgate sensor. To make these small changes, the voltage applied to the PID coils

(set-point voltage) was adjusted whilst the resonance feature was recorded. Examination of the resonance feature allowed the set-point voltage to be fixed at the value where the central frequency of the feature reached a minimum. These data are displayed for the y-axis coil and x-axis coil set-point voltages in Figure 7.10. In this instance a y set-point voltage of -0.104 V and a x set-point voltage of -0.210 V were applied. The set-point for the z-axis coil was not adjusted as these were used to apply the bias field and therefore used to tune the resonant frequency.

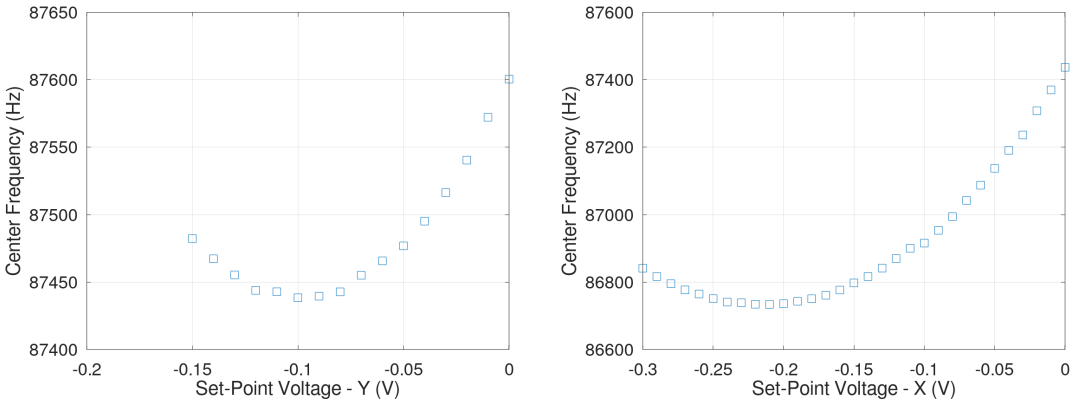

(a) y Set-point Voltage

(b) x Set-point Voltage

Figure 7.10: Centre frequency of the in-phase resonance feature as a function of the set-point voltages, and therefore DC off-set of the compensation fields applied along the y and x-axes.

7.2.2 RF Magnetic Field Strength

Once the set-point voltages within the coil cancellation system were specified to minimise all fields other than the bias field, the strength of the RF field was adjusted to maximise the ratio given in equation 7.2. This step was required whenever the resonant frequency was significantly altered. This is due to a change in the inductance of the drive coil with increasing frequencies that results in a decrease in the field generated at each voltage. The height and FWHM of the in-phase component was determined by recording the

resonance feature at each RF voltage and fitting the data with a Lorentzian distribution of the form given in equation 3.41. An example of this optimisation is displayed in Figure 7.11a which displays the calculated FWHM and height of the resonance feature as a function of RF voltage. These data were obtained at a bias field corresponding to a resonant frequency of 76 kHz. The FWHM of the in-phase component can be seen to increase as a function of voltage ranging from 560 Hz up to 720 Hz indicating RF broadening across this range, however, this is also accompanied by an increase in height that improves the SNR. The optimisation ratio that balances these parameters is given in Figure 7.11b in which the optimum value occurred at 1.1 V. As it was difficult to measure this field strength at this frequency, the value was estimated in COMSOL to be 3 nT [112] at the centre point of the cell. This voltage was carried forward into the next stage of optimisation.

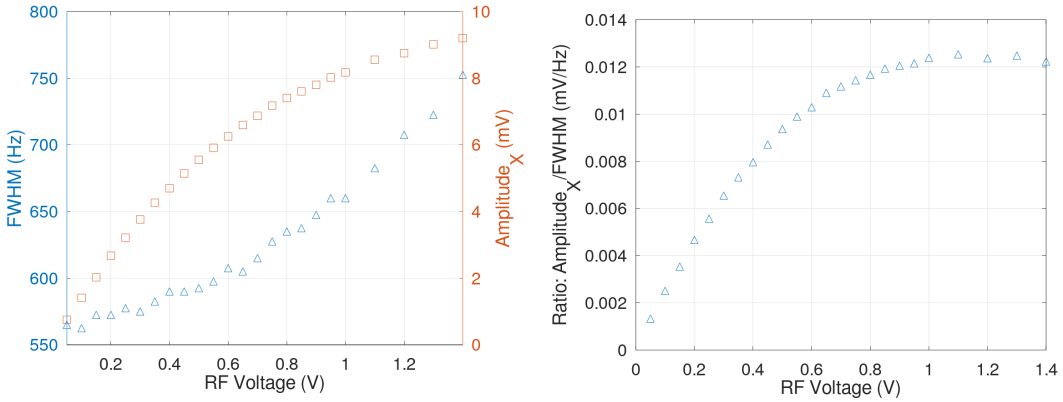

(a) FWHM and Amplitude (b) Ratio

Figure 7.11: FWHM (blue) and height (red) of the in-phase resonance feature as a function of RF voltage (left) along with the corresponding ratio FWHM/Ratio (right).

7.2.3 Pump and Probe Power

The same optimisation principle can also be applied to the power of the pump and probe beams; both of which were measured using a power meter. The pump beam was

optimised first, with the probe beam set to a minimal power to reduce any broadening resulting from pumping with the probe beam orthogonal to the bias field. This power was set to be 30 μW with a beam diameter of 2 mm which results in a power density of 0.97 mW/cm^2. As described in Section 7.1, the probe beam was red detuned by 700 MHz by double passing through an AOM.

The pump power was varied by adjusting the orientation of the HWP that balanced the power between the pump and probe beams. The probe power was adjusted where required using the AOM. Figure 7.12a displays the FWHM and height of the resonance feature as a function of power scanned from 100 μW to 1000 μW. Reducing both the pump and probe powers reduce the FWHM down to 360 Hz suggesting power broadening within the previous results. This is followed by a significant reduction in the height as the number of pumped atoms also decreases. Increasing the power of the pump beam increases the FWHM and height up to a value of 1.38 mV above which the height saturates but the FWHM continues to increase. The optimisation ratio for these data are displayed in Figure 7.12b; these data specify a power of 550 μW corresponding to a power density of 1.1 mW/cm^2 with a FWHM of 430 Hz.

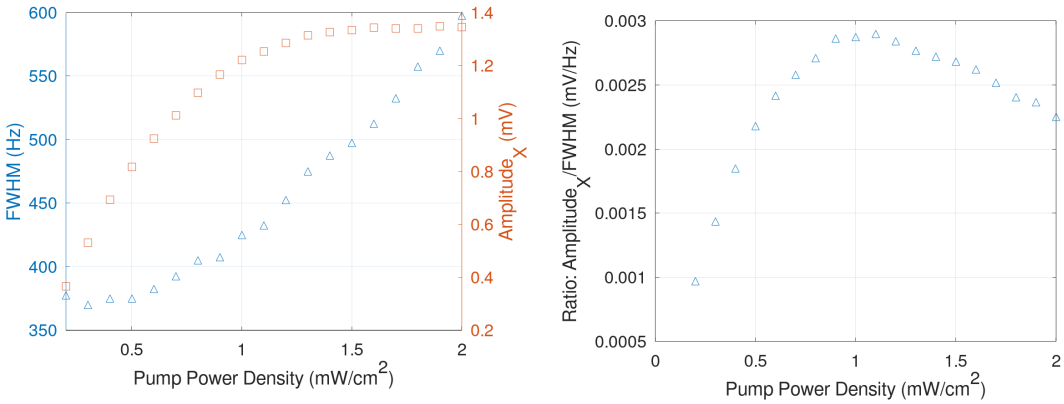

(a) FWHM and Height (b) Ratio

Figure 7.12: FWHM (blue) and height (red) of the in-phase resonance feature as a function of pump power (left) along with the corresponding ratio FWHM/Ratio (right). Data obtained at an RF voltage of 0.5V and a probe power of 30 μW.

At the fixed pump power of 550 μW, the probe power was adjusted using the AOM, scanning the value between 1 μW to 890 μW. As with the previous two data sets, the FWHM and height of the resonance feature were recorded and are displayed in Figure 7.13a. Both values increase with increasing probe powers, with the ratio plateauing above values 600 μW. As such a probe power of 600 μW was selected which corresponds to a power density of 19 mW/cm^2 and a FWHM of 645 Hz.

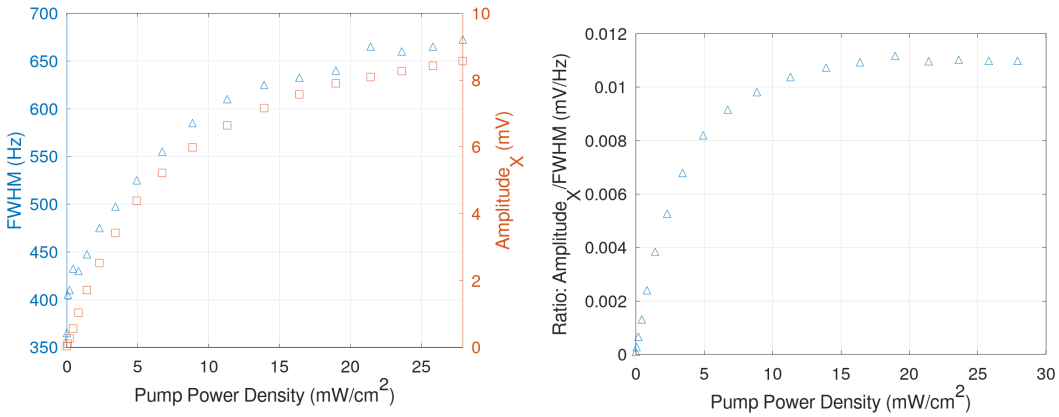

(a) FWHM and Height (b) Ratio

Figure 7.13: FWHM (blue) and height (red) of the in-phase resonance feature as a function of probe power (left) along with the corresponding ratio FWHM/Ratio (right). Data obtained at an RF voltage of 1.1 V and a pump power of 650 μW.

Examination of all these data indicates that even at the lowest value of pump and probe powers there is still a magnetic resonance broadening of 350 Hz. This value may indicate issues with other components in the system which are sub-optimally aligned. Effort was made to ensure optimisation of other components such as the QWP used to circularly polarise the pump beam and the HWP used to linear polarise the probe. Such broadening may also be attributed to the homogeneity or alignment of the cancellation fields. More uniform fields and therefore a narrower resonance may be achieved using larger cancellation coils which would have the dual advantage of a larger homogeneous region and also allow the distance between the fluxgate and the cell to be increased. This may also require optimisation to ensure the fluxgate was also sufficiently close to

the vapour cell to accurately measure the field for cancellation.

7.2.4 Vapour Temperature

In addition to the alignment, power and polarisation of the pump and probe beams, the temperature of the cell was also adjusted to improve the sensitivity of the AM. The previous data sets were all obtained at room temperatures between 25-30°C, the equation [70],

$$n = \frac{1}{T} 10^{21.866+4.857-4215/T} \tag{7.3}$$

equates these temperatures to vapour densities of 1.3-2.1$\times 10^{10}\,\mathrm{cm}^{-3}$ for rubidium.

As discussed previously, a larger density can result in a greater signal to noise ratio, with the spin-projection noise decreasing with $\sqrt{N}$ where N is the number of atoms contributing to the signal. Despite an initial gain in the SNR, this will eventually decrease with vapour density due to the increased number of spin-exchange/spin-destruction collisions, before improving once again as the SERF regime is reached. As the SERF regime is not utilised in this system, the temperature must be optimised. These data are displayed in Figure 7.14a, which display the FWHM and height of the resonance feature in a temperature range between 20-50°C corresponding to vapour densities of 0.75-15$\times 10^{10}\,\mathrm{cm}^{-3}$.

In this instance there is very little broadening of the resonance feature, with the FWHM maintaining a value of approximately 620 Hz across the temperature range. Conversely, the height increases significantly from a value of 8 mV to 98 mV. As such, there is no optimised value within this temperature range as can be seen in Figure 7.14b, just a trend of improved optimisation ratio with increasing temperature. These data were obtained at a RF heating frequency of 150 kHz which was chosen to minimise magnetic field noise that originated from the heater switching on and off to maintain the specified

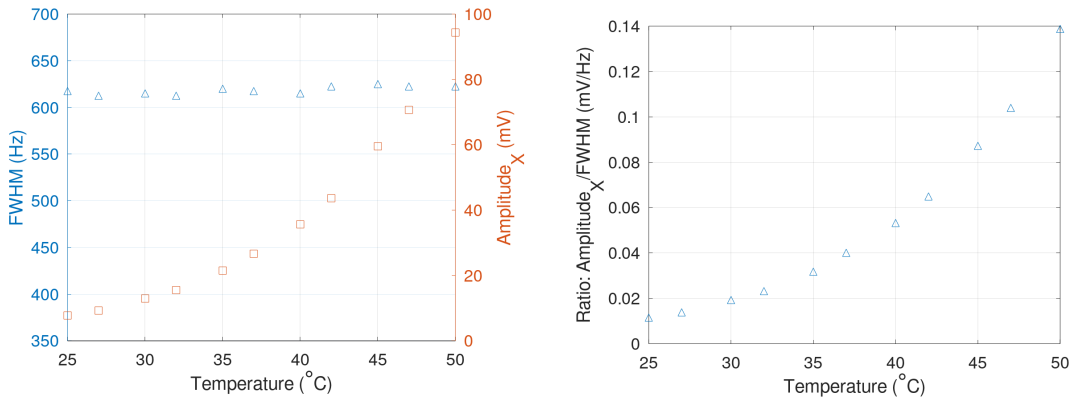

(a) FWHM and Height (b) Ratio

Figure 7.14: FWHM (blue) and height (red) of the in-phase resonance feature as a function of Temperature (left) along with the corresponding ratio FWHM/Ratio (right). Data obtained at an RF voltage of 1.1V, a pump power of 550 μW and a probe power of 600 μW. The RF heater was operated at a frequency of 150 kHz.

temperature. Due to the high frequency, the system was limited in the current supplied to the heating pad which resulted in difficulties in maintaining a consistent temperature too far above the room ambient value. The small non-magnetic oven allowed a higher temperature to be reached, however this was still limited to 50 °C. A value of 47° was chosen which balanced a maximal value with one which could be maintained by the heater; limiting drift in the height of the resonance feature due to changing vapour density.

7.2.5 DC Sensitivity

The optimisation described in the preceding Sections aimed to maximise the SNR of the in-phase resonance feature whilst minimising the FWHM. This achieves the greatest gradient in the quadrature component of the resonance feature about the Larmor frequency. The in-phase and quadrature components obtained using these optimised parameters can be seen in Figure 7.15a. From these data a FWHM of 597 Hz can be obtained. To aid in the maximisation of the sensitivity, the optimisation ratio was calcu-

lated with the height of the in-phase resonance feature, however, to better estimate the SNR, the power spectral density (PSD) function can be calculated. This is displayed in Figure 7.15b as a function of detuning frequency from a resonance of 76.36 kHz. Using these data a SNR of 53400 was calculated. This value is combined with the FWHM as in equation 7.1 to give a DC sensitivity estimate of $24\,\mathrm{pT}/\sqrt{\mathrm{Hz}}$ with the heater switched off.

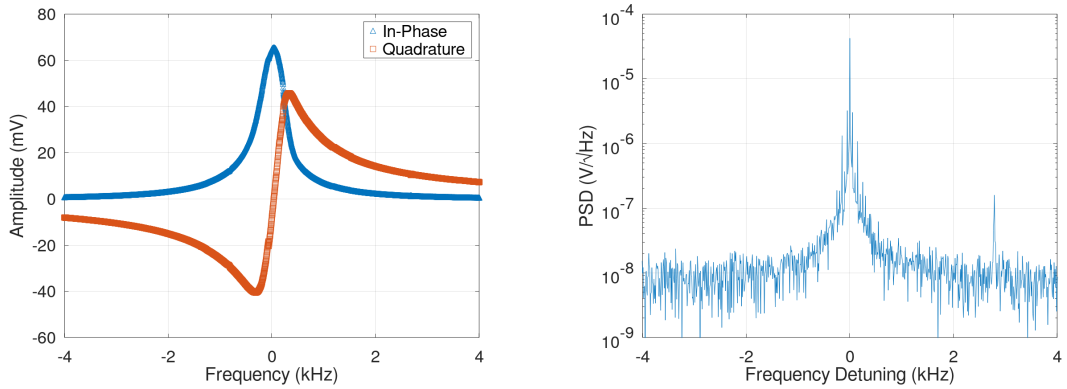

(a) Resonance feature (b) PSD of Output

Figure 7.15: In-phase and quadrature components of the resonance feature (left) and the PSD function of the balanced polarimeter (right) as a function of detuning frequency from a resonance of 76.36 kHz. Data obtained with optimised values of RF voltage = 1.1 V, pump power = 550 μW, probe power = 650 μW and temperature = 47°C. PSD data obtained whilst the heater was off.

Examination of the PSD function in Figure 7.15b shows the presence of 50 Hz side bands about the resonance peak. These correspond to the mains power indicating incomplete cancellation using the three-axis Helmholtz coils. This noise can also be seen in the complete PSD function shown in Figure 7.16. In addition to the mains power lines, a noise source is observed at 100 Hz with resonances observed up to 1 kHz. This is thought to originate from the overhead fluorescent lighting which flickers at twice the mains frequency and was detected by the photo-diode. Other noise sources include the sampling frequency of the fluxgate magnetometer at 15.8 kHz and the RF heating

frequency at 150 kHz.

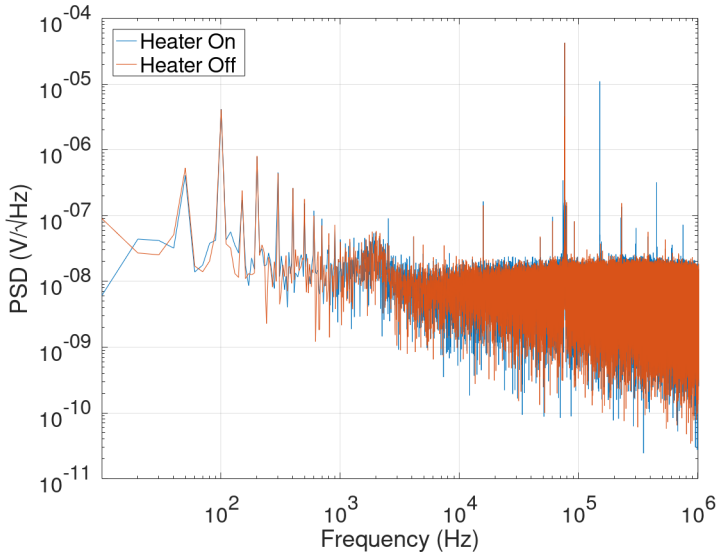

Figure 7.16: PSD function calculated from the output of the RF AM balanced polarimeter when the RF heater is switched on (blue) compared to when it is switched off (red).

7.3 Target Detection

The construction of the RF AM enables ECI measurements to be obtained over a frequency range not possible using the QuSpin QZFM sensor. The objective of this is to detect materials with either a lower conductivity and/or smaller targets. The imaging set-up introduced in Section 7.1.1 allows these measurements to be obtained. In each experiment the target was placed on a non-conductive arm and was scanned between the vapour cell and the RF coil which was orientated perpendicular to both the pump and probe beams.

This Section describes the images which were obtained using this system, focussing on the detection of the hafnium and bismuth targets as surrogates for uranium and plutonium. The images were assessed for quality using the metrics defined in Chapter 5. In addition to imaging, the phase change as a function of target conductivity is examined.

These measurements aimed to assess the premise introduced in Chapter 2 and simulated in Chapter 4 which would maximise the phase response for hafnium/bismuth over higher conductivity metals such as aluminium or copper.

7.4 ECI Imaging

The RF AM measurement recorded the resonance feature over a 3 kHz frequency sweep centred on the Larmor frequency. These data were obtained at each pixel and were used to construct images in phase or magnitude. Figure 7.17 displays a selection of images obtained using the RF AM; these include a background measurement with no target, with a 25 mm ×25 mm ×1 mm hafnium target and a 25 mm ×25 mm ×1 mm bismuth target (SNM surrogates). The images displayed were obtained on resonance at 76.2 kHz and off resonance at 77.5 kHz. A comparison between these images demonstrate that the RF AM can successfully image these targets, including the bismuth (plutonium surrogate) which was not imaged using the QuSpin QZFM at lower frequencies. However, also showed that the images obtained on-resonance were of a lower quality than those off resonance.

Whilst this quality decrease can be observed visually, it can also be quantified as discussed in Chapter 5. Figure 7.18 displays the quality of fit metric, R^2, and the noise metric, RS, as a function of the excitation frequency. Both metrics show a decrease in image quality reaching a minimal value around the resonance of the RF AM. A greater amount of noise, RS, likely resulted in a poorer fit to the expected shape. This effect originated from a distortion of the in-phase component which occurred because of movement of the linear stages which modified the DC bias field. The stages were located 1 m away and off-axis from the cell, however the movement still created this shift in the DC magnetic field, resulting in a shift in the resonant frequency. This effect can be seen in Figure 7.19 which extracts the in-phase and quadrature components of the

resonance feature for the central pixel and a pixel on the edge of the image. Shifting in the resonance feature as the stage moves has a greater effect for those obtained on-resonance, producing the images seen in Figure 7.17. This highlights a refinement that is needed on the implementation of the RF AM imaging set-up. Improvements could be made by increasing the distance between the stages and the cell, however it would become increasingly difficult to support the target. A simpler solution would be to replace the stages with those made of less conductive materials.

Despite the distortion of the on-resonance results, even at the sub-optimal frequencies both the hafnium and bismuth targets could be successfully imaged.

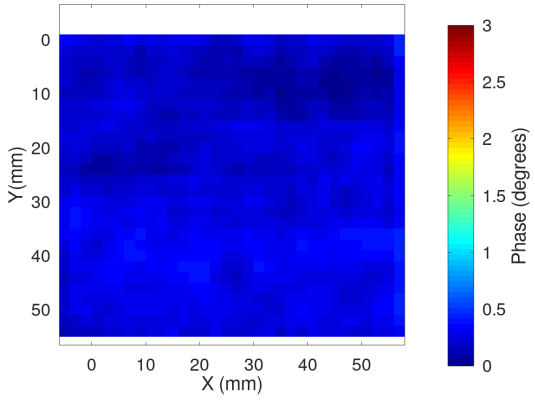

(a) None, 77.5 kHz

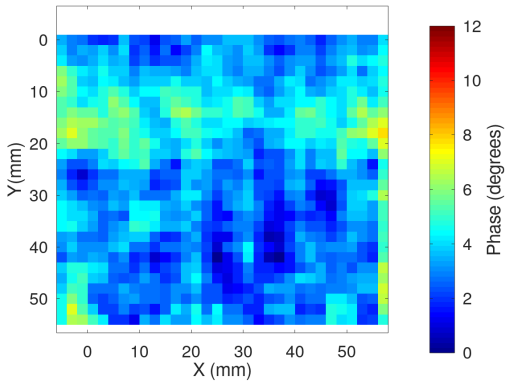

(b) None, 76.2 Hz

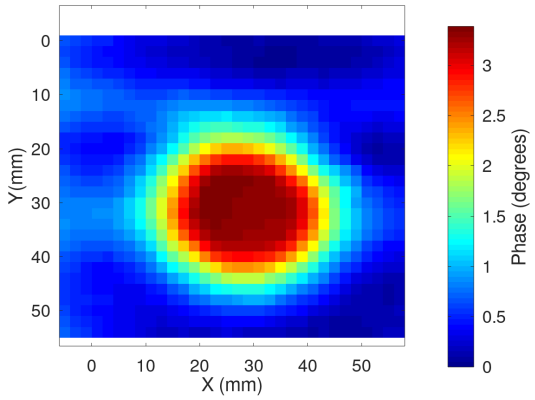

(c) Hafnium, 77.5 kHz

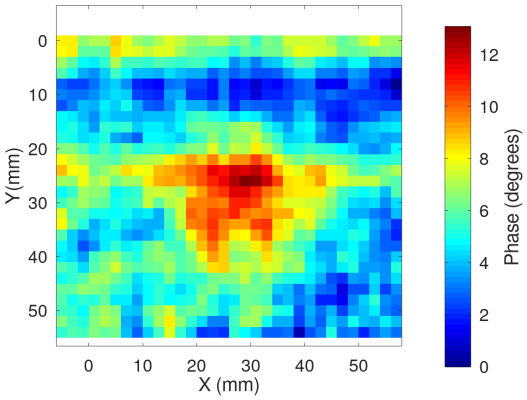

(d) Hafnium, 76.2 Hz

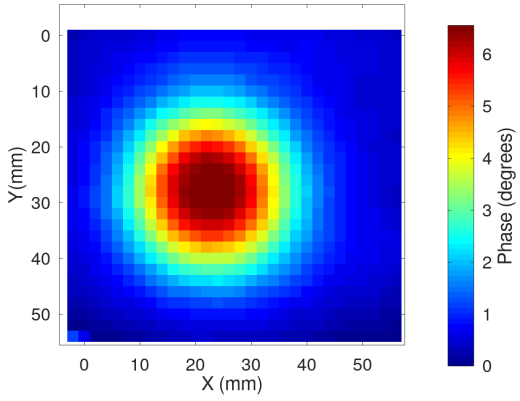

(e) Bismuth, 77.5 kHz

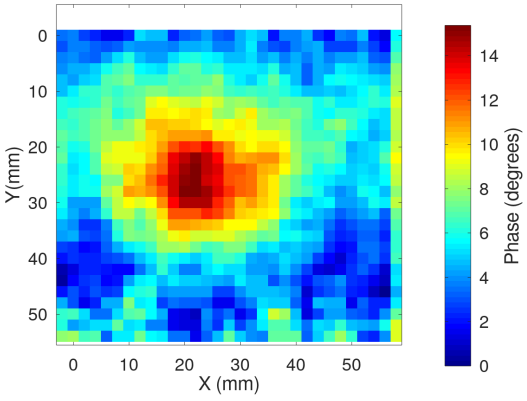

(f) Bismuth, 76.2 Hz

Figure 7.17: Images obtained using the RF atomic magnetometer. Data obtained off resonance at 77.5 kHz (left) and on resonance at 76.2 Hz (right). Images are obtained without a target (a,b) and with 25 mm ×25 mm ×1 mm hafnium (c,d) and bismuth (e,f) targets.

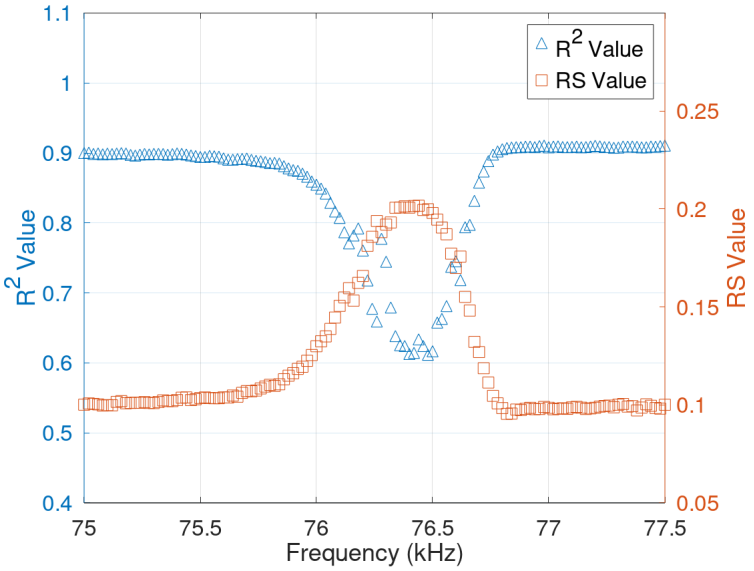

Figure 7.18: Image quality metrics determining the closeness of fit to an expected shape, R^2 (blue triangle), and a quantification of the noise, RS (red square). Metrics were evaluated as a function of the excitation frequency, scanning through the resonance of the RF AM in the presence of a bismuth target.

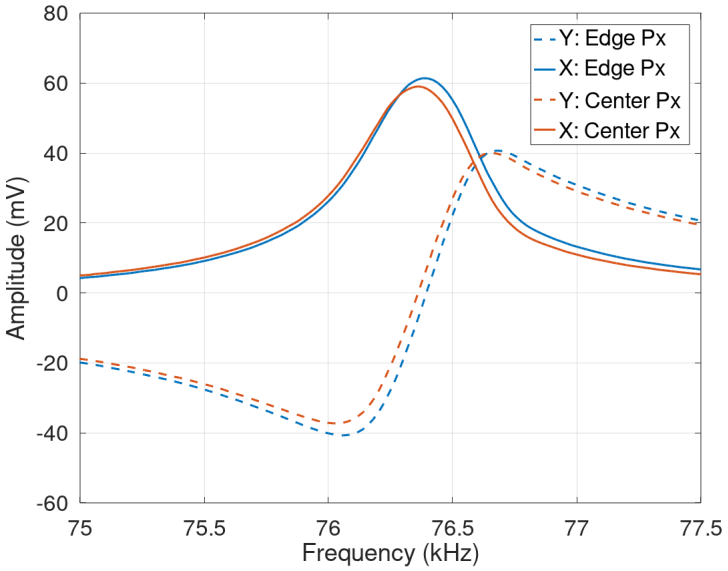

Figure 7.19: In-phase (solid) and quadrature (dashed) components of the resonance feature obtained at a (red) central pixel (x = 25, z = 28) and a pixel on the edge (blue) of the image (x = 0, z = 28). Data obtained without a target present.

7.5 Optimising Frequency for SNM

Discussion of the turning points in phase response as a function of the induced eddy current wavelength parameter L, highlighted the ability to tune the excitation frequency within ECI to maximise phase change for a particular conductivity. This could have applications within material identification, where a frequency scan could identify turning points indicative of the material properties. This principle was explored using the RF AM by adjusting the bias field and tuning the RF resonance. The turning point in the phase can be estimated from the simulated data in Chapter 4, specifically from Figure 4.19, which defined a phase frequency turning point, F_p, expressed as

$$F_p = \frac{71964}{\sigma}. \tag{7.4}$$

For SNM materials with conductivities between uranium and plutonium this equates to excitation frequencies between 24 kHz and 90 kHz.

To explore this, the phase change was measured as a function of target conductivity, where the targets ranged from bismuth (0.8 MS/m) to copper (59 MS/m) with dimensions of 25 mm ×25 mm ×1 mm. As discussed in the previous Section, the movement of the scanning stages resulted in variations in the bias field which in turn shifted the resonance frequency. As a consequence, these measurements were obtained for a single pixel, removing the object from the arm to obtain a measurement of the phase change. The phase response with conductivity is displayed in Figure 7.20 for both frequencies of 24 kHz and 76 kHz; these frequencies correspond to the approximate turning points for SNM conductivities as found from Figure 4.19 in Chapter 4. These data show, that unlike the low frequency measurements made using the QZFM sensor, a maximal phase change can be observed at conductivities below 10 MS/m. This phase turning point can be shifted to lower conductivities by increasing the frequency. Here, this is demonstrated at 24 kHz with a maxima occurring between 5-7 MS/m (niobium/vanadium) compared

with a maxima at 0.8 MS/m (bismuth) for a frequency of 76 kHz. Whilst these values are similar to those obtained from the COMSOL simulations, there is slight variation, with the peak at 24 kHz occurring for conductivities 2 MS/m higher than predicted. Similarly, a peak was observed for the bismuth target at 76 kHz as opposed to 90 kHz. However, as seen in Figure 4.19a, at these lower conductivities the phase turning points are broad; spanning tens of kHz. Images of these samples captured on resonance are displayed in Figure 7.21.

At both these frequencies, the SNM materials of interest, simulated using hafnium and bismuth, have a greater response than more common materials such as aluminium or copper. These results approximate those simulated in COMSOL, with a higher frequency pushing the phase maxima to lower conductivities.

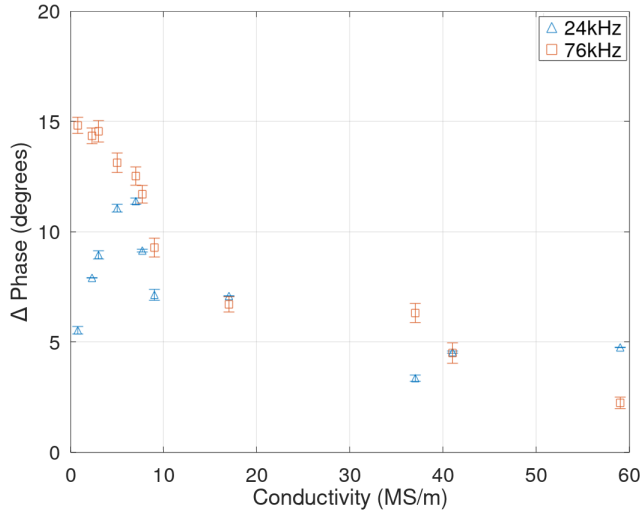

Figure 7.20: Change in phase as a function of target conductivity. Data obtained at a resonant frequency of 76.2 Hz for a series of 25 mm ×25 mm ×1 mm targets.

The characteristic shape in Figure 7.20 and in COMSOL simulations within Chapter 4 suggest it may be possible to tune the RF AM for the ECI measurement of SNM materials over other high conductivity clutter. It should be noted that the value of magnitude or phase will also be dependent on the geometric parameters of the targets

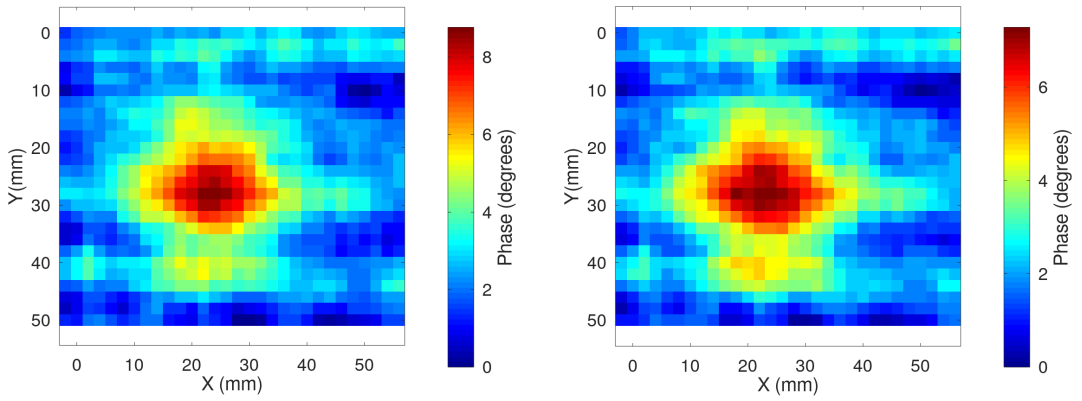

(a) Hafnium, 76 kHz

(b) Bismuth, 76 kHz

Figure 7.21: Images obtained using the RF atomic magnetometer. Data obtained on resonance at 76 Hz of 25 mm ×25 mm ×1 mm hafnium (a) and bismuth (b) targets.

making this processes challenging in operational scenarios. Discussion within Chapter 4 demonstrated that the position of the tuning point as a function of L was comparatively invariant with changes in the radius of the target. Therefore it may be preferable instead to identify materials based on the frequency location of the turning point rather than the absolute phase values. The current RF AM set-up is limited in ability to dynamically adjust the excitation frequency. Due to inductance changes in the coil, whenever the frequency of the excitation field is changed the optimisation process is repeated. This prohibits fast scanning of the resonant frequency required to obtain these frequency scans with this particular configuration. However, such frequency scans should be possible and may be implemented in future.

Chapter 8

Conclusions

8.1 Project Summary

The objective of this work was to examine the applicability of atomic magnetometry within nuclear threat reduction applications; specifically within eddy current induction (ECI) imaging. The project was completed at the Atomic Weapons Establishment (AWE) who conduct fundamental level research for the development of new detector technologies as part of its nuclear threat reduction (NTR) remit. The range of applications which could be met within NTR by ECI methods were discussed in Chapter 1. The broad scope of these applications necessitated the use of a magnetometer technology which could operate at both high and low frequencies. Atomic magnetometers (AM) were selected, with low frequency ($< 300\,\mathrm{Hz}$) applications met by a commercially available sensor [60] and high frequency (kHz) applications using an in-house constructed Radio-Frequency (RF) AM. Both sensors were integrated into a raster scanning imaging system in which the sensor and an on-axis excitation coil were held static and a target object was scanned in the plane between them. Scanning was achieved using two orthogonal linear stages, with the targets mounted on non-conductive arms designed and 3D printed in PLA plastic.

Images could be constructed in either magnitude and phase of the total field projection along the sensor-coil axis. Phase was primarily used as it is insensitive to changes in the magnitude of the field and therefore less susceptible to magnetic field noise. This was found to allow images to be obtained across a greater frequency range. To quantify the quality of images a number of metrics were defined which examined the contents of each image for an expected distribution and made a measurement of the noise.

Low frequency measurements initially focussed on the detection of targets with conductivities ranging between copper (59 MS/m) and bismuth (0.8 MS/m). These measurements determined that images could be obtained of $25 \times 25 \times 1$ mm targets down to 1.1 MS/m (titanium). These results were obtained for frequencies below 300 Hz, at a sensor to excitation coil separation of 176 mm and with an excitation field strength of 0.13 μT at the target. Within these materials, hafnium (3 MS/m) and bismuth (0.8 MS/m) were highlighted as conductivity surrogates for special nuclear materials (SNM), uranium and plutonium respectively. The implications of these results are that uranium may be imaged unshielded at these dimensions but plutonium would not. Both materials could be imaged when the sample size was increased to $50 \times 50 \times 1$ mm, with the image quality degrading for smaller frequencies and conductivities.

This work was extended to the imaging of these materials behind conductive (aluminium), ferrous (steel) and high density (lead) shielding; the excitation coil to sensor distance in these measurement was extended to 220 mm. The nature of the QuSpin AM optimises its operation in the DC and low frequency regime which is required for penetration of magnetic fields through shielding materials. A high conductivity copper target ($40 \times 40 \times 3$ mm) was deemed to be successfully imaged, as defined by the quality metrics, behind aluminium shielding up to 63 mm thick, steel shielding up to 12 mm and lead block shields up to 100 mm thick. The most challenging shielding from an ECI context would be aluminium due to its high conductivity and therefore large ECI signal; a value of 63 mm thick was greater than any found within the literature. The

imaging of the target behind the 12 mm of steel was very minimally effected in quality and a much larger thickness is thought to be possible and here was just limited by the materials available. The inclusion of the aluminium shielding shifted the optimal frequencies for imaging down from the maximal value (300 Hz) to values between 60-120 Hz; this highlights the importance of imaging within this frequency regime, where even high conductivity targets necessitate these values.

In addition to the copper target, a $50 \times 50 \times 1$ mm hafnium target (uranium surrogate) was also examined in these shielding configurations. Images of acceptable quality were obtained behind aluminium 35 mm thick, steel 12 mm thick and lead 100 mm thick. Imaging hafnium behind the aluminium indicated again an optimal frequency range of 60-120 Hz. The steel shielding showed a similarly low level of attenuation as it did for the copper target. In addition to these ECI shielding materials, lead was also investigated due to its use as a shielding material for conventional radiological signatures. The lead shields were constructed from individual lead blocks with an increased sensor to coil distance of 320 mm. In this configuration, the lead was considered to impact minimally on the phase signature. It is expected that the object would be image-able through thicker values, with a greater reduction in the response coming from the increased coil to sensor distance. Few examples of ECI detection of uranium values of conductivity were found in the literature; of those from a security perspective all were either unshielded or minimally shielded. No examples were found imaging through the thickness values achieved here. The plutonium surrogate (bismuth) was not conclusively detected behind the thicker shielding materials using the QZFM, having a much smaller conductivity than the uranium surrogate (hafnium).

In the high frequency regime, a RF AM was constructed which used orthogonal pump and probe beams tuned to the D2 transition of rubidium 85. A bias field along the pump set the resonant frequency and an RF field was applied orthogonal to the pump and probe plane to perturb the polarisation state. Rotation in the polarisation of the

probe beam was detected using a balanced polarimeter set-up which was demodulated at the frequency of the RF field. ECI images were obtained by raster scanning the target between the rubidium cell and the RF coil, utilised to apply the primary field. Optimisation of the RF AM was detailed including an three axis active field cancellation system used to apply the bias field and cancel any other DC or AC components. Values of the RF, pump and probe powers were explored, along with the vapour temperature. A sensitivity of $24\,\mathrm{pT}/\sqrt{\mathrm{Hz}}$ was achieved in a heated cell. Limitations in this sensitivity are thought to be due to limitations in sufficient cancellation of the ambient magnetic fields. Improvements to this could be made by increasing the size of the coils to allow more uniform fields to be created and to increase the separation of the cell and the fluxgate magnetometer which was used to dynamically cancel the fields. A greater sensitivity could be also achieved by heating the cell to a higher temperature. A temperature of 46°C was used, however this was sub-optimal with the system limited by the heating power of the pad at frequencies high enough to minimise magnetic noise. This may be improved by creating a more effective oven around the cell or by considering non-inductive heating methods such as heated air or laser heating. More broadly, the system could be improved by changing the pumping scheme to D1 rather than D2, with a more complete pumping of the ensemble improving the signal to noise ratio. With these improvements resulting in additional narrowing of the resonance feature, greater sensitivity may be achieved through re-optimisation of the RF, pump and probe powers.

As in the low frequency measurements, the magnitude and phase of the total field were recorded at each pixel to construct images of the hafnium and bismuth targets. These results demonstrated that it was possible to image both SNM surrogates for the smaller sample size of $25 \times 25 \times 1\,\mathrm{mm}$ at a sensor to target distance of 82 mm. The image quality off-resonance was found to be of good quality, however shifting of the resonance frequency by the movement of the stages produced noisy results on-resonance. Despite this the targets were still detected and this could be mitigated against by increasing the

distance between the stages and the vapour cell or replacing the stages with a solution made of non-ferrous materials.

Whilst ECI imaging using an RF AM has previously been achieved with materials of lower conductivities than uranium or plutonium, the frequency of the RF AM can be tuned such that the phase response from specific materials can be maximised over others. This concept of phase and magnitude turning points was discussed in Chapter 2 and is attributable to the balance between the linear phase increment through a material and the exponential decay of the magnitude of the secondary field. Using this principle, the measurements of the phase as a function of target conductivity were obtained at 24 kHz and 76 kHz moving the maximal phase response from vanadium (6-7 MS/m) to bismuth (0.8 MS/m), producing minimal phase changes for higher conductivity materials such as copper or aluminium (37 MS/m).

Whilst this technique was explored as a function of conductivity, the definition of an eddy current wavelength parameter, L, indicates that the phase response could also be constructed as a function of frequency. In this instance, the frequency of the phase turning point is also comparatively invariant of object radius and stand-off distance. This may allow for object conductivity or thickness to be determined.

8.2 Applicability of AM within NTR

In the introduction of this work, the application space was examined by categorising them into groups and the potential ECI configurations into scenarios. The context was defined as low TRL scientific research towards future techniques and not aligned with current systems. These were cross-referenced against NTR areas of interest which were linked to current Government strategy. This was summarised in Table 1.1 which can be re-evaluated against the work described here. This re-evaluation is displayed in Table 8.1 where entries are classified as good (green), poor (orange) or very poor (red) according

to how well they are addressed by ECI using atomic magnetometry.

Within Nuclear Treaty Verification (NTV) the ability to confirm material properties of enclosures constructed from aluminium or lead can support the validation of treaty statements. This could include confirmation of the thickness and material of the enclosures to indicate if any radiological signatures are being altered. ECI images are inherently indistinct in a way which may be sufficient to maintain the counter proliferation of nuclear weapons technologies. However, if information is processed to give the frequency position of the phase and magnitude turning points this becomes even less closely linked to target size.

The RF AM also has the potential to meet the detection of explosive materials if it can be extended to sufficiently high excitation frequencies allowing the measurement of very low conductivity materials. This has been achieved by other groups [38] able to measure ECI signatures of $< 1\,\mathrm{S/m}$. Both low and high frequency AMs may be able to determine if an enclosure has been tampered with, specifically if discontinuities have been introduced to a metallic enclosure which will modify eddy current distributions.

Fewer applications are likely to be met within Nuclear Forensics (NF). As demonstrated in this work, materials with conductivities comparable to SNM can be detected, any alloying change will alter the electrical structure and therefore be detectable. Changes in alloy content of uranium with the addition of niobium or molybdenum can alter the conductivity on the MS/m scale [113]. ECI is limited in the detection of powders or very small sample sizes and would be unable to provide isotopic information. Whilst these are unlikely to be met with ECI, they may still be met using AM technologies. AM may also be used for other magnetic signatures such as NQR or NMR which would be able to give isotopic data.

Finally, a number of the applications within Detection Science may be met using ECI and atomic magnetometry. As previous, biological and chemical may be detectable at MHz frequencies, however this work has demonstrated the detectability of nuclear

materials in both non-conductive and conductive shielding configurations. This also applies to radiological materials which also have conductivities in this range such as caesium or (5 MS/m) potassium (14 MS/m), but would be limited based on the size of these samples. The discrimination of these materials from NORM sources may also be possible with many such sources being having low conductivities such as stone or cat litter. ECI with AMs may also address non-radiological or nuclear materials such as gun components.

8.3 Future Work

ECI can contribute to many applications within NTR, with atomic magnetometry providing a sensor technology which is highly sensitive across low and high frequency regimes. The next challenge for ECI within NTR applications is conversion from laboratory based systems to operational focussed implementation. This work has demonstrated the ability of the technique to measure materials on the conductivity scale of SNM but has highlighted the dependence of these signatures on object shape and size. Imaging provides a method with which to bound these parameters, potentially allowing identification of these materials. However, imaging can be slow with poor resolution although this was not quantified within this discussion. The imaging systems primarily used within this work were raster scans which took several hours to complete. A system was briefly demonstrated based on an array of coils which were excited in sequence, this allowed images to be constructed with no moving component; taking minutes instead of hours. The scope of this could be extended to investigate the potential of coded illumination within magnetic fields. This is currently examined in the context of single pixel imaging using patterned illumination of an object which allows an image to be constructed in less pattern iterations than pixels in the image.

The low frequency work specifically, could be extended to image within enclosures

rather behind single sided shields. Variations of the methodology could be explored such as single sided imaging which would be preferable for certain applications. Modifications could be made to the experimental set-up including substitution of the magnetically shielded enclosure for an active cancellation system as was used in the RF AM measurements. Removal of the enclosure may allow for the system to become more portable.

The high frequency system requires the most improvement, as would be expected from a non-commercial system. Several avenues could be explored to improve sensitivity, these include switching the pumping regime to D1, from D2 where a greater degree of polarisation would be achieved. The integration of a heterodyne module would allow the frequency of the laser to be scanned over a wider band and also allow the probe beam detuning to be optimised. Other improvements which could be made concern refinement of the cancellation coil system and modification of the linear stages to reduce DC magnetic fields which introduce noise into the images. Before the RF magnetometer could be implemented in any operational system, miniaturization of the system would be required. This would involve the replacement/rationalisation of many of the components; alternatively single beam systems could be investigated.

A future avenue of investigation which could be applied to either system would be to move away from imaging which is inherently slow and investigate the utilisation of frequency sweeps for material identification. This would involve characterisation of the phase and magnitude turning points and quantify the limitations which make it comparatively invariant with object size and stand-off distance. This could mitigate against the primary concerns of ECI imaging where the shape, size of stand-off distance of an object are so interdependent that a phase magnitude measurement is non-unique and therefore makes material identification challenging. This approach was found to theoretically apply across a range of target radii greater than 50 mm, however, the boundaries of this would be critical.

	Nuclear Treaty Verification (NTV)	Nuclear Forensics (NF)	Detection Science (DS)
Group 1: Chemical or Biological	N/A	N/A	**Scenarios III, IV:** **[Poor]** Detection of chemical and biological agents are of interest for a multi-mode detection system but not within the DS remit.
Group 2: Radiological	N/A	N/A	**Scenarios I, II:** **[Good]** Detection of radiological samples obscured in a range of non-conductive (parcels/handbags) and conductive (briefcases) enclosures. **[Poor]** Applications in constrained (bag scanner) and unconstrained (passive monitoring) environments. Imaging preferable. **Scenarios III, IV:** **[Poor]** Discrimination of naturally occurring radioactive sources (NORM) to reduce alarm rates.
Group 3: Nuclear	**Scenarios III, IV:** **[Good]** Required to validate a warhead disarmament declaration adhering to the non-proliferation of nuclear weapons technology. Determining the presence of nuclear material/alloys but not the isotope mixture. **[Poor]** Technology should not image the container contents. **[Good]** The containers are typically made of aluminium and lead. The exact specifications are known.	**Scenario III**: **[Poor]** Examine nuclear material signatures during the fuel cycle to find origin. Isotopic and alloying information needed. **Scenario III**: **[Very Poor]** Examine materials from a nuclear event. Isotopic and alloying information required. Potential sub-gram sample size.	**Scenarios I, II:** As above
Group 4: Explosives	**Scenario III:** **[Poor]** Determine the presence/type of explosive materials within a container but not shape. Containers are non-metallic The exact specifications are known.	**Scenario III**: **[Good]** Distinguish explosive material from nuclear. **[Very Poor]** Information on the type of explosive required.	**Scenario III, IV:** **[Poor]** Detection of explosives is of interest for a multi-mode system but not within the DS remit.
Other	**Scenarios I,IV:** **[Poor]** Determine types of conductive materials within a sealed container but not shape. **Scenarios I:** **[Good]** Determine if a container has been tampered with. Exact specifications are known.	N/A	**Scenario I-IV:** **[Good]** Detection of gun-components and other illicit items are of interest as part of a multi-mode. system.

Table 8.1: ECI-NTR application matrix providing detail on the applications for the detection of materials of interest within NTR. Entries are evaluated and assigned a designation. Designations are good (green), poor (orange) or very poor (red).

Bibliography

[1] UK Government. The National Security Strategy - Strong Britain in an Age of Uncertainty. https://www.gov.uk/government/publications/the-national-security-strategy-a-strong-britain-in-an-age-of-uncertainty, 2010. Online, accessed: 03-11-2020.

[2] UK Government. Counter-Terrorism Strategy (CONTEST) 2018. https://www.gov.uk/government/publications/counter-terrorism-strategy-contest-2018, 2018. Online, accessed: 03-11-2020.

[3] Organisation for the Prohibitation of Chemical Weapons (OPCW). Chemical Weapons Convention. https://www.opcw.org/chemical-weapons-convention/articles/article-ii-definitions-and-criteria, 1997. Online, accessed: 03-11-2020.

[4] United Nations Office at Geneva (UNOG). Biological Weapons Convention: What are Biological and Toxin Weapons. https://www.unog.ch/80256EE600585943, 2020. Online, accessed: 03-11-2020.

[5] IAEA. IAEA Safeguards Glossary. International Nuclear Verification Series, No. 3, 2001.

[6] United Nations. Transport of Dangerous Goods: Model Regulations. United Nations, 2019.

[7] D. Rifai *et al.* An Eddy Current Testing Platform System for Pipe Defect Inspection Based on an Optimized Eddy Current Technique Probe Design. *Sensors*, 17(3):1–24, 2017.

[8] Lian Xie *et al.* Coupling Pulse Eddy Current Sensor for Deeper Defects NDT. *Sensors and Actuators A: Physical*, 293:189–199, 2019.

[9] P. Bevington *et al.* Imaging of Material Defects with a Radio-Frequency Atomic Magnetometer. *Review of Scientific Instruments*, 90(1):1–4, 2019.

[10] H. Fukutomi *et al.* Remote Field Eddy Current Technique Applied to Non-Magnetic Steam Generator Tubes. *NDT & E International*, 34(1):17–23, 2001.

[11] Ghoni *et al.* Defect Characterization Based on Eddy Current Techniques: Technical Review. *Advances in Mechanical Engineering*, 6:1–11, 2015.

[12] T. Reyno *et al.* Surface Profiling and Core Evaluation of Aluminium Honeycomb Sandwich Aircraft Panels using Multi-Frequency Eddy Current Testing. *Sensors*, 17(2114):1–12, 2017.

[13] Dehui Wu *et al.* Non-Destructive Testing for Carbon-Fibre-Reinforced Plastic (CFRP) using a Novel Eddy Current Probe. *Composites Part B: Engineering*, 177(15):1–9, 2019.

[14] Yating Yu *et al.* Quantitative Approach for Thickness and Conductivity Measurement of Monolayers Coating by Dual-Frequency Eddy Current Technique. *IEEE Transactions on Instrumentation and Measurement*, 66(7):1874 – 1882, 2017.

[15] Wei Li *et al.* A Thickness Measurement System for Metal Films Based on Eddy Current Method with Phase Detection. *IEEE Transactions on Industrial Electronics*, 64(5):3940 – 3949, 2017.

[16] Gong Cheng. A Survey on Object Detection in Optical Remote Sensing Images. *ISPRS Journal of Photogrammetry and Remote Sensing*, 117(1):11–28, 2016.

[17] Young-Kil Shin*et al.* Signal Characteristics of Differential-Pulsed Eddy Current Sensors in the Evaluation of Plate Thickness. *NDT & E International*, 42(3):215–221, 2009.

[18] Zhiwei Zeng *et al.* Characteristics of Eddy Current Attenuation and Thickness Measurement of Metallic Plate. *Chinese Journal of Mechanical Engineering*, 32(106), 2019.

[19] Yong Li *et al.* Pulse-Modulation Eddy Current Inspection of Sub-Surface Corrosion in Conductive Structures. *NDT & E International*, 79:142–149, 2016.

[20] Keiji Tsukada *et al.* Magnetic Detection of Steel Corrosion at a Buried Position near the Ground Level using a Magnetic Resistance Sensor. *IEEE Transactions on Magnetics*, 54(11):1–4, 2018.

[21] R. Guilizzoni *et al.* Sub-Surface Corrosion Detection in Industrial Steel Structures. *IEEE Magnetics Letters*, 10:1–5, 2019.

[22] Xiaoyu Ma *et al.* Full-Reference Image Quality Assessment Based on the Analysis of Distortion Process. *4th International Conference on Systems and Informatics (ICSAI)*, 1:1256–1260, 2017.

[23] H. Griffiths *et al.* Magnetic Induction Tomography: A Measurement System for Biological Tissues. *Electrical Bioimpedance Methods: Applications to Medicine and Biotechnology*, 871(1):335–345, 1999.

[24] Zhili Xiao *et al.* Multi-Frequency Difference Method for Intra-Cranial Haemorrhage Detection by Magnetic Induction Tomography. *Physiological Measurement*, 39:055006, 2018.

[25] Yixuan Chen *et al.* Combined Planar Magnetic Induction Tomography for Local Detection of Intracranial Hemorrhage. *IEEE Transactions on Instrumentation and Measurement*, 70:1–11, 2020.

[26] L. Marmugi *et al.* Optical Magnetic Induction Tomography of the Heart. *Scientific Reports*, 6(23962):1–8, 2016.

[27] J. R. Feldkamp *et al.* Single-Coil Magnetic Induction Tomographic Three-Dimensional Imaging. *Journal of Medical Imaging*, 2(1):1–16, 2015.

[28] L. A. Marsh *et al.* Determination of the Magnetic Polarizability Tensor and Three Dimensional Object Location for Multiple Objects using a Walk-Through Metal Detector. *Measurement Science and Technology*, 25(5):055107, 2014.

[29] Zhipeng Qi *et al.* First Results from Drone-Based Transient Electromagnetic Survey to Map and Detect Unexploded Ordnance. *IEEE Geoscience and Remote Sensing Letters*, 17(12):2055–2059, 2020.

[30] B. E. Barrowes *et al.* Detection of Conductivity Voids and Land-mines using High Frequency Electromagnetic Induction. *International Seminar/Workshop on Direct and Inverse Problems of Electromagnetic and Acoustic Wave Theory (DIPED)*, 1:118–122, 2016.

[31] A. Abdel-Rehim Omar *et al.* Magnetic Polarizability Tensor Spectroscopy for Low Metal Anti-Personnel Mine Surrogate. *IEEE Sensors Journal*, 16(10):3775–3783, 2016.

[32] Jack Wood *et al.* Effect of Shielding Conductivity on Magnetic Induction Tomography Security Imaging. *IEEE Transactions on Magnetics*, 53(4):1–6, 2017.

[33] R. Ward *et al.* Magnetic Induction Tomography of Objects for Security Applications. *SPIE Proceedings: Emerging Imaging and Sensing Technologies for Security and Defence III*, 104380:1–8, 2017.

[34] A. Langley *et al.* Assessment of Tunnelling Magneto-Resistors for Magnetic Imaging Tomography. *SPIE Proceedings: Emerging Imaging and Sensing Technologies for Security and Defence III*, 10438:66–74, 2017.

[35] B. J. Darrer *et al.* Magnetic Imaging: A New Tool for UK National Nuclear Security. *Scientific Reports*, 5(7944):1–6, 2015.

[36] B. J. Darrer *et al.* Toward an Automated Set-up for Magnetic Induction Tomography. *IEEE Transactions on Magnetics*, 51(1):1–4, 2015.

[37] A. J. Hiles *et al.* Sparsity and Level Set Regularization for Near-Field Electromagnetic Imaging in 3D. *Inverse Problems*, 36(2):025012, 2020.

[38] C. Deans. Electromagnetic Induction Imaging with Atomic Magnetometers. PhD dissertation, University College London, 2018.

[39] C. Deans *et al.* Through Barrier Electromagnetic Imaging with an Atomic Magnetometer. *Optics Express*, 25(15):17911–17917, 2017.

[40] Sarah Hussain. Application of Quantum Magnetometers to Security and Defence Screening. PhD dissertation, University College London, 2018.

[41] "R. Sikora *et al.*". Eddy Current Testing of Thick Aluminium Plates with Hidden Cracks. *"Review of Progress in Quantitative NDE"*, 22:427–434, 2003.

[42] R. E. Cofield. Eddy Current Electrical Conductivity Measurement as an Analysis for Molybdenum in Binary Molybdenum-Uranium Alloys. Uranium Carbide Nuclear Company, USA, 1957.

[43] F. Shubitidze *et al.* High Frequency EMI Sensing for Estimating Depleted Uranium Radiation Levels in Soil. *SPIE Proceedings: Detection and Sensing of Mines, Explosive Objects and Obscured Targets*, 10628:1–8, 2018.

[44] F. Shubitidze *et al.* Ultra-Wide-Band EMI Sensing for Sub-Surface Deplete Uranium Detection and Classification. *SPIE Proceedings: Detection and Sensing of Mines, Explosive Objects and Obscured Targets*, 1018216:1–10, 2017.

[45] Roberta Guilizzoni. A Resonant System for Electromagnetic Induction Imaging of Concealed Conductive Targets. PhD dissertation, University College London, 2018.

[46] I. M. Savukov *et al.* Detection of NMR Signals with a Radio-Frequency Atomic Magnetometer. *Journal of Magnetic Resonance*, 185(2):214–220, 2007.

[47] F. Primdahl. The Fluxgate Magnetometer. *Journal of Physics E: Scientific Instruments*, 12(4):241–253, 1972.

[48] R. H. Koch *et al.* Fundamental Limits to Magnetic-Field Sensitivity of Flux-Gate Magnetic-Field Sensors. *Applied Physics Letters*, 75(24):3862–3864, 1999.

[49] J. Deak *et al.* A Low-Noise Single-Domain Fluxgate Sensor. *Applied Physics Letters*, 69(8):1157–1159, 1996.

[50] Bartington Instruments. Precision Magnetometers. `https://www.bartington.com/high-precision-magnetometers/`, 2021. Online, accessed: 21-06-2021.

[51] P. P. Freitas *et al.* Magnetoresistive Sensors. *Journal of Physics: Condensed Matter*, 19:1–10, 2007.

[52] Xiaolu Yin *et al.* Recent Progress in the Development of High-Sensitivity Tunnelling Magneto Resistive Sensors. *Proceedings of SPIE*, 11090:1–10, 2019.

[53] Mouser Electronics. TMR-Based Magnetic Sensor. `https://www.mouser.com/datasheet/2/89/RedRock-111TMR-Datasheet-LongVersionTDS-Feb2018-1290909.pdf`, 2020. Online, Accessed: 10-11-2020.

[54] M. I. Faley *et al.* Superconducting Quantum Interferometers for Non-destructive Evaluation. *Sensors*, 17(12):1–16, 2017.

[55] J. Clarke & A. I. Braginski. The SQUID Handbook. Wiley, Germany, 2004.

[56] D. Budker & M. Romalis. Optical Magnetometry. *Nature Physics*, 3:227–234, 2007.

[57] M. P. Ledbetter *et al.* Spin-Exchange-Relaxation Free Magnetometry with Cs Vapour. *Physical Review A*, 77(3):033408, 2008.

[58] C. Deans *et al.* Electromagnetic Induction Imaging with a Radio-Frequency Atomic Magnetometer. *Applied Physics Letters*, 108(10):1–5, 2016.

[59] A. Horsley *et al.* Frequency-Tunable Microwave Field Detection in an Atomic Vapour Cell. *Applied Physics letters*, 108(211102):1–5, 2016.

[60] QuSpin Ltd. QZFM-Gen-2. `https://quspin.com/products-qzfm/`, 2020. Online, accessed: 10-11-2020.

[61] I. Savukov *et al.* High-Sensitivity Operation of Single Beam Optically Pumped Magnetometer in a kHz Frequency Range. *Measurement Science and Technology*, 28:1–7, 2008.

[62] W. R. Smythe. Static and Dynamic Electricity. CRC Press, USA, 1989.

[63] N. Gaspar. Personal Communication. 20-11-2020.

[64] H. Scharafetter *et al.* Biological Tissue Characterisation by Magnetic Induction Spectroscopy: Requirements and Limitations. *IEEE Transactions on Biomedical Engineering*, 50(7):870–880, 2003.

[65] Dmitry Budker & Jackson Kimball. Optical Magnetometry. Cambridge University Press, UK, 2013.

[66] E. C. Simmons. Rubidium: Element and Geochemistry. Spinger, Netherlands, 1998.

[67] Daniel Adam Steck. Cesium D Line Data. `http://steck.us/alkalidata`, 2019. Online, accessed: 03-11-2020.

[68] Tobias Tiecke. Properties of Potassium. `https://www.tobiastiecke.nl/archive/PotassiumProperties.pdf`, 2019. Online, accessed: 03-11-2020.

[69] Daniel Adam Steck. Rubidium-85 Line Data. `http://steck.us/alkalidata`, 2019. Online, accessed: 03-11-2020.

[70] S. J. Seltzer. Developments in Alkali-Metal Atomic Magnetometry. PhD dissertation, Princeton University, USA, 2008.

[71] M. V. Romalis. Pressure Broadening of Rb D1 and D2 Lines by ^{3}He, ^{4}He, N_2 and Xe: Line Cores and Near Wings. *Physical Review A*, 56(6):4569–4578, 1997.

[72] T. Ida *et al.* Extended Pseudo-Voigt Function for Approximating the Voigt Profile. *Journal of Applied Crystallography*, 33:1311–1316, 2000.

[73] G. Breit & I. I. Rabi. Measurement of Nuclear Spin. *Physical Review Journal Archive*, 38:2082–2083, 1931.

[74] Alan Corney. Atomic and Laser Spectroscopy. Oxford University Press, UK, 1977.

[75] Daniel Adam Steck. Rubidium-87 Line Data. `http://steck.us/alkalidata`, 2019. Online, accessed: 03-11-2020.

[76] Michael J. Haji-Sheikh & Subhas C. Mukhopadhyay Asaf Grosz. High Sensitivity Magnetometers. Springer, Switzerland, 2017.

[77] Sho Ito *et al.* Temperature Characteristics of K-Rb Hybrid Optically Pumped Magnetometers with Different Density Ratios. *Optics Express*, 27(6):8037–8047, 2019.

[78] F. Bloch. Nuclear Induction. *Physical Review*, 70(7 & 8):460–474, 1946.

[79] D. K. Walter *et al.*. Magnetic Slowing Down of Spin-Relaxation due to Binary Collisions of Alkali-Metals with Buffer Gas Atoms. *Physical Review Letters*, 88(9):093004, 2002.

[80] N. W. Ressler *et al.*. Measurement of Spin-Exchange Cross Sections for ^{133}Cs, ^{87}Rb, ^{85}Rb and ^{23}Na. *Physical Review Letters*, 184(1):102–118, 1969.

[81] N. W. Ressler *et al.*. Spin-Exchange Cross Sections for ^{87}Rb-^{87}Rb and ^{87}Rb- ^{133}Cs Collisions. *Physical Review Letters*, 153(1):132–151, 1967.

[82] J. C. Allread *et al.*. High-Sensitivity Atomic Magnetometer Unaffected by Spin-Exchange Relaxation. *Physical Review Letters*, 89(13):130801, 1998.

[83] M. V. Balabas *et al.*. Magnetometry with Millimeter Anti-Relaxation Coated Alkali-Metal Vapour Cells. *Journal of the Optical Society of America B*, 23(6):1001–1234, 2006.

[84] S. J. Seltzer & M. V. Romalis. High-Temperature Alkali Vapour cells with Anti-Relaxation Surface Coatings. *Journal of Applied Physics*, 106(114905):1–8, 2009.

[85] A. P. Colombo *et al.*. Four-Channel Optically Pumped Atomic Magnetometer for Magnetoencephalography. *Optics Express*, 24(14):15403–15416, 2016.

[86] W. Happer & A. C. Tam. Effect of Rapid Spin-Exchange on the Magnetic-Resonance Spectrum of Alkali Vapours. *Physical Review A*, 16(5):1877–1891, 1977.

[87] Osborne *et al.*. Fully Integrated, Standalone Zero Field Optically Pumped Magnetometer for Bio-magnetism. *Proceedings of SPIE*, 10548(9):638–639, 2018.

[88] J. Dupont-Roc *et al.*. Detection of Very Weak Magnetic Fields (10^{-9} Gauss) by ^{87}Rb Zero-Field Level Crossing Resonances. *Physics Letters*, 28A(9):638–639, 1969.

[89] S. Pustelny *et al.*. Magnetometry Based on Nonlinear Magneto-Optical Rotation with Amplitude-Modulated Light. *Journal of Applied Physics*, 103(063108):1–8, 2008.

[90] COMSOL. COMSOL Multi-Physics. `https://uk.comsol.com/`, 2020. Online, accessed: 20-11-2020.

[91] Liu Ce *et al.* Noise Estimation from a Single Image. *IEEE Computer Society Conference on Computer Vision and Pattern Recognition*, pages 901–908, 2006.

[92] F. Mokhtar *et al.* Analysis of Wavelet-Based Full Reference Image Quality Assessment Algorithm. *Bulletin of Electrical Engineering and Informatics*, 8:527–532, 2019.

[93] K. Seshadrinathan *et al.* Unifying Analysis of Full Reference Image Quality Assessment. *15th IEEE International Conference on Image Processing*, 1:1200–1203, 2008.

[94] R. Soundararajan *et al.* RRED Indices: Reduced Reference Entropic Differencing for Image Quality Assessment. *IEEE Transactions on Image Processing*, 21(2):517–526, 2012.

[95] Qiang Li & Zhou Wang. Reduced Reference Image Quality Assessment Using Diversive Normalisation-Based Image Representation. *IEEE Journal of Selected Topics in Signal Processing*, 2(3):202–211, 2009.

[96] M. Carnec *et al.* Objective Quality Assessment of Color Images Based on a Generic Perceptual Reduced Reference. *Signal Processing: Image Communication*, 23(4):239–256, 2008.

[97] C. Keiichi *et al.* Reduced-Reference Image Quality Assessment using Distributed Source Coding. *IEEE International Conference on Multimedia and Expo*, 1:609–612, 2008.

[98] Wei Liu *et al.* Additive White Gaussian Noise Level Estimation in SVD Domain for Images. *IEEE Transactions on Image Processing*, 22(3):872–883, 2013.

[99] K. Rank *et al.* Estimation of Image Noise Variance. *IEEE Proceedings on Visual Signal Processes*, 146(2):80–84, 1999.

[100] S. I. Olsen *et al.* Estimation of Noise in Images: An Evaluation. *Graphical Models and Image Processing*, 55(4):319–323, 1993.

[101] M. Ponomarenko *et al.* Blind Estimation of White Gaussian Noise Variance in Highly Textured Images. *Electronic Imaging*, 1:1–5, 2017.

[102] X. Huang *et al.* Blind Noisy Image Quality Assessment using Block Homogeneity. *Computers and Electrical Engineering*, 40:796–807, 2014.

[103] Emir Turajlic. Adaptive Block-Based Approach to Image Noise Level Estimation in the SVD Domain. *Electronics*, 7(297):1–18, 2018.

[104] Wei Liu *et al.* Additive White Gaussian Noise Level Estimation based on Block SVD. *IEEE Workshop on Electronics, Computer and Applications*, pages 960–963, 2014.

[105] P. Sridhar *et al.* Noise Standard Deviation Estimation for Additive White Gaussian Noise. *International Journal of Innovative Technology and Exploring Engineering*, 8(11):424–431, 2019.

[106] D. Chaudhuri *et al.* Semi-Automated Road Detection from High Resolution Satellite Images by Directional Morphological Enhancement and Segmentation Techniques. *IEEE Journal of Selected Topics in Applied Earth Observations and Remote Sensing*, 5(5):1538–1544, 2012.

[107] D. Chaudhuri *et al.* Object Detection Based on Sparse Representation and Hough Voting for Optical Remote Sensing Imagery. *IEEE Journal of Selected Topics in Applied Earth Observations and Remote Sensing*, 8(5):2053–2062, 2015.

[108] R. Ward. Significant Contribution: Previously Developed LabView Software for X-Y Stage Control. 01-10-2020.

[109] J. Vaughan-Williams. Significant Contribution: Apparatus constructed in student project. 01-10-2020.

[110] Sun M.J *et al.* Single-Pixel Three-Dimensional Imaging with Time-Based Depth Resolution. *Nature Communications*, 7(12010):1–6, 2016.

[111] J. Boakes. Significant Contribution: Design and construction of H-bridge circuit. 01-09-2020.

[112] J. Collard. Significant Contribution: COMSOL model provided. 01-12-2020.

[113] B. S. Chandrasekhar *et al.* The Electrical Resistivity and Super Conductivity of Some Uranium Alloys and Compounds. *Journal of Physical and Chemical Solids*, 7(2-3):259–267, 1958.